Design and Development of Metal Hydride System for Thermal Energy Storage and Hydrogen Storage Applications

A thesis submitted in partial fulfilment of the requirements for the degree of

Doctor of Philosophy

by

J. Sunku Prasad
(Roll No: 166103002)

Department of Mechanical Engineering
Indian Institute of Technology Guwahati
Guwahati-781039, India
December 2022

Department of Mechanical Engineering
Indian Institute of Technology Guwahati
Guwahati - 781039, Assam, India

CERTIFICATE

This is to certify that the work contained in the thesis entitled "**Design and Development of Metal Hydride System for Thermal Energy Storage and Hydrogen Storage Applications"** submitted by **J. Sunku Prasad (Roll No. 166103002)**, to the Indian Institute of Technology Guwahati for the award of the degree of **Doctor of Philosophy** has been carried out under my supervision in the Department of Mechanical Engineering, Indian Institute of Technology Guwahati. This work has not been submitted elsewhere for the award of any other degree or diploma.

Prof. P. Muthukumar
Department of Mechanical Engineering
Indian Institute of Technology Guwahati
Guwahati – 781039, India

Dedicated to my parents

Mr. J. Sunkanna (Late)

and

Mrs. J. Aswarthamma

Acknowledgment

First and foremost, I feel it is a great privilege to express my deepest and most sincere gratitude to my supervisor Prof. P. Muthukumar for his invaluable guidance, encouragement and support during my M. Tech and Ph.D. research work. His inspiring guidance, motivation and sincere advice have enabled me to overcome all the difficulties during my research. I look forward to working with him and further developing our relationship.

I am thankful to my doctoral committee members, Prof. Manmohan Pandey, Dr. Dipankar Narayan Basu, and Prof. Pugazhenthi, for giving their valuable suggestions and encouragement, which helped in the successful completion of this thesis. I sincerely thank Prof. S. K Dwivedi (ex. HOD) and Prof. K.S.R.K Murthy (HOD) for providing all the facilities in the department needed for my research work. I take this opportunity to thank Prof. Gautham Biswas, Prof. Vinay Kulkarni, Prof. Hrishikesh Gadgil, and Prof. Amaresh Dalal for inspiring me with their excellent teaching.

I also thank Prof. S.S Murthy, Prof. Pradip Dutta, and Mr. Malleswara Rao from Energy storage laboratory, Interdisciplinary Centre for Energy Research, IISC Bangalore for providing the magnesium-nickel alloy for my experiments. The support from Prof. Anil Kumar and Mr. Sarath Babu from Thermal Engineering Laboratory, Department of Mechanical Engineering, IIT Tirupati in obtaining the P-C-I data is highly appreciated.

I want to thank the Department of Science and Technology (DST), Government of India, for their financial support in the fabrication of the experimental setup (Project No: DST/TM/SERI/2K10/53(G)) and the international travel grant for presenting the research output in the international conference on Polygeneration (ICP–2019) held at Kyushu University, Fukuoka, Japan (Grant Id: ITS/2019/ 000946).

I thank my research collaborators, Dr. Fenil Desai and Prof. Muhammad M. Rahman, Wichita State University, USA, for their encouragement and inspiring discussions.

I especially thank my lab technician, Mr. Gabinda Boro, for his support during the experimental setup fabrication. I also thank the departmental personnel, Mr. N.K Das, Mr. Gokul Das, Mr. Dilip Chetri, Mr. Mrinal Sarma, Mr. Dulumoni Das, Mr. Santush Gogoi, Mr. Jiten Basumatary, Mr.

Ratan Medhi, and Mr. Nip Borah, for their help during the fabrication of the reactors and experimental setup.

I am thankful to the metal hydride research team at IIT Guwahati comprising of Dr. Nithin Narmada, Dr. Alok Kumar, Mr. Sayantan Jana, Mr. Abhishek Parida, and Mr. Shubham Parashar for their constant support and encouragement. I further thank my lab colleagues, Mr. Sureandhar, Dr. Mrinal Bhowmik, Mr. Arun Kumar, Mr. Masresha, Dr. Sunita Deb, Ms. Pratibha Maurya, Mrs. Juri Sonowal, Mr. Suraj Tat, Mr. Aswin, Ms. Nayanita Kalita, Ms. Akshini and Mr. Abhishek Jaiswal for their support and friendship.

The encouragement and guidance from my seniors, Dr. Hakeem Niyas, Dr. Satya Sekhar, Dr. Viswanth, Dr. Ravi Chandra Rao, Dr. Kiran Naik, Dr. Vigneshwaran, Dr. Gurpreet Singh, and Dr. Lav Kumar Kaushik are highly appreciated.

I also thank my friends, Mr. Sandilya, Mr. Satish, Mr. Sudarshan, Mr. Vimal, Dr. Shashidhar Reddy, Mr. Yaswanth, Dr. Nirmal M.S, Mr. Arnab Lahiri, Mr. Soma Malli Karjuna, and Mr. Jyothish, for their love, support and motivation throughout my research career at IIT Guwahati.

I want to thank all the weekend cricket teammates in IIT Guwahati for their valuable time, love and support.

I express my sincere gratitude to my brother, Mr. Suryanayana, for inspiring and encouraging me in all parts of my life. My sister, Mrs. Sulochana, is highly acknowledged for her love and continuous support.

Above all, I am thankful to the Almighty God for giving me strength, health, and spirit for conducting my research work.

Date: 22-12-2022

J. Sunkuprasad

(J. Sunku Prasad)

Abstract

The world is progressing toward renewable energy resources because of the increase in demand for energy, the price of fossil fuels and the global warming effect. A major shift from fossil fuels to renewable energy sources is needed to save the environment from global warming and climate change. Therefore, the world is now investing in renewable energy technologies to meet the increasing energy demand and reduce greenhouse gas emissions. Solar, wind, tidal, and geothermal are the primary resources explored effectively, where solar energy is one of the promising large-scale power generation technologies among the other renewables. Solar energy can be converted into electricity in two ways, i.e., using solar photovoltaic or concentrated solar thermal power technology. Renewable energy sources are often limited for commercial use due to their intermittent nature, i.e., inconsistent energy supply and demand. This issue in concentrated solar thermal power (CSTP) technology can be addressed by integrating a thermal energy storage (TES) system. The excess thermal energy is stored in the TES system during sunshine hours. The stored energy is retrieved for producing electricity during the off-sun hours, making the CSTP plant operate continuously throughout the day and night. Thermal energy can be stored in three different ways: sensible heat storage (SHS), latent heat storage (LHS), and thermochemical energy storage (TCES). The TCES system offers high energy density, wide operating temperatures, and long-term storage among all TES systems.

Another promising technology for storing excess renewable energy is in the form of hydrogen. Hydrogen as an energy carrier offers large-scale, long-term, and seasonal storage of excess renewable energy. The excess electricity produced by renewables (primarily wind and solar PV) during low energy demand periods generates hydrogen using an electrolyzer. The stored hydrogen is utilized in stationary fuel cells for combined power and heat as per the demand.

Metal hydrides (MHs) are the most promising solid-gas TCES reactions for TES and hydrogen storage applications. Metal hydrides (MHs) are compounds formed by the reversible reaction of hydrogen and metallic atom. As per the TES is concerned, MHs have high energy density (up to 2.8 MJ/kg of hydride) and a wide range of operating temperatures (up to 1100°C) with no environmental encroachment. For hydrogen storage, MHs offer higher volumetric storage density at near-ambient conditions. Therefore, this dissertation studies the TES and hydrogen storage

aspects of MHs. The main objectives of the present work are (a) to develop a mathematical model for analyzing the absorption and desorption characteristics of the MH reactor, (b) to design a simple, lightweight and efficient MH reactor for large-scale TCES and hydrogen storage applications, and (c) to conduct a detailed experimental study on MH-based TES and hydrogen energy storage systems.

A numerical model is developed to study the heat and mass transfer characteristics of the porous MH bed during absorption and desorption processes. Firstly, the discharging behavior of the tubular reactors filled with magnesium-nickel hydride is analyzed for the heat transfer coefficient of 250 W/m^2-K. Therminol VP1 is considered as a heat transfer fluid (HTF). For tubular reactors, the discharging time increased with the diameter. However, the energy storage density increased with the diameter of the tubular reactor. The drawbacks of a smaller diameter tubular reactor are less energy storage density and the requirement of a greater number of tubes for the given energy storage capacity. Therefore, an annular MH reactor is proposed to reduce the discharging time of the tubular reactor without a significant drop in its energy storage density. With the proposed annular MH reactor, the discharging time of a 2.5-inch tubular reactor is reduced up to 70%, with only 16% comptonization in gravimetric energy storage density. Also, the average specific discharge power of the 2.5-inch tubular reactor is increased by ~2.5 times with the annular MH reactor.

For real-time TES storage applications, the discharging time of the reactors present near the MH array outlet section is much higher than 360 min (the DOE target's limit). Therefore, radial fins are incorporated in the annular MH reactor to improve the heat transfer characteristics of the reactors present near the outlet section of the MH array. The addition of radial fins reduced the discharging time to 333 min, i.e., 1.93 times lower than the case without fins. Finally, the system level gravimetric storage density of the annular MH reactor with radial fins is 560 kJ/kg of system, which is much higher than the material level energy storage density of the sensible (maximum of 108 kJ/kg of material) and latent heat (maximum of 360 kJ/kg of material) storage systems.

Further, the design of the annular MH reactor is extended to hydrogen storage application with $LaNi_5$ as MH material. The absorption and desorption characteristics of the annular porous MH reactor filled with $LaNi_5$ are investigated. Three reactor configurations are compared to analyze

the effect of HTF flow direction and adding radial fins on the absorption and desorption processes. The absorption time of 945 s is obtained with the finned tube reactor under the supply pressure of 15 bar and cooling fluid temperature of 25°C. During desorption, the finned tube reactor achieved a desorption time of 1290 s for the HTF temperature of 50°C. The addition of fins enhanced the absorption and desorption rates by 1.84 and 1.85, respectively. Finally, a modular design of annular porous MH reactors with radial fins is proposed for large-scale hydrogen storage applications.

Based on the numerical results, lab-scale prototypes of the annular MH reactor with radial fins are fabricated. Two MH alloys, namely, $LaNi_5$ and $La_{0.7}Ce_{0.1}Ca_{0.3}Ni_5$ are experimented under different operating conditions for hydrogen storage applications. A mass of 9 kg was filled inside the reactor for each alloy. The developed MH reactor offered a hydride-to-reactor mass ratio of 1.44 with a working pressure of 80 bar. The $LaNi_5$ reactor showed system-level gravimetric and volumetric storage densities of 0.73% and 20.4 kg of H_2 per m^3, respectively. The same for $La_{0.7}Ce_{0.1}Ca_{0.3}Ni_5$ reactor are 0.8% and 22.4 kg of H_2 per m^3, respectively. Further, the $La_{0.7}Ce_{0.1}Ca_{0.3}Ni_5$ reactor offered an energy storage efficiency of 77.54%. Overall, the annular MH reactor with internal radial fins is a promising option for medium to large-scale hydrogen storage applications due to its higher weight ratio, ease of fabrication, savings in pumping power, and better performance.

Further, the annular metal hydride reactor with internal radial fins was experimented for thermal energy storage applications. The magnesium-nickel alloy and air are chosen as MH material and HTF for the experiments. The reactor was filled with 3.76 kg of magnesium-nickel alloy. Firstly, the absorption and desorption characteristics of the magnesium-nickel alloy were studied in a single reactor mode. Magnesium-nickel alloy is activated in the seventh activation cycle, reaching 3.91 wt.%. The alloy absorbed 104, 142, and 143 g of hydrogen in 122, 78.3, and 62.5 min, respectively, under the supply pressure of 10, 20, and 30 bar. Also, the desorption time is approximately two times more than the absorption time, and increasing the desorption temperature has not shown any significant effect on the desorption rate.

Finally, a thermal-driven coupled MH reactor system is studied with two alloy pairs: magnesium-nickel alloy/ $LaNi_5$ and magnesium-nickel alloy/ $La_{0.7}Ce_{0.1}Ca_{0.3}Ni_5$. The charging and discharging times are within 360 min, except for the charging process at 374°C for magnesium-nickel alloy/ $La_{0.7}Ce_{0.1}Ca_{0.3}Ni_5$. In the thermal-driven coupled MH reactor system, the line pressure was

influenced by the equilibrium pressure of the hydrogen storage alloy due to its faster reaction kinetics and better heat transfer characteristics. Also, a compressor-driven MH-based TES system is proposed to produce an additional cooling effect in the hydrogen storage reactor.

Nomenclature

A	: Material constant
B	: Material constant (K)
c	: Concentration
C	: Reaction rate constant (s^{-1})
C_p	: Specific heat (J kg^{-1} K^{-1})
d, D	: Diameter (mm)
E	: Activation energy (J mol^{-1}) or Energy (J)
$\bar{h}$	: Average heat transfer coefficient
ΔH	: Reaction enthalpy (J mol^{-1})
k	: Thermal conductivity (W m^{-1} K^{-1})
K	: Permeability (m^2)
$\dot{m}$	: Hydrogen mass transferred per unit time and unit volume (kg m^{-3} s^{-1})
M	: Molecular weight (kg mol^{-1})
n	: Number of moles
N	: Number of atoms
$\overline{Nu}$	: Average Nusselt number
P	: Power (W)
Pr	: Prandtl number
ΔP	: Pressure drop (Pa)
r, z	: Coordinate axes
R_g	: Specific gas constant for hydrogen (J mol^{-1} K^{-1})
Re	: Reynolds number
R_u	: Universal gas constant (J kg^{-1} K^{-1})
t	: Time (s)
T	: Temperature (K)

u, v	: Velocities (m s^{-1})
$wt.\%$	: Weight percentage
V	: Volume (m^3)

Greek letters

β	: Hysteresis factor
ε	: Porosity
μ	: Dynamic viscosity (Pa. s)
ϕ_s	: Slope factor
ϕ_0	: Slope constant
ρ	: Density (kg m^{-3})

Subscripts

a/ abs	: Absorption
d/ des	: Desorption
c	: Combustion
e	: Effective
eq	: Equilibrium
f	: Heat transfer fluid
g	: Gas
H_2	: Hydrogen gas
i	: Initial
o	: Empty
s	: Solid/ hydride
sat	: Saturation
sd	: Solid domain
w	: Water
in	: Inlet
out	: Outlet

Abbreviations

CSTP	: Concentrated solar thermal power
ECT	: Embedded cooling tube
ENG	: Expanded natural graphite
HHV	: Higher heating value
HTF	: Heat transfer fluid
HTMH	: High temperature metal hydride
IEA	: International energy agency
LHS	: Latent heat storage
LTMH	: Low temperature metal hydride
MH	: Metal Hydride
NL	: Normal litre
PCM	: Phase change material
PEMFC	: Proton exchange membrane fuel cells
SCSD	: System volumetric storage density
SGSD	: System gravimetric storage density
SHS	: Sensible heat storage
SOEC	: Solid-oxide electrolyzer cell
SOFC	: Solid-oxide fuel cell
STP	: Standard temperature and pressure conditions
TCES	: Thermochemical energy storage
TES	: Thermal energy storage

Contents

List of Figures

List of Tables

Chapter 1

Introduction

1.1 Preface

Deteriorating reserves of fossil fuels, mounting concern over global warming, and the accelerating rise in energy requirements have forced the power-producing industries to shift their focus from conventional modes to renewable resources. The Paris Agreement, signed by 195 countries in a fight against climate change, demands that each participating nation plans and implements actions to alleviate global warming. While an ideal scenario would envisage the complete transformation from fossil fuels to renewable energy, only about 23% of the potential global renewable energy needs to be harnessed (Peng et al., 2017), leaving ample opportunity for improvement and innovation. The target of net zero emissions by 2050 can only be achieved by increasing the share of renewables in the power, cooling and heating sectors. Further, the current share of renewable energy has to be increased to 86% from the present value of 26% to achieve net-zero emissions by 2050 (IRENA, 2020). Solar, wind, tidal, and geothermal are the primary resources explored to date, with solar being the most prevalent option for obvious reasons. As a gross estimate, 173,000 TW of solar energy reaches the earth continuously, which is 10,000 times more than the total energy needs of the world (Erin, 2016). However, the power generated from solar and wind is variable across daily and seasonal timescales. Therefore, there is an essential need to match energy supply and demand by integrating energy storage technologies in the renewable energy supply chain. Energy storage technologies enable a stable, flexible, and cheaper energy infrastructure. In this aspect, thermal energy storage and hydrogen as an energy carrier are the two enabling technologies for storing excess renewable energy.

1.2 Thermal energy storage (TES) system

The TES system provides an excellent remedy for correcting the mismatch between energy supply and demand. TES system can help high penetration of renewable energy in power generation, industry and buildings (IRENA, 2020). During the hours of solar insolation, the excess energy can be stored in a TES system, which can be retrieved for electricity production during off-sun hours. Thermal energy can be stored in three different ways: sensible heat

storage (SHS), latent heat storage (LHS), and thermochemical energy storage (TCES)(Pardo et al., 2014b). Based on the operating temperature range, the TES systems are classified as low temperature (below 150°C), medium temperature (150 to 400°C), and high temperature (above 400°C) (IRENA, 2020). Details of the corresponding storage principle and other relevant aspects for each of these three techniques are summarized in Table 1.1.

Table 1.1 Comparison of SHS, LHS, and TCES techniques (Pardo et al., 2014b; Zalba et al., 2003; Zhang et al., 2016)

Feature	**SHS**	**LHS**	**TCES**
Principle	• Thermal energy is stored as sensible heat in storage material by increasing its internal energy (i.e., change of temperature of storage media). • Energy storage capacity depends on the specific heat of the storage material and its allowable temperature increase.	• Thermal energy is stored by phase change of material at constant or near-constant temperature as the heat of fusion. • Energy storage capacity depends on latent heat.	• TCES relies on energy absorbed (endothermic) and released (exothermic) in breaking and reforming molecular bonds in an entirely reversible chemical reaction. • Energy storage capacity depends on reaction enthalpy and the number of moles of reactant involved.
Energy stored/released	$E = mC_p(T_f - T_i)$	$E = m_{pcm}H_{fg}$	$E = n \cdot \Delta H_r$
Other factors affecting energy storage/release characteristics	• Thermal conductivity of storage material • Diffusivity • Vapor pressure (in case of liquid storage media)	• Thermal conductivity of PCM • Super cooling and phase segregation	• Thermal conductivity of reaction materials • Supply pressure of reactant gas • Catalyst activity
Materials	*Solid media:* Pebble beds, concrete, bricks, sand, cast steel, cast iron, etc. *Liquid media:* Water, molten salts, mineral oils, petroleum-based oils, etc.	*Organic:* Paraffin, non-paraffin. *Inorganic:* Salt hydrates, metals. *Eutectics:* Inorganic-organic, inorganic-inorganic, and organic-organic.	Ammonia synthesis/ dissociation, methane reforming, metal hydrides, metal oxides, carbonates, hydroxides, etc.
Volumetric energy storage density (E_v)	Small (~50 kWh/m^3)	Medium (~100 kWh/m^3)	High (~500 kWh/m^3)
Gravimetric energy storage density (E_g)	Small (0.02–0.03 kWh/kg)	Medium (0.05–0.1 kWh/kg)	High (0.5–1 kWh/kg)
Storage temperature	Charging step temperature	Charging step temperature	Ambient temperature
Storage period	Limited due to significant heat loss to surroundings	Limited due to significant heat loss to surroundings	Theoretically unlimited
Energy transport	Very small distance	Very small distance	Relatively long distance (more than 100 km)

Feature	**SHS**	**LHS**	**TCES**
Maturity of technology	Industrial scale	Pilot-scale	Laboratory and pilot-scale

About 47% of current CSTP plants employ SHS adopting two-tank molten salt storage to generate electricity on demand (Medrano et al., 2010; Pelay et al., 2017). The major concerns associated with these systems are inferior energy density, massive storage volume requirement, expensive heat exchangers, the obligation of heavy insulation to minimize energy leakage, and the necessity of installing axillary heaters to avoid the freezing of molten salts in the heat-transfer fluid (HTF) circuits. In contrast to the SHS system, the LHS system has the advantage of higher energy density and the ability to operate at near-constant temperatures. However, phase change material (PCM) suffers from several drawbacks, including corrosion of metallic walls, phase segregation, chemical instability, supercooling, improper re-solidification and uncertainty over long-term thermal behavior (Lefebvre and Tezel, 2017). The reversible TCES system stores and releases heat during reverse endothermic and exothermic reactions. In a forward endothermic reaction, the thermal energy is stored as chemical potential by dissociating the product of the reaction. The stored energy is retrieved during the reverse exothermic reaction by recombining the chemical reactants. The TCES system offers a high energy storage density (usually five to ten times higher than SHS and LHS systems), a wide operating temperature range (from 100°C to over 800°C), and long-term storage (André et al., 2016). Hence, the TCES system is best suited as an energy storage system for storing excess renewable energy. In addition, the ideas and methodology of TCES can also be extended to a much broader range of applications (Fig. 1.1).

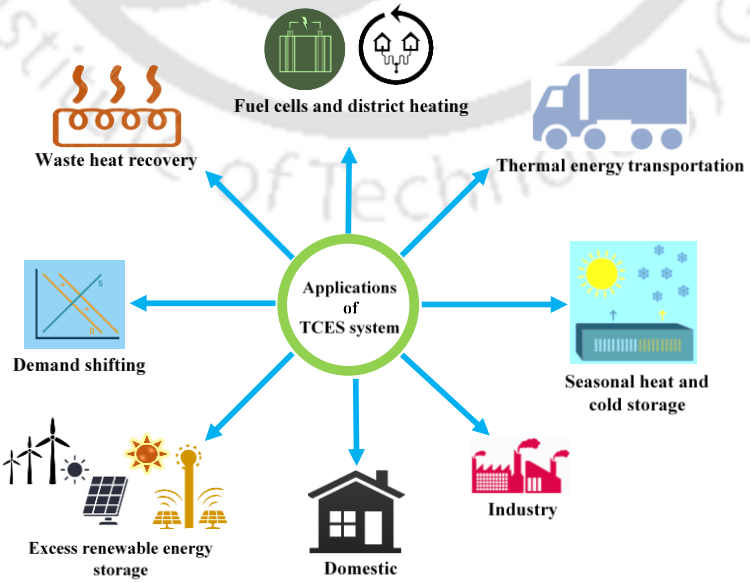

Fig. 1.1. Applications of TCES system

1.2.1 Thermochemical energy storage (TCES) system

The thermochemical reactions are reversible, with thermal energy supplied and released during the endothermic and exothermic steps. The operation of the TCES system involves three major steps: charging, storage, and discharging, and the schematic representation of these chemical reactions is shown in Fig. 1.2. Charging is an endothermic reaction. Thermal energy is used to dissociate the chemical reactant (AB) into products (A and B). After the charging process, the sensible heat contained in the products (A and B) is recovered in a heat exchanger. These products are separated and stored at ambient temperature. Subsequently, the products are sensibly heated to the reaction temperature (preheating) before initiating the discharge process. After preheating, the products (A and B) are combined through an exothermic reaction to retrieve the reactant (AB). The energy released during discharge is supplied to the power cycle for producing electricity. The advantages of the TCES system over the other TES systems are high energy storage density and, a wider range of working temperature and pressure, the ability to control the rate of heat evolution.

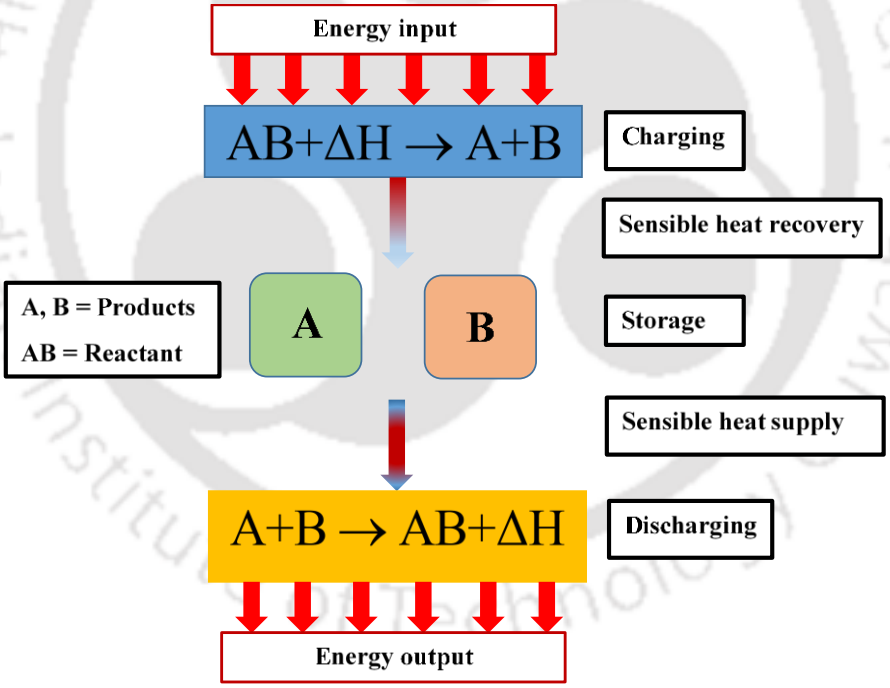

Fig. 1.2. Schematic of steps involved in TCES system: charging, storage, and discharging

Thermochemical energy storage reactions are classified as reversible reaction-based storage and sorption-based energy storage (Solé et al., 2015). Reversible reaction-based storage systems involve a reversible reaction of two separate chemical substances where a high amount of energy is generated as a result of an exothermic reaction. In a sorption-based energy storage system, thermal energy is stored by breaking the binding force between the sorbent and the

sorbate in terms of chemical potential. Following the available literature, TCES reactions are classified into solid-gas, liquid-gas, and gas-gas (Fig. 1.3) (Ervin, 1977; Yan et al., 2015). Table 1.2 shows the storage properties of solid-gas and gas-gas TCES reactions suitable for medium to high-temperature applications.

Among all the TCES materials, Metal hydrides (MHs) are promising sorption materials for TES and heating applications. They provide high energy density (as high as 2814 kJ/kg of hydride), a wide range of operating temperatures (up to 1100°C with no environmental encroachment (d'Entremont et al., 2018; Rönnebro et al., 2015). Also, MH-based TES system offers a volumetric storage density of about 90 kWh_{th}/m^3, which is 3.6 times more than the US Department of Energy SunShot target (Mellouli et al., 2018).

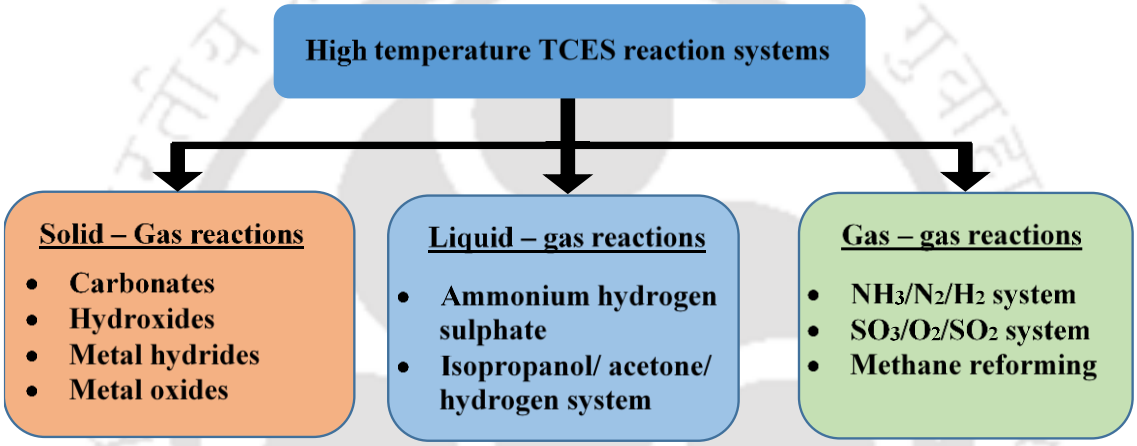

Fig. 1.3. Classification of high-temperature TCES reactions

Table 1.2 Promising high-temperature TCES reactions

Reaction	**T_{range} (°C)**	**P_{range} (bar)**	**ΔH (kJ/mol)**	**E_g (kJ/kg)**	**E_v (MJ/m^3)**	**Reference**
SOLID-GAS REACTION SYSTEM						
Carbonates:						
$CaCO_{3(s)} + \Delta H \rightleftharpoons CaO_{(s)} + CO_{2(g)}$	973–1273	0–10	178	3029	3260	(Kyaw et al., 1997; Meier et al., 2004; Pardo et al., 2014b)
$SrCO_{3(s)} + \Delta H \rightleftharpoons SrO_{(s)} + CO_{2(g)}$	900–1200	0–2	234	300–1000	1200–1500	(Bagherisereshki et al., 2018)
$BaCO_3 + \Delta H \rightleftharpoons BaO_{(s)} + CO_{2(g)}$	~1290	–	273	–	–	(Yan et al., 2015)(André and Abanades, 2017)
$PbCO_{3(s)} + \Delta H \rightleftharpoons PbO_{(s)} + CO_{2(g)}$	573–1730	0–1	88	–	–	(Pardo et al., 2014b)
$MgCO_{3(s)} + \Delta H \rightleftharpoons MgO_{(s)} + CO_{2(g)}$	320 – 431	0.1 – 2	116.4	–	–	(Shkatulov et al., 2019)
Hydroxides:						
$CaO + H_2O \rightleftharpoons Ca(OH)_2 + \Delta H$	400–600	0.1–10	104.4	~2000	1640	(Schaube et al., 2011; Yan and Zhao, 2015; Yan et al., 2015)s
Metal Hydrides:						
Reaction	**T_{range} (°C)**	**P_{range} (bar)**	**ΔH (kJ/mol.H_2)**	**Wt%**	**E_g (kJ/kg)**	**E_v (MJ/m^3)**	**Reference**
$Mg + H_2 \rightleftharpoons MgH_2 + \Delta H$	300–480	1–63	75	5.8	2160	3995	(Wierse et al., 1991)
	300–500	1–100	74	6	2814 (theo.) 2204 (expt.)	3996 (theo.) 1763 (expt.)	(Bogdanovi et al., 2002)

$2Mg + Fe + 3H_2 \rightleftharpoons Mg_2FeH_6 + \Delta H$	300–500	0–60	77.4	5.0	2106 (theo.) 1921 (expt.)	5768 (theo.) 2344 (expt.)	(Felderhoff and Bogdanović, 2009)
$Mg_2Ni + 2H_2 \rightleftharpoons Mg_2NiH_4 + \Delta H$	253–523	1–20	64.6	3.62	1159.7	3142.7	(Møller et al., 2017; Reilly and Wiswall, 1968a)
$NaH+Mg+H_{2(g)} \rightleftharpoons NaMgH_3+\Delta H$	475–575	7–37	86.6	3.3	1721	~ 1721	(Sheppard et al., 2014)
$NaF+Mg+H_{2(g)} \rightleftharpoons NaMgH_2F+\Delta H$	510–605	7–37	96.8	2.5	1416	1968	(Sheppard et al., 2014)
$2TiH + H_2 \rightleftharpoons 2TiH_2 + \Delta H$	650–750	1–10	170	1.05	890	4014	(Friedlmeier et al., 1994)
$Ca + H_2 \rightleftharpoons CaH_2 + \Delta H$	1100 –1400	1–5	186	4.5	3857	7374	(Møller et al., 2017; Rönnebro et al., 2015)
$CaAl_2+H_2 \rightleftharpoons CaH_2+2Al+\Delta H$	~600	–	83.1	2.1	865	~1488	(Ward et al., 2018)
$Na + 0.5H_2 \rightleftharpoons NaH + \Delta H$	600	53	117	4.2	2072	2890.8	(Manickam et al., 2019)
Metal Oxides:							
Reaction	**T_{range} (°C)**	**P_{range} (bar)**	**ΔH (kJ/mol)**		**E_g (kJ/kg)**	**E_v (MJ/m^3)**	**Reference**
$2Co_3O_4+\Delta H \rightleftharpoons 6CoO+O_2$	~900	~1	200		844	720	(Agrafiotis et al., 2014; Neises et al., 2012)
$2BaO_2+\Delta H \rightleftharpoons 2BaO+O_2$	~740	~1	79.4		527.18	3015	(Fahim and Ford, 1983)
	727– 1027	0.11–1	77.3		468	2900	(Bowrey and Jutsen, 1978; Møller et al., 2017)
$6Mn_2O_3+\Delta H \rightleftharpoons 4Mn_3O_4+O_2$	T_{eq} = 1000	~1	32		204	225	(Agrafiotis et al., 2016; Álvarez De

						Miguel et al., 2013)
$4CuO+\Delta H \rightleftharpoons 2Cu_2O+O_2$	T_{eq} = 1030	<1	64	811	–	(Agrafiotis et al., 2016; Jafarian et al., 2017)
LIQUID-GAS REACTION SYSTEM						
$NH_4HS.O_{4(l)}+\Delta H \rightleftharpoons NH_{3(g)}+H_2O_{(g)}+SO_{3(g)}$	417	1.48	336	–	3016 (theo.)	(Pardo et al., 2014b)
GAS-GAS REACTION SYSTEM						
Ammonia Synthesis/Dissociation:						
$2NH_{3(g)} + \Delta H \rightleftharpoons N_{2(g)} + 3H_{2(g)}$	400–700	100–300	66.9	3924	0.675	(Dunn et al., 2012)
Methane Reforming:						
$CH_{4(g)}+H_2O_{(g)}+\Delta H \rightleftharpoons 3H_{2(g)}+CO_{(g)}$	1000–1500	20–150	250	–	28.1	(Pelay et al., 2017)
$CH_{4(g)}+CO_{2(g)}+\Delta H \rightleftharpoons 2H_{2(g)}+2CO_{(g)}$	1000–1500	3.5	247	–	27.7	(Pelay et al., 2017)
$SO_3/O_2/SO_2$ System:						
$2SO_{3(g)}+\Delta H \rightleftharpoons 2SO_{2(g)}+O_{2(g)}$	1000–1500	1–5	197.9	–	2325.6	(Pelay et al., 2017; Prieto et al., 2016)

– Data not available; wt% = amount of hydrogen absorbed per kg of MH alloy

1.3 Hydrogen economy: hydrogen as an energy carrier

Storing the excess renewable energy in the form of hydrogen is another potential option to solve the intermittent nature of renewables. Hydrogen as an energy carrier offers a large-scale, long-term, and seasonal storage of excess renewable energy. The schematic of hydrogen as an energy carrier is shown in Fig. 1.4. The excess electricity produced by renewables during low energy demand periods is used to generate hydrogen using an electrolyzer. The produced hydrogen is stored in compressed gas in high-pressure tanks, cryogenic liquid, and metal hydrides for later use. The stored hydrogen is utilized in stationary fuel cells for combined power and heat as per the energy demand. The produced hydrogen can also be used as an industrial feedstock for ammonia/ methanol production and injected into natural gas networks to reduce carbon footprint.

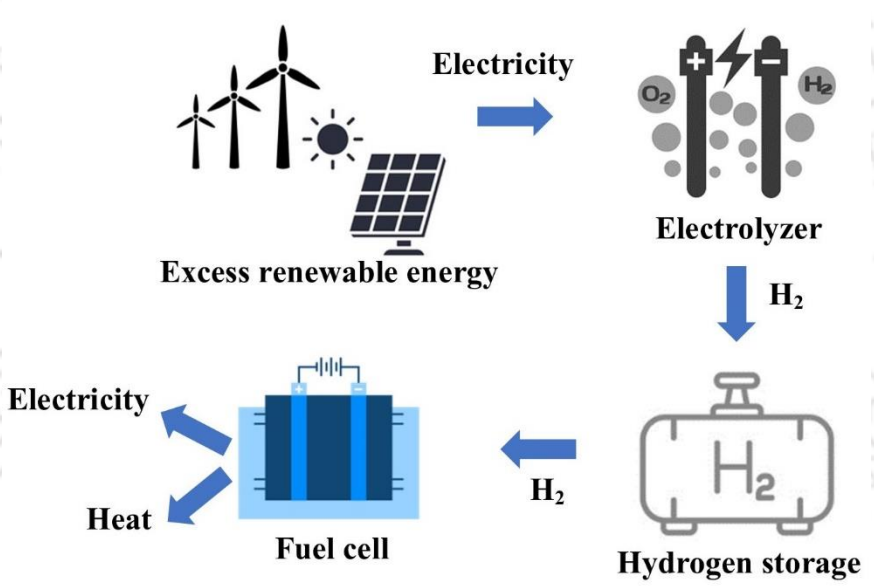

Fig. 1.4. Schematic of hydrogen economy: hydrogen as an energy carrier

In a hydrogen economy, the main steps include production, storage, and utilization of hydrogen. Electrolyzers are used to produce green hydrogen using excess renewable energy. Today's electrolyzers operate at an efficiency (based on the lower heating value of hydrogen) of up to 81%. Proton exchange membrane electrolyzers operate with 56-60% efficiency, whereas solid oxide electrolyzer cell operates at 74-81% (IEA, 2019). When it comes to utilization, the Proton Exchange Membrane Fuel Cells (PEMFC) work at an efficiency of up to 60% (Rivard et al., 2019). The hydrogen gas is stored in a high-pressure tank by compressing it to 250-350 bar. About 8.5% of the energy content of the hydrogen is consumed in compressing the hydrogen to 350 bar. On the other hand, storing hydrogen at cryogenic

temperatures (below 20 K) in a well-insulated cryogenic storage vessel consumes approximately 25%–30% of the energy content of the stored hydrogen (El-Eskandarany, 2020). Another promising storage method is solid-state hydrogen storage using metal hydrides. Solid state hydrogen storage is one of the best solutions that can work from kWh to GWh scale units (Jehan and Fruchart, 2013). Metal hydrides offer higher volumetric storage density at near-ambient conditions (Muthukumar et al., 2018). Unlike other storage methods, MHs need only waste heat available at 40-100°C as an energy input for their operation. Around 40% of the energy content of the hydrogen (i.e., 114.2 kJ/mol based on HHV) is released as heat in the fuel cells (Nguyen and Shabani, 2021). The reaction enthalpy of MHs (AB, AB_2, A_2B, AB_5, and some complex hydrides used in hydrogen storage applications) is well below 80 kJ/mol (Lototskyy et al., 2017; Weiss-Ungethüm et al., 2014). Hence, a part of the exhaust heat of the fuel cell could be utilized for desorbing the hydrogen from the MH tank without needing any external work. Using waste heat instead of electrical energy for operating the hydrogen storage system is a promising way to increase the hydrogen economy's overall efficiency. Another method of operating the solid-state hydrogen storage system is storing its exothermic heat in a phase change material and utilizing it for desorbing the hydrogen. In such a system, the PCM stores the exothermic heat during absorption and releases the endothermic heat during desorption of the MH bed.

Energy storage technologies will play a crucial role in increasing the share of renewables in the current energy infrastructure. TES is the most attractive technology within the available energy storage systems due to its energy storage efficiency (up to 95%-97%), cost-effectiveness (cost is only 1/30 of a large-scale electrical battery), and long cycle life. The sorption-based TCES is a promising technology for seasonal storage and offers higher energy storage density and wide operating temperatures. On the other hand, hydrogen storage is another promising technology for solving the problem of the intermittent nature of renewable energy resources. In this perspective, MHs are promising technology for both TES and hydrogen storage.

1.4 Metal Hydrides

Metal hydrides are compounds formed/decomposed by the reversible chemical reaction of hydrogen and a metal (Fig. 1.5) by releasing/absorbing thermal energy. The general reaction between metals/alloys with hydrogen to form metal hydrides is shown below.

$$M + \frac{x}{2}H_2 \Leftrightarrow MH_x + \Delta H$$

where M is a metal or an intermetallic compound, MH_x is the respective hydride, and ΔH refers to the heat of reaction.

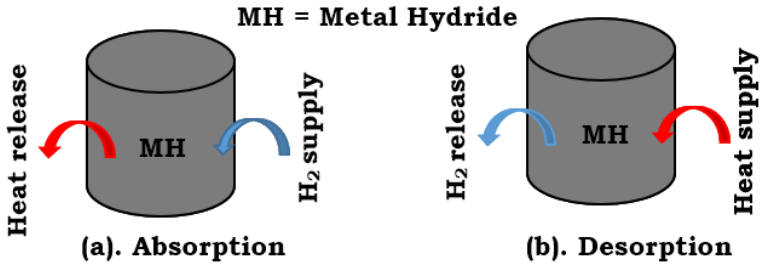

Fig. 1.5. Absorption and desorption process of the metal hydrides

1.4.1 Formation of metal hydrides

The process of hydride formation/ decomposition involves three stages including (i) surface dissociation of H_2 molecules/ recombination of H atoms, (ii) diffusion of H atoms in solid solution in the metal, (iii) formation / decomposition of hydride phase where H atoms are located in between the atoms of the metallic matrix. Initially, the hydrogen molecule interacts with several atoms on the solid's metallic surface, leading to a physisorbed state. In the next step of the hydrogen-metal interaction, the hydrogen has to overcome an activation barrier to create catalytically active sites for the dissociative chemisorption of hydrogen. After dissociation on the metal surface, the H atoms have to diffuse into the bulk to form M-H solid solution commonly referred to as α-phase. After reaching a saturated state, the hydride phase (β – phase) or metal hydride forms by chemical reaction $MH_{\alpha}+H \longrightarrow MH_{\beta}$ with the coexistence of α (solution) and β (hydride) phases: intermediate plateau region. The following equation represents the whole process of hydrogen uptake by the metal.

$$M+\frac{y}{2}H_2 \longleftrightarrow MH_y \qquad (\alpha-\text{phase})$$

$$MH_y+\frac{x-y}{2}H_2 \longleftrightarrow MH_x \ (\beta-phase)$$

Generally, the equilibrium data for metal hydrides is obtained by measurement of pressure and concentration of the hydrogen in the metal sample at constant temperature in a closed system, referred to as pressure-concentration-isotherms (PCI) (shown in Fig. 1.6) (Lutz, 2021). Three distinct regions are observed in the P-C-I curves. The initial steep slope corresponds to hydrogen going into solid solution or α-phase. After reaching the solution's saturation limit, the metal hydride forms a distinct second solid phase, the β – phase. From then on, the pressure remains constant while the concentration of the hydrogen increases with the progressive

conversion of the α-phase into β – phase. With the further addition of hydrogen, a second solution phase begins with hydrogen dissolution in the β – phase, and the hydrogen pressure rises steeply again. The flat (α+β) region is the most critical part of the PCT diagram as most of the hydrogen is absorbed in this region under constant pressure. Metal hydrides with wide plateau regions are advantageous because they absorb large hydrogen quantities under constant pressure. It can be observed that the width of the plateau reduces as the temperature increases and vanishes at the critical temperature T_C where α and β -phases become invariant.

The P-C-I shown in Fig. 1.6 represents the ideal situation that is rarely realized in actual metal hydride systems. P-C-I of real systems generally exhibit sloping, rather than flat, horizontal plateaus, indicating that different parts of the substrate material absorb/desorb hydrogen at different equilibrium pressures because of surface inhomogeneities, impurities and stresses. Additionally, it is experimentally observed that the PCI curves are different for hydrogen absorption and desorption, which may be called hysteresis. The enthalpy (ΔH) and entropy (ΔS) changes per hydrogen molecule on hydride formation can be calculated via the temperature (T) dependence of the plateau pressure (p) using the van't Hoff relation given by the following equation. Due to the hysteresis, a separate line for absorption and desorption can be obtained.

$$\ln\left(\frac{p}{p_0}\right) = \frac{\Delta H}{RT} - \frac{\Delta S}{R}$$

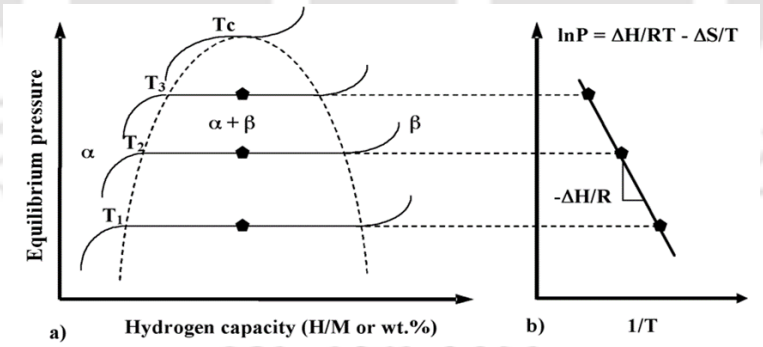

Fig. 1.6. (a). Ideal P-C-I diagram and (b). van't Hoff plot of the metal hydride

1.5 Applications of metal hydrides

MHs have been widely investigated for hydrogen storage applications. A large amount of heat is absorbed or released during the formation/ decomposition of MHs. These heat interactions attract the attention of researchers toward the applications of MHs to thermal machines. The following are the major applications of the MHs.

- Hydrogen storage, compression, and purification (Muthukumar et al., 2018)
- Thermal energy storage (Claudio Corgnale et al., 2014)
- Metal hydride heat pumps, refrigerators, and heat transformers (Muthukumar and Groll, 2010)

The performance of MHs depends on P-C-I properties (i.e., equilibrium pressure, plateau slope, reversible storage capacity, hysteresis, etc.), thermal stability, reaction kinetic properties, thermal conductivity, specific heat, etc. The selection of MHs and operating conditions for a particular application is made based on these properties.

1.6 MH based thermal energy storage system

Metal hydrides absorb thermal energy by releasing hydrogen during the charging process and deliver thermal energy by absorbing hydrogen during the discharging process, as shown in Fig. 1.7. Hydrogen released during the charging process from the MH reactor can be stored as compressed gas or directed towards another MH operating at near ambient temperatures. For compressed gas storage, H_2 is compressed and stored in either a pressure vessel or a salt cavern/ lined rock cavern (Sheppard and Buckley, 2019). In the latter case, a low-temperature metal hydride is employed for H_2 storage without any compressor work. However, the two-reactor configuration is the most widely accepted metal hydride-based TES system (Aswin et al., 2016). As discussed, one reactor is used for thermal energy storage and the other is for hydrogen storage. The energy storage reactor will operate at high temperatures, and the hydrogen storage bed will operate at near ambient temperatures. The charging and discharging processes of the two-reactor system are thermally controlled, as the temperature influences the pressure of absorption/ desorption of both reactors.

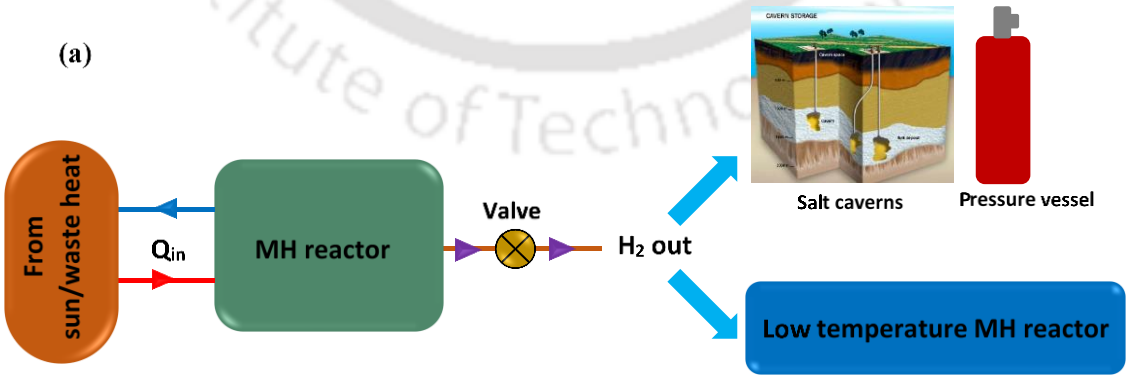

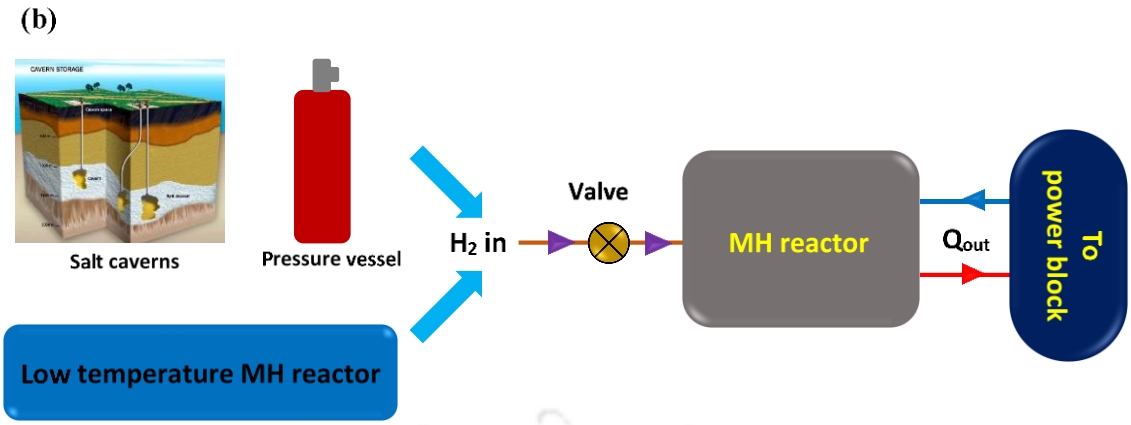

Fig. 1.7. (a). Charging and (b) discharging processes of MH-TES system

The reaction temperature of a MH can be adjusted with the gas pressure and vice versa. This characteristic is different for every MH material. A coupled MH-based TES system operates using this characteristic of the MHs. The schematic of the charging and discharging processes of the coupled MH-based TES system is shown in Fig. 1.8. The high-temperature MH (HTMH) receives heat from the source and decomposes it into metal and hydrogen during the charging process. During charging, the low-temperature MH (LTMH) generates heat at ambient temperature by consuming hydrogen from HTMH. After the decomposition, the HTMH is disconnected from the LTMH and cooled to ambient temperature for long-term storage purposes. During discharging, the LTMH supplies the hydrogen (by absorbing external heat) to the HTMH to liberate heat by exothermic hydride formation reaction. The LTMH throughout acts as a storage device for consuming and generating hydrogen, respectively, during charging and discharging processes. The hydrogen flow between the beds is entirely due to the difference in pressure between the reactors.

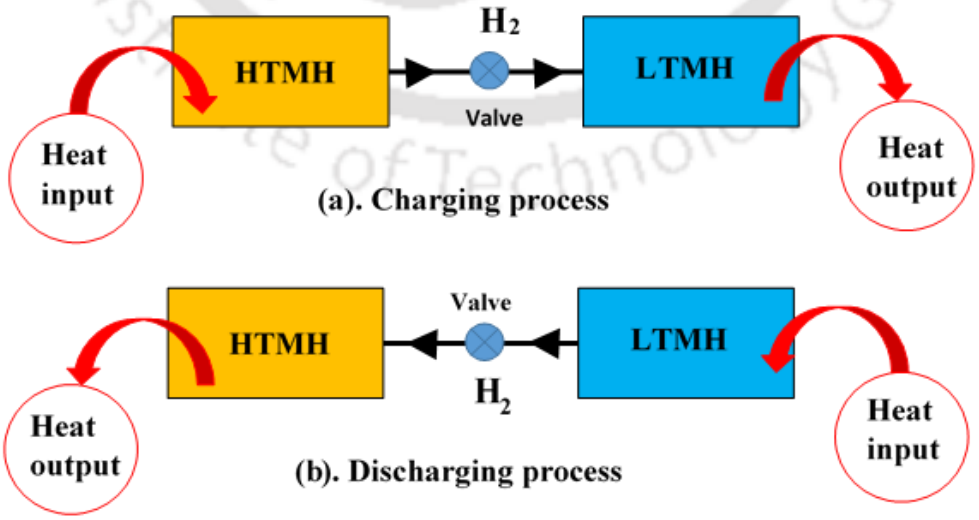

Fig. 1.8. Charging and discharging process of MH based thermal energy storage system

1.7 Scope and motivation of the thesis

Energy storage technologies will play a crucial role in increasing the share of renewables in the current energy infrastructure. TES is the most attractive technology within the available energy storage systems due to its energy storage efficiency (up to 95%-97%), cost-effectiveness (cost is only 1/30 of a large-scale electrical battery), and long cycle life. The sorption-based TCES is a promising technology for seasonal storage and offers higher energy storage density and wide operating temperatures. Despite the massive potential for future energy storage technology, TCES technology is not commercialized and is less studied due to its complexity than the other TES technologies.

On the other hand, hydrogen storage is another promising technology for solving the problem of the intermittent nature of renewable energy resources. In this perspective, MHs are a promising technology for both TES and hydrogen storage. Hence, the present thesis is dedicated to study the design and developmental aspects of the coupled MH-based TCES system for medium-temperature applications (250-400°C). The medium-temperature applications include power generation, waste heat recovery, steam generation for process industries, distilling, nitrate melting, dyeing, and compression (IRENA, 2020). The MH reactor is studied in TES and the hydrogen storage perspective in this work.

The reactor design plays a crucial role in the efficient operation of MH-based hydrogen storage and thermal energy storage systems. The absorption and desorption times of the MH-based hydrogen storage/ thermal energy storage system should be minimized to achieve better hydrogen/ heat transfer rates. On the other hand, a simple and lightweight reactor is the additional requirement for attaining a cost-efficient system. Hence, primary importance is given to heat transfer enhancement and adaptability to large-scale applications. Further, the challenges and possible improvements in a coupled MH-based TES system are also explored.

1.8 Thesis structure

The present thesis work is organized into seven chapters. The details of each chapter are described below.

Chapter 1 starts with a brief introduction to various methods and concepts of TES systems. The advantages of TCES systems over the other TES systems are elucidated. The formation of metal hydrides, working principle and applications of MH-based thermal energy storage system, and motivation of the present thesis are presented.

Chapter 2 presents a state-of-art on various aspects of MH hydride systems. The literature published on the MH-based hydrogen storage system, MH-based thermal energy storage system, and coupled MH-based systems are presented. The main focus was on the various reactor designs and experimental investigations under different operating conditions. Based on the conclusions of the literature survey, the objectives of the present thesis work are framed.

Chapter 3 is devoted to the design and numerical simulation of the MH reactors for thermal energy storage application. The detailed description of the numerical model and the results obtained from the numerical model are discussed. The numerical study is conducted on a high-temperature reactor with Mg_2Ni as MH alloy.

Chapter 4 is devoted to numerical simulation of the MH reactors for hydrogen storage application. The reactors proposed in Chapter 3 are numerically studied with $LaNi_5$ as hydrogen storage material. The results are compared with the literature.

Chapter 5 describes the reactor prototypes, experimental setup, and followed procedure for testing hydrogen storage reactors. This chapter includes the experimental investigations of the hydrogen storage reactor ($LaNi_5$ and $La_{0.7}Ce_{0.1}Ca_{0.3}Ni_5$). The results of the experimental studies are discussed.

Chapter 6 describes the reactor prototype, experimental setup, and procedure for testing the high-temperature MH reactor. Further, the experimental setup and procedure for the coupled reactor system are described. This chapter includes the experimental investigations on the HTMH reactor filled with magnesium-nickel alloy for TCES applications. The results of the experimental studies on magnesium-nickel alloy are discussed. Also, the experimental results of magnesium-nickel alloy-$LaNi_5$ and magnesium-nickel alloy-$La_{0.7}Ce_{0.1}Ca_{0.3}Ni_5$ alloy pairs are presented. Finally, a compressor-driven MH-based TES system is proposed for attaining simultaneous heating and cooling effect. The experimental results of the proposed system are discussed.

Chapter 7 encompasses the major conclusions from the numerical and experimental studies of the MH reactor prototypes. Scope for future work and recommendations are also given in this chapter.

1.9 Summary

This chapter started with a brief introduction of the energy scenario and various methods and concepts of energy storage systems for storing excess renewable energy. The principles of TCES system and MH-based TES system are explained. Further, the motivation of the thesis is discussed, and finally, the thesis structure is clearly explained.

Chapter 2

State of the Art

2.1 Preface

The large-scale installation of renewable energy systems is essential to combat global warming and climate change. The intermittent nature of renewable energy resources (primarily wind and solar) is the major challenge that needs to be addressed for a revolutionary transformation of the energy sector towards 100% carbon-free energy systems. Renewable energy resources require an effective energy storage system to balance energy supply and demand. In this regard, thermal energy storage and hydrogen storage are two potential options to address the problem of the intermittent nature of renewables. In recent years, metal hydrides (MHs) gained considerable importance for many engineering applications, viz hydrogen storage, hydrogen compression, heating and cooling, and thermal energy storage. MHs offer high volumetric and gravimetric energy storage densities, wide operating temperatures and pressures for TES and hydrogen storage applications. Hence, several researchers studied the various aspects of MH-based TES systems both numerically and experimentally. However, there is always a need for developing a simple, compact and high energy and power density MH-based TES systems. Developing a mathematical model is highly important to study the design and operating aspects of the MH based TES system. On the other hand, experimental studies are also important to understand the real time working of the developed system, the challenges involved in operating the system, and to validate and correct the developed numerical models. Therefore, several researchers developed various mathematical models to study the several aspects of MH-based TES system such as sizing of the MH reactor, heat-transfer enhancement techniques, and influence of operating parameters. Further, some experimental studies on the performance of the MH-based TES system are reported in the literature. In this chapter, a detailed literature survey on the heat and mass transfer studies of MH reactor, various designs of MH reactor, experimental aspects of MH-based thermal systems, studies of MH reactors coupled to fuel cell and coupled reactor-based TES systems are presented.

2.2 Heat and mass transfer characteristics of MH reactor

The essential requirements of the MH-based hydrogen storage system are high energy storage density, fast charging and discharging rates, and cyclic stability (Han et al., 2020). The MH reactor's performance is mainly affected by the internal heat transfer constraint imposed by the low thermal conductivity (~1 W/m-K) (Mazzucco et al., 2014; Zhang and Yang, 2018) of the MH bed and the geometrical parameters for example, thickness of the bed (Mohammadshahi et al., 2016) of the reactor. Hence, designing an efficient MH reactor should aim to attain faster charging and discharging rates and achieve a higher weight ratio i.e., the ratio of the mass of MH powder to the empty reactor mass. Also, the charging and discharging rates of an MH tank are also affected by the driving force for the hydriding/ dehydriding reaction: the pressure of hydrogen inside the reactor exceeds/ falls behind the hydride's equilibrium pressure (Oliva et al., 2018). The relation between the equilibrium pressure and the temperature of the MH bed is given by van 't Hoff equation (Chabane et al., 2019). The equilibrium pressure decreases with decrease in hydride temperature according to the van't Hoff equation. Therefore, the better control of MH bed temperature during absorption/ desorption favors faster charging and discharging rates. Hence, a heat transfer efficient MH reactor is essential for attaining faster charging and discharging rates. The design of the MH reactor plays an important role similar to the selection of MH material while installing MH-based thermal systems, which motivated the researchers to design the MH reactors from an energy-efficient perspective. The state-of-the-art performance enhancement techniques include developing new heat exchanger configurations, optimizing process parameters, doping thermal conductivity enhancers, and developing novel MH materials (Shafiee and McCay, 2016).

Mellouli et al., (2007) conducted an experimental study on an MH reactor equipped with a spiral heat exchanger and filled with 1 kg of $LaNi_5$. They studied the effect of supply pressure, absorption temperature, and overall heat transfer coefficient on the absorption time of the MH tank. The results showed that the heat transfer coefficient did not show any significant effect on the absorption time. The results also revealed that the absorption time is reduced from 5000 s to 1000 s with a helical coil reactor compared to the reactor cooled by natural convection.

Mellouli et al., (2009a) performed a numerical study on three different heat exchanger configurations for a cylindrical metal hydride reactor filled with 1 kg $LaNi_5$. The heat exchange options considered in their work were an outer cooling jacket, spiral coil, and spiral coil with an outer cooling jacket. The spiral coil with an outer cooling jacket configuration reduced the

absorption duration by 70% when compared to outer cooling jacket configuration due to the higher heat transfer area.

Linder et al., (2010) carried out an experimental investigation of a capillary tube bundle reactor filled with $LmNi_{4.91}Sn_{0.15}$. They compared the reaction bed dynamics and intrinsic reaction kinetics. They found that the reaction dynamics are not limited by hydrogen distribution inside an MH bed. They concluded that the desorption dynamics of the reactor are limited by the intrinsic reaction kinetics of $LmNi_{4.91}Sn_{0.15}$. Also, the reactor was charged within 100 s.

Souahlia et al., (2011) experimentally compared two reactors (external cooling jacket and central cooling tube with circular fins) filled with $LaNi_5$. They reported that the time to reach 0.4 wt.% was reduced by three times in the reactor with central fins compared to the other reactor.

Tange et al., (2011) experimentally studied a hydrogen storage tank filled with 50 kg of Mm-based MH for load leveling of electricity in commercial buildings. The hydrogen tank was integrated with an electrolyzer and fuel cell systems. Charging and discharging of 5,400 NL of hydrogen were successfully achieved in 9 h and 13 h, respectively. Further, 43.2% of the total reaction heat was recovered in the hydrogen storage system.

Visaria and Mudawar, (2012) experimentally studied the hydriding characteristics of a newly designed coiled tube heat exchanger filled with 4 kg of $Ti_{1.1}CrMn$. The heat exchanger occupied only 7% of the storage volume and reduced the filling time by 75%. They also observed that coolant fluid temperature significantly impacts the rate of hydriding among all operating parameters.

Halıcıoğlu et al., (2013) experimentally compared the performance of three different reactor designs (tubular reactor, tubular reactor with fins and tubular reactor with outer liquid cooling channel), each filled with 105 g of TiFe+C powder. They found that the liquid cooled reactor has 84% less charging time than the reactor cooled by natural convection.

Andreasen et al., (2013) compared a tubular metal hydride reactor with and without fins subjected to natural and forced convection. The reactors of each were filled with 0.5 kg of $MmNi_{4.7}Al_{0.3}$. The results showed that the use of external fins does not cause a significant improvement in the desorption behavior under forced convection.

Chung et al., (2013) compared the bare tubular reactor with the finned heat pipe tubular reactor. The results showed that with the use of heat pipes, the absorption and desorption times were reduced by ~50% and 44%, respectively.

Meng et al., (2013) compared the performance of a mini-channel reactor with conventional reactors (tubular and disc reactors). The mini-channel reactor achieved ~3.5 times faster absorption than the conventional reactors.

Andreasen et al., (2013) experimentally investigated the discharge behavior of an MH container equipped with internal (radial) and external (axial) fins. The MH container's response was observed when immersed in a thermostatic water bath and exposed to air. The use of external fins has positive results when exposed to air rather than immersed in water. They suggested that the effectiveness of a particular MH container should be evaluated for fixed external convective conditions.

Boukhari and Bessaïh, (2015) studied an annulus disc reactor embedded with cooling tubes. The results revealed that the addition of more cooling tubes and increasing their radii significantly enhanced the heat and mass transfer characteristics. Further, the absorption time was reduced by 60% when six cooling tubes were used instead of four cooling tubes.

Satya Sekhar et al., (2015) numerically examined the performance of different heat exchanger options for a cylindrical metal hydride container filled with $MmNi_{4.6}Al_{0.4}$. Four different cooling arrangements were considered: internal straight tube, internal helical, external cooling channel and external cooling channel with internal transverse fins. The results showed that the improvement in hydrogen absorption rate increases in the order of inner straight tube, external cooling, internal helical coil, and external cooling with fins.

Kang et al., (2016) experimentally compared copper foam and copper fin integrated MH reactor filled with ZrCo alloy. They found that the copper foam was more efficient than the copper fin arrangement in removal of reaction heat from the MH bed. The 90% desorption rate of the copper foam bed is 10% higher than the copper fin bed. Whereas the same is 17% for a 95% desorption rate.

Weckerle et al., (2017) experimentally showed that very short reaction times of the order of 60 s are feasible with plate heat exchangers. However, the limitations of the plate heat exchanger are a lower maximum operating pressure (30 bar) and a lower weight ratio (<1).

Singh et al., (2017) experimentally investigated a finned tube hydrogen storage device filled with 1 kg of $LaNi_5$ for hydrogen storage application. The reactor consisted of two "U" shaped cooling tubes and perforated annular copper fins. They also used copper flakes between the fins to increase effective thermal conductivity. The results of the finned tube reactor showed that the alloy could reach 1.2 wt.% capacity in 610 s at a supply pressure of 15 bar and a cooling

fluid temperature of 25°C. Also, with the insertion of 80 g of copper flakes, the charging time was reduced by 11%.

Zhang and Yang, (2018) used longitudinal and circumferential fins to enhance the reaction rate of the $LaNi_5$ MH bed. The results showed that the reaction rate was improved by 25% with the allocation of material to circumferential fins instead of longitudinal fins.

Gkanas et al., (2018a) studied rectangular MH tanks with embedded cooling tubes. The study compared three different MH alloys, namely $LaNi_5$, $MmNi_{4.6}Al_{0.4}$, and AB_2-intermetallic, during hydrogenation. They also investigated the effect of heat transfer coefficient and bed thickness on the hydrogenation performance. As per the comparison, AB_2-intermetallic can store over 90% of the theoretical amount of H_2 in less than 30 min, due to its high thermal conductivity. The results indicated an optimum value for the MH bed thickness was 10.39 mm, and a heat transfer coefficient over 2000 W/m^2. K did not enhance the hydrogenation rate by more than 5%.

In another work, Gkanas and Khzouz, (2019) studied the hydrogenation behavior of $MmNi_{4.6}Al_{0.4}$ filled inside a finned heat exchanger with embedded cooling tubes. They analyzed the effect of fin number, fin thickness and heat transfer coefficient on the hydrogenation of 13 kg of $MmNi_{4.6}Al_{0.4}$. The results showed that the optimum number of fins is 65 for the 800 mm length of the tank. Also, the optimum convective heat transfer coefficient was found in the range of 2000 to 5000 W/m^2-K.

Kumar et al., (2019) tested a large-scale MH reactor for hydrogen storage application. The reactor consisted of 99 embedded cooling tubes filled with 40 kg of $LaNi_{4.7}Al_{0.3}$. The results showed that the alloy absorbed 402.6 g of hydrogen in 1908 s under the supply pressure of 2 bar and inlet temperature of HTF of 30°C. The absorption time was decreased by 37% when the supply pressure was increased to 10 bar. During desorption, the alloy showed very slow desorption kinetics. An amount of 395.812 g was desorbed in 3720 s at 80°C.

Kim et al., (2020) proposed a copper-mesh structure design for enhancing the thermal conductivity of the $La(Ce)Ni_5$ powder. The proposed reactor used a compact fan for improving the forced convection heat transfer. The experimental results showed that the copper mesh design with a fan reduced the charging time by 73.5% when compared to a simple reactor under natural convection.

Bürger et al., (2021) designed and fabricated an aluminum-based tubular MH reactor using additive manufacturing techniques to obtain a lightweight MH reactor and achieved a reactor-

to-hydride mass ratio of 0.97 for the maximum working pressure of 10 bar. Also, the system delivered a specific thermal power of up to 2.1 kW/kg MH.

Kumar et al., (2021) studied an embedded cooling tube reactor filled with 4 kg $MmNi_{4.7}Fe_{0.3}$ alloy. The reactor consisted of 55 cooling tubes for supplying/ removing the reaction heat. The absorption results revealed that the alloy needed a supply pressure of 70 bar to absorb 45.984 g in 676 s at 25°C. During desorption, the alloy produced a cooling effect of 463 kJ by desorbing 47.729 g in 388 s at 30°C for a fixed absorption of 50 g. Also, ice formation was observed on the surface of the reactor during desorption.

Jana and Muthukumar, (2021) compared the performance of the tube bundle reactor with an ECT reactor. The results showed that the tube bundle reactor yielded a 1.17 times higher alloy-to-container weight ratio than the ECT reactor. Despite having a higher heat transfer area, the tube bundle reactor did not significantly improve the absorption performance due to a higher MH bed thickness.

Zhuo et al., (2021) studied the effect of adding copper fins and aluminum foam to the embedded cooling tube reactor on desorption efficiency. An improvement of 50% was obtained in the desorption rate with the copper fins and aluminum foam.

Eisapour et al., (2021a) proposed a novel air-cooled multi-zone configuration of a metal hydride reactor for efficient hydrogen storage in magnesium hydride. The designed reactor uses the concept of enhancing the heat transfer area and the number of cooling channels to accelerate the absorption rate. The results showed that the absorption performance was improved by 64% when the number of air passages was increased from two to four.

MH reactor equipped with an outer cooling jacket is simple and easy to construct. Several such tubes containing the MH alloy are arranged inside a shell called a tube bundle (TB) reactor for large-scale applications. Subsequently, the reactor with an inner cooling tube (Feng et al., 2019b; Y. Liu et al., 2021a) was proposed as another simple reactor where the exothermic/ endothermic heat is removed/ supplied using heat transfer fluid (HTF) which is circulated through the cooling tube located at the core of the reactor. However, this reactor includes poor reaction sites near the walls of the reactor. Hence, several studies (Afzal et al., 2021; Kang et al., 2016; Singh et al., 2015; Visaria et al., 2011) were conducted with the addition of internal fins and heat conductive material to such simple reactors for improvement of the heat transfer rate from MH bed to the HTF. It is also found that helical coil heat exchangers showed better heat transfer coefficients than straight tubes due to higher heat transfer area and secondary

circulation (Mathew et al., 2021; Visaria and Mudawar, 2012; Wu et al., 2014). A comparison study (Satya Sekhar et al., 2015) showed that the finned heat exchanger with external cooling has better heat transfer performance than the helical coil tube heat exchanger. Moreover, the heat transfer enhancement of the finned tube reactor depends on the fin number and thickness of the fin. The details of large-scale metal hydride reactors reported in the literature are presented in Table 2.1. The schematic of the commonly used MH reactors is shown in Fig. 2. 1. It is observed that most of the large-scale MH hydrogen tanks are of shell and tube type (Gkanas et al., 2016; Johnson et al., 2011; Karmakar et al., 2021; A. Kumar et al., 2019). Also, the shell and tube-type reactors equipped with internal fins reduce the number of cooling tubes to achieve equivalent performance. A few studies (Afzal et al., 2021; Lototskyy et al., 2020) focused on the reactors with internal fins cooled from the outer surface. However, only internal fins without any cooling tube could not deliver better performance than the ECT reactor. From this, it is understood that the finned tubes enhance the reaction kinetics effectively instead of multiple ECTs.

Table 2.1 Large-scale metal hydride reactors studied in the literature

Author(s)	**Design**	**Alloy used**	**Observations/ Remarks**
Johnson et al., (2011)	Tube bundle reactor (total of four modules)	86 kg of sodium alanate–graphite mixture	• Each module consisted of 12 tubes arranged in a staggered array. Each tube was filled with 1.79 kg of MH. • The system was designed to store 3 kg of hydrogen. • The system was operated between 120 and 220°C. • The desorption rate of 2 g/s was achieved.
Gkanas et al., (2016)	Shell and tube	$LaNi_5$	• Compared the performance of ECT reactor with and without fins. • The reactor with 12 longitudinal finned tubes showed the equivalent performance to the reactor with 60 ECT.
Kumar et al., (2019)	Shell and tube	40 kg of $LaNi_{4.7}Al_{0.3}$	• The reactor consisted of 99 cooling tubes. • Under 15 bar supply pressure, 425.7 g of H_2 was absorbed in 1017 s. • At 80°C, the alloy desorbed 395.812 g of H_2 in 3720 s.
Karmakar et al., (2020)	Shell and tube	10 kg of $LaNi_5$	• The cooling system consisted of four cooling tubes and an outer cooling jacket. • The MH bed reached 1.12 wt% in 1980 s under a supply pressure of 15 bar. • At 80°C, complete desorption happened in 2700 s.

Lototskyy et al., (2020)	MH cassette encased in the lead (each cassette comprising several MH containers embedded with perforated copper fins)	3 kg of AB_2-type alloy	• A hydrogen storage tank for heavy-duty fuel cell utility vehicles was developed. • The tank could supply the hydrogen at 120 NL/min to operate an 11-kW fuel cell stack. • The refueling time of the MH tank was about 15-20 min at the supply conditions: T=15-20°C and P_{H2} =100-150 bar
Afzal et al., (2021)	Reactor with hexagonal honeycomb inserts	47.5 kg of $La_{0.9}Ce_{0.1}Ni_5$	• The reactor equipped with hexagonal honeycomb fins was cooled from the outer surface. • Under 25 bar supply pressure, the reactor consumed 5400 s to reach a reacted fraction of 0.9. • At 50°C of heating fluid temperature, the desorption time was 10000 s.

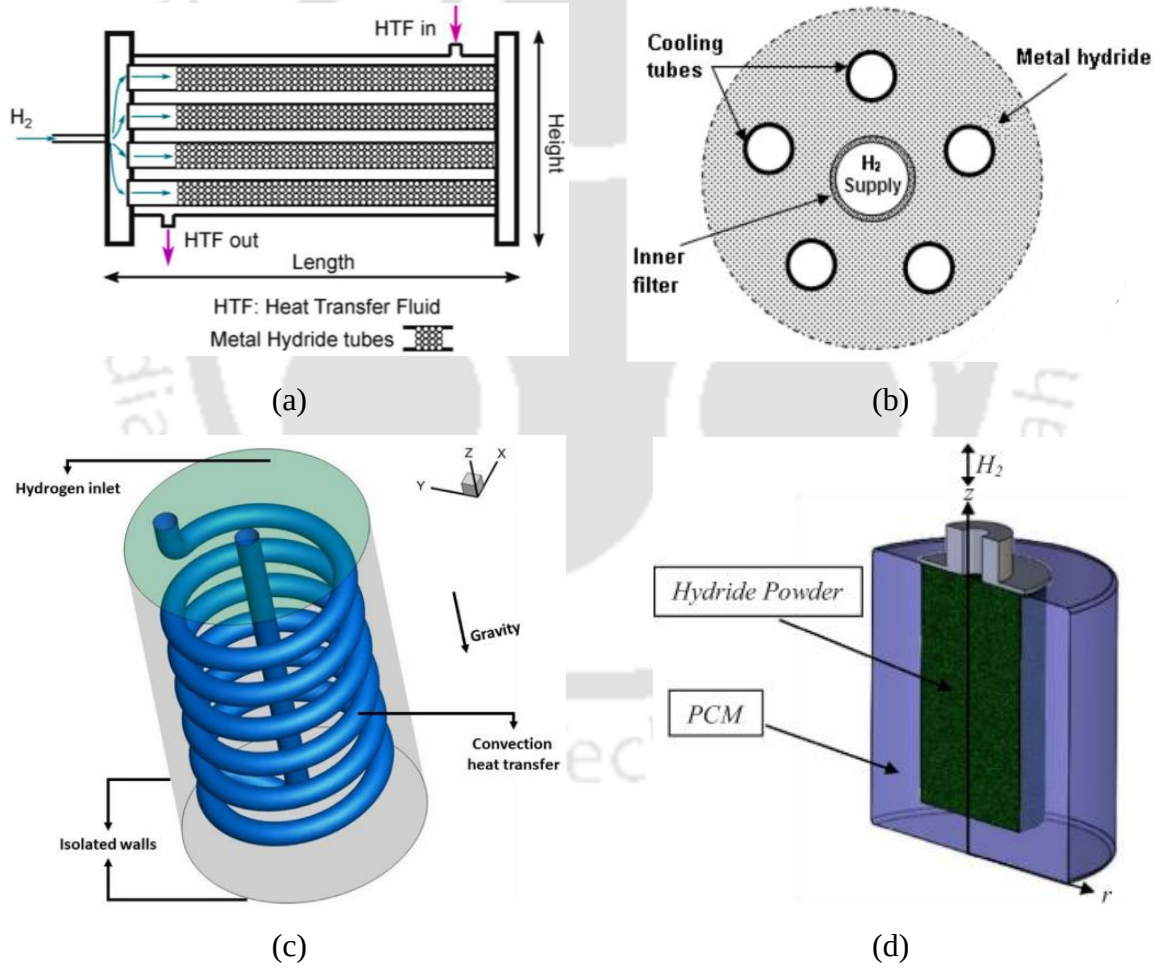

Fig. 2. 1. Schematic of (a) tube bundle reactor (Jana and Muthukumar, 2021), (b) embedded cooling tube reactor (Boukhari and Bessaïh, 2015), (c) helical coil heat exchanger (Eisapour et al., 2021b) and (d) MH reactor with PCM jacket (Ben Mâad et al., 2018)

Other MH reactor designs include an outer phase change material (PCM) jacket that eliminates the necessity of an HTF circuit (Ardahaie et al., 2021a; Mellouli et al., 2016a; Ye et al., 2020). In such a system, phase change enthalpy of the PCM is used to store the exothermic heat during absorption and supply the endothermic heat during the desorption of the MH bed. The performance of these systems is mainly affected by latent heat and the thermal conductivity of PCM. The PCM-jacketed MH tanks are used only for hydrogen storage applications. Rabienataj Darzi et al., (2016) simulated a tubular $LaNi_5$ reactor integrated with a phase change material jacket. The reported absorption and desorption times were of the order of 100 min. Mellouli et al., (2016b) studied four different configurations of the MH tank integrated with PCM. The four configurations are MH compact surrounded by PCM, MH disc incorporated with 48 spherical PCM capsules, MH disc incorporated with 48 hexagonal PCM capsules, and MH disc incorporated with 48 cylindrical PCM capsules. They considered Mg_2Ni and $NaNO_3$ as MH and PCM, respectively. The results showed that configuration 4 reduced the hydrogen filling time by 58.1% compared to configuration 1. For configuration 4, the hydrogen filling time was 25000 s. The PCM jacketed MH bed suffers from significantly slower reaction rates. The reaction completion time achieved with PCM jacketed MH reactor was more than 5000 s, which is not competitive with the other existing reactor designs. Being a poor thermally conductive material, PCM acts as an additional barrier for better heat transfer.

The driving force is also affected by the operating parameters along with the heat exchanger design. The operating parameters that influence the performance of the MH systems are supply/ discharge pressure, initial temperature, the inlet temperature of HTF, and the mass flow rate of the HTF. Several researchers conducted parametric studies to find the optimal process parameters to maximize the driving potential (Jiao et al., 2012; Karmakar et al., 2021; Wang et al., 2019) and reduce the reaction completion times.

Muthukumar et al., (2005) tested the performance of MH-based hydrogen storage devices filled with $MmNi_{4.6}Fe_{0.4}$ and $MmNi_{4.6}Al_{0.4}$ using a tubular reactor with an outer cooling jacket. The results showed that the supply pressure and fluid temperature have a significant influence on the absorption, whereas the overall heat transfer coefficient has negligible influence.

Mellouli et al., (2007) experimentally studied the absorption and desorption characteristics of an MH tank of embedded spiral heat exchanger type filled with 1 kg of $LaNi_5$. They noticed that the supply pressure and desorption temperature significantly affect the rate of reaction. Ben Mâad et al., (2013) studied the effect of operating parameters on the desorption process of

the Mg_2Ni alloy. The results showed that the heat transfer coefficient of the HTF and the effective thermal conductivity of the MH bed are two critical parameters that reduced the discharge time. Bao et al., (2013) performed a sensitivity analysis on a magnesium hydride-based MH tank and found that the absorption process is accelerated by increasing the supply pressure, decreasing HTF inlet temperature and increasing HTF velocity.

Anbarasu et al., (2014) numerically studied the performance of an embedded cooling tube (ECT) reactor for hydrogen storage using $LmNi_{4.91}Sn_{0.15}$. They found that the supply pressure and hot fluid temperature are the most influencing parameters on absorption and desorption, respectively. Whereas increasing the effective thermal conductivity of MH facilitated a substantial reduction in the absorption and desorption times. Singh et al., (2015) designed and studied an embedded annular heat exchanger with radial circular copper fins filled with 1 kg $LaNi_5$. The reactor system achieved 1.34 wt. % in 18 min at a supply pressure of 15 bar. Also, they concluded that the supply pressure and cooling fluid temperature have a predominant effect on the absorption time.

Keshari and Maiya, (2018) numerically studied a pin fin heat exchanger filled with 1 kg $LaNi_5$. Their study showed that the supply pressure of H_2 is the most influencing parameter on the absorption time than mass flow rate and inlet temperature of HTF. They achieved the maximum storage capacity in 636 s at a supply pressure of 15 bar.

The parametric studies revealed that the higher supply pressure and a lower inlet temperature of HTF positively affected the absorption kinetics. On the other hand, a higher inlet temperature of HTF positively affected the desorption kinetics. The mass flow rate of the HTF showed significant improvement in absorption and desorption kinetics. However, the higher mass flow rate of the HTF is not significantly affecting the absorption and desorption kinetics after a specific value for the designed MH reactor.

2.3 MH reactors coupled with electrolyzer and fuel cell

Several researchers investigated MH tanks for stationary fuel cell applications (Lototskyy et al., 2017; Nguyen and Shabani, 2021). Mainly, the MH tank's performance was evaluated with and without coupling the exhaust heat of the FC. The MH tank absorbs the required desorption heat from the surroundings without thermal coupling with the FC by convective heat transfer. The lower ambient temperatures result in lower discharge rates from the MH tank. The natural convection heat transfer mechanism is suitable for low rates of hydrogen discharge. Whereas

for higher discharge rates, the MH tank's temperature drops to a low level such that the MH tank is unable to supply hydrogen at the rates required by the PEMFC (Omrani et al., 2020). Hence, more MH alloy is needed to meet the required hydrogen flow rate under natural convection than the designed storage capacity (Omrani et al., 2019). In contrast, utilizing the exhaust heat of the FC to desorb the hydrogen from the MH tank facilitates higher desorption rates and eliminates the need for extra MH material. Hence, the active cooling/ heating of the MH tank is the most promising option to operate the system as per the demand.

Tange et al., (2011) proposed a totalized hydrogen energy utilization system for on-site energy storage. As a part of this system, they studied a shell tube and tube-type MH tank filled with 50 kg of Mm-based metal hydride. The tank consisted of 24 U-shaped cooling tubes and seven hydrogen supply tubes. The tank was designed for a working pressure of 90 bar and had a weight ratio of 0.3. The tank's 100% charging and discharging at absorption and desorption rates of 10 NL/min and 6.9 NL/min, respectively, were attained.

Gonzatti et al., (2016) studied an integrated power plant using a fuel cell stack, electrolyzer, and metal hydrides. The plant was installed with a 3-kWh alkaline electrolyzer that generates hydrogen at 6.6 7 NL/min. The hydrogen storage unit consisted of 46 kg of $LaCeNi_5$ that could store 7140 L of hydrogen. A 3 kW PEM fuel cell that consumes hydrogen at a 42 NL/min flow rate was installed. All the components of the plant were operated below 15 bar. The overall efficiency of the power plant oscillated between 2.1 and 11.2%. The main reason for such low efficiency was losses in the control modules of the electrolyzer and fuel cell. The MH hydrogen storage tank has no effect on the overall efficiency as its cold and hot water requirements were fulfilled by renewable sources.

Andreasen et al., (2016) studied the performance of an MH tank integrated with a fuel cell stack of 300 W peak power. The MH tank was a simple cylindrical design with internal and external aluminum fins. The MH tank was filled with $MmNi_{4.7}Al_{0.3}$. The MH tank operating at 20°C without any thermal interaction with the fuel cell delivered hydrogen at 0.5 L/min for 140 min, allowing the fuel cell to use at 50W power output. Further, the MH tank showed the best performance by utilizing the fuel cell exhaust heat and delivering hydrogen at 4 L/min for 16 min, providing a power output of 280 W in the fuel cell.

Bürger et al., (2017) studied a tube bundle-type MH reactor with air as a cooling medium. The reactor was equipped with aluminum foam on the outer surface to enhance heat transfer and had a weight ratio of 0.2. The reactor was filled with a composite compact of Hydralloy C5

and five wt% ENG. The experiments showed that the reactor could desorb the desired amount of hydrogen to operate a fuel cell at 160 W_{el} for 100 min by providing a utilization factor of 93%. Also, the metal hydride alloy did not show any degradation during 38 cycles.

Yan et al., (2020) studied the performance of the metal hydride tank integrated with a 20W PEMFC. The study used 554.3 g of $LaNi_5$ filled inside a cylindrical tank. The results showed that the desorption temperature over 60°C has not significantly affected the set input hydrogen flow rate of 280 mL/min.

Liu et al., (2021) developed a gaseous and solid-state hybrid hydrogen storage tank that could offer a volumetric hydrogen storage density of 40.07 kg H_2/m^3. The designed storage tank was operated at a pressure of 50 bar and was integrated with a 10-kW fuel cell. The storage system used 63.4 kg of $Ti_{0.95}Zr_{0.05}Mn_{1.4}Cr_{0.35}V_{0.25}$ (1.7 wt.%). The energy storage efficiency of the storage tank was found to be 86.4%–95.9% when combined with the fuel cell. The exciting feature of the tank was that it could release hydrogen at 100 L/min for 15 min operating at a temperature of -15°C even in the absence of the fuel cell exhaust heat. This is due to the gaseous hydrogen present in the free volume of the tank. The tank released hydrogen at 100 L/min for 111 min while operating at 60°C using fuel cell exhaust heat.

Davids et al., (2016) studied an MH tank coupled with a 130 W PEMFC. The developed MH tank was a tubular reactor with external aluminum fins. The MH tank was filled with 560 g of multi-component AB_2 alloy (90% of AB_2 + 10% of AB_5 and 12 wt. % TEG). The storage capacity of the tank was 90 NL of H_2. The warm exhaust air of the PEMFC was used to heat the MH tank during the desorption process. The MH tank discharged the hydrogen at 1.1, 1.97, and 2.24 L/min for 75, 41, and 35 min, enabling the PEMFC to operate at 60, 100, and 120 W.

Bedrunka et al., (2021) studied an MH-based hydrogen storage system for forklift application. The results showed that the charging process highly influences the design of the MH reactor for forklift application due to its highly dynamic nature than discharging process. It was also observed that 80% of the charging was completed in 50% of the time compared to full charge.

Weiss-Ungethüm et al., (2014) studied a sodium alanate MH tank (300 g) coupled with a high-temperature PEMFC (400 W). The developed MH reactor desorbed 2 wt.% of hydrogen at a 6 mg/s flow rate at a temperature of 160°C. The study suggested that modular storage tanks reduce the thermal masses and simplify the heat transfer from the FC to the MH tank. Also, the storage tank should be installed with more MH material than the required capacity if heat transfer enhancement is not provided.

Han et al., (2020) investigated the suitable charging and discharging characteristics of the MH hydrogen storage system for an electrolyzer and a fuel cell system. They compared $La_{0.6}Ce_{0.4}Ni_5$ (AB_5-type) and $TiMn_{1.5}$ (Cr, V, Zr)/V-rich (AB_2-type) alloys in their analysis. The results showed that the AB_2 type is a suitable candidate than the AB_5 type due to its high hydrogen storage capacity and higher desorption pressures, despite of longer charging period. Kumar et al., (2019) performed an experimental and simulation study of an MH hydrogen storage system integrated in a microgrid. The results showed that the inlet temperature and flow rate of heating water have no significant effect on discharging rate for operating a 1 kW fuel cell. Further, they showed that the thermal management of an MH reactor plays a key role in providing high hydrogen demand.

2.4 MH-based TES systems

In this section, state-of-the-art research on MH-based TES systems is presented. The major focus was given to numerical and experimental aspects of MH-based TES systems. The desirable properties of heat-storage MH alloys are a high hydrogen-storage capacity, flat plateau (amount of hydrogen that can be stored reversibly with no variations in pressure and temperature), low hysteresis, fast kinetics, easy activation, and high melting point. Alloys with a high heat of formation and low disassociation pressure at higher temperatures are preferable. The MHs that have been primarily investigated to date for energy-storage applications are magnesium hydride (MgH_2), titanium hydride (TiH_2), and calcium hydride (CaH_2) (Rönnebro et al., 2015). The promising MH reactions with stable and better reaction kinetics are shown in Table 2 of Chapter 1. Apart from these, some complex metal hydrides involving lighter elements such as boron, nitrogen, or aluminum, which offer extreme hydrogen densities (up to 20%), have also been explored, only to demonstrate poor thermodynamic and kinetic properties and limited reversibility (Javadian, 2017; Møller et al., 2017).

The MgH_2-Mg system has been identified to be the most attractive high-temperature heat-storage material because of its substantial hydrogen-storage capacity and high energy density (Bogdanovic et al., 1990). The cyclic stability of pure MgH_2, however, drops by 75% after 500 cycles, which can be improved by doping with nickel or iron, thus leading to consistent cyclic stability over 500 cycles (Paskevicius et al., 2015). Kawamura et al., (1983, 1982) explored the possibility of employing Mg_2Ni for a heat-storage application. They developed a simple prototype using 6.27 kg of Mg_2Ni, and their results showed that the heat-transfer coefficient as

well as the insulation of the system, plays a major role in producing a large temperature gain of the HTF.

Wierse et al., (1991) designed a laboratory-scale solar thermal-powered Stirling engine with a metal hydride-based TES system. Two potassium heat pipes were used for heat transfer between the solar receiver, MH store, and Stirling engine. The storage system was operated between 300°C and 480°C, with a heat-storage capacity of 12 kWh, which achieved an overall efficiency of 12%. Wierse and Groll, (1996) tested Ni-doped MgH_2 on a laboratory scale. Their heat-storage model consisted of 24 kg of Mg powder placed in a stainless-steel container and tested for about 1200 h at 280–500°C. A heat-storage capacity of 5.3 kWh_{th} was reported.

Bogdanovlc et al., (1993) also investigated details of the kinetics, the extent of hydrogen loading, and cycling stability for both Ni-doped and pure MgH_2/Mg systems, and they discussed several doping methods. The Ni-doped MgH_2 showed a decrease in H_2-storage capacity at high operating pressure and temperature (i.e., 35–100 bar and 430–500°C). Friedlmeier et al., (1994) explored the possibility of using TiH_2 to improve the efficiency of the solar thermal power plant (STPP). They compared MgH_2/Mg and TiH_2/TiH stores and showed the latter to have double the conversion efficiency and a higher volumetric storage density. Their study also highlighted the storage-capacity degradation due to sintering and the high diffusion rate of hydrogen as the limitations of using TiH_2 as energy-storage material.

Felderhoff and Bogdanović, (2009) presented an overview of research work on the Mg-based TCES system carried out at the Max Planck Institute for Coal Research in Germany. They compared the molten salt (mixture of sodium and potassium nitrate)-based two-tank SHS system with the Mg/MgH_2-based system, considering Andasol-1 (50 MWe) solar thermal power plant as the reference. The storage system consists of two insulated storage tanks (cold tank at 260°C and hot tank at 390°C), each 14 m high and 36 m in diameter, with an overall heat-storage capacity of about 1 GWh. One major issue related to this system was maintaining the temperature of the cold tank above the melting point of the molten salt (~225°C). For storing the same amount of heat with the MgH_2-Mg system having a heat-storage capacity of 0.9 kWh/kg, Mg could demand only 1,100 tons of Mg powder. However, a secondary hydrogen-storage system was necessary for the Mg-based storage system to store the hydrogen released during the dissociation of MgH_2 into Mg. This can be done by either pressurized gaseous storage or in the form of a low-temperature metal hydride such as La-, Mm-, and Zr-

based hydrides. Compared to the molten salt-storage system, MH-based heat storage faces no issues of corrosion and freezing of the materials at near ambient temperature.

Verga et al., (2009) designed and tested a sample of 500 g MgH_2+0.5 mol% Nb_2O_5+1 wt% C under different operating conditions. Nb_2O_5 was added to the test sample as a catalyst to improve the absorption/desorption kinetics, which led to a satisfactory hydrogen-storage capacity of 5.3 wt%. Results showed about 50% decay in the overall storage capacity after 20 cycles due to local powder heating, fragmentation, and subsequent compaction. Chaise et al., (2010) tested the MgH_2 tank for hydrogen storage application. They found that low thermal conductivity and poor thermal management are responsible for the slow hydriding behavior of MgH_2. In order to increase the thermal conductivity, they prepared MgH_2 with expanded natural graphite compact. The results showed that the developed new MH system could absorb 100 NL H_2 in only 25 min.

Satya Sekhar et al., (2012) conducted the performance tests on Mg + 30% $MmNi_4$-based TES system. The results showed a maximum hydrogen storage capacity of 2.5 wt% and a heat storage capacity of 0.714 MJ/kg. Delhomme et al., (2012) experimented with a large-scale MgH_2 tank holding 10 kg MgH_2 powder and was able to store 0.6 kg of H_2 reversibly. The system included MH compacts with 10 wt% expanded natural graphite (ENG) to enhance thermal exchanges and improve storage time. The MH tank, having an energy density of 360 Wh/kg, was coupled to a high-temperature heat source using synthetic oil as the HTF. The discharging time was measured to be three times longer than the charging time due to the smaller temperature difference between the wall and the MgH_2. Results also showed a large improvement in thermal conductivity after the first cycle, which remained constant for ten cycles.

Shen and Zhao, (2013) studied the magnesium hydride tank with and without aluminum foam. With the addition of the aluminum foam of 0.92 porosity, the effective thermal conductivity of the MH bed was raised to 5.5 W/m-K from 1 W/m-K. The metal foam helped a 40% reduction in reaction time and a 60% improvement in the peak exothermic power. Without metal foams, the time for 95% completion of the reaction was 5990 s, whereas the same for adding metal foam was 3485 s.

Urbanczyk et al., (2017) investigated a 5 kg prototype of Mg_2FeH_6 for short and long-term TES applications. The developed test setup utilized molten salt as an HTF. A tube bundle reactor design consisting of 13 tubes was used and each tube was filled with 372 g of Mg_2Fe alloy. In

their preliminary tests, the theoretical storage capacity was not reached due to higher heat losses caused by insufficient insulation: Only 64% of the theoretically possible heat storage capacity was released, and 59% was stored.

Wang and Chen, (2018) studied a disc-type MH reactor for TES application. Compressed air was used as an HTF to extract the exothermic heat from the reactor. The results showed that the reactor achieved an average power of 0.348 kW and reaction completion time of 114.2 min.

Poupin et al., (2019) studied a sodium magnesium hydride ($NaMgH_3$) TES prototype on a 150 g scale. The MH material was added with TiB_2 and exfoliated natural graphite to enhance thermal and cycling properties. The alloy exhibited extremely slower reaction kinetics. Even at 8 bar supply pressure, a peak flow rate of 10 g/h was achieved. They observed that the heat loss from the MH reactor to the surrounding were decreased by a factor of 3 when the supply pressure was increased from 2 bar to 5 bar (the HTF extracted heat at a greater chance due to faster reaction rates). They also found that the 3 kg stainless steel reactor diverted around 5-40% of thermal energy that was supposed to transfer to HTF. To avoid this problem, they suggested having a higher weight ratio.

Lutz et al., (2019) proposed a novel adiabatic hydrogen storage reactor based on magnesium hydride coupled with a magnesium hydroxide TCES system. The reactor utilized the exothermic heat of hydration reaction for desorbing hydrogen from the MH tank. Under the 5-bar pressure of water vapor, the dehydrogenation time of within 132 min was achieved. The dehydrogenation time of the MH tank was decreased with the pressure of water vapor. In another experimental study, Lutz et al., (2020) showed proof of concept of the adiabatic hydrogen storage reactor. The experimental results suggested that the 100% conversion was not achieved due to poor reaction kinetics and thermal losses. Also, the poor heat transfer between the beds was another primary reason for not achieving 100% conversion. A steam pressure of 10 bar in the magnesium hydroxide reactor was needed to desorb hydrogen from MH.

Feng et al., (2019b) obtained a stabilized discharge performance of an MH reactor by controlling the supply pressure using a proportional-integral technique. The authors identified gravimetric exergy-output rate (GEOR) as a comprehensive index for characterizing the MH-based TES system. The results showed that the length, diameter, and mass flow rate of the HTF affected the optimum discharge performance. Further, they proposed a tapered bed to achieve

a uniform reaction rate at the top and bottom of the reactor. The tapered bed improved the GEOR by as high as 84%.

Liu et al., (2021b) studied a magnesium hydride MH reactor equipped with a variable cross-section annular fin to avoid inhomogeneous reaction sites. The proposed reactor showed excellent performance in eliminating inhomogeneous reaction along the length.

Poupin et al., (2021) developed a thermal battery using Mg_2FeH_6 as a storage material. The developed prototype utilized eight tubular reactors encircled by a 12 m long tube for HTF flow. The reactor was filled with 0.9 kg of Mg_2FeH_6, and pressurized water was used as HTF. The results showed that the absorption and desorption times were in the range of 8 h. The storage capacity of the developed thermal battery was found to be 1650 kJ, which is 87% of the theoretical value. The reactor delivered a peak power of 150 W under a supply pressure of 50 bar and an HTF flow rate of 65 ml/min.

Ardahaie et al., (2021b) studied a Mg_2Ni-based TES system equipped with a hybrid heat exchange system: combined PCM jacket and spiral tube heat exchanger. The study focused on analyzing the effect of various spiral configurations, shapes, and thicknesses of PCM jackets on the charging and discharging processes. The results showed that the absorption and desorption performances of the hybrid heat exchanger were improved by 44% and 20%, respectively, compared to without the PCM case.

Dubey and Kumar, (2022) studied the effect of the number of embedded cooling tubes and aspect ratio on the heat transfer characteristics of the energy storage module. The energy storage efficiency increased with an increase in the aspect ratio. The energy storage efficiencies of 91%, 91.77%, and 93.27% were obtained for aspect ratios 0.5, 1, and 2, respectively.

2.5 Integration of MH reactor with reversible solid oxide fuel cell device

Apart from solar thermal power plants and waste heat recovery, the MH-based TES system can also be integrated with a reversible solid oxide fuel cell (RSOFC), which operates at temperatures above 600°C (Yiotis et al., 2014) and promises to be more efficient (~70%) without any harmful emissions (Di Giorgio and Desideri, 2016). RSOFC devices can operate in either the solid oxide fuel cell (SOFC) mode or the solid oxide electrolyzer cell (SOEC) mode. In the SOEC mode, H_2 is produced through steam electrolysis by consuming the electricity and heat produced from renewable energy resources (solar, wind, biomass, etc.). In the SOFC mode, electricity and heat are generated by the electrochemical combination of air

with H_2 gas (Akikur, 2014). The RSOFC can be viewed as an energy-storage device because it can consume excess electricity from SPV panels during on-sun hours and produce electricity during off-sun hours. The complete details regarding the design, operation, and applications of an RSOFC can be found in the work of Kendall and Kendall, (2015). The RSOFC device demands a hydrogen-storage system in SOEC mode and a thermal energy storage system in SOFC mode, and the MH-based TES system can serve as both, as shown in Fig. 2.2.

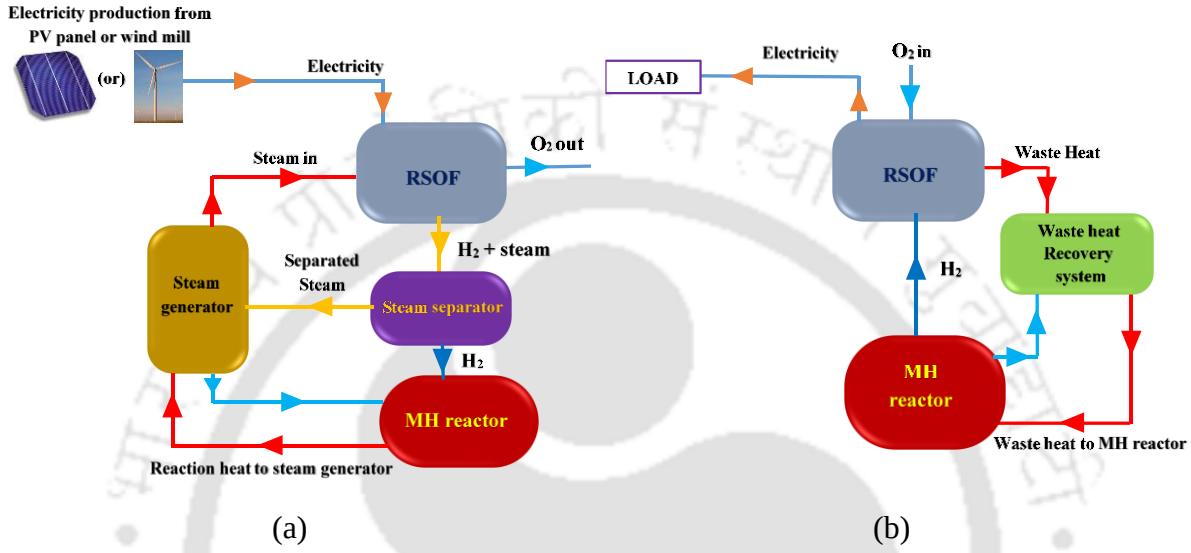

Fig. 2.2. Schematic of operating modes of RSOFC: (a) SOEC mode and (b) SOFC mode

In the SOEC mode, hydrogen released from the RSOFC gets absorbed in the MH reactor, releasing heat in an exothermic reaction. This heat is supplied to the steam generator for generating steam, which is fed back to the RSOFC. In the SOFC mode, the MH reactor desorbs the H_2 in an endothermic reaction by absorbing the waste heat generated from the RSOFC (McElroy et al., 2004; Shiraki et al., 2013). Delhomme et al., (2013) experimentally tested a combined heat and power (CHP) system by integrating a 1kWe SOFC with an MgH_2 hydrogen storage tank capable of storing 1200 liter of hydrogen. Their results showed that the SOFC and the MgH2 tank integration is feasible if the SOFC exhaust is at a temperature above 350°C. This study also suggested that the MH tank heat exchanger should be improved to obtain a higher exchange efficiency and lower pressure drop.

Several thermodynamic and numerical studies (Gkanas and Makridis, 2016; Yiotis et al., 2014) have tested the feasibility of coupling MH reactors with the SOFC. These studies focussed on the dehydration characteristics of a metal hydride tank using the exhaust heat of the SOFC. Shiraki et al., (2013) theoretically compared the standalone RSOFC device with systems equipped with an MgH_2 MH reactor. In the SOEC mode, the energy-storage efficiency of a

94% higher heating value (HHV) for a standalone system and a 107% HHV for a combined system were achieved, thereby demonstrating that the excess heat generated at the MH bed was able to compensate for energy loss within the system. At present, the integration of an MHTES system with an RSOFC lacks experimental investigation, thus necessitating more studies to envisage the dynamic behavior of the coupled system. Giap et al., (2020) studied a coupled reversible solid oxide fuel cell system and an MH tank. They compared the round-trip efficiencies of integrating two MH materials: MgH_2+5 at. % V and $LaNi_5$. The results showed that the round-trip efficiencies of MgH_2+5 at. % V and $LaNi_5$ systems were 45.6% and 48.1%, respectively. This is due to the heat requirement of MgH_2 tank is higher than $LaNi_5$ in fuel cell mode.

2.6 MH-based coupled reactor systems

In this section, state-of-the-art research on MH-based coupled reactor systems is addressed with respect to the relevant aspects of the present work. These include theoretical, numerical, and experimental aspects of MH-based coupled reactor systems.

Bogdanovic et al., (1995) built and tested an MgH_2/Mg-based high-temperature TES system for a process steam generator. They used 14.5 kg of MgH_2 for the heat storage and 80 kg of $Ti_{0.98}Zr_{0.02}V_{0.43}Fe_{0.09}Cr_{0.05}Mn_{1.2}$ for the H_2 storage to achieve an energy storage of 4 kWh_{th}. To improve the conversion efficiency, they suggested using a regenerator to extract the sensible heat of H_2 flowing in the pipeline from an HTMH to an LTMH.

Bedbak and Gopal, (2005) performed a thermodynamic analysis on the compressor-driven MH-based air conditioner. The results showed that the efficiency of the compressor had a significant effect on the performance of the system. The COP of the MH cooling system was lower than the commercially available vapor compression refrigeration system for the same heat extraction and heat rejection temperatures. It was also reported that parasitic losses during thermal cycling are the major reason for low COP values.

Park et al., (2007) developed a compressor-driven MH-based heat storage unit prototype for utilizing the pulsating heat load of a direct energy weapon unit. They used 10 kg of $Ca_{0.6}Mm_{0.4}Ni_5$ alloy storage material in a shell and tube-type reactor. From this system, they have achieved 4.4 kW heat storage in 250 s of operation with a regeneration period of 500 s. The heat source and sink temperatures used were 30 °C and 25 °C, respectively.

Payá et al., (2009) performed experiments and simulations on coupled bed MH reactor for the thermally driven cooling system at heat source/ambient/sink temperatures of 130/35/20°C. The considered alloys were $LmNi_{4.91}Sn_{0.15}$ (HTMH) and $Ti_{0.99}Zr_{0.01}V_{0.43}Fe_{0.09}Cr_{0.05}Mn_{1.5}$ (LTMH). They reported a mean specific cooling power of 303 W/kg of cooling alloy.

Mellouli et al., (2009b) developed a lumped parameter model of a coupled reactor for the thermally driven cooling system. The system employed $MmNi_{4.5}Al_{0.4}$ and $MmNi_{4.2}Al_{0.1}Fe_{0.7}$ as HTMH and LTMH, respectively. They found that the average system COP lies within 0.5 at different operating conditions.

Yang et al., (2011) developed a 2D mathematical model of a single-stage heat transformer using $LaNi_5$–$LaNi_{4.7}Al_{0.3}$ pair. They reported an average temperature lift of 6.8 °C when an 85°C waste heat source was used. Further, they achieved a system COP and a specific heating power (SHP) of 0.407 and 70.5 W/kg, respectively, when the heat source was supplied at 100 °C.

Ronnebro et al., (2014) developed a new reversible metal hydride TES system for high-temperature applications. Their system was based on a two-reactor concept, which included a titanium alloy as the HT reservoir and a transition metal alloy as the LT reservoir, with operating temperatures of 600°C and 100°C, respectively. The system yielded a minimum energy density of about 750 kJ/kg and a least volumetric energy density of about 3,000 kWh/m^3.

Considering the heating, ventilation, and air conditioning system for vehicles as a potential application, Fang et al., (2015) developed a two reactor-type thermal battery prototype using catalyzed MgH_2 and $TiV_{0.62}Mn_{1.5}$ as the HT and LT hydrides, respectively. They reported a cooling COP of 0.384, alongside total cooling and heating energies of 13.6 and 35.4 Wh, respectively.

Nasri et al., (2016) developed a lumped thermal model and performed a simulation for MH assisted TES unit for a high-temperature fuel cell vehicle. They engaged two different MH alloys, namely $LaNi_{4.75}Al_{0.25}$ as HTMH and $LmNi_{4.91}Sn_{0.15}$ as LTMH. High-temperature alloy served the purpose of energy storage, whereas low-temperature alloy was used for battery cooling purposes. It was reported that an increase in the driving range of the fuel cell vehicle by 17% at -20 °C ambient temperature with the inclusion of an MH-based heat recovery unit.

d'Entremont et al., (2017) simulated the performance of an MH- based TES system comprising Mg_2FeH_6 as HTMH and Na_3AlH_6 as LTMH. The proposed system was operated between 450

and 500°C, with hydrogen pressures between 30 and 70 bar. A simple tubular reactor with uniform and constant temperature boundary conditions on the outer wall was modeled in their study. The proposed working pair showed a volumetric energy storage density of ~132 kWh/m^3. Further, the developed system showed an energy storage efficiency of about 83%.

Feng et al., (2018) proposed a multi-level configuration of MH pairs to intensify the discharging process. The proposed system used MgH_2 as HTMH and $LaNi_5$ as LTMH. The flow directions of oil (in HTMH) and water (in LTMH) were arranged in counter-flow. In the multi-level configuration, there is an increase in the hydrogen pressure along the oil flow direction. Due to this, the inherent decrease of the temperature difference between the oil and HTMH bed is countered by the increasing hydrogen pressure along the oil flow direction. The results showed that the six-level configuration decreased the discharging time from 17,350 s to 14,688 s and increased the oil outlet temperature by ~5°C to the single-level system. Hence, it is recommended to develop a modular type TES system than a single large-scale system.

Nyamsi et al., (2018a) conducted a simulation study to estimate the energy storage density and efficiency using combinations of $LaNi_5$, Mg, Mg_2Ni and Mg_2FeH_6 alloys for an MH-based TES system. They reported storage density ranged from 1.3 to 2.4 GJ/m^3 and storage efficiency of ~80% for Mg-based hydrides.

Feng et al., (2019a) performed a techno-economic analysis of two different hydride alloy pairs, namely MgH_2-LaNiAl and MgH_2-TiFeMn, intended to be used for an MH-based TES system. For a designed thermal capacity of 910 MWh_{th} (7 h), the calculated input power during charging and output power during discharging was 130 MW_{th} and 120 MW_{th}, respectively.

Poupin et al., (2020) demonstrated a coupled MH-based TES storage system using Mg_2FeH_6 as HTMH and $TiMn_{1.5}$ as LTMH on a laboratory scale. From the equilibrium pressures of the MH alloys, it was found that the Mg_2FeH_6 has to operate between 350°C and 500°C with $TiMn_{1.5}$ operating at an ambient temperature of 20°C. This is due to the pressure hysteresis displayed by $TiMn_{1.5}$. The results showed that the system reached 71.2% of the HTMH's theoretical capacity, offering an energy density of 1488 kJ/kg, with $TiMn_{1.5}$ operating at 20°C. Further, an increase in the operating temperature of $TiMn_{1.5}$ to 30°C from 20°C elevated the temperature of the Mg_2FeH_6 to~520°C, utilizing the nearly total hydrogen capacity of both hydrides. The study suggested that the hysteresis of LTMH should be minimum such that the large temperature differentials in the HTMH during the charging and discharging processes could be eliminated.

Mellouli et al., (2018) conducted a numerical investigation on coupled MH-based TES systems with Mg_2FeH_6 as HTMH and Na_3AlH_6 as LTMH. The reactor used an inclined fin design for enhancing heat transfer. The energy storage density of 90 kWh_{th}/m^3 was obtained with the proposed system. The charging of Mg_2FeH_6 was conducted at 773K, whereas the discharging was conducted at 723K. From numerical results, it is observed that 90% of the system's maximum storage capacity is successfully achieved in each cycle during charging and discharging.

Malleswararao et al., (2020a) developed a 3-D numerical model to predict the performance of an MH-TES system using Mg_2Ni as HTMH and $LaNi_5$ as LTMH. They reported an energy storage density of 156 kWh/m^3 with an energy storage efficiency of 89.4% at charging and discharging temperatures of 300°C and 230°C.

Nyamsi et al., (2020) conducted a numerical study on coupled reactor-based TES systems using $Mg_2Ni/LaNi_5$ as MH pair. A simple tubular reactor design with an outer cooling jacket was used for both HTMH and LTMH reactors. A heat transfer oil was used to supply/ extract the thermal energy to the Mg_2Ni reactor. A PCM store is integrated into the $LaNi_5$ reactor to store and restore the heat of the reaction. They studied the effect of the thermophysical properties of the PCM on power density, energy density, and storage efficiency. From the numerical results, it was observed that there was an increase in the energy density and power output with a melting temperature range of up to 45–48°C, then fell after that. This was because the driving force between MH beds was the same during heat charging and discharging at that melting point. Further, enhancing the thermal conductivity of the PCM with the addition of graphite showed an improvement of as high as 23% in melting rate to the plain PCM. Furthermore, the proposed TES system showed a power density, energy storage, and energy storage efficiency of 67.8 W/kg-Mg_2Ni, 50.16 kWh_{th}/m^3, and 61.75%, respectively.

Bhogilla, (2021) modeled the coupled MH reactor-based TES system with Mg_2Ni as HTMH and TiFeMn as LTMH. The model used a variable wall boundary condition to capture the HTF temperature variation along the axial direction of the reactor. The temperatures of LTMH and HTMH are maintained at 350°C and 20°C during charging and 300°C and 30°C during discharging processes, respectively. Under these operating conditions, the tubular reactor with an outer cooling jacket obtained a charging and discharging time of 90 min and 42 min, respectively. Further, the results showed a thermal energy storage coefficient (defined as the ratio of the total useful energy output of the MHTES system to the total energy supplied to the MHTES system) value of 0.71.

Nyamsi and Tolj, (2021) studied the effect of active and passive thermal management techniques applied to the LTMH reactor on the overall performance of the coupled MH reactor-based TES system. The LTMH was subjected to five different thermal management techniques in their study, including active cooling with water and air as HTF and passive cooling techniques such as natural convection, thermal conductivity augmentation with graphite, and PCM. The operating temperatures of LTMH and HTMH were selected as 350°C and 20°C during charging and 300°C and 80°C during discharging processes, respectively. For active cooling, the results showed that the TES system achieved an energy storage density of 670 $MJ.m^{-3}$ and an energy storage efficiency of 78.53% for water as HTF. Whereas the energy storage efficiency dropped to 37% for air as HTF. This was due to the substantially increased fan power for air than water pumping power. Further, the energy storage density and efficiency were decreased to 578 $MJ.m^{-3}$ and 74%, respectively, with the addition of 15% graphite to the MH bed. Finally, the PCM-based passive technique reduced the storage density and energy storage efficiency to 142 $MJ.m^{-3}$ and 49%, respectively. From the results, the active cooling technique with liquid cooling media is recommendable.

2.7 Literature closure

The following conclusions are made from the above-discussed works of literature.

- Most researchers modeled the MH reactor's heat exchange system by simply considering a convective heat transfer coefficient on the heat exchange surfaces instead of solving for velocity and temperature fields of HTF. Further, most studies have not included the correlations for the heat transfer coefficient of different MH bed geometries.
- The performance of the MH tank is influenced by the heat and gas transport properties of the MH bed. The heat transfer characteristics of the MH reactor for both hydrogen storage and TES applications should be improved for faster charging and discharging times.
- The MH reactor's main characteristics are efficient thermal management and lower parasitic thermal mass. The design pressure and the heat management level decide the reactor's total weight for the given mass of MH material.
- The MH reactor's design and operation strategy play a significant role in successfully implementing the MH-based TES and hydrogen storage systems. Several MH reactor geometries, such as cylindrical tubes, shell and tube, internal annular rings, coiled tubes,

rectangular tanks, and microchannel reactors, were studied in the literature. The literature includes a simple heat exchanger design with slower reaction rates or a complex design with reasonably faster reaction rates. Hence, a simple reactor design with reasonably higher reaction rates is needed to achieve higher system-level energy storage densities and a cost-effective system.

- The energy efficiency of the MH-based hydrogen storage system is not studied by researchers. The MH alloy properties, heat exchanger design, and other operating parameters influence the storage tank's efficiency.
- Most of the MH reactors were studied under a forced convective environment. However, there is no evidence of pumping power's effect on the hydride reactors' energy efficiency.
- Magnesium-based alloys are the most attractive heat storage materials because of their substantial H_2 storage capacity and high energy density (Bogdanovic et al., 1990). However, minimal experimental studies were reported on a prototype scale. Further, most developed prototypes are based on simple tubular reactor designs.
- From the literature, it is clear that Mg-based hydrides suffered from two undeniable challenges: slow intrinsic kinetics and thermal management of the MH tank (Nyamsi and Tolj, 2021). The former problem could be alleviated with catalysts and pre-processing techniques of hydride powder, such as high-energy reactive ball milling (HRBM). To eliminate the latter situation, intensive efforts must be made to reactor design.
- The majority of the research works (Kang and Yabe, 1996; Mohan et al., 2019; Muthukumar et al., 2018; Muthukumar and Groll, 2010) on coupled-reactor systems were limited to low-temperature applications (< 200°C). However, minimal research (experimental) (Bogdanovic et al., 1995, 1990; Fang et al., 2015; Nyamsi et al., 2018b) has been carried out on the coupled MHTES system for medium to high-temperature applications (>200°C).
- For the case of coupled reactor systems, the hysteresis of LTMH should be minimum such that the large temperature differentials in the charging and discharging temperatures of HTMH could be eliminated. However, most of the research works reported higher temperature differential in the charging and discharging temperatures, due to which the exergy output of the TES system is reduced. Therefore, there is a need

to design the MH-based TES system with minimal difference between the charging and discharging temperatures without hampering the reaction rate.

Considering the above literature, this thesis intends to design and develop MH-based hydrogen storage and TES system scalable to large-scale applications. Given the above literature closure, the following aspects are considered in the Ph.D. thesis work.

- To develop a mathematical model for analyzing the absorption and desorption characteristics of the metal hydride reactor.
- To design a simple, lightweight, and efficient MH reactor for large-scale TCES and hydrogen storage applications.
- To design and fabricate the experimental test facility for testing MH-based TCES and hydrogen storage reactors.
- To conduct a detailed experimental study and evaluate the performance of the hydrogen storage system in terms of reaction time, gravimetric and volumetric storage densities.
- To perform a detailed experimental study and evaluate the performance of the MH-based TCES system in terms of reaction time, specific power, and gravimetric and volumetric storage densities.
- To build, integrate and test the coupled MH reactor system for TCES application.

Chapter 3

Numerical studies: HTMH reactor

3.1 Preface

The reactor design and operation strategy play a significant role in successfully implementing the MH-based TCES system. Several MH reactor designs, namely, a tubular reactor (Urbanczyk et al., 2017), a reactor with helical coil heat exchanger (Bogdanovic et al., 1995; Eisapour et al., 2021b), an embedded cooling tube reactor (Tiwari and Sharma, 2022), etc., were studied by researchers for high-temperature MH-based TES system. Tubular reactors are simple, easy to construct, and involve comparatively lesser hydraulic losses than all the existing reactor designs (Yang et al., 2010). In the tubular reactors, the lower the tube diameter, the better the heat transfer rate from the MH bed due to decreased volume-to-surface area ratio. The better heat transfer rates lead to faster charging and discharging of the TES system. However, the total number of tubes should be minimized to reduce the overall system cost. Hence, an in-depth analysis of the tubular reactors is necessary with respect to which design of an efficient MH reactor for TES, heating and cooling applications could be carried out.

The design and optimization of MH reactors require a thorough analysis of the heat and mass transfer characteristics of porous MH beds. In this chapter, a 2D transient numerical study is performed to analyze the heat and mass transfer characteristics of the MH bed during absorption (discharging) and desorption (charging) processes. The model solves temperature distribution inside the MH bed, gas flow distribution inside the porous MH bed, and velocity and temperature distribution of HTF.

Mg_2Ni alloy is selected as TCES material, which operates in the temperature range of 250 – 400°C. The main reason for selecting the Mg_2Ni is its lower operating pressure (up to 30 bar), faster absorption and desorption rates, and higher energy storage density (C. Corgnale et al., 2014; Nyamsi et al., 2018a). Therminol VP-1 is chosen as the HTF to extract or supply the thermal energy from/ to the MH bed. The thermophysical properties of Mg_2Ni alloy are shown in Table 3.1. The thermophysical properties of Mg_2Ni are assumed to be independent of temperature, pressure, and concentration. The reported thermal conductivity of the Mg_2Ni powder is in the range of 0.83 – 1.2 W/m-K (Dubey and Kumar, 2022; Eisapour et al., 2021b;

Y. Liu et al., 2021b; Malleswararao et al., 2020b; Nyamsi et al., 2020). In the present numerical study, the thermal conductivity of the metal powder is selected as 0.83 W/m-K. Hence, the effective thermal conductivity of the MH bed is 0.478 W/m-K. The variation of equilibrium pressure with temperature during the absorption and desorption processes of Mg_2Ni is shown in Fig. 3.1. The thermophysical properties of Therminol VP1 are shown in Table 3.2. Linear interpolation is used to obtain the thermophysical properties at the intermediate temperatures for Therminol VP1.

Table 3.1 Thermophysical properties of pure Mg_2Ni (Malleswararao et al., 2020b; Nyamsi et al., 2020)

Property	Mg_2Ni	Hydrogen
Molecular weight (g/mol)	107.3	2.01
Specific heat (J/kg-K)	1414	14283
Thermal conductivity (W/m-K)	0.83	0.127
Reaction Enthalpy, ΔH (J/mol)	-64000 (absorption) -64500 (desorption)	-
Reaction Constant, C (1/s)	175.1 (absorption) 5452.3 (desorption)	-
Activation Energy, E (J/mol)	52200 (absorption) 63460 (desorption)	-
Density (kg/m^3)	3200	-
Maximum H_2 storage capacity ($wt.\%_{max}$)	3.6	-
Porosity	0.5	-
Permeability (m^2)	10^{-8}	-
Universal gas constant (J/mol-K)	8.314	-
van't Hoff constants: A, B [K]	-7697.85, 14.698	-
Constants:		-
Slope factors, (ϕ_s) (ϕ_o)	0.0085 0.0036	-
Hysteresis factor (β)	0.243	-

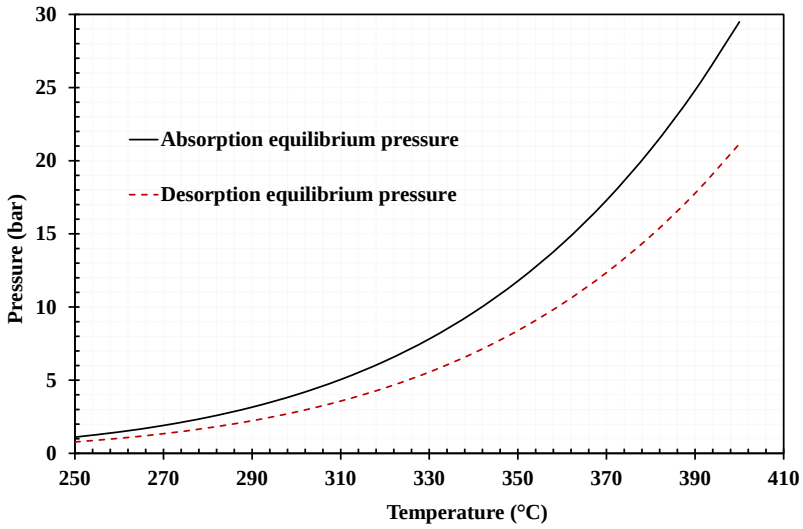

Fig. 3.1. Variation of equilibrium pressure with temperature during absorption and desorption processes of Mg_2Ni

Table 3.2 Thermophysical properties of Therminol-VP1 (Therminol, 2022)

Temperature (°C)	Density (kg/m^3)	Specific heat (J/kg-K)	Thermal conductivity (W/m-K)	Dynamic viscosity (Pa-s)
250	867	2181	0.1055	0.000288
260	857	2207	0.1038	0.000272
270	848	2234	0.102	0.000258
280	838	2260	0.1002	0.000244
290	827	2287	0.0983	0.000232
300	817	2314	0.0964	0.000221
310	806	2341	0.0945	0.000211
320	796	2369	0.0925	0.000202

Firstly, the numerical model is used to study the heat and mass transfer characteristics of the tubular reactors during the discharging process. The average MH bed temperature, reacted fraction, and energy transfer rates are analyzed for the tubular reactor. Further, the tubular reactors are compared in terms of discharging time, energy storage density, specific discharge power, and pressure drop in the HTF flow channel. Furthermore, the advantages and drawbacks of the tubular are highlighted. An annular MH reactor is proposed to overcome the disadvantages of tubular reactors. An annular MH reactor is cooled/ heated on internal and external surfaces using an inner cooling tube and an outer cooling jacket. The annular MH reactor is studied and compared with the tubular reactor.

3.2 Mathematical formulation

A 2D mathematical model is developed for analyzing the absorption and desorption processes in a porous MH bed. Mass, momentum, and energy conservation laws are applied to the porous material. The dependent variables of interest are the density of the hydride, the temperature of hydrogen gas/hydride, the velocity components of hydrogen gas in two directions, and the pressure of hydrogen gas. The MH reactor is cooled/ heated during the absorption/ desorption processes by supplying the HTF. The flow behavior of the HTF is simulated in two different ways. One is considering a convective heat transfer coefficient on the outer surface of the reactor, which is modeled using a convective cooling boundary condition without modeling the flow behavior of the HTF. In another method, the continuity, momentum, and energy equations are solved for the HTF flow field instead of considering the heat transfer coefficient on the heat exchanger's outer walls. The assumptions, governing equations, and initial and boundary conditions are explained in the following sections.

3.2.1 Assumptions

The assumptions associated with the absorption and desorption processes are described below. The assumptions considered in the present study are well-validated in the literature (Jana and Muthukumar, 2021; Malleswararao et al., 2020b; Mathew et al., 2021; Rabienataj Darzi et al., 2016; Wu et al., 2014).

1. Hydrogen behaves as an ideal gas: MH reactor of the present study is operated in the pressure range of 5-40 bar, and the compressibility factor of hydrogen is nearly unity in this pressure range; hence ideal gas assumption is valid.
2. Local thermal equilibrium is valid between MH and hydrogen gas: Hydrogen gas velocity inside the MH bed is very low (Re < 1) during absorption and desorption processes. Hence, local thermal equilibrium is valid for a slow-moving flow (up to Re < 10).
3. Metal hydride material is homogeneous and isotropic: Composition and distribution of MH alloy are uniform within the reactor bed with nearly uniform particle size.
4. Porosity and permeability are uniform
5. The thermophysical properties of MH are independent of temperature, concentration, and pressure.
6. The expansion and contraction of metal hydride during hydriding and dehydriding processes are neglected.

3.2.2 Governing Equations

Governing equations for MH bed

Hydride mass balance:

The mass conservation of the solid metal hydride is given by Eq. 3.1.

$$(1-\varepsilon)\frac{\partial \rho_s}{\partial t} = (1-\varepsilon)\dot{m} \tag{3.1}$$

Hydrogen gas mass balance

Variation of hydrogen gas density in the MH bed is due to hydrogen flow and simultaneous absorption/ desorption in metal hydride. The mass balance equation for hydrogen gas is given by Eq. 3.2.

$$\varepsilon\frac{\partial \rho_g}{\partial t} + \frac{1}{r}\frac{\partial}{\partial r}\left(r\rho_g u_r\right) + \frac{\partial}{\partial z}\left(\rho_g u_z\right) = -(1-\varepsilon)\dot{m} \tag{3.2}$$

The reaction rate during absorption and desorption are given by Eqs. 3.3 and 3.4, respectively.

$$\dot{m} = C_a \exp\left(-\frac{E_a}{R_u T}\right)\ln\left(\frac{P_g}{P_{eq}}\right)(\rho_{sat} - \rho_s) \qquad (Absorption) \tag{3.3}$$

$$\dot{m} = C_d \exp\left(-\frac{E_d}{R_u T}\right)\left(\frac{P_g - P_{eq}}{P_{eq}}\right)(\rho_s - \rho_o) \qquad (Desorption) \tag{3.4}$$

Momentum equation

Darcy's law (Eq. 3.5) describes the velocity of the hydrogen in porous metal hydride.

$$u_r = \frac{-K}{\mu_g}\frac{\partial P_g}{\partial r}$$
$$u_z = \frac{-K}{\mu_g}\frac{\partial P_g}{\partial z} \tag{3.5}$$

Where the pressure, P_g satisfies the ideal gas equation (Eq. 3.6)

$$P_g = \rho_g R_g T \tag{3.6}$$

Energy equation

The energy equation for the MH bed under the assumption of thermal equilibrium between the MH bed and hydrogen gas is given by Eq. 3.7.

$$(\rho C_p)_e\frac{\partial T}{\partial t} + \rho_g C_{p_g} u_r\frac{\partial T}{\partial r} + \rho_g C_{p_g} u_z\frac{\partial T}{\partial z} = \frac{1}{r}\frac{\partial}{\partial r}\left(rk_e\frac{\partial T}{\partial r}\right) + \frac{\partial}{\partial z}\left(k_e\frac{\partial T}{\partial z}\right) - (1-\varepsilon)\dot{m}\left(\frac{\Delta H}{M_{H_2}}\right) \tag{3.7}$$

Where the effective heat capacity and thermal conductivity are determined as follows

$$\left(\rho C_p\right)_e = \varepsilon\left(\rho C_p\right)_g + \left(1-\varepsilon\right)\left(\rho C_p\right)_s$$

$$k_e = \varepsilon k_g + \left(1-\varepsilon\right)k_s$$

Equilibrium pressure

In reality, MHs exhibit pressure hysteresis during hydrogen absorption and desorption due to the development of mechanical strain in the metal lattice with the insertion of hydrogen atoms into interstitial sites. Metal hydrides also exhibit sloping behavior in the plateau region of pressure-composition-isotherm due to inhomogeneities in composition. Nishizaki et al., (1983) proposed an equation (Eq. 3.8) for equilibrium pressure by curve-fitting experimental P-C-I data that considers the hysteresis and slope effects.

$$P_{eq} = \exp\left\{\left[A - \frac{B}{T}\right] + \left(\varphi_s \pm \varphi_0\right)\tan\left[\pi\left(\frac{c}{c_{sat}} - \frac{1}{2}\right)\right] \pm \frac{\beta}{2}\right\} \times 10^5 \tag{3.8}$$

Here the sign '+' is for absorption and '–' is for desorption

The relations between concentration, hydride density, and wt.% are given as follows (Busqué et al., 2018)

$$\text{Concentration, } c = \frac{2\left(\rho_s - \rho_o\right)M_{MH}}{\rho_o M_{H_2} N_{MH}} \tag{3.9}$$

$$\text{Weight percentage, } wt.\% = \frac{\text{mass of hydrogen absorbed/desorbed (g)}}{\text{mass of alloy used (g)}} = \frac{100\left(\rho_s - \rho_o\right)}{\rho_o} \tag{3.10}$$

Reacted fraction (i.e., the fraction of hydrogen reacted with metal alloy) is defined as the ratio of the amount of hydrogen transferred with respect to time to the total transferable amount of hydrogen for the given initial and boundary conditions (Eq. 3.11).

$$\text{Reacted fraction} = \frac{\text{amount of hydrogen transfered with time}}{\text{total transferable amount of hydrogen}} \tag{3.11}$$

Governing equations for HTF

The governing equations for incompressible fluid flow are as follows.

Continuity equation:

$$\frac{1}{r}\frac{\partial\left(ru_r\right)}{\partial r} + \frac{\partial u_z}{\partial z} = 0 \tag{3.12}$$

Momentum equation:

$$\frac{\partial u_r}{\partial t}+u_r\frac{\partial u_r}{\partial r}+u_z\frac{\partial u_r}{\partial z}=-\frac{1}{\rho_f}\frac{\partial p}{\partial r}+\frac{\mu_f}{\rho_f}\left\{-\frac{u_r}{r^2}+\frac{1}{r}\frac{\partial}{\partial r}\left(r\frac{\partial u_r}{\partial r}\right)+\frac{\partial^2 u_r}{\partial z^2}\right\}$$
$$\frac{\partial u_z}{\partial t}+u_r\frac{\partial u_z}{\partial r}+u_z\frac{\partial u_z}{\partial z}=-\frac{1}{\rho_f}\frac{\partial p}{\partial z}+\frac{\mu_f}{\rho_f}\left\{\frac{1}{r}\frac{\partial}{\partial r}\left(r\frac{\partial u_z}{\partial r}\right)+\frac{\partial^2 u_z}{\partial z^2}\right\} \quad (3.13)$$

Energy equation:

$$\rho_f C_{p_f}\left(\frac{\partial T}{\partial t}+u_r\frac{\partial T}{\partial r}-u_z\frac{\partial T}{\partial z}\right)=\frac{1}{r}\frac{\partial}{\partial r}\left(rk_f\frac{\partial T}{\partial r}\right)+\frac{\partial}{\partial z}\left(k_f\frac{\partial T}{\partial z}\right) \quad (3.14)$$

Governing equation(s) for reactor tube

The conduction heat transfer phenomena inside the solid domain (reactor tube, HTF tube, and fins) are modeled using the following energy equation.

$$\rho_{sd}C_{psd}\frac{\partial T}{\partial t}=\frac{1}{r}\frac{\partial}{\partial r}\left(rk_{sd}\frac{\partial T}{\partial r}\right)+\frac{\partial}{\partial z}\left(k_{sd}\frac{\partial T}{\partial z}\right) \quad (3.15)$$

The numerical solution for Eqs. (3.1-3.15) have been obtained using the finite element-based simulation tool COMSOL Multiphysics 5.3. Non-isothermal flow Multiphysics coupling is used between fluid flow and heat transfer phenomenon. All simulations are performed on a Dell Precision T7610 workstation equipped with two Intel Xeon E5-2650 v2 processors and 64 GB RAM. The resulting linear equations are solved using the segregated approach with a direct linear solver, PARDISO.

3.3 Physical system

3.3.1 Tubular reactor

The schematic of the tubular reactor is shown in Fig. 3.2a. The tubular reactor consists of two concentric tubes. The MH alloy is filled inside the inner tube and the HTF flows through the cooling channel between the inner and outer tubes (Fig. 3.2a). Several such tubes containing the MH alloy are arranged inside a shell called a tube bundle reactor for large-scale applications. A commercially available ASTM A321 standard tube of SS316 material is selected for the tubular reactors (the dimensions are shown in Table 3.3). Maximum working pressure of 60 bar is considered for the operation of the TES system, as most MH-based TES operates below this pressure range (Sandrock, 1999a). The length of the reactor is kept at 1 m. The heat discharge behavior of the tubular reactor under constant supply pressure is modeled in COMSOL Multiphysics 5.3. A 2D mathematical model is formulated for the discharging process as the reactor is axisymmetric (Fig. 3.2b). Mass, momentum, and energy conservation

laws are applied in the MH bed zone (as described in section 3.2). Hydrogen is charged from the top of the reactor during the heat discharging, as shown in Fig. 3.2b. The tubular reactor is cooled from the outer surface during the discharging process by supplying the HTF.

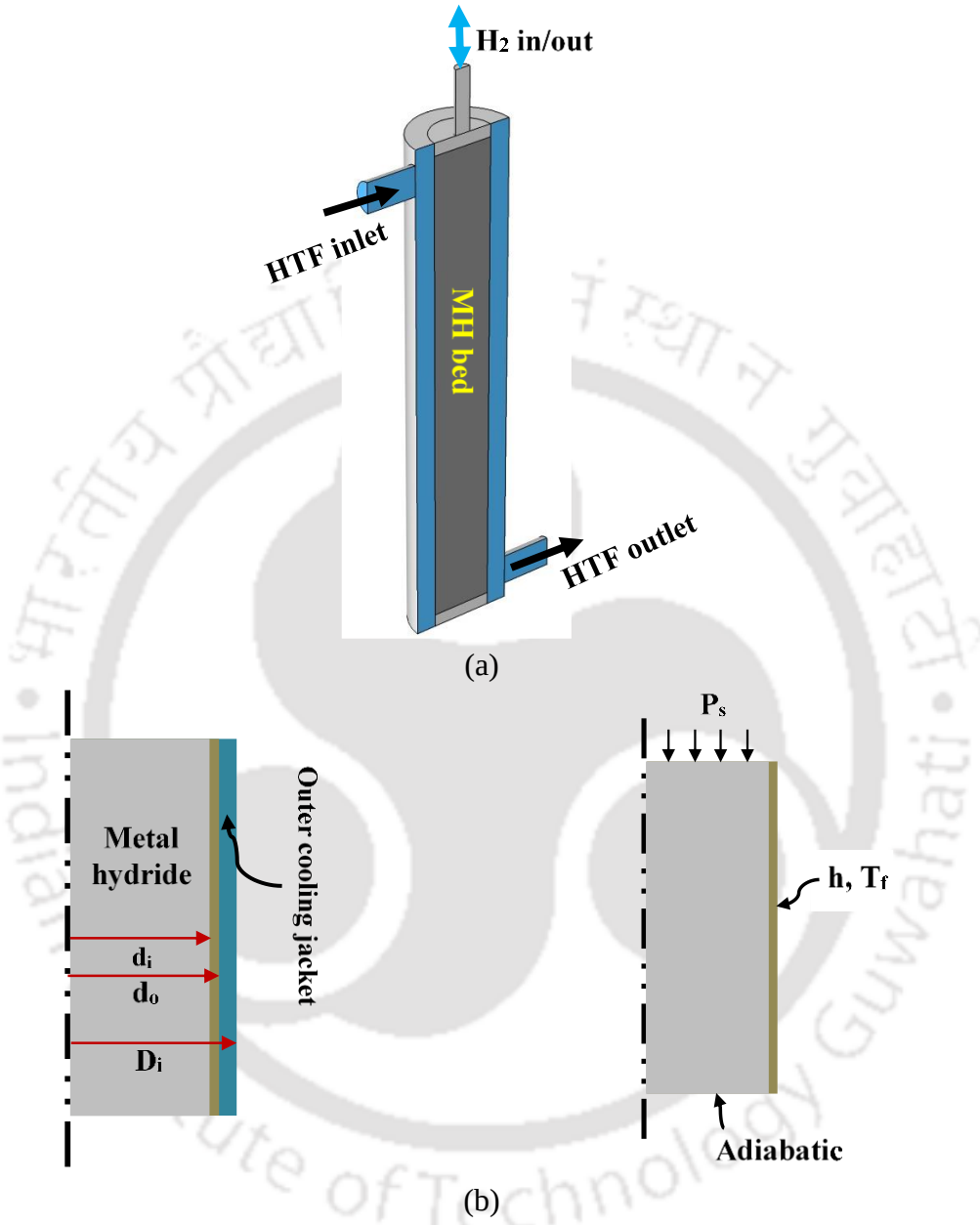

Fig. 3.2. (a) Schematic and (b) 2D axisymmetric computational domain and boundary conditions of the tubular reactor with outer cooling jacket (not to scale)

Table 3.3. Specifications of the tubular MH reactors

Nominal diameter (inch)	d_o (mm)	d_i (mm)	D_i (mm)	Mass of reactor (kg)	Working pressure at 400°C (bar)	Mass of Mg_2Ni filled for $\varepsilon = 0.5$ (kg)	Weight ratio	$\frac{V}{A_s}$ (mm)
3/8	17.15	13.85	25.15	0.645	204	0.24	0.37	3.5

3/4	26.67	23.37	34.67	1.041	127	0.685	0.66	5.8
1	33.4	30.1	41.4	1.321	100	1.137	0.86	7.5
1½	48.26	44.96	56.26	1.94	68	2.53	1.3	11.2
2	60.33	57.03	68.33	2.442	54	4.07	1.67	14.3
2½	73.03	68.81	81.03	3.75	60	5.93	1.58	17.2

3.3.2 Annular reactor

An annular MH reactor that is cooled/ heated on internal and external surfaces using an inner cooling tube and an outer cooling jacket is proposed. For the same mass of MH alloy, the annular MH reactor offers less resistance to heat transfer than the tubular reactor. A steady state analysis is presented in Appendix I to show the better heat transfer characteristics of the annular MH reactor over the tubular reactor. Under steady state heat transfer conditions, the annular MH reactor subjected to uniform internal heat generation showed less maximum temperature than the tubular reactor due to better heat transfer conditions. The schematic of such an annular MH reactor is shown in Fig. 3.3a. The annular porous MH reactor consists of an inner cooling tube and an outer cooling jacket. An axial disc filter is fitted near the reactor's left wall for passing H_2 gas in/out of the reactor.

The main aim of proposing the annular MH reactor is to reduce the number of tubular reactors without affecting the average specific discharge power and discharge time of the tubular reactors. The specifications of the annular MH reactors based on a 2.5-inch tubular reactor are shown in Table 3.4. The combination of inner and reactor tubes is selected to maintain a minimum weight ratio of 1. The schematic, computational domain and boundary conditions of the annular MH reactor are shown in Fig. 3.3.

Table 3.4. Specifications of annular MH reactors

Case No.	d_1 (mm)	d_2 (mm)	d_3 (mm)	d_4 (mm)	Mass of reactor (kg)	Mass of Mg_2Ni filled for $\varepsilon = 0.5$ (kg)	$\frac{V}{A_s}$ (mm)	Weight ratio
1	13.85	17.15	68.81	73.03	4.4	5.58	12.92	1.27
2	18.04	21.34	68.81	73.03	4.57	5.38	11.87	1.17
3	23.37	26.67	68.81	73.03	4.79	5.05	10.54	1.05

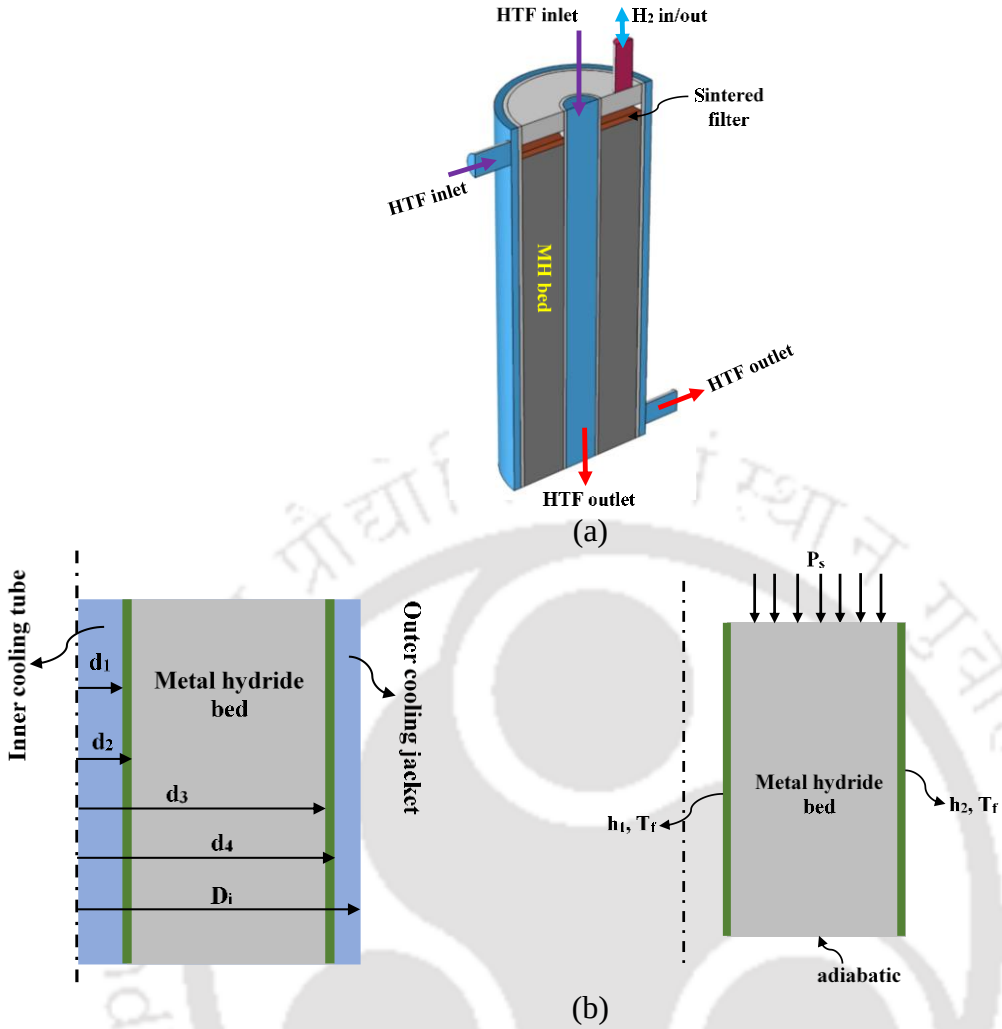

Fig. 3.3. (a) Schematic and (b) computational domain and boundary conditions of the annular MH reactor (not to scale)

3.4 Initial and boundary conditions: tubular and annular reactor

3.4.1 Initial conditions

The initial conditions used in modeling the discharging process of tubular and annular reactors are presented in Table 3.5.

Table 3.5. Initial conditions

$T(r,z,0) = T_{o,d} = 250°C$
$P(r,z,0) = P_{eqi,d} = 1bar$
$\rho_s(r,z,0) = \rho_{si,d} = 3204.5 \frac{kg}{m^3}$
$c(r,z,0) = c_{i,d} = 0.05$

3.4.2 Boundary conditions

The boundary conditions used in the model are presented in Table 3.6. The inlet pressure is ramped/ reduced from the initial equilibrium pressure to the supply/ discharge pressure using Eq. 3.16 to avoid convergence issues.

$$P_{inlet}(t) = P_{eqi} + D(t)\left(P_{\sup ply} - P_{eqi}\right) \tag{3.16}$$

D(t) is a step function defined at t = 0.05 s.

Table 3.6. Boundary conditions

Name of boundary condition	Boundary condition
Adiabatic condition on the outer walls	$\frac{\partial T}{\partial n} = 0$
No slip and non-permeability on the walls of the HTF tube	$u_r = u_z = 0$
Hydrogen inlet (supply pressure) and no flow condition	At the inlet of the reactor, $p = P_{\sup ply} = 5 bar\,(discharging)$ On walls of MH reactor, $\frac{\partial p}{\partial n} = 0$ or $\vec{n} \cdot \rho\vec{V} = 0$
Heat flux continuity	On the interface between the heat exchanger tube and the MH reactor: $-k_{MH} \nabla T\big\|_{MH} = -k_{tube} \nabla T\big\|_{tube}$ Tubular reactor: On the outer surface of the tubular reactor: convective cooling $\vec{n} \cdot k_{tube} \nabla T = h\left(T_f - T\right)$ $T_f = 250°C$ Annular reactor: convective cooling $at\ r = R_1; \vec{n} \cdot k_{tube} \nabla T = h_1\left(T_f - T\right)$ $at\ r = R_4; \vec{n} \cdot k_{tube} \nabla T = h_2\left(T_f - T\right)$ $T_f = 250°C$

The convective heat transfer phenomenon on the outer surface of the reactor is modeled using a convective cooling boundary condition without modeling the flow behavior of the HTF (i.e., Eqs. (3.12-3.14) are not solved). The heat transfer coefficient for the tubular reactor (or annular reactor) with the outer cooling jacket is calculated using Eq. 3.17 (Nyamsi and Tolj, 2021).

$$\overline{Nu} = 0.86\left(\frac{D_i}{d_o}\right)^{0.16} \times 0.116\left(1+\left(\frac{d_h}{L}\right)^{2/3}\right)\left(\mathrm{Re}_D^{2/3}-125\right)\mathrm{Pr}^{1/3} \qquad for\ 3000 < \mathrm{Re_D} < 10,000$$

$$\overline{Nu} = 0.86\left(\frac{D_i}{d_o}\right)^{0.16} \times 0.023\left(1+\left(\frac{d_h}{L}\right)^{0.7}\right)\mathrm{Re}_D^{0.8}\,\mathrm{Pr}^{1/3} \qquad for\ \mathrm{Re_D} > 10,000$$

$$\overline{Nu} = \frac{\bar{h}d_h}{k} \tag{3.17}$$

$$\mathrm{Re} = \frac{\rho V d_h}{\mu}$$

$$d_h = \textit{characteristic length} = D_i - d_o = 8\ \text{mm in the present study}$$

The heat transfer coefficient on the inner cooling tube (in the case of an annular MH reactor) is calculated using Eq. 3.18 (Incropera et al., 2011). Heat transfer fluid properties at 250°C are used to calculate the heat transfer coefficient during the discharging process of both tubular and annular reactors.

$$\overline{Nu} = 0.023\mathrm{Re}_D^{0.8}\,\mathrm{Pr}^n; n = 0.4\ \textit{for heating and}\ n = 0.3\ \textit{for cooling}$$

$$\begin{bmatrix} 0.7 \le \mathrm{Pr} \le 160 \\ \mathrm{Re}_D \ge 10,000 \\ \dfrac{L}{D} \ge 10 \end{bmatrix} \tag{3.18}$$

3.5 Numerical modeling

The effect of relative tolerance on the average equilibrium pressure is shown in Fig. 3.4a. The relative tolerance significantly affected the solution to the problem. Using relative tolerance of 0.001 in the simulation resulted in the average equilibrium pressure higher than the supply pressure (i.e., 5 bar) towards the end of the discharging process, which is erroneous. Hence, it is recommended to use a relative tolerance lesser than 0.001. From Fig. 3.4a, it is found that there is no significant deviation in the results of average equilibrium pressure between the relative tolerance of 10^{-5} and 10^{-6}. Hence, all the simulations are performed for the relative tolerance of 10^{-5}. An adaptive time-stepping scheme, Euler's backward difference formula (BDF), is used to solve the present time-dependent problem. According to this, the solver of COMSOL Multiphysics will automatically adjust the timestep size to maintain the desired relative tolerance. Free triangular elements are used for meshing the domains. Special meshing features of COMSOL Multiphysics, such as boundary layers and corner refinement, are used to have a finer mesh near the walls of the computational domain. A mesh independence study is performed to find the optimal mesh size and minimize the computational cost without compromising the solution accuracy. The average equilibrium pressure is plotted for different

mesh sizes, as shown in Fig. 3.4b. The mesh size has not influenced the solution significantly; hence a fine mesh with minimum element quality of 0.6 is chosen for all the reactors studied in the present study.

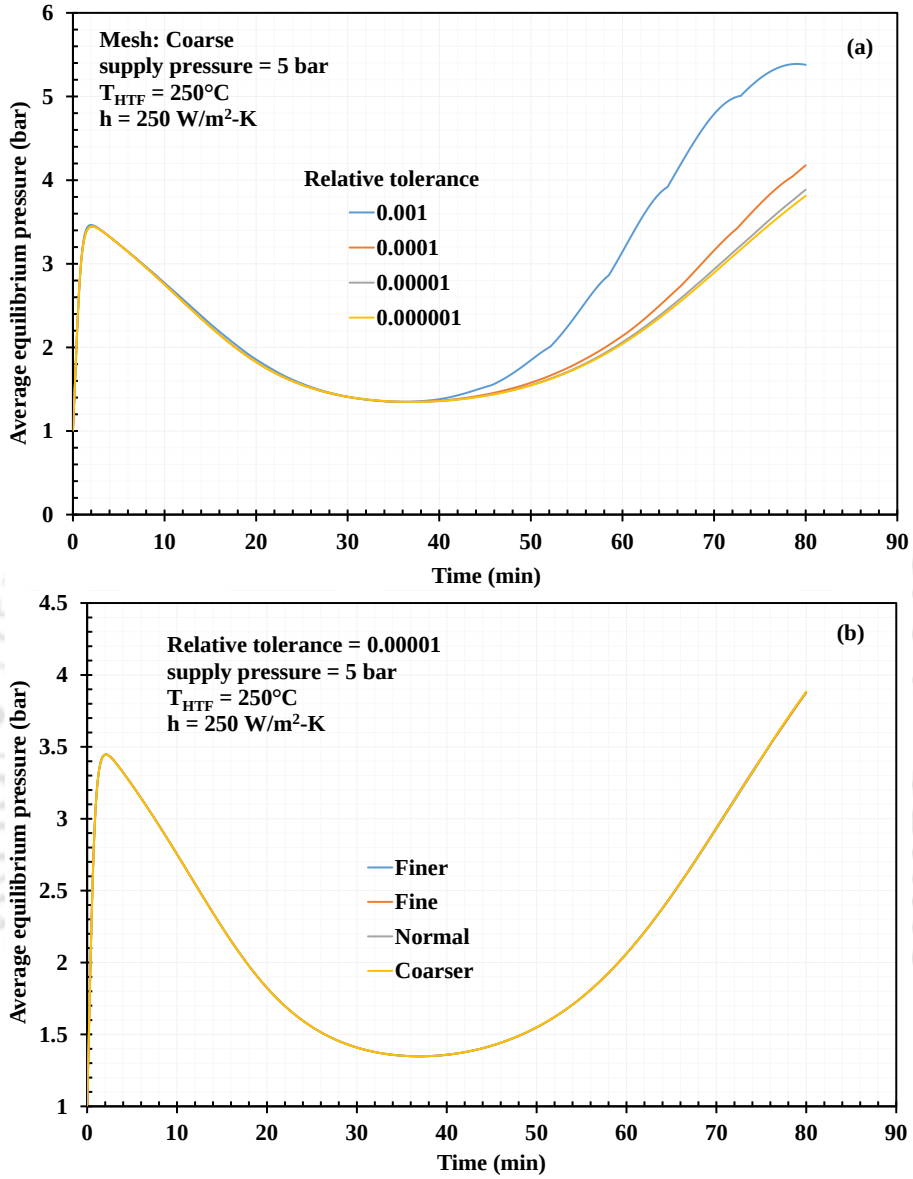

Fig. 3.4. (a) Relative tolerance and (b) mesh size effect on the average equilibrium pressure of the MH bed

3.6 Model validation

The present numerical results are validated with the experimental work of Muthukumar et al., (2005) (MH reactor with outer cooling jacket) and Singh et al., (2015) (MH reactor with finned tube). The results obtained and the corresponding operating conditions used for the validation are shown in Fig. 3.5. It is observed that the predicted numerical results are in good agreement with the experimental data.

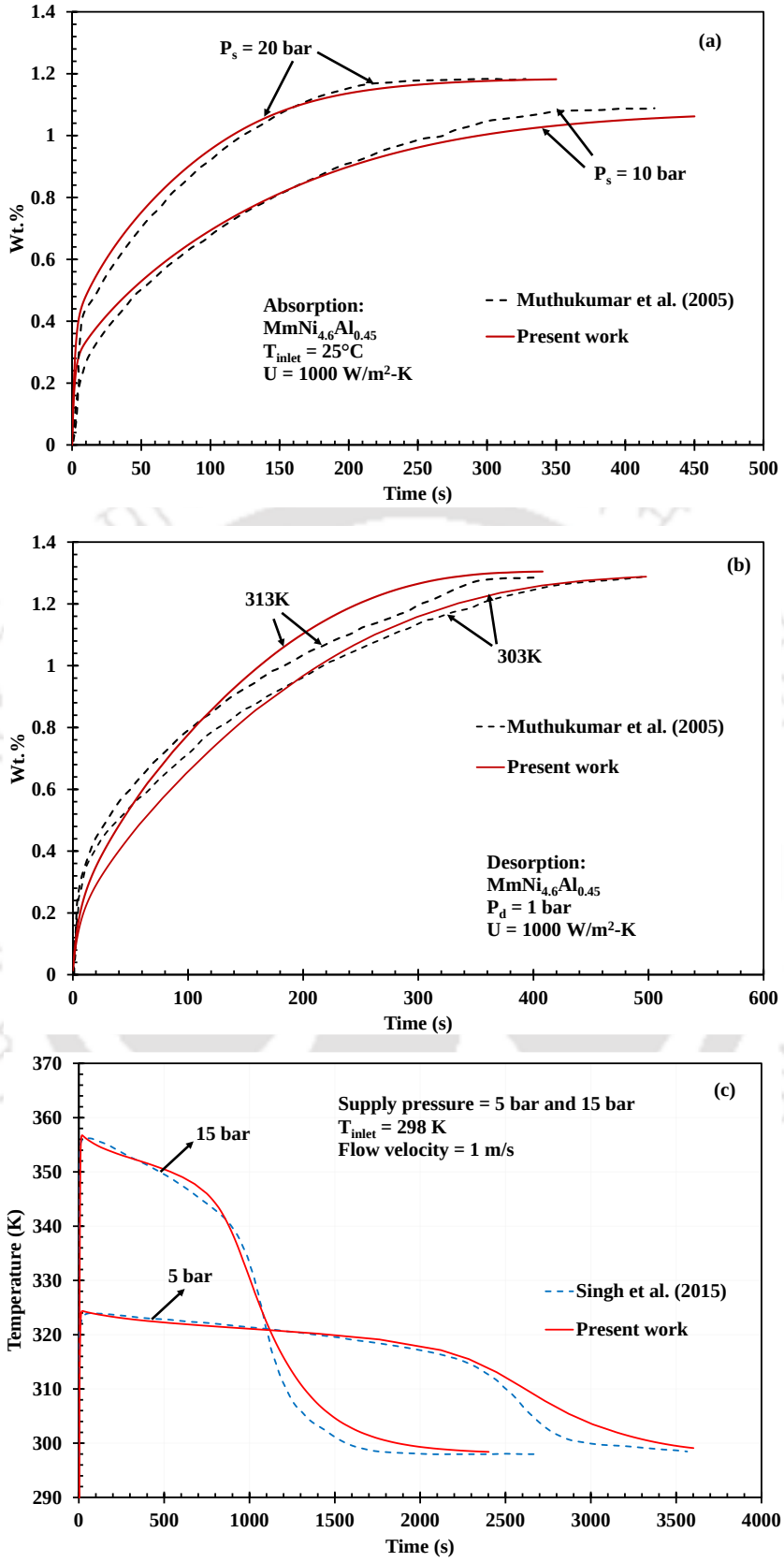

Fig. 3.5. Validation of the present numerical model with experimental work (a) absorption, (b) desorption of Muthukumar et al. (2005) and (c) temperature profile of Singh et al. (2015)

The present numerical results are also validated with the experimental results of the present study. The experimental results of the annular MH reactor filled with $LaNi_5$ have been selected for validation, as described in section 5.4.2. The wt.% variation during absorption under 10 bar supply pressure is compared and shown in Fig. 3.6. A maximum deviation of 10.3% is observed between the experimental and numerical results. The perforations in the fins are not considered in the numerical model, which is one of the possible reasons for the deviation.

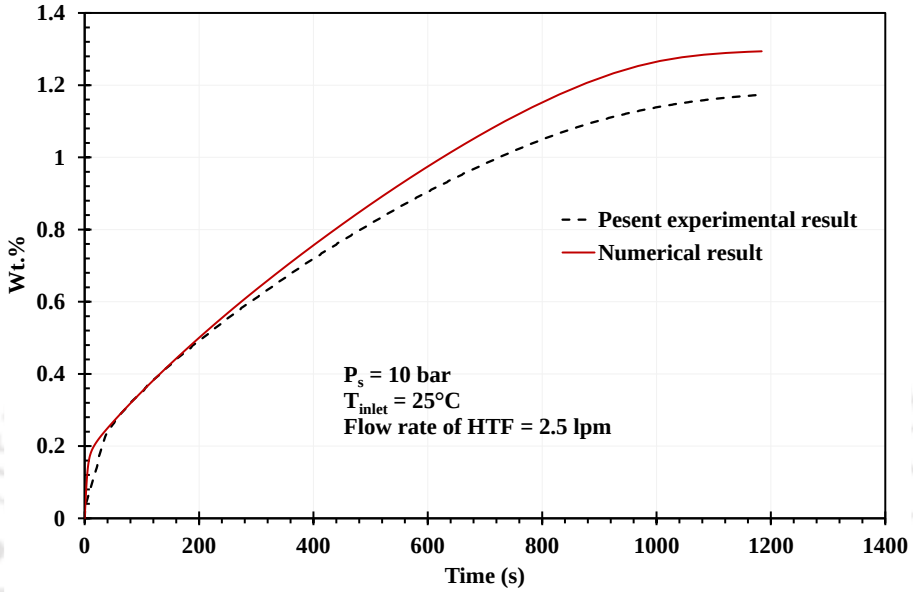

Fig. 3.6. Validation of the numerical model with present experimental work under 10 bar supply pressure

3.7 Definitions

3.7.1 Weight ratio (WR)

A weight ratio defined as the ratio of the mass of MH alloy to the mass of the empty reactor is shown in Eq. 3.19. The weight ratio signifies the thermal mass of the whole reactor. The weight ratio of the MH reactor depends on the working pressure of the reactor and the heat transfer enhancement provided.

$$\text{Weight ratio } (WR) = \frac{Mass\ of\ metal\ hydride\ alloy}{Mass\ of\ the\ empty\ reactor} \tag{3.19}$$

3.7.2 System-level storage density

The system-level gravimetric and volumetric storage densities of the MH-based TES system are given in Eq. 3.19. The amount of energy exchanged with HTF is considered for the period of discharge.

$$SGSD = \frac{amount\ of\ energy\ exchanged\ with\ HTF}{total\ mass\ of\ the\ system}\left(\frac{kJ}{kg\ of\ the\ system}\right)$$
$$SVSD = \frac{amount\ of\ energy\ exchanged\ with\ HTF}{total\ volume\ of\ the\ system}\left(\frac{kJ}{m^3\ of\ the\ system}\right) \quad (3.20)$$

3.7.3 Specific discharge power (SDP)

The system-level specific discharge power of the MH-based TES system is given by Eq. 3.21.

$$SDP = \frac{instantaneous\ energy\ exchange\ rate\ with\ HTF}{total\ mass\ of\ the\ system}\left(\frac{W}{kg\ of\ the\ system}\right) \quad (3.21)$$

3.8 Results and discussion: tubular and annular MH reactors

In this section, the performance of the tubular and annular MH reactors is compared during the discharging process. The tubular and annular MH reactors are modeled using a convective cooling boundary condition on the outer heat transfer surface. The heat transfer coefficient reported in the literature for MH-based reactors was 250 – 10000 W/m^2-K (Afzal and Sharma, 2018; Bao et al., 2013; Wu et al., 2014). In the present study, the tubular reactors are studied under the convective heat transfer coefficient of 250 W/m^2-K to ensure that the designed reactor meets the performance targets even in the lower convective heat transfer coefficient range. Also, all the simulations are performed under the supply pressure of 5 bar for the same reason. All the simulations are performed under the supply pressure of 5 bar. The average MH bed temperature, reacted fraction, and energy transfer rates are presented for a tubular reactor. Further, the tubular reactors are compared in terms of discharging time, energy storage density, specific discharge power and pressure drop in the HTF flow channel. The annular MH reactor is studied by subjecting to a heat transfer coefficient obtained for the equivalent mass flow rate of HTF of a tubular reactor. Three cases of the annular MH reactors are studied and compared with tubular reactors. Finally, the annular MH reactor is studied by applying boundary conditions experienced by the reactors near the real-time TES system outlet section.

3.8.1 Tubular reactors

3.8.1.1 Heat transfer rate, average bed temperature, and reacted fraction

The time variation of the heat generation rate, heat accumulation rate, convective heat transfer rate, average MH bed temperature, and reacted fraction for the 3/8-inch reactor is shown in Fig. 3.7. The supply pressure, the inlet temperature of the HTF, and convective heat transfer

coefficient are set to 5 bar, 250°C, and 250 W/m^2-K, respectively. The heat generation (i.e., heat source) is very high during the initial stages of the reaction due to the higher driving potential (i.e., the difference between the supply pressure and equilibrium pressure). As the heat generation is rapid, the heat accumulation rate is more than the convective heat transfer rate (for the given convective heat transfer boundary conditions), as shown in Fig. 3.7a. At t = 0.2 min, the heat source rate is 451.76 W, out of which 402.17 W is accumulated, and -54 W is transferred to the HTF by convection (*Note*: the convective heat transfer rate is negative, indicating heat is transferred from the MH bed to HTF). Therefore, there is a sharp rise in the MH bed temperature due to the accumulated heat rate, as shown in Fig. 3.7b. The increase in the bed temperature causes the convective heat transfer rate to increase. The accumulated heat rate is positive up to 2.1 min, and after that, it becomes negative, indicating the convective heat transfer rate dominates the total heat generation rate. Due to this, the bed temperature decreases and reaches the inlet temperature of the HTF (i.e., 250°C). The discharging process is said to be completed when the MH bed temperature reaches its initial temperature value. However, the temperature difference for heat transfer becomes very low toward the end of the discharge process. Hence, the present study defines the discharging time as the time required for the MH bed to reach nearer to its initial temperature, i.e., 250.5°C.

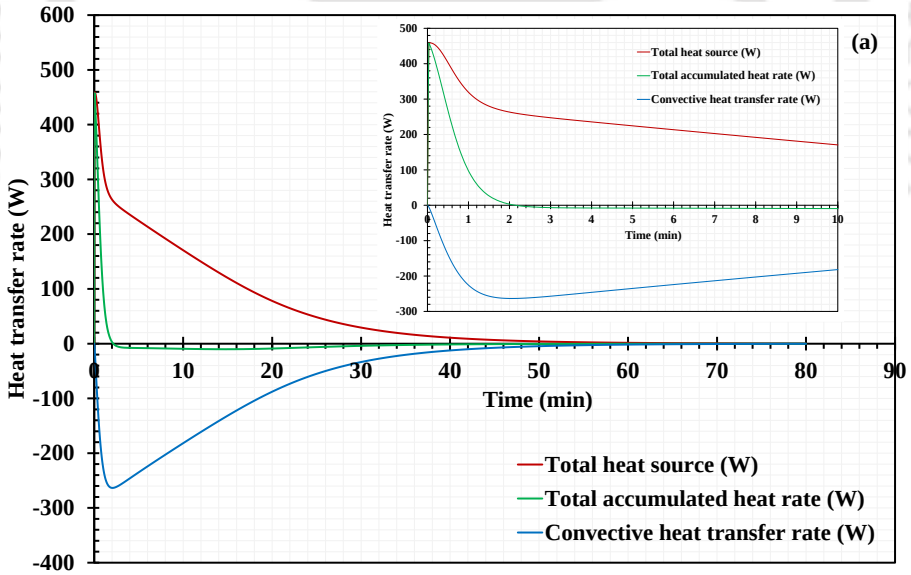

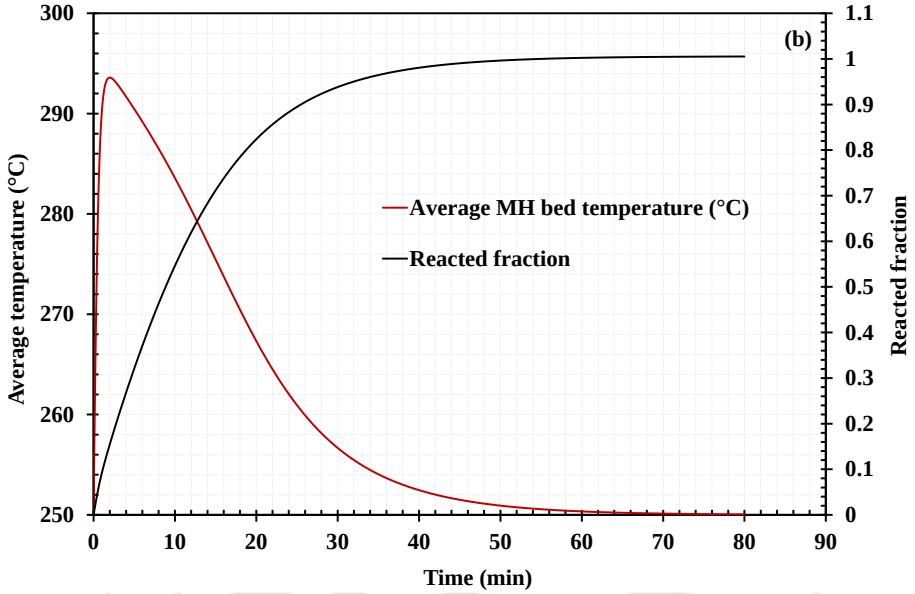

Fig. 3.7. Time variation of (a) total heat source, total heat accumulation rate, convective heat transfer rate and (b) average MH bed temperature and reacted fraction for 3/8-inch reactor

The convective heat transfer rate (multiplied with -1 to show in positive Y-axis) and the reacted fraction are plotted with respect to time, as shown in Fig. 3.8 for the 3/8-inch reactor. The energy transferred from the MH bed to HTF (i.e., the area under the convective heat transfer rate curve, also defined in Eq. 3.22) is indicated in Fig. 3.8. The total energy released from the MH bed during the discharge process is 264.16 kJ (area A). The areas A_1 and A_2 are 118.33 kJ (44.8%) and 145.83 kJ (55.2%), respectively. This indicates that 44.8% of the total stored energy is transferred to the HTF in the first 8.93 min (536 s), during which the reacted fraction reaches from 0 to 0.5. That means for the first 50% of the reaction (i.e., up to X = 0.5), only 44.8% of the generated energy is transferred to the HTF, and the rest, 5.2% of energy is accumulated in the MH bed. The remaining 55.2% of the total energy is transferred in 71.1 min (4266 s), during which the reacted fraction X reached from 0.5 to 1. During the initial period (up to 8.93 min), more energy is transferred to the HTF in less time due to high heat transfer rates caused by the higher driving potential for heat transfer.

$$A = A_1 + A_2$$

A = total amount of thermal energy transferred to HTF form MH reactor during discharge process

A_1 = energy transferred to HTF for X reaching from 0 to 0.5

A_2 = energy transferred to HTF for X reaching from 0.5 to 0.996 (3.22)

t_1 = time taken for transferring A_1 amount of energy to HTF

t_2 = time taken for transferring A_2 amount of energy to HTF

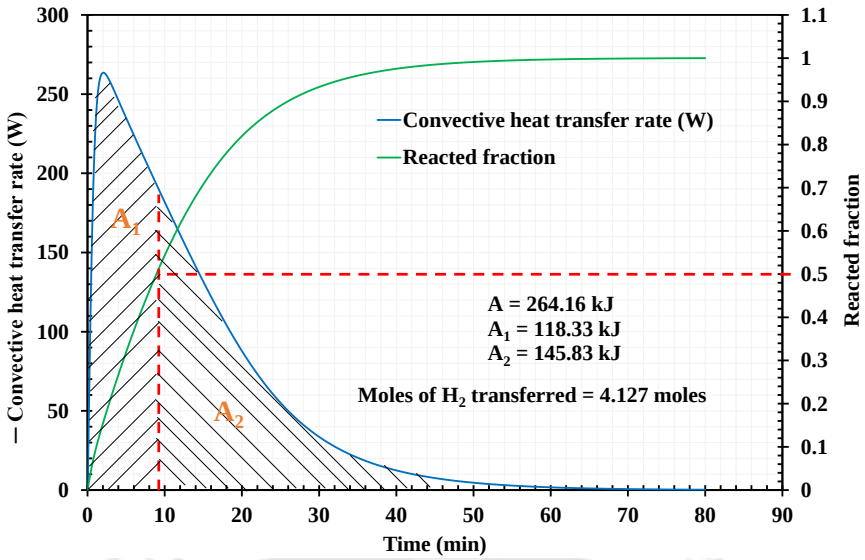

Fig. 3.8. The convective heat transfer rate and reacted fraction vs. time for the 3/8-inch reactor

3.8.1.2 Discharging time, energy storage density, discharge power and pressure drop in HTF

The system-level energy storage density is a critical parameter that plays a vital role in the final cost of the TES system. Hence, a comparison of system-level gravimetric and volumetric storage density and discharging time of the tubular reactors is presented in Table 3.7. The discharging time increases with the increase in the size of the reactor. As the size of the reactor increases, the volume to surface area ratio increases, due to which the generated heat inside the MH bed dissipates at a slower rate. The targeted charging/ discharging time for a TES system as per the DOE SunShot program is 6 h (360 min) (Sheppard and Buckley, 2019). For the given operating conditions, the discharging time of all the tubular reactors is observed within 360 min except for the 2.5-inch reactor. The discharging time of the 2.5-inch reactor is 395.93 min. As per the DOE target of the discharging time, smaller diameter tubes such as 3/8-inch are unnecessary, increasing the system's complexity despite having faster-discharging rates.

The gravimetric and volumetric energy storage density of the tubular reactors are also presented in Table 3.7. The energy storage density increases with the size of the reactor. The gravimetric energy storage density increases substantially from 296.8 to 688 kJ/ kg of the system (2.32 times increment) when the reactor size is increased from 3/8-inch to 2-inch. This is because the heat transfer area per kg of the alloy is decreased with the reactor size, which in turn reduces the weight of the reactor. On the other hand, volumetric storage density is not significantly affected by the reactor size. It is also observed that there is a slight decrease in the gravimetric storage density for the 2.5-inch reactor due to an increase in the tube thickness to 2.11 mm compared to 1.65 mm for the 2-inch reactor. However, the 2-inch reactor is not satisfying the

working pressure condition of 60 bar. The 2.5-inch reactor achieved a system gravimetric and volumetric storage densities of 674 kJ/kg of the system and 1486 MJ/m^3 of the system, respectively, much higher than the sensible (maximum of 108 kJ/kg of material and 180 MJ/m^3 material) and latent heat (maximum of 360 kJ/kg of material and 360 MJ/m^3 of material) storage systems (Pardo et al., 2014a).

Table 3.7. Energy storage density and discharging time of the tubular reactors

Nominal diameter (inch)	Mass of system (kg)	Heat transfer area per kg of alloy (m^2/kg of alloy)	SGSD (kJ/kg of the system)	SVSD (MJ/m^3 of the system)	Number of reactors	Discharging time (min)
3/8	0.885	0.2245	296.84	1093	24.8	56.13
3/4	1.7265	0.1232	435.88	1286.5	8.7	83.60
1	2.4582	0.09286	508.42	1360.2	5.2	110.20
1½	4.47	0.06	623.67	1452.64	2.3	192.63
2	6.512	0.0466	688.56	1494.3	1.5	284.80
2½	9.68	0.0387	674.03	1485.74	1.0	395.93

Another critical parameter to consider while designing a TES system is system-level specific discharge power. The system-level specific discharge power for tubular reactors is shown in Fig. 3.9a. The peak and average specific discharge power decrease with an increase in the size of the tubular reactor. The average specific discharge power of the 3/8-inch reactor is 88.22 W/kg of the system, whereas the same for the 2.5-inch reactor is 28.37 W/kg of the system. Despite having less energy storage density (Table 3.7), the smaller diameter tubes offer higher average specific discharge power. Further, peak and average discharge power are also shown in Fig. 3.9b. The peak and average discharge power increases with an increase in the size of the reactor due to increasing heat transfer area with the size of the reactor.

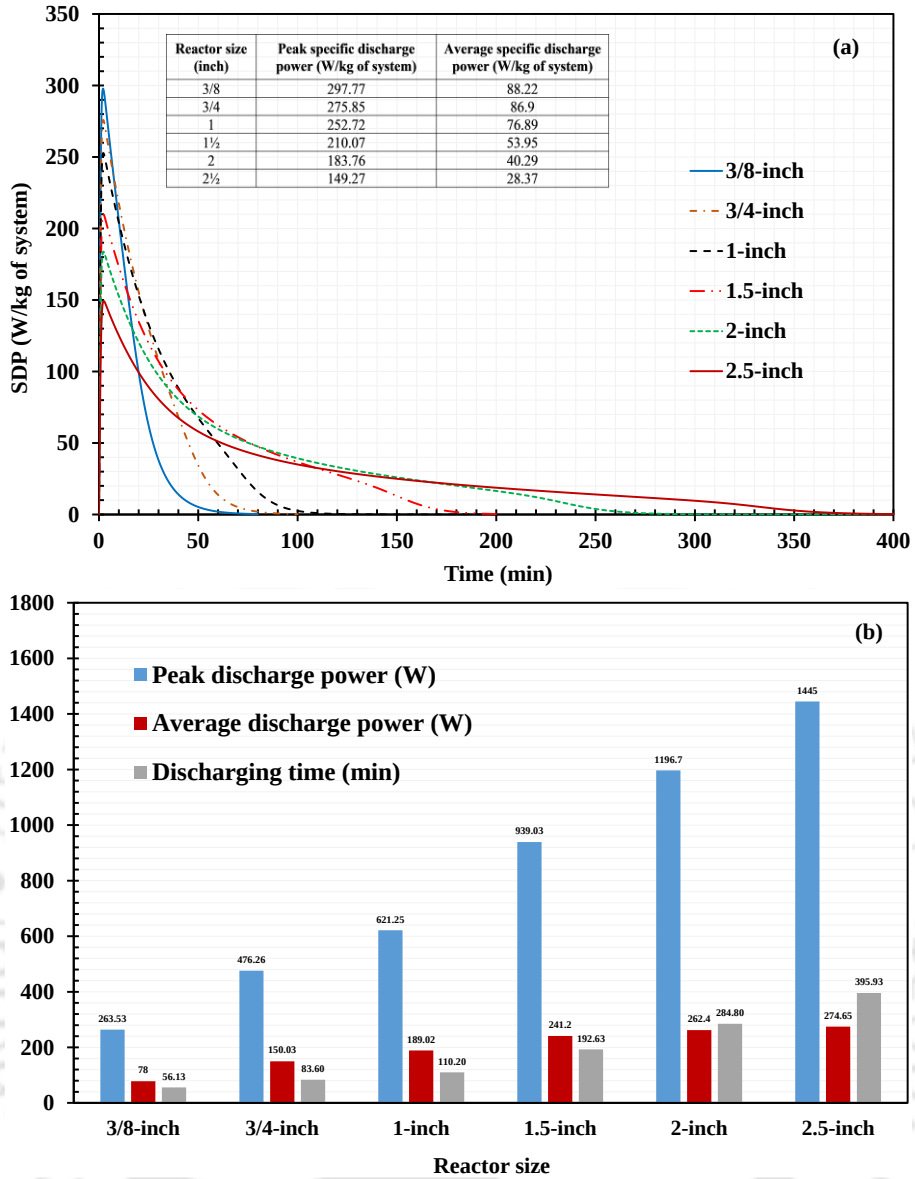

Reactor size (inch)	Peak specific discharge power (W/kg of system)	Average specific discharge power (W/kg of system)
3/8	297.77	88.22
3/4	275.85	86.9
1	252.72	76.89
1½	210.07	53.95
2	183.76	40.29
2½	149.27	28.37

Fig. 3.9. (a) System level specific discharge power (b) peak and average discharge power and discharging time for various tubular reactors

The major drawbacks of a smaller diameter tubular reactor are less energy storage density and the requirement of a greater number of tubes for the given energy storage capacity. For the storage capacity equivalent to a 2.5-inch reactor, approximately 25 number of 3/8-inch tubular reactors are needed. An increase in the number of tubes for the given storage capacity increases the complexity during the fabrication as well as the alloy filling phase of the reactor. However, smaller tubular reactors offer higher specific discharge power, higher discharging rates and lower discharging times than the larger diameter tubular reactors. Hence, there is a need to develop a larger diameter tubular reactor with greater discharge power without affecting its energy storage density, which will help reduce the number of tubular reactors for the given energy storage capacity. In this perspective, an annular tubular reactor is proposed to achieve

higher discharging rates without affecting the gravimetric and volumetric energy storage densities.

For the heat transfer coefficient of 250 W/m^2-K, the Reynolds number and the required mass flow rate of the HTF are calculated using the correlation defined in Eq. 3.17 and shown in Table 3.8. The pressure drop in the HTF flow along the tubular reactor is obtained from the flow simulation of the outer cooling jacket (the details of the flow simulation are not in the scope of the present work). To achieve the same heat transfer coefficient, the mass flow rate of HTF for the 2.5-inch reactor is 3.75 times higher than the 3/8-inch reactor. However, there is no significant increase in the pressure drop when the reactor size is increased up to 2.5 inches.

Table 3.8. Mass flow rate and pressure drop for tubular reactors under h = 250 W/m^2-K

Nominal diameter (inch)	d_o	D_i	Re	Velocity (m/s)	Mass flow rate (kg/s)	ΔP (Pa)
3/8	17.15	25.15	3259.2	0.1363	0.0314	42.743
3/4	26.67	34.67	3300.4	0.1380	0.0461	43.337
1	33.4	41.4	3316.9	0.1387	0.0565	43.618
1½	48.26	56.26	3338.4	0.1396	0.0795	44.102
2	60.33	68.33	3348.6	0.14	0.0981	44.277
2½	73.03	81.03	3355.9	0.1403	0.1178	44.426

3.8.2 Annular MH reactor

From the analysis of tubular reactors, it is found that the 2.5-inch reactor showed higher energy storage densities with a working pressure of 60 bar (as shown in Table 3.7). However, the 2.5-inch reactor exhibited significantly less average specific discharge power (28.37 W/kg of the system) and a longer discharging time (~396 min). Hence, an attempt has been made to improve the average specific discharge power and reduce the discharge time of the 2.5-inch reactor with the help of the annular MH reactor design. The mass flow rate of HTF of 0.1178 kg/s (Table 3.8) is used for the calculation of the heat transfer coefficient on the inner cooling tube (i.e., h_1). The heat transfer coefficient of 250 W/m^2-K is kept the same on the outer surface (i.e., h_2). The heat transfer coefficient on the inner cooling surface is obtained as 1368, 850, and 533, respectively, for Case 1, Case 2, and Case 3.

The system-level gravimetric energy storage density and discharging time of the annular MH reactors are presented in Table 3.9. There is a significant decrease in the discharging time of

the annular MH reactor compared to the 2.5-inch tubular reactor. The discharging time of the 2.5-inch tubular reactor is observed as ~396 min (Table 3.7). In contrast, the discharging time of annular MH reactors is 153, 136, and 119 min, respectively, with Case 1, Case 2, and Case 3. The discharging time of the 2.5-inch tubular reactor is reduced by 61, 65, and 70%, respectively, with Case 1, Case 2, and Case 3 annular MH reactors. Further, the gravimetric energy storage density of the 2.5-inch tubular reactor is observed as 674 kJ/kg of the system (Table 3.7). The same for Case 1, Case 2, and Case 3 are 613, 593, and 563 kJ/kg of the system. The gravimetric energy storage density is only reduced by 9, 12, and 16%, respectively, with Case 1, Case 2, and Case 3 than the 2.5-inch tubular reactor. Hence, the annular MH reactors significantly decreased the discharging time with little compromise in gravimetric energy storage density.

Among the annular MH reactors, the discharging time decreases from Case 1 to Case 3 due to an increase in heat transfer area per kg of alloy and a decrease in the MH bed's thickness. There is a decrease of 11% in discharging time with Case 2 than in Case 1. The same for Case 3 is 15% compared to Case 2.

Table 3.9. Energy storage density and discharging time of the annular MH reactors

Case No.	Mass of system (kg)	Heat transfer area per kg of alloy (m^2/kg of alloy)	SGSD (kJ/kg of system)	SVSD (MJ/m^3 of the system)	Discharging time (min)	% reduction in discharging time compared to a 2.5-inch tubular reactor	% reduction in storage density compared to a 2.5-inch tubular reactor
1	9.98	0.02735	613	1463	153	61	9
2	9.95	0.02875	593	1410	136	65	12
3	9.84	0.03078	563	1325	119	70	16

The system-level specific discharge power for all the cases of the annular MH reactors is shown in Fig. 3.10a. There is no significant deviation in the variation of the specific discharge power among annular MH reactors. The peak and average specific discharge power of the 2.5-inch tubular reactor (Fig. 3.9a) are boosted from 149.27 W/kg of the system and 28.37 W/kg of the system to a maximum of 221 W/kg of the system and 79 W/kg of system with the help of the annular MH reactor (Case 3). It is observed that the average specific discharge power of the 2.5-inch tubular reactor is increased by ~2.5 times with the annular MH reactor. Further, the peak and average discharge power of the annular MH reactor are also boosted to 2180 W and 780 W, respectively (Fig. 3.10b).

Table 3.7 and 3.9 show that the annular MH reactor (~118 – 153 min) produced discharging times approximately equivalent to the 1-inch tubular reactor (~110 min). However, the gravimetric storage density of the annular MH reactor is higher than the 1-inch reactor. For the given alloy mass (i.e., storage capacity), one annular MH reactor is equivalent to five 1-inch reactors with identical thermal performance. Hence, the number of reactors is reduced from five to one for equivalent discharging time and storage capacity with the proposed annular MH reactor design. The pressure drop in the HTF flow along the annular MH reactor is obtained from the flow simulation. From the simulation results, the pressure drop for Case 1, Case 2, and Case 3 is obtained as 589 Pa, 192 Pa, and 78 Pa, respectively. The pressure drop for Case 3 is lower due to the larger inner diameter of the cooling tube than Case 1 and Case 2. Further, the pressure drop in the HTF line is increased by 33 Pa for case 3 compared to the 2.5-inch tubular reactor under the same mass flow rate condition. However, the operating time for the 2.5-inch tubular reactor is 3.3 times higher than the annular reactor of Case 3.

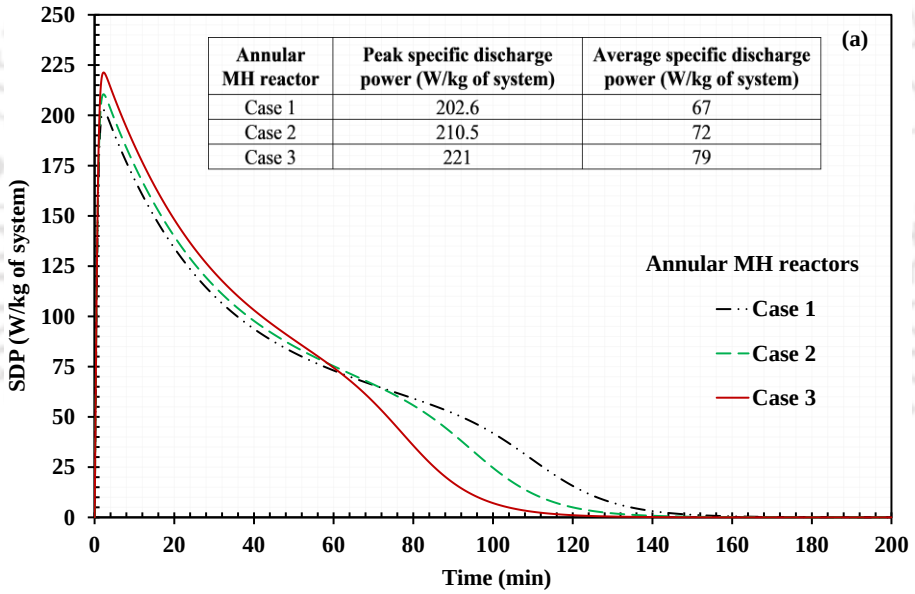

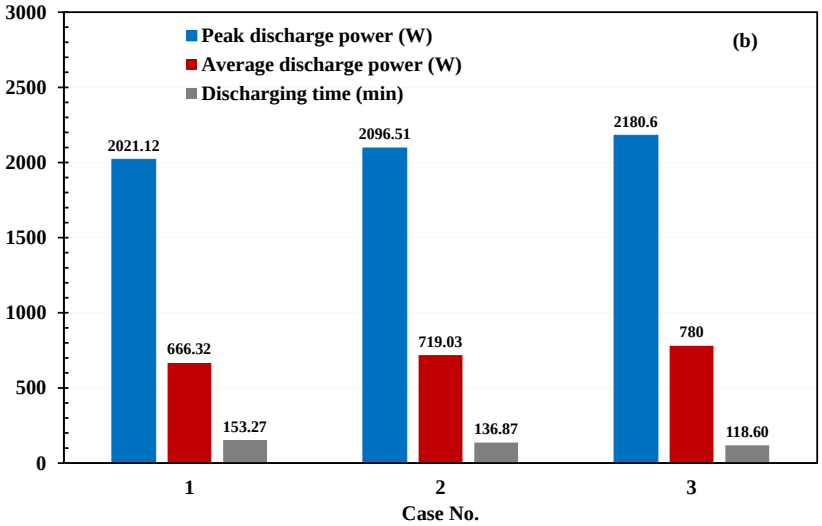

Fig. 3.10. (a) System level specific discharge power and (b) peak and average discharge power and discharging time for various annular MH reactors

3.8.3 MH reactor array for large-scale TES application

For large-scale TES applications, the MH reactors are arranged in an array (as shown in Fig. 3.11) as per the designed/ required storage capacity. The reactors present near the outlet section of the array experience slower reaction kinetics due to an increase in the temperature of HTF along the length of the array. Hence it is appropriate to consider the charging/ discharging time of the reactors present near the outlet section of the MH reactor array for deciding the overall charging / discharging time of the MH-based TES system. For the supply pressure of 5 bar, the MH bed can reach a maximum temperature of 311°C. Hence, the outlet HTF temperature of the MH reactor array cannot exceed 311°C under any circumstances for the supply pressure of 5 bar. Therefore, it is very much necessary to evaluate the discharging/ charging time of the annular MH reactor by applying the boundary conditions experienced by the reactors near the outlet section of the MH reactor array. Considering a temperature difference of 10°C for heat transfer, the HTF temperature for convective heat transfer is selected as 300°C. The annular MH reactor of Case 2 is modeled with 300°C as HTF temperature while all other boundary conditions are kept the same.

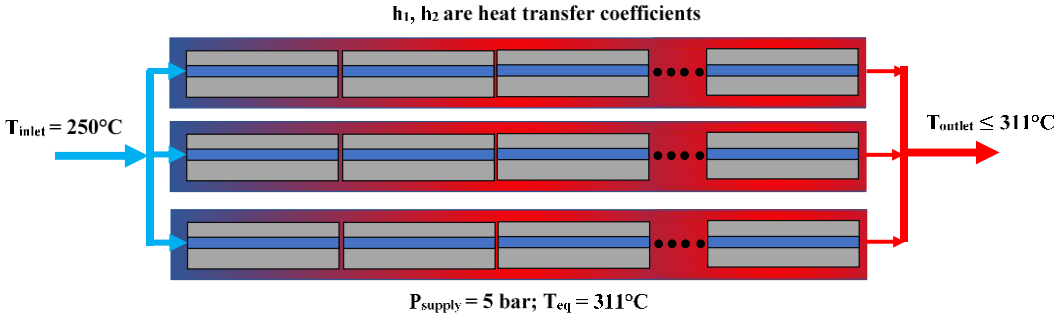

Fig. 3.11. Schematic of an array of MH reactors for real-time TES application

The average MH bed temperature and reacted fraction of the annular reactor (Case 2) are shown in Fig. 3.12a for the HTF temperature of 300°C. The initial temperature of the reactor is also kept at 300°C. The discharging time of the MH bed for 300°C inlet temperature is 641.5 min. The discharging time for HTF temperature of 250°C is 4.7 times lower than the 300°C. The driving potential (i.e., pressure differential and density difference) and convective heat transfer rate of the annular MH reactor (Case 2) for the HTF temperature of 250°C and 300°C are shown in Fig. 3.12(b and c). From Fig. 3.12b, it is observed that the driving potential is higher for the HTF temperature of 250°C than 300°C, due to which the slower rate of discharging is observed for 300°C. Further, c demonstrates that the amount of energy exchanged during discharging is approximately the same for both 250 and 300°C but with different discharging rates. The peak and average convective heat transfer rates are higher for 250°C than 300°C. This demonstrates that the discharging time of the reactors present near the outlet section of the MH array does not fall within the DOE target's limit.

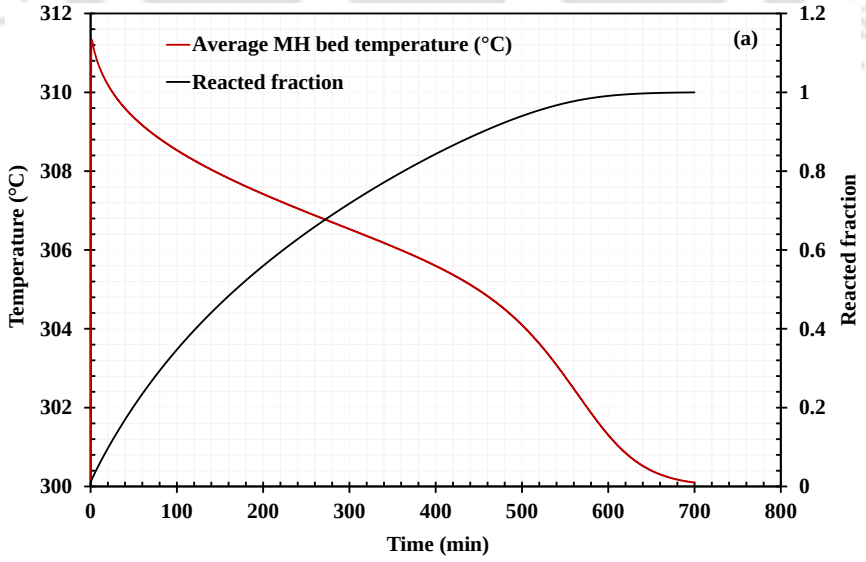

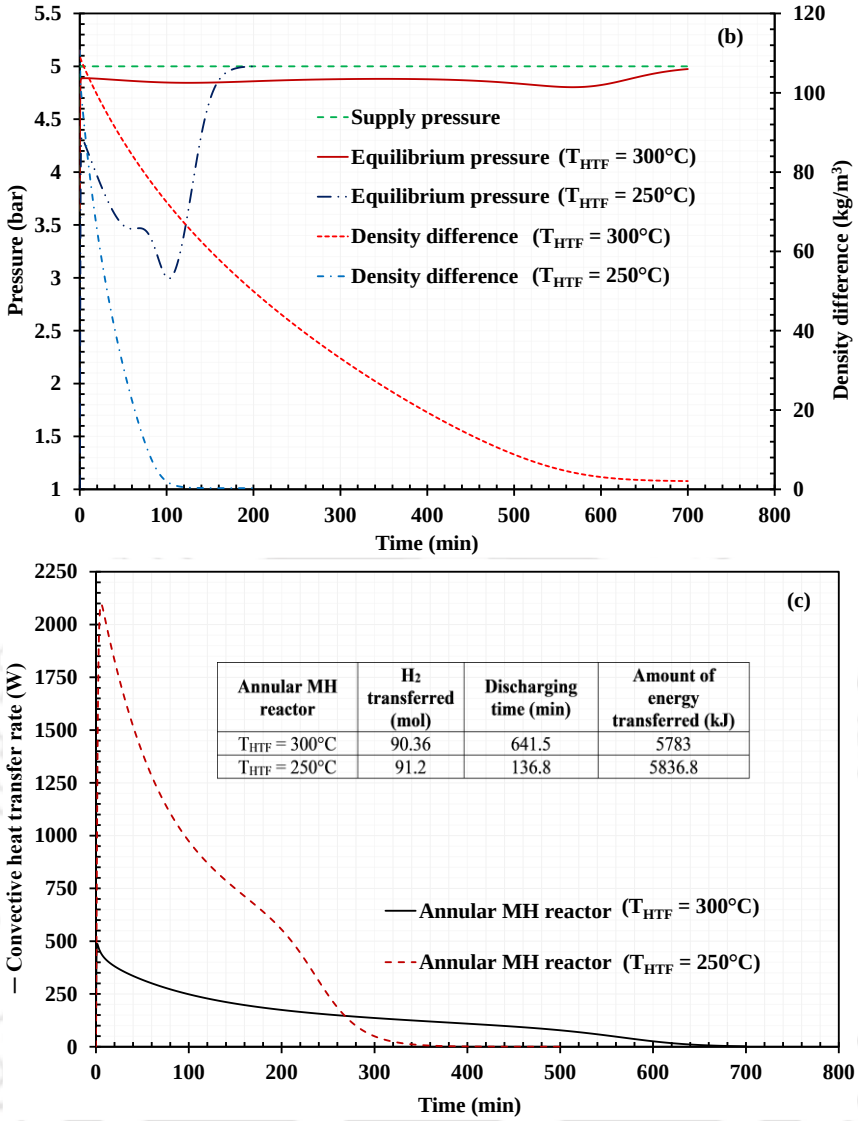

Annular MH reactor	H_2 transferred (mol)	Discharging time (min)	Amount of energy transferred (kJ)
T_{HTF} = 300°C	90.36	641.5	5783
T_{HTF} = 250°C	91.2	136.8	5836.8

Fig. 3.12. (a). Average MH bed temperature and reacted fraction, (b). driving potential and (c) convective heat transfer rate for annular MH reactor subjected to HTF temperatures of 300°C and 250°C

Hence, there is a need to improve further the heat transfer characteristics of the annular MH reactor. The possible options for reducing the discharging time are internal heat transfer enhancement and varying operating parameters (such as supply pressure, inlet temperature, heat transfer coefficient, etc.). Therefore, the present work is focused on studying the internal heat transfer enhancement of the MH bed with radial fins, which is discussed in the next section of this chapter.

3.8.4 Annular MH reactor with radial fins

Radial fins are added to the annular MH reactor (Case 2) to enhance the heat transfer rate to/ from the MH reactor from/ to the HTF. The literature suggested an optimum value of MH bed

thickness of ~10.4 mm (Gkanas et al., 2018b). Hence, the pitch of the radial fins is selected as 10.4 mm. Aluminum is selected as a fin material due to its lightweight and good thermal conductivity. A total of 95 fins (thickness 0.5 mm, pitch 10.4 mm) are placed inside the reactor. The schematic and computational domain, along with boundary conditions of the annular MH reactor with radial fins, are shown in Fig. 3.13. With the addition of fins, the fillable mass of alloy is reduced from 5.38 kg to 5.14 kg, which is a 4.3% drop. The main objective of studying the annular MH reactor with radial fins is to achieve the discharging time of the reactors near the outlet section of the MH array within the DOE target. Therefore, the annular MH reactor with radial fins is modeled with 300°C as fluid temperature while all other boundary conditions are kept the same as in section 3.8.3.

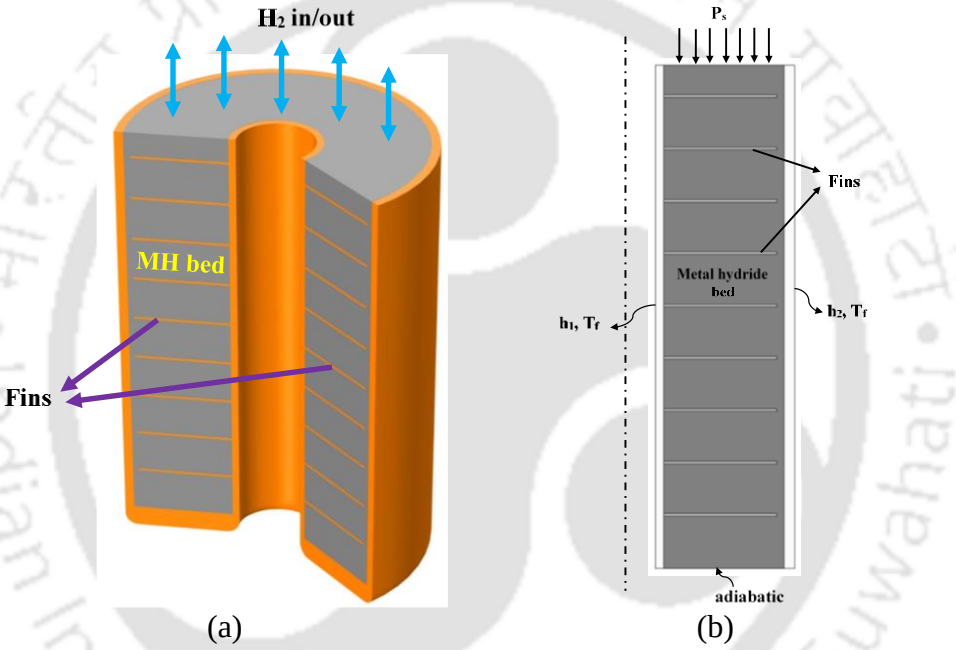

Fig. 3.13. Annular MH reactor with radial fins (a) schematic and (b) computational domain with boundary conditions (not to scale)

The average MH bed temperature and reacted fraction are compared for the annular reactor with and without radial fins are shown in Fig. 3.14a. The radial fins greatly enhanced the heat transfer rate, reducing the discharging time from 641.5 min to 333 min. The discharging time of the annular MH reactor is reduced by 1.93 times with the addition of radial fins. The driving potential is also enhanced (as shown in Fig. 3.14b) due to better heat transfer characteristics offered by the radial fins. With the addition of radial fins, the energy storage capacity is reduced from 5783 kJ to 5531 kJ (Fig. 3.14c).

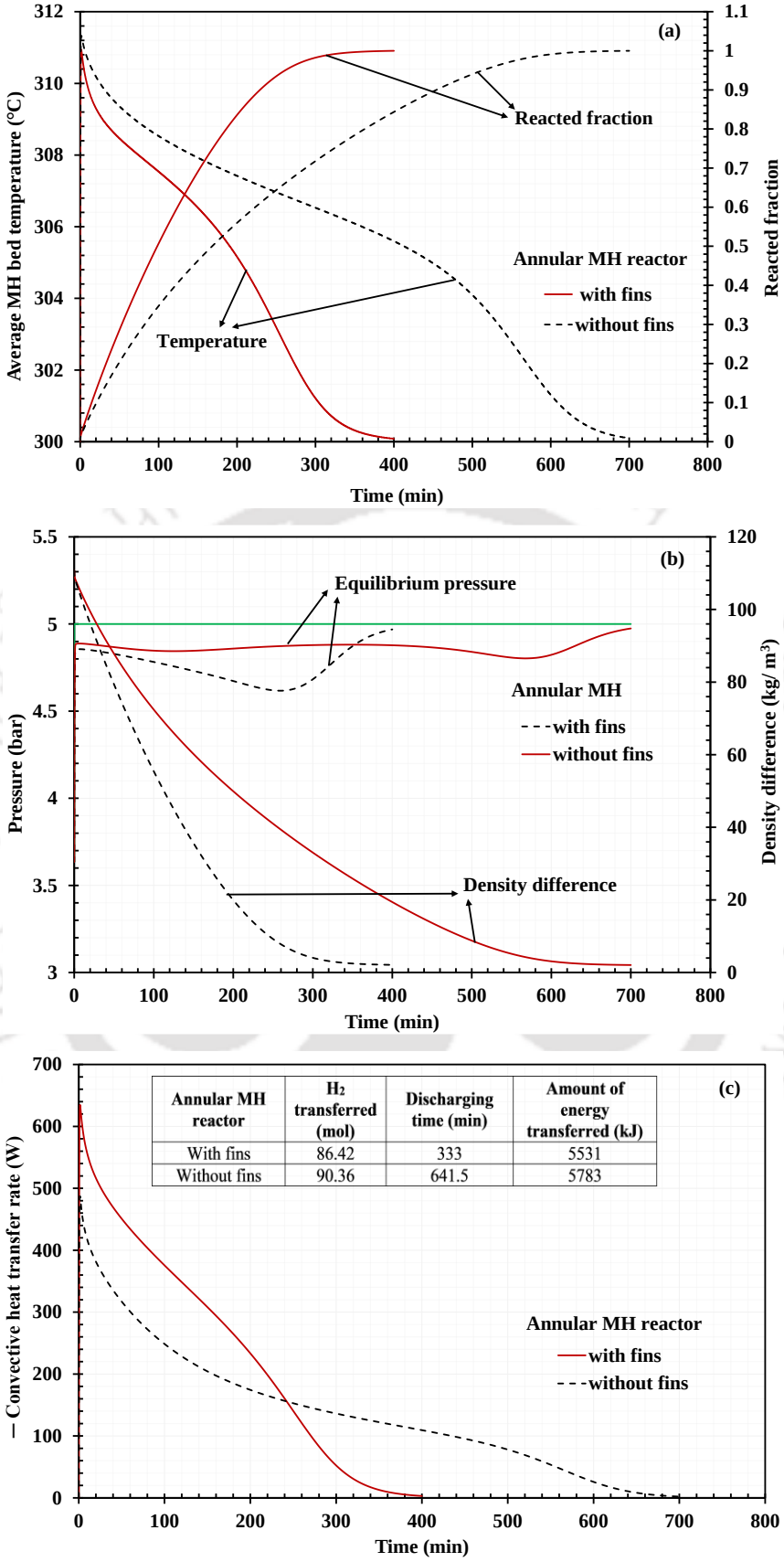

Annular MH reactor	H_2 transferred (mol)	Discharging time (min)	Amount of energy transferred (kJ)
With fins	86.42	333	5531
Without fins	90.36	641.5	5783

Fig. 3.14. Comparison between annular MH reactor with and without fins (a) average MH bed temperature and reacted fraction, (b) driving potential and (c) convective heat transfer rate

Therefore, the addition of radial fins kept the discharging time within the DOE's target of 360 min, even for the annular MH reactor near the outlet section of the MH array. Hence, the design of an annular MH reactor with radial fins is best-suitable for achieving favorable discharging times. A comparison of energy storage density, discharging time, and average discharge power of all the reactors studied so far is shown in Fig. 3.15 for an HTF temperature of 250°C. The gravimetric energy storage density of the annular MH reactor with radial fins is decreased by 17% compared to the 2.5-inch tubular reactor. However, the annular MH reactor with radial fins positively affected the discharging time and average discharge power. With the annular MH reactor with radial fins, the average discharging power is increased by four times, whereas the discharging time is decreased by 4.7 times than the 2.5-inch tubular reactor.

Further, the discharging time of the annular MH reactor with radial fins is equivalent to a 3/8-inch reactor, i.e., 84 min. For the given alloy mass (i.e., storage capacity), one annular MH reactor with radial fins is equivalent to seven 3/8-inch reactors with identical thermal performance. Hence, the number of reactors is reduced from seven to one for equivalent discharging time and storage capacity with the proposed annular MH reactor with radial fins. Finally, the system level gravimetric storage density of the annular MH reactor with radial fins is 560 kJ/kg of system, which is much higher than the material level energy storage density of sensible (maximum of 108 kJ/kg of material) and latent heat (maximum of 360 kJ/kg of material) storage systems. Hence, the design of an annular MH reactor with radial fins is recommended for further analysis.

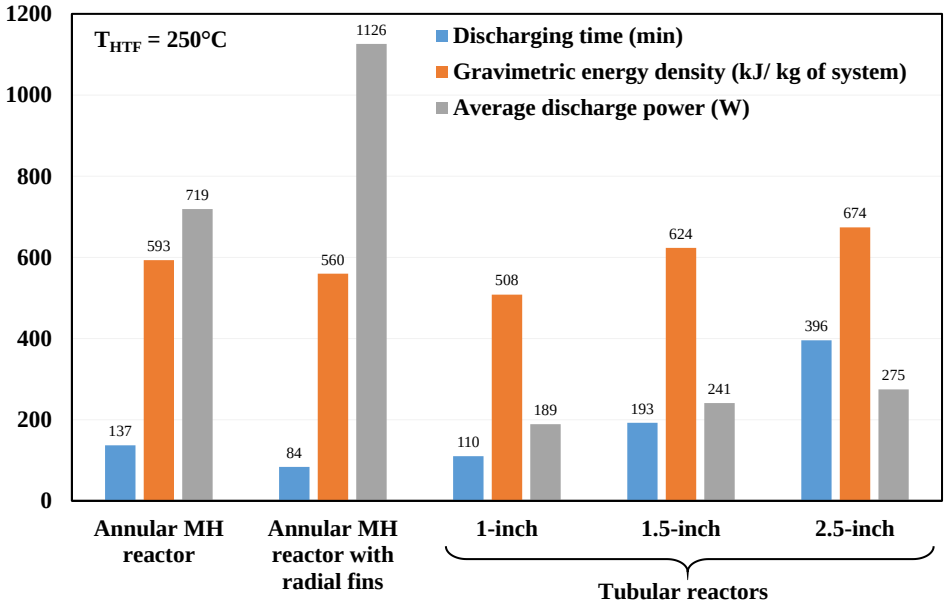

Fig. 3.15. Comparison of energy storage density, discharging time, and average discharge power for tubular and annular reactors

The system-level energy storage densities are evaluated for a single MH reactor in the present work. However, the two-reactor configuration is the most widely accepted metal hydride-based TES system (Mellouli et al., 2018; Nyamsi et al., 2020). The two-reactor configuration consists of an energy and hydrogen storage reactor. For the two-reactor configuration, the volume of the hydrogen storage reactor has to be considered, which reduces the reported system-level volumetric energy storage density. However, the gravimetric energy storage density and specific discharge power will not change even for the two-reactor configuration.

3.9 Summary

A numerical model is developed to investigate the heat and mass transfer characteristics of the MH reactors. Tubular reactors are simple MH reactors studied in the literature for the MH-based TES system. Firstly, the discharging behavior of the tubular reactors filled with magnesium-nickel hydride is analyzed in this chapter. Therminol VP1 is considered as the heat transfer fluid in the study. From the analysis, the advantages and drawbacks of the tubular reactor are highlighted. An annular MH reactor is proposed to overcome the disadvantages of tubular reactors.

Further, the performance of the annular MH reactor is studied and compared with the tubular reactor. The results are presented in terms of discharging time, energy storage density, and specific discharge power. Also, DOE's target of charging and discharging time (i.e., 360 min) is considered while designing the MH reactor for the TES application. The following points give a summary of the results of the numerical study.

- The discharging time increased with the diameter of the tubular reactor. The smaller tubular reactors provided a lesser volume-to-surface area ratio, due to which higher discharging rates were achieved. However, the energy storage density increased with the diameter of the tubular reactor.
- The discharging time of the 2.5-inch reactor is 396 min, which exceeded the DOE target. Whereas the discharging time of the tubular reactors below 2.5-inch size is less than 360 min.
- The major drawbacks of a smaller diameter tubular reactor are less energy storage density and the requirement of a greater number of tubes for the given energy storage capacity. For the storage capacity equivalent to a 2.5-inch reactor, approximately 25 3/8-inch tubular reactors are needed.

- With an annular MH reactor, the discharging time of a 2.5-inch tubular reactor is reduced by up to 70%, with only a 16% compromise in gravimetric energy storage density. Also, the average specific discharge power of the 2.5-inch tubular reactor is increased by ~2.5 times of the annular MH reactor.
- For real-time TES storage applications, the discharging time of the reactors present near the MH array outlet section is much higher than the DOE target's limit. The discharging time for HTF temperature of 250°C (boundary condition for MH reactors present near the inlet section of the array) is 4.7 times lower than the 300°C (boundary condition for MH reactors present near the outlet section of the array).
- Radial fins are incorporated in the annular MH reactor to improve the heat transfer characteristics of the reactors present near the outlet section of the MH array. The addition of radial fins reduced the discharging time to 333 min, i.e., 1.93 times lower than the case without fins.
- For the given storage capacity, the annular MH reactor achieved thermal performance equivalent to a 1-inch reactor, and the number of reactors was reduced from five to one. Whereas the annular MH reactor with radial fins achieved thermal performance equivalent to a 3/8-inch reactor, the number of reactors was reduced from seven to one.
- Finally, the system level gravimetric storage density of the annular MH reactor with radial fins is 560 kJ/kg of system, which is much higher than the material level energy storage density of the sensible (maximum of 108 kJ/kg of material) and latent heat (maximum of 360 kJ/kg of material) storage systems.

Chapter 4

Numerical studies: LTMH reactor

4.1 Preface

The LTMH reactor for hydrogen storage application is numerically studied in this chapter. The 2D mathematical model developed in Chapter 3 is used to analyze the absorption and desorption behavior of the LTMH reactor. The MH material is selected to be $LaNi_5$ as it is extensively studied in the literature and, thus, enables an easier comparison of the present results. The three annular porous MH reactor configurations are studied in this chapter. The absorption and desorption characteristics of the three configurations are compared in terms of reaction time and outlet temperature of the HTF. Further, a sensitivity analysis of the annular MH reactor equipped with radial fins is performed to study the effect of operating parameters on absorption and desorption characteristics. Furthermore, the numerical results of the annular MH reactor are compared with different reactor designs in the literature.

4.2. Physical system and numerical modeling

In this chapter, the three reactor configurations based on the annular MH reactor design (discussed in Chapter 3) are developed and analyzed for hydrogen storage application. The mass of hydrogen absorbed in both reactors should be the same for a coupled reactor system. The ratio of the mass of hydrogen absorbed by Mg_2Ni to $LaNi_5$ is ~1.1. Hence, the dimensions of the annular reactor developed in Chapter 3 are used for hydrogen storage. The dimensions of the three configurations studied are shown in Fig. 4.1. In this chapter, the continuity, momentum, and energy equations are solved for the velocity, pressure, and temperature distribution inside the HTF domain instead of considering the heat transfer coefficient on the heat exchanger's outer walls (discussed in Chapter 3). $LaNi_5$ and water are selected as MH alloy and HTF for the analysis. The thermophysical properties of the $LaNi_5$ and water are shown in Table 4.1 and 4.2, respectively.

4.2.1 Configuration 1

Configuration 1 is simple annular geometry with cooling/ heating provided on inner and outer surfaces. It consists of two inlets and one outlet for the HTF. The HTF enters at inlet

temperature through the inlet ports provided in the inner cooling tube and outer cooling jacket and exits from the common outlet, as shown in Fig. 4.1(a). The total mass flow rate of the HTF is distributed as per the cross-sectional area of the inner cooling tube and outer cooling jacket.

4.2.2 Configuration 2

A double-pass heat exchanger concept is introduced to achieve a higher peak in the HTF outlet temperature for the given mass flow rate, as shown in Fig. 4.1(b). The reactor consists of one inlet and one outlet for the HTF. The HTF enters through the inlet of the inner cooling tube and exits from the outlet of the outer cooling jacket. This design is simple and reduces the number of HTF ports. However, there is a slight increase in the pressure drop in HTF flow due to the double pass. The purpose of studying configuration 2 is to evaluate the improvement in reaction times and the rise in the outlet temperature of HTF compared to configuration 1.

4.2.3 Configuration 3

Configuration 3 is similar to configuration 2 with additional radial fins inside the MH reactor. Since internal heat transfer is a limiting factor for the MH reactor of 2.5-inch size nominal diameter, radial fins are added to enhance the heat transfer rate to/ from the MH reactor from/ to the HTF. The optimum value of MH bed thickness was found to be ~10.4 mm (Gkanas et al., 2018b). Hence, the pitch of the radial fins is selected as 10.4 mm. Aluminum is selected as a fin material due to its lightweight and good thermal conductivity. A total of 95 fins (thickness 0.5 mm, pitch 10.4 mm) are placed inside the reactor. The schematic of configuration 3 is shown in Fig. 4.1(c). The radial fins occupied 4.6% of the reactor's total volume. The key objective of considering configuration 3 is to analyze the heat transfer rate enhancement achieved in the MH due to the addition of radial fins.

The hydrogen gas enters the MH reactor through the supply line (which is not axisymmetric). It is then collected in the small gap between the axial disc filter and the reactor closing flange before entering into the reactor. The pressure drop is negligible when the hydrogen gas enters from the supply line to the gap between the axial disc filter and the reactor closing flange. Hence the gas exerts uniform pressure on the entire cross-section of the axial disc filter. Therefore, the gas enters the rector through the axial disc filter with uniform pressure. Hence, the assumption of the axisymmetric model is justified.

For a $LaNi_5$ bed of 0.5 porosity, the weight ratio offered by configuration 1, configuration 2, and configuration 3 is 2.14, 2.14, and 2.01, respectively. The weight ratio of configuration 3 is

reduced to 2.01, i.e., a 6% decrease in the weight ratio due to the addition of the radial fins. Here, the outer cooling jacket is made of stainless steel material. However, the outer cooling jacket can be made with either plastic or aluminum alloy to increase the weight ratio further. The mass of metal hydride present in configuration 1, configuration 2, and configuration 3 is 14.1, 14.1, and 13.5 kg, respectively, for a porosity of 0.5. There is a slight reduction in the mass of MH present in configuration 3 due to the addition of fins. The schematic of the computational domain of the annular MH reactor is shown in Fig. 4.2.

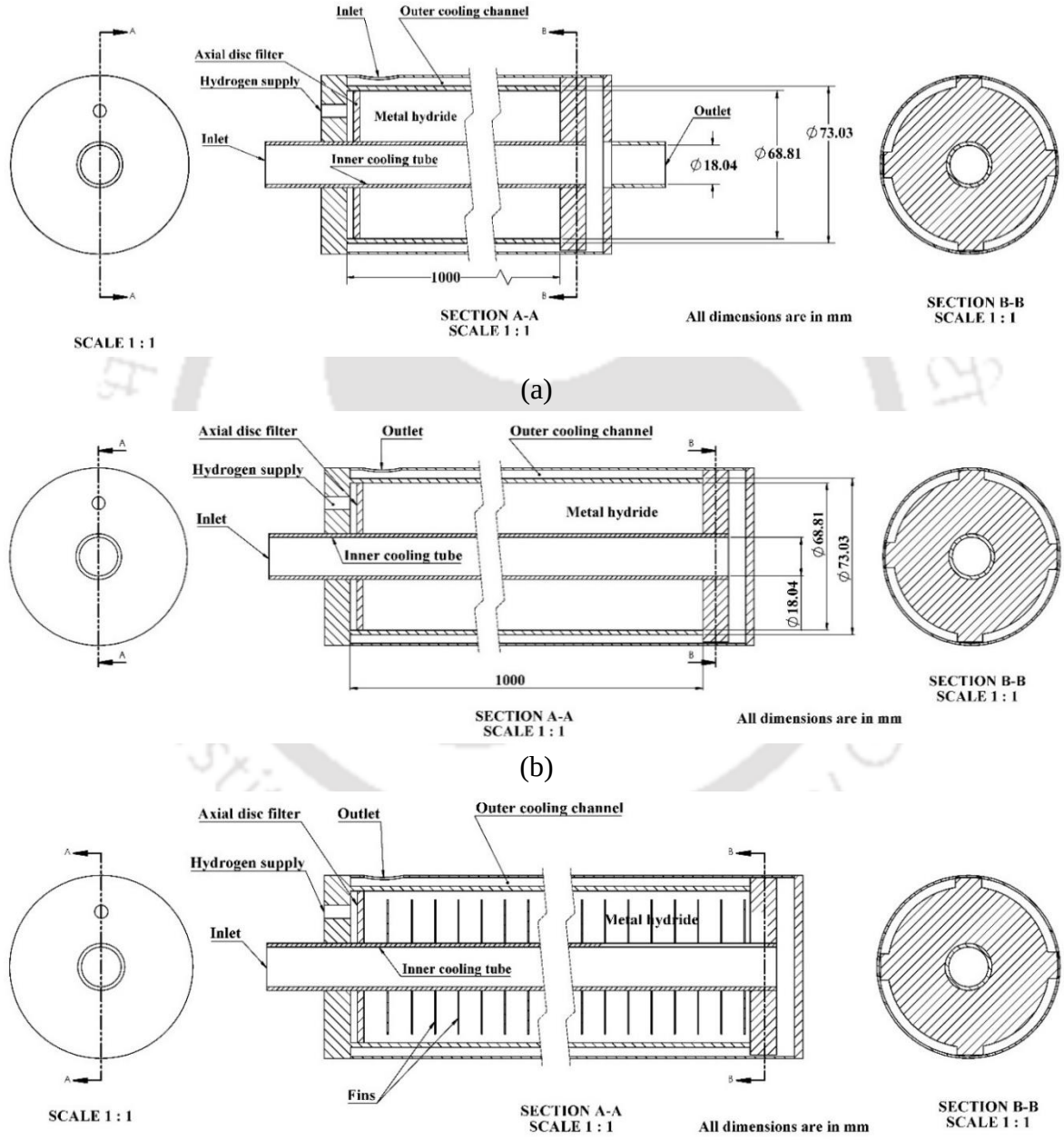

Fig. 4.1. Annular MH reactors studied (a) configuration 1 (b) configuration 2 (c) configuration 3

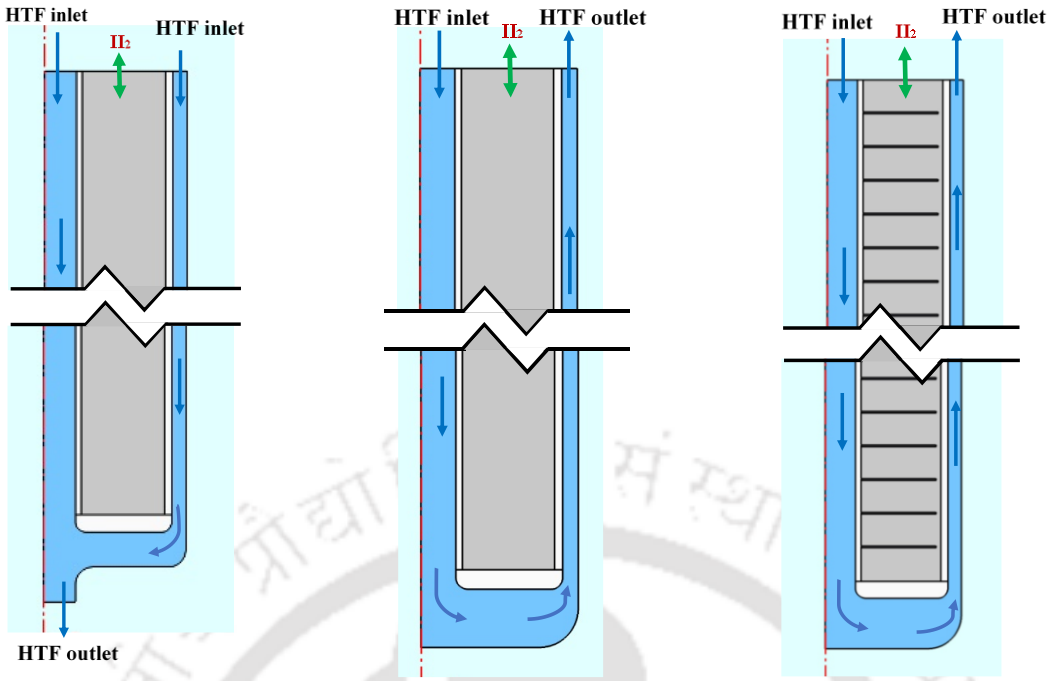

(a) (b) (c)

Fig. 4.2. Two-dimensional axisymmetric computational domain (not to scale) (a) configuration 1, (b) configuration 2 and (c) configuration 3

Table 4.1. Thermo-physical properties of $LaNi_5$ and hydrogen (Busqué et al., 2017; Jiao et al., 2012; Malleswararao et al., 2020b)

Property	**$LaNi_5$**	**Hydrogen**
Molecular weight (g/mol)	434	2.01
Specific heat (J/kg. K)	419	14283
Thermal conductivity (W/m. K)	1.32	0.127
Reaction Enthalpy, ΔH (J/mol)	-29879	-
Reaction Constant, C (1/s)	59.187 (absorption) 9.57 (desorption)	-
Activation Energy, E (J/mol)	21170 (absorption) 16445 (desorption)	-
Density (kg/m^3)	8400	-
Maximum H_2 storage capacity ($wt.\%_{max}$)	1.379	-
Porosity	0.5	-
Permeability (m^2)	10^{-8}	-
Universal gas constant (J/mol. K)	8.314	-
van't Hoff constants: A, B [K]	13.44, 3780	-
Constants:		-
Slope factors, (ϕ_s, ϕ_o)	0.038, 0	-
Hysteresis factor, (β)	0.137	-

Table 4.2. Properties of water

Property	Value
Density (kg/m^3)	$\rho = 838.466135 + 1.40050603 \times T^1 - 0.0030112376 \times T^2 + 3.71822313E-7 \times T^3$
Specific heat (J/kg-K)	$C_p = 12010.1471 - 80.4072879 \times T^1 + 0.309866854 \times T^2 - 5.38186884E-4 \times T^3 + 3.62536437E-7 \times T^4$
Thermal conductivity (W/m-K)	$k = -0.869083936 + 0.00894880345 \times T - 1.58366345E-5 \times T^2 + 7.97543259E-9 \times T^3$
Dynamic viscosity (Pa-s)	$\mu = 1.3799566804 - 0.021224019151 \times T + 1.3604562827E-4 \times T^2 - 4.6454090319E-7 \times T^3 + 8.9042735735E-10 \times T^4 - 9.0790692686E-13 \times T^5 + 3.8457331488E-16 \times T^6$

4.2.4 Initial and boundary conditions

3.8.4.1 Initial conditions:

The initial conditions used in the present work during absorption and desorption are presented in Table 4.3.

Table 4.3 Initial conditions

Metal hydride		*Heat transfer fluid*
Absorption: $T(r,z,0) = T_{o,a}$ $P(r,z,0) = P_{eqi,a}$ $\rho_s(r,z,0) = \rho_{si,a}$ $c(r,z,0) = c_{i,a}$	Desorption: $T(r,z,0) = T_{o,d}$ $P(r,z,0) = P_{eqi,d}$ $\rho_s(r,z,0) = \rho_{si,a}$ $c(r,z,0) = c_{i,d}$	$T(r,z,0) = T_{o,a/o,d}$ $P(r,z,0) = P_o$ $u_r(r,z,0) = u_z(r,z,0) = 0$

3.8.4.2 Boundary conditions:

The boundary conditions used in the model are presented in Table 4.4. The inlet pressure is ramped/ reduced from the initial equilibrium pressure to the supply/ discharge pressure using the following equation to avoid convergence issues.

$$P_{inlet}(t) = P_{eqi} + D(t)\left(P_{\text{sup}ply/discharge} - P_{eqi}\right)$$

D(t) is a step function defined at t = 0.05 s.

Table 4.4. Boundary conditions

Type	*Boundary condition*
Adiabatic condition on the outer walls	$\frac{\partial T}{\partial n} = 0$
No slip and non-permeability on the walls of the HTF tube	$u_r = u_z = 0$
Hydrogen inlet (supply pressure for absorption and discharge pressure for desorption) and No flow condition	At the inlet of the reactor, $p = P_{\text{supply/discharge}}$

	On the wall of the MH reactor, $\frac{\partial p}{\partial n}=0$ or $\vec{n}\cdot\rho\vec{V}=0$
Inlet temperature and velocity for HTF	$u_z = U_{inlet}$ $T = T_{inlet}$
Outlet and outflow condition for HTF	$p = P_o$ $\frac{\partial T}{\partial n}=0$
Heat flux continuity	On the interface between the heat exchanger tube and the MH reactor: $-k_{MH}\nabla T\big\|_{MH} = -k_{tube}\nabla T\big\|_{tube}$ On the interface between HTF and heat exchanger tube: $-k_{tube}\nabla T\big\|_{tube} = -k_f\nabla T\big\|_f$

4.3. Results and discussion

The performance comparison of three reactor configurations during the absorption and desorption of $LaNi_5$ is presented. The supply pressure is set to 15 bar during absorption since a commercial electrolyzer typically supplies hydrogen at 15 bar (Eichman et al., 2020; Gkanas et al., 2018a; NREL, 2004). Simultaneously, the inlet temperature and flow rate of the HTF are maintained at 25°C and 0.042 kg/s, respectively. During desorption, the discharge pressure of the hydrogen is set to 1 bar gauge pressure. The inlet temperature and the flow rate of the HTF are set to 50°C and 0.042 kg/s, respectively. For all the simulations, the initial concentration of hydrogen of the MH bed is considered as 0.049 and 0.939 during absorption and desorption, respectively. The results of the three configurations are compared in terms of the average temperature of the MH bed, weight percentage, outlet temperature of HTF, and amount of hydrogen transferred. A sensitivity analysis is conducted on configuration 3 to find the effect of operating conditions on the absorption and desorption times. Furthermore, the performance of the finned tube reactor (configuration 3) is compared with the literature.

4.3.1 Comparison between reactor configurations during absorption

Absorption is an exothermic reaction during which the MH bed releases heat by absorbing the hydrogen. The average bed temperature, amount of hydrogen absorbed in terms of reacted fraction, and the outlet temperature of HTF are compared for all three configurations during absorption, as shown in Fig. 4.3. The MH bed reached a reacted fraction of 0.1 in 6s for all

three configurations due to the rapid rate of absorption (Fig. 4.3a). During the initial stages of the reaction, the driving potential (difference between the supply pressure and the equilibrium pressure of the bed) for mass transfer is very high, which causes higher absorption rates. The rate of exothermic heat generation is immensely higher than the rate of heat removal by the HTF during the initial stages of the reaction. Due to this, the bed temperature increases and reaches a peak value. The peak temperatures attained by configuration 1, configuration 2, and configuration 3 are 77.15, 76.75, and 76.53°C, respectively. The increase in the bed temperature causes a decrease in the driving potential, reducing the absorption rate. On the other hand, the heat transfer rate between the MH bed and the HTF increases due to increased bed temperature. After that, the temperature of the MH bed drops and tends to reach the inlet temperature of the HTF. The average bed temperature of configuration 3 reached 25.5°C in 1621 s, whereas the same for configuration 2 is 2841 s (Fig. 4.3a). The total amount of hydrogen transferred during absorption for all the configurations is also indicated in Fig. 4.3a. There is a 4g reduction in stored hydrogen for configuration 3 because of reduced fillable alloy volume due to the presence of fins. It is observed that the time required to reach a reacted fraction of 0.95 is 2004, 1735, and 945 s, respectively, for configuration 1, configuration 2, and configuration 3. The absorption time of configuration 2 is decreased by 13.4% compared to configuration 1. This is because the mass flow rate of the HTF at any particular cross-section of the inner cooling tube and the outer cooling jacket is higher for configuration 2 than configuration 1. Configuration 3 showed a decrement of 45.5% in absorption time compared to configuration 2 due to its high heat transfer area provided by the addition of radial fins. Configuration 3 is 1.84 times faster than configuration 2 to reach 0.95 reacted fraction, while fins occupy only 4.6% of the reactor volume.

The outlet temperature of the HTF for three reactor configurations during absorption is compared in Fig. 4.3b. It is observed that the outlet temperature of the HTF is improved with configuration 2 than with configuration 1. The peak outlet temperature attained by configuration 1 and configuration 2 is 38.6 and 44.3°C, respectively. The main reason for enhancement in the HTF outlet temperature is the double pass effect of the HTF. However, it could be noticed that the total amount of energy extracted from both configurations 1 and 2 is the same. Configuration 3 also enhanced the peak in the HTF outlet temperature to 47°C. The average temperature difference between the inlet and outlet temperatures of HTF obtained during absorption (up to a reacted fraction of 0.95) are 6.47, 8.31, and 14.3, respectively, for configuration 1, configuration 2, and configuration 3. The absorption results suggest that

configuration 3 is recommended for achieving faster reaction rates and higher outlet temperatures of HTF.

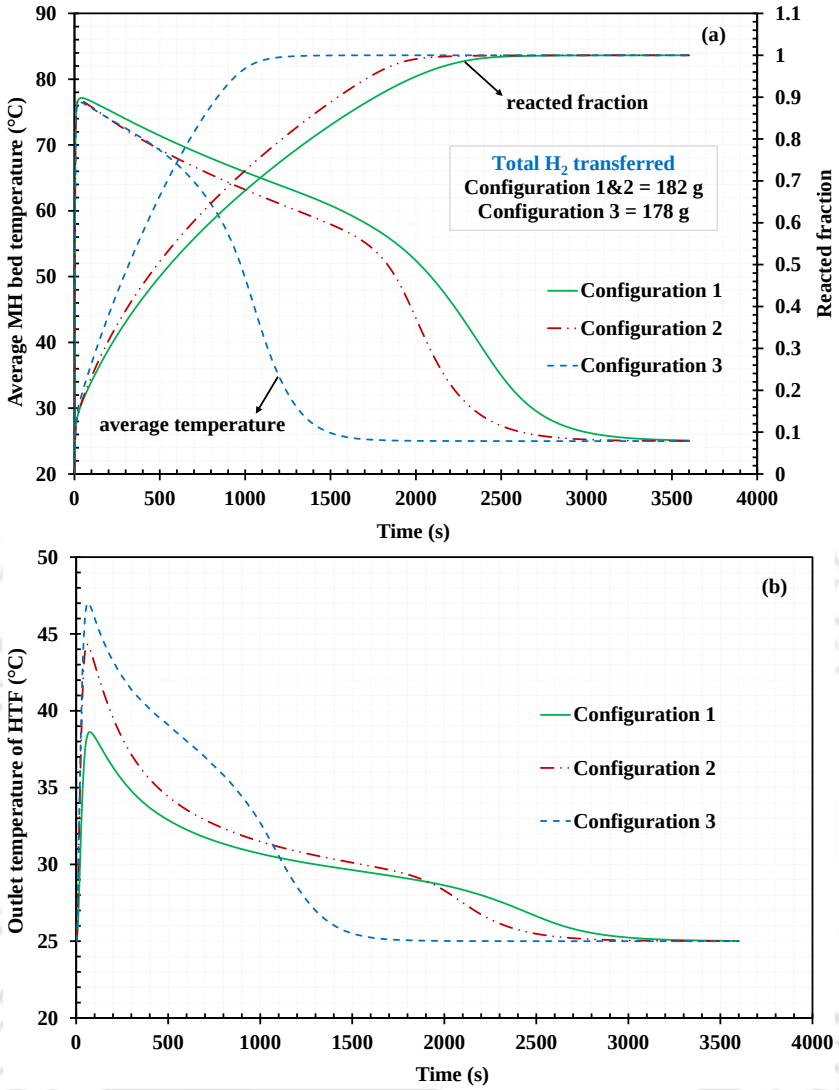

Fig. 4.3. Comparison between three reactor configurations during absorption (a) average bed temperature and weight percentage and (b) outlet temperature of HTF

4.3.2 Comparison between the reactor configurations during desorption

Desorption is an endothermic process during which the MH bed releases hydrogen by absorbing the heat from HTF. The average bed temperature, reacted fraction, and the outlet temperature of HTF are compared during desorption, as shown in Fig. 4.4. Initially, the temperature of the MH bed is at 50°C. The inlet temperature and flow rate of HTF are 50°C and 2.5 lpm, respectively. During the initial stages, there is a sudden drop in the temperature of the MH bed due to the rapid endothermic reaction. The rapidity of the endothermic reaction is due to higher driving potential. The rate of endothermic heat absorption is much higher than the heat transfer rate from the HTF to the MH bed during the early stages of the reaction. Due

to this, the bed temperature decreases and reaches the lowest value. The average temperature of the MH bed dropped to the lowest value of 10.4, 10.8, 11.5°C for the case of configuration 1, configuration 2, and configuration 3, respectively, during the early stages (within 60 s) of the desorption (Fig. 4.4a). The decrease in the bed temperature causes a reduction in the driving potential, resulting in a reduction in the desorption rate. On the other hand, the heat transfer rate between the MH bed and the HTF increases due to the decrease in the bed temperature. After that, the temperature of the MH bed rises and tends to reach the inlet temperature of the HTF. The average bed temperature of configuration 3 reached 49.5°C in 1959 s, whereas the same for configuration 2 is 3543 s (Fig. 4.4a). From Fig. 4.4a, it is observed that the time required to reach the reacted fraction of 0.05 is 2709, 2388, and 1290 s, respectively, for configurations 1, configurations 2, and configurations 3. Configuration 2 showed a 13.44% improvement in the desorption rate compared to configuration 1 to reach the reacted fraction of 0.05. The reason for the improvement is explained in section 4.3.1. On the other hand, configuration 3 showed 85.2% improvement in the desorption rate compared to configuration 2 due to its high heat transfer area provided by the addition of radial fins. Configuration 3 is 1.85 times faster than configuration 2 to reach the reacted fraction of 0.05.

The outlet temperature of the HTF for three reactor configurations during desorption is compared in Fig. 4.4b. The lowest value of the outlet temperature attained by configuration 1, configuration 2, and configuration 3 is 40.13, 36.8, and 34.2°C, respectively. Further, the average temperature difference between the inlet and outlet temperatures of HTF obtained during desorption is 3.56, 4.65, and 8°C, respectively, for configuration 1, configuration 2, and configuration 3. Similar to the absorption process, it is also observed that the enhancement in the outlet temperature of HTF is achieved during desorption with configuration 2 and configuration 3 compared to configuration 1 for the same mass flow rate of the HTF.

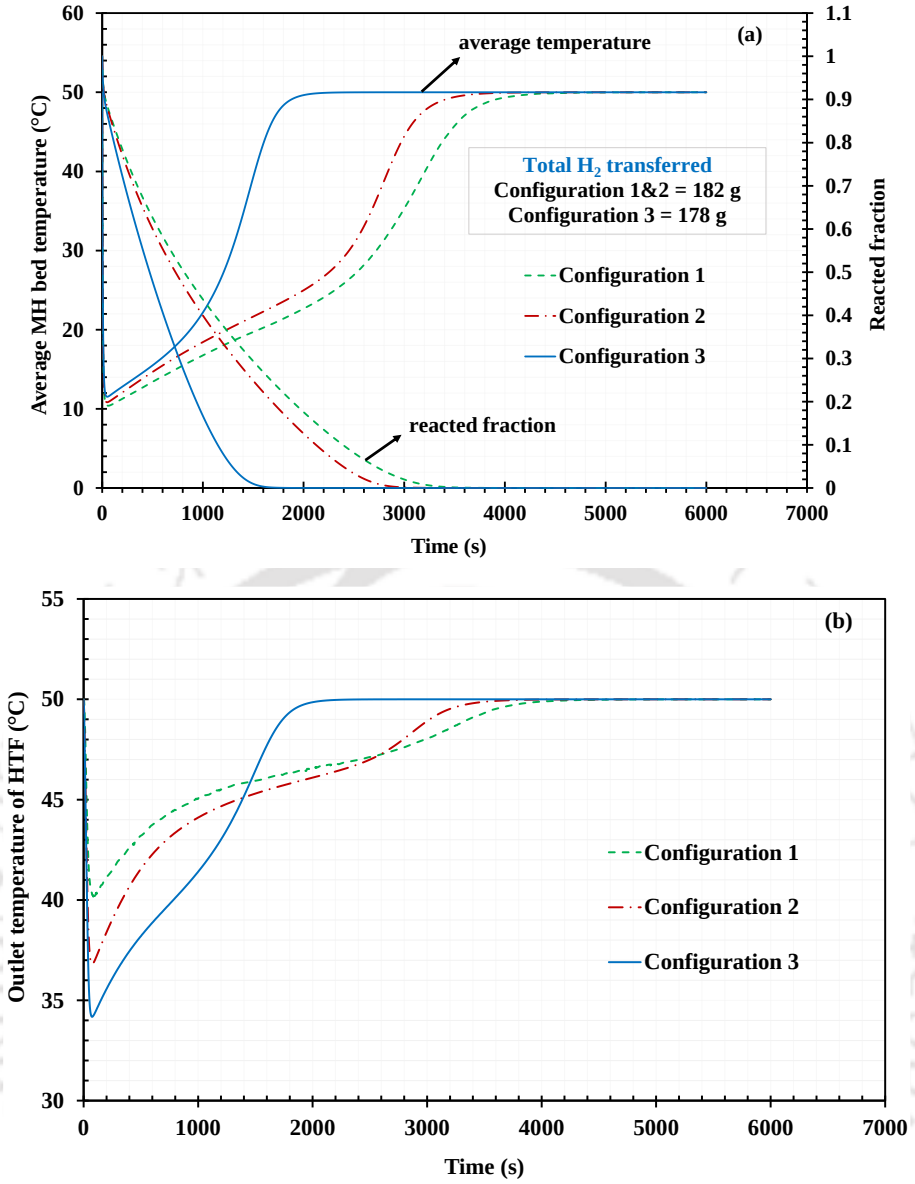

Fig. 4.4. Comparison between the reactor configurations during desorption (a) average bed temperature and weight percentage and (b) outlet temperature of HTF

From the average bed temperature profiles (Fig. 4.3a and Fig. 4.4a), it is observed that radial fins have less influence during the early stages of the absorption and desorption processes. During the later stages, the average bed temperature of configuration 3 reached the HTF inlet temperature at a faster rate due to the increased heat transfer rate than configuration 1 and configuration 2. With the change in the flow configuration, there is an enhancement in the reaction rate and outlet temperature of HTF (Fig. 4.3b and Fig. 4.4b). On the other hand, the pressure drop in the HTF flow is increased from 44.7 Pa (configuration 1) to 54 Pa (configurations 2 and 3). Configuration 2 enhanced the peak in the outlet temperature of the HTF by 5.7°C during absorption and 3.33°C during desorption, while the pressure drop was

increased by only 9.3 Pa. In this regard, the present design's pressure drop is compared with the ECT reactor studied by Kumar et al. (A. Kumar et al., 2019). The pressure drop inside an ECT (inner diameter = 4.57 mm; length = 1000 mm) is varied from 43 Pa (for the total flow rate of 10 lpm) to 129 Pa (for the total flow rate of 30 lpm). From this analysis, it is understood that the pressure drop of configuration 3 is in proximity to the ECT reactor.

4.3.3 Sensitivity analysis

The effect of the supply/discharge pressure, inlet temperature, and mass flow rate of the HTF on the time required to reach 1.26 wt.% during absorption/ desorption (referred to as absorption/ desorption time) is presented in this section. The effect of the mass flow rate of the HTF and supply pressure on absorption time is shown in Fig. 4.5a when the inlet temperature of the HTF is fixed at 25°C. The absorption time is reduced by increasing both the supply pressure and the mass flow rate of the HTF. It is observed that the supply pressure has a significant effect on lowering the absorption time than the mass flow rate of the HTF. The percentage decrease in the absorption time is in the range of 38.26% to 41.4% when the supply pressure is increased from 10 to 20 bar for the considered range of mass flow rate of the HTF, whereas the same is 16.67% to 19.26% when the mass flow rate of the HTF is increased from 0.0167 to 0.0333 kg/s for the considered range of supply pressure. The percentage reduction in absorption time when the mass flow rate of the HTF is increased from 0.0167 kg/s to 0.05 kg/s is 26.1% at the supply pressure of 10 bar, whereas the same is 29.8% at the supply pressure of 30 bar. The effect of the inlet temperature of the HTF and the supply pressure on absorption time is shown in Fig. 4.5b when the mass flow rate of the HTF is fixed at 0.042 kg/s. The absorption time is reduced by increasing the supply pressure and decreasing the inlet temperature of the HTF. The absorption time is reduced by 27.1% when the inlet temperature of HTF is reduced from 35 to 25°C for the supply pressure of 10 bar, whereas the same is 15% for the supply pressure of 30 bar. Hence, by increasing the inlet temperature, the HTF is effective at lower supply pressures than at higher supply pressures.

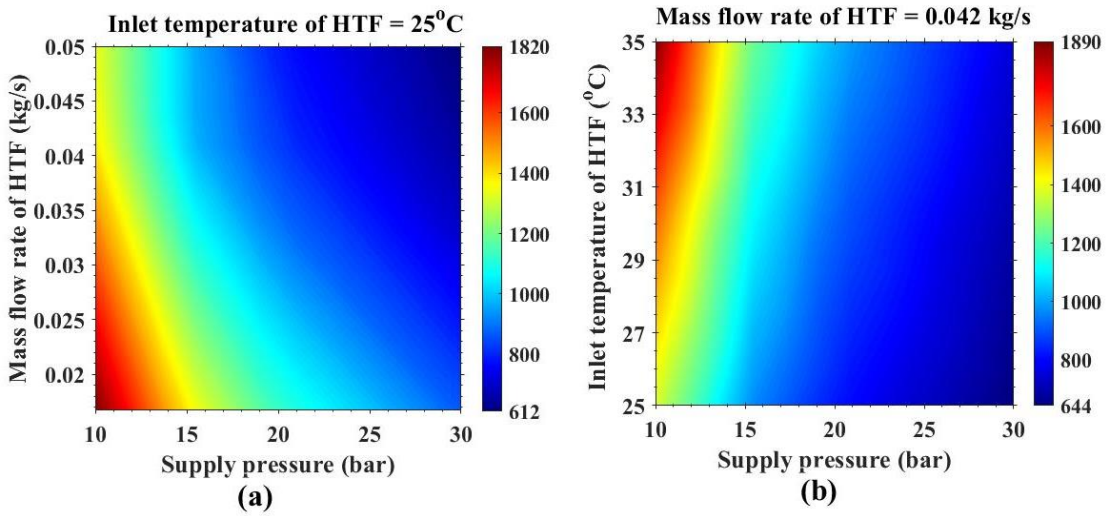

Fig. 4.5. Effect of supply pressure, inlet temperature, and mass flow rate of HTF on absorption time

The effect of the heating fluid temperature and mass flow rate of the HTF on desorption time is shown in Fig. 4.6 when the discharge pressure of the hydrogen is fixed at 1 bar (gauge). The desorption time is reduced by increasing both the heating fluid temperature and the mass flow rate of the HTF. It is observed that the heating fluid temperature has a significant effect on lowering the desorption time than the mass flow rate of the HTF. The percentage decrease in the desorption time is ~52% when the heating fluid temperature is increased from 40°C to 70°C for the considered range of mass flow rate of the HTF. The percentage reduction in desorption time is 26.5% when the mass flow rate of the HTF is increased from 0.0167 kg/s to 0.05 kg/s at the heating fluid temperature of 40°C, whereas the same is 25.75% at the heating fluid temperature of 70°C.

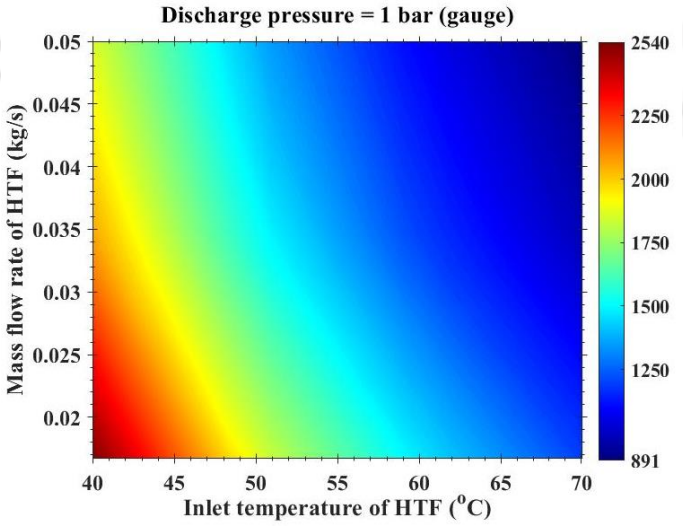

Fig. 4.6. Effect of heating temperature and mass flow rate of HTF on desorption time

Further, the sensitivity contours explicitly explain the relative influence of the operating parameters on the magnitude of the reaction completion times. These are effective in selecting suitable operating parameters for the efficient operation of MH reactors.

4.3.4 Comparison of the performance of configuration 3 with the literature

The absorption performance of configuration 3 is compared with relevant studies from the literature. The details of the reactors considered for the comparison and their operating conditions are shown in Table 4.5. The reactors are modeled under similar working conditions and the mass flow rate of the HTF is selected based on the mass of the alloy filled inside the reactor. The time to reach 1.26 wt.% during absorption is compared, and the percentage reduction in the absorption time obtained by configuration 3 over the other reactors is shown in Fig. 4.7.

Table 4.5 Metal hydride reactors filled with $LaNi_5$ that are considered for the comparison

Author	Type of reactor	Mass of alloy (kg)	Operating conditions
Present study	*Configuration 3*: Finned tube (single tube with 95 radial fins) reactor with outer cooling jacket	13.5	$P_s = 15$ bar; $T_{inlet} = 25°C$; $\dot{m}_{HTF} = 3$ lpm
Raju and Kumar (2012)	*Tube bundle reactor:* One single tube is modeled with the following dimensions.		
	Inner diameter = 25 mm Thickness = 2 mm Length = 1000 mm	2.06	$P_s = 15$ bar; $T_{inlet} = 25°C$; $\dot{m}_{HTF} = 0.458$ lpm
	Inner diameter = 30 mm Thickness = 2 mm Length = 1000 mm	2.96	$P_s = 15$ bar; $T_{inlet} = 25°C$; $\dot{m}_{HTF} = 0.66$ lpm
	Inner diameter = 35 mm Thickness = 2 mm Length = 1000 mm	4	$P_s = 15$ bar; $T_{inlet} = 25°C$; $\dot{m}_{HTF} = 0.9$ lpm
Singh et al., (2015)	An embedded annular heat exchanger tube with radial circular copper fin	1.12	$P_s = 15$ bar; $T_{inlet} = 25°C$; $\dot{m}_{HTF} = 0.25$ lpm
Chandra et al., (2020)	Multi-tube reactor with conical fins (4 tubes and 10 conical fins)	5.1	$P_s = 15$ bar; $T_{inlet} = 25°C$; $\dot{m}_{HTF} = 1.13$ lpm

Configuration 3 (finned tube reactor) showed improved performance over the multi-tubular reactors. The heat transfer rate is enhanced because of the radial fins and the annular bed geometry of configuration 3. The comparative study shows that providing heat transfer

enhancement inside the MH bed is more effective than using multiple ECTs. On the other hand, for the tube bundle reactor, a diameter of less than 25 mm is required to obtain a comparative performance with the present design, increasing the total number of tubes inside the tube bundle reactor. As the number of tubes increases inside the ECT reactor/tube bundle reactor, the pressure drop in the HTF flow and fabrication complexity also increase. Hence, it is believed that the proposed annular porous MH reactor equipped with radial fins is a competitive design for large-scale hydrogen storage applications.

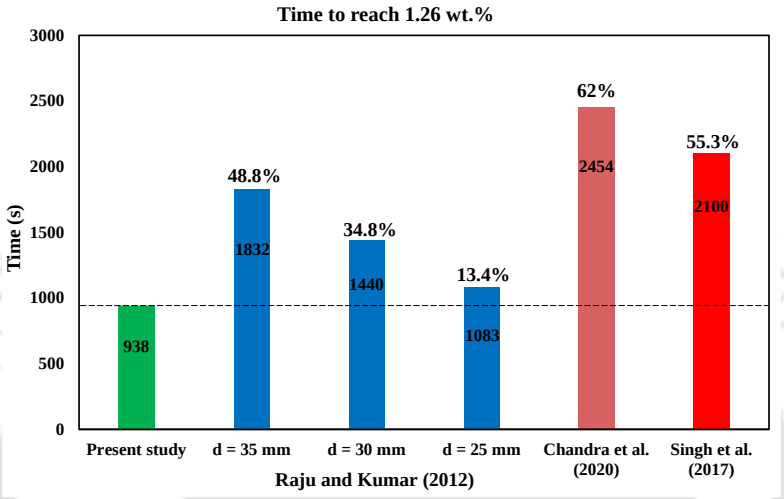

Fig. 4.7. Comparison of configuration 3 with literature during absorption

4.4 Proposed modular design of large-scale applications

A modular design for a large-scale MH-based hydrogen storage system is proposed in this section. The main objectives of the modular design are to reduce the total weight of the MH reactor and easy fabrication without compromising thermal performance. The modular design concept considers several small reactors connected in parallel rather than a single large reactor, as shown in Fig. 4.8. The annular porous bed equipped with radial fins is parallelly arranged inside each module. Since several annular porous metal hydride reactors are connected in parallel, a minimum loss of alloy exists due to any accidental leakage of HTF into the reactor. In a single large-scale hydrogen storage unit, all the MH material in the system must be heated or cooled irrespective of the hydrogen demand, resulting in large parasitic heat loss. With the modular design, each module can be operated independently as per the demand, resulting in less parasitic heat loss and a better response time.

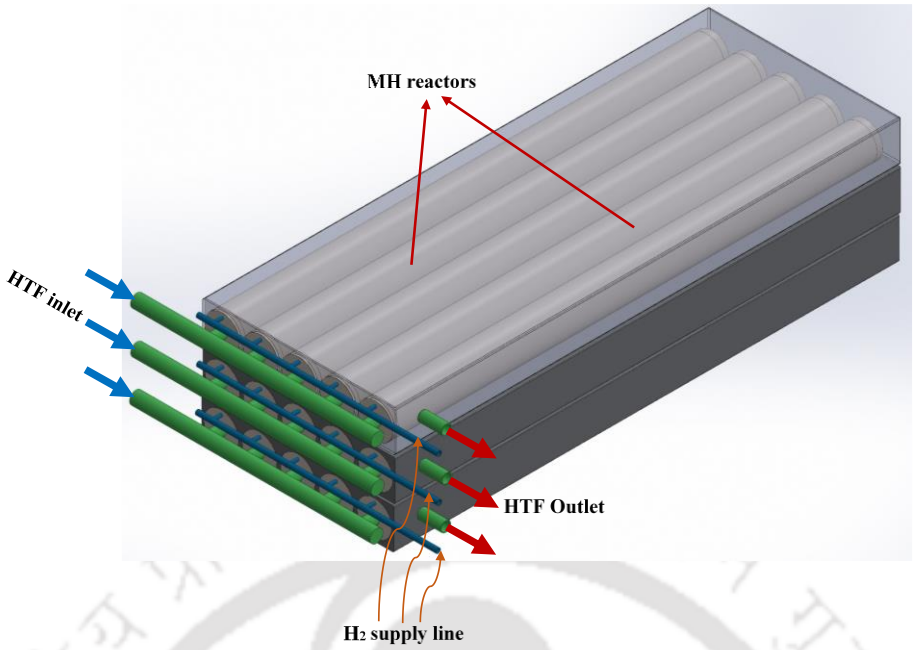

Fig. 4.8. Proposed modular design for large-scale hydrogen storage applications

4.5 Summary

The absorption and desorption characteristics of the annular porous MH reactor filled with $LaNi_5$ are investigated. Three reactor configurations are compared to analyze the effect of fluid flow direction and adding radial fins on the absorption and desorption processes. Further, a sensitivity analysis is carried out on the finned tube reactor to study the impact of operating parameters on absorption and desorption times. Furthermore, the performance of the finned tube reactor is compared with the literature. Based on the results of the present numerical study, the following key observations are made:

- The absorption time of 945 s is obtained with the finned tube reactor under the supply pressure of 15 bar and cooling fluid temperature of 25°C. During desorption, the finned tube reactor achieved a desorption time of 1290 s under the discharge pressure of 1 bar and heating fluid temperature of 50°C.
- The addition of fins enhanced the absorption and desorption rates by a factor of 1.84 and 1.85, respectively.
- Changing the HTF flow direction (configuration 2) enhanced the peak outlet temperature by 5.7°C during absorption and 3.33°C during desorption.
- From sensitivity analysis, it is observed that the supply pressure and desorption temperature are the most influencing parameters during the absorption and desorption processes, respectively.

- The absorption performance of configuration 3 is compared with the literature. It is observed that the heat transfer rate is enhanced much better with radial fins inside the annular bed than with tube bundle and multi-tube reactors.

Finally, a modular design of annular porous metal hydride reactors is proposed for large-scale hydrogen storage applications.

Chapter 5

Experimental studies: LTMH reactor

5.1 Preface

This chapter presents details of the annular MH reactor equipped with radial fins and the experimental protocol for hydrogen storage. The details of the MH reactor, experimental setup, and experimental procedure for the hydrogen storage system are presented. Two AB_5-metal hydrides, $LaNi_5$ and $La_{0.7}Ce_{0.1}Ca_{0.3}Ni_5$, are selected as LTMH due to their faster reaction kinetics and good storage capacity. Further, the reason for choosing $LaNi_5$ is due to the availability of extensive studies on this AB_5-type alloy, which enables an easier comparison of the present results with the literature. $La_{0.7}Ce_{0.1}Ca_{0.3}Ni_5$ is selected due to its increased storage capacity than $LaNi_5$. The effect of supply pressure and inlet temperature of the HTF during absorption and the effect of inlet temperature of the HTF during desorption was studied. The results obtained from the hydrogen storage system are presented in terms of MH bed temperature variations, absorption and desorption times, system-level energy densities, and energy storage efficiency. Further, the obtained experimental results are compared with the literature. Finally, the major conclusions of the experimental study are summarized. These experimental results will help design efficient industrial-scale MH-based hydrogen and TES systems.

5.2 Details of LTMH reactor

The annular MH reactor equipped with radial fins was fabricated. A 3D sectional view and schematic of the annular MH reactor equipped with radial fins are shown in Fig. 5.1(a). The reactor is made up of three concentric tubes of SS316 material. The MH alloy is filled inside the annular space between the inner and middle tubes. The annular MH bed is cooled/ heated by circulating the HTF through the inner tube and the annular space between the middle and the outer tubes. A double-pass heat exchanger concept is used to achieve a higher gain/ drop in the temperature of HTF during absorption/ desorption without affecting the reaction rate of the MH bed. Water is used as an HTF, which enters the reactor through the inner tube and is redirected through the outer annular space before exiting from the reactor, as shown in Fig. 5.1 (a). The hydrogen line and a sintered porous filter are attached to the left end of the reactor to

facilitate the supply/ discharge of hydrogen gas to/ from the MH reactor. Further, heat transfer effectiveness is increased by providing perforated radial fins over the inner tube within the MH bed. Furthermore, the reactor is provided with provisions for the temperature and pressure sensors, as shown in Fig. 5.1(a).

The 2D sectional view of the reactor with the dimensions indicated is shown in Fig. 5.1(b). The reactor is designed for a maximum working pressure of 80 bar. A sintered porous filter made of SS316 (Outer diameter: 12 mm; length: 100 mm; pore size: 2 µm) is used for separating the MH powder particles and hydrogen gas. An ASTM A312 standard seamless tubes of SS316 material are selected for fabrication of the reactor. The dimensions of the tubes used for the fabrication of the reactor are presented in Table 5.1. 91 perforated radial fins of 0.6 mm thick are placed inside the MH bed for heat transfer enhancement. The fins are made of aluminum and attached to the inner tube using the press-fit method. The fins occupied 4% of the total inside volume of the reactor. The perforations (8 mm in diameter) on the fins facilitate the free flow of hydrogen along the length of the reactor and provision for easy filling of the MH powder. The two ends of the reactor are welded with standard flat circular heads.

Table 5.1. Dimensions of the MH reactor

Tube location	Geometrical parameters	Value
Inner tube		
	Inner diameter (mm) Outer diameter (mm)	18.04 21.34
Middle tube		
	Inner diameter (mm) Outer diameter (mm)	68.81 73.03
Outer tube		
	Inner diameter (mm) Outer diameter (mm)	83.03 83.23

The pictorial view of the fabricated annular MH reactor is shown in Fig. 5.1(c). The total fillable volume inside the MH reactor is 3.2×10^{-3} m^3. The widely reported porosity and particle density values of $LaNi_5$ are 0.5 and 8400 kg/m^3, respectively (Gonzatti and Farret, 2017; Lin et al., 2019). The reactor is filled with 9 kg of $LaNi_5$ powder (80 mesh), which occupies 70% of the total volume (i.e., 2.24×10^{-3} m^3) at a porosity of 0.52. The remaining 30% of the total volume (i.e., 0.96×10^{-3} m^3) is left for free expansion of the MH powder. The free expansion space is provided to avoid the stresses developed on the reactor walls (Ao et al., 2005; Heubner et al., 2017). However, it should be noted that the packing density of the powder bed varies as the number of cycles increases and reaches a stable state. The size distribution becomes invariant with further cycling (Smith and Fisher, 2012). The MH powder is filled through the

thermocouple ports. During filling, the reactor is shaken at regular intervals to ensure uniform distribution of the powder. The weight ratio (the mass of metal hydride alloy to the mass of the empty reactor) is obtained as 1.44. Here, the mass of the empty reactor includes the mass of three concentric tubes, perforated fins, and endplates. Similarly, another reactor was filled with 9 kg of $La_{0.7}Ce_{0.1}Ca_{0.3}Ni_5$ (80 mesh size). The technical details of the $La_{0.7}Ce_{0.1}Ca_{0.3}Ni_5$ reactor are shown in Table 5.2. The P-C-I characteristics of $LaNi_5$ and $La_{0.7}Ce_{0.1}Ca_{0.3}Ni_5$ at 25 and 45°C are shown in Fig. 5.2.

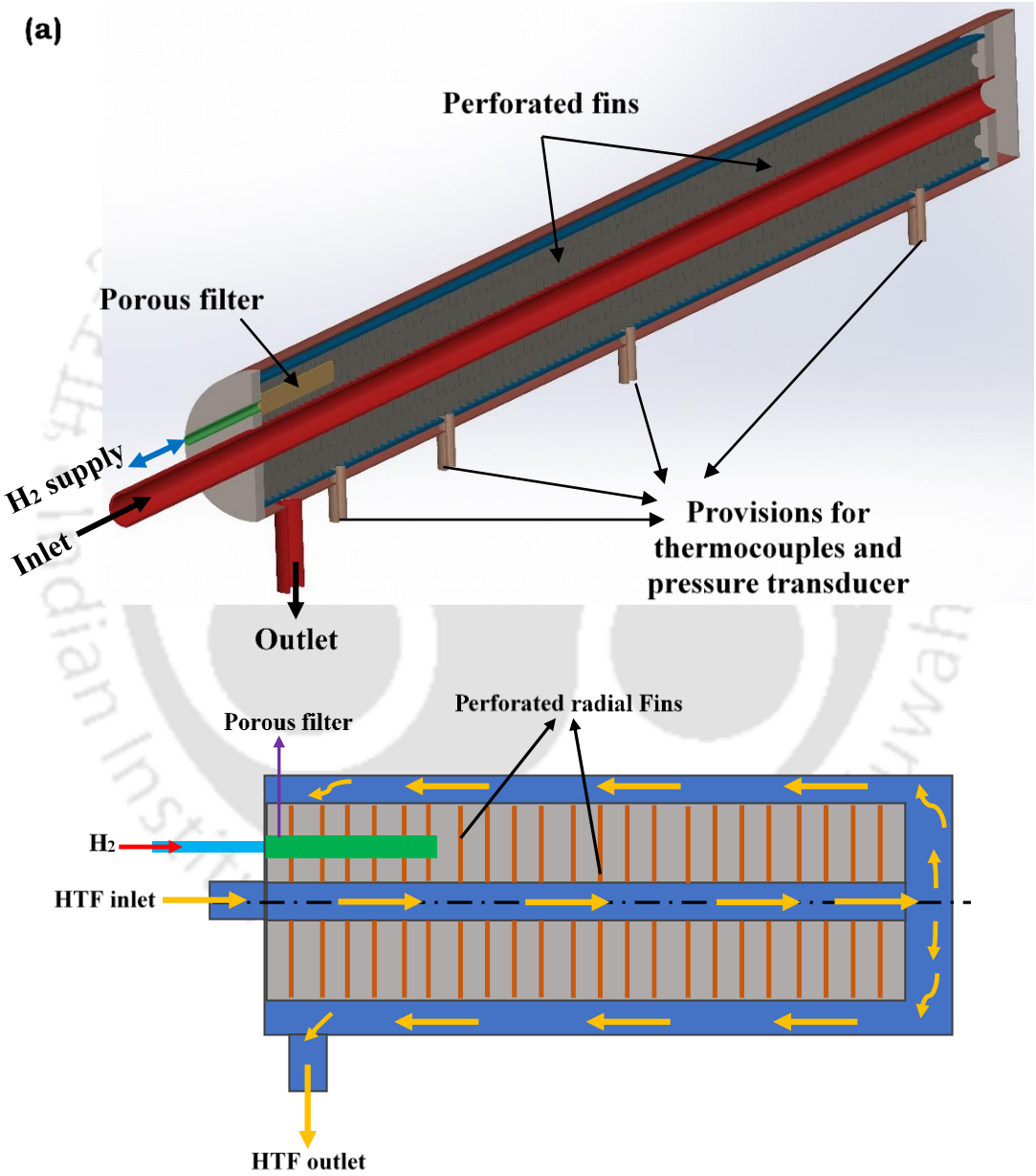

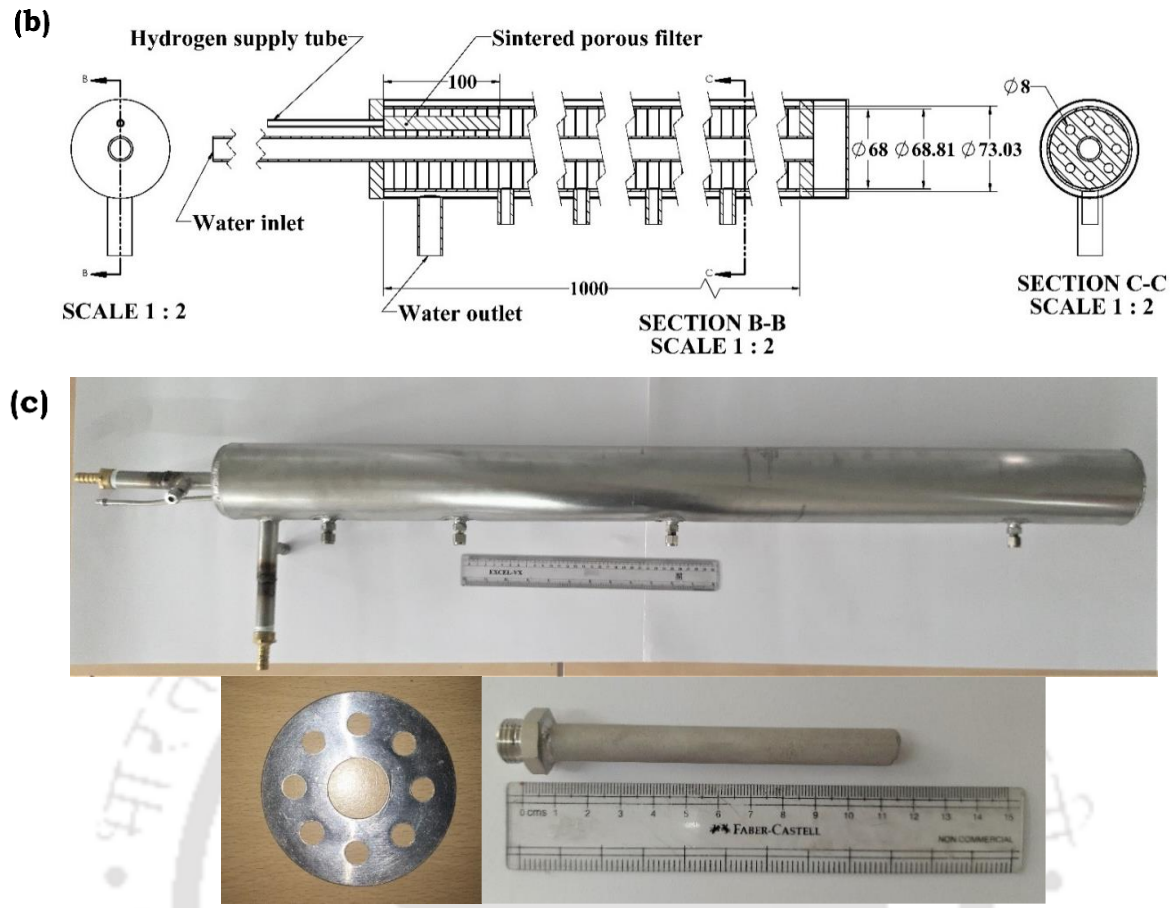

Fig. 5.1. (a) 3D sectional view and schematic of annular MH reactor with internal fins, (b) 2D sectional view of the annular MH reactor with internal fins with dimensions, and (c) pictorial view of the fabricated reactor, perforated aluminum fin, and sintered porous filter

Table 5.2. Technical details of the $La_{0.7}Ce_{0.1}Ca_{0.3}Ni_5$ reactor

Details	**value**
Alloy mass	9 kg
Mass of the empty reactor	6.25 kg
Maximum working pressure	80 bar
Maximum storage capacity	1390 L at STP (0.125 kg)
Heat transfer surface area	Tube area = 0.296 m^2 Finned area = 2×0.261 m^2
Absorption conditions:	Temperature: 25°C Supply pressure: 5-20 bar
Desorption conditions:	Temperature: 30-50°C Discharge pressure: to ambient

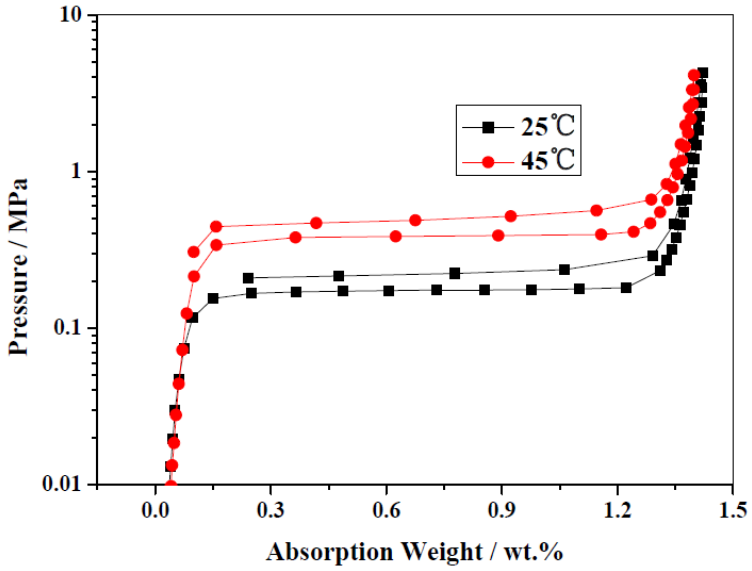

(a)

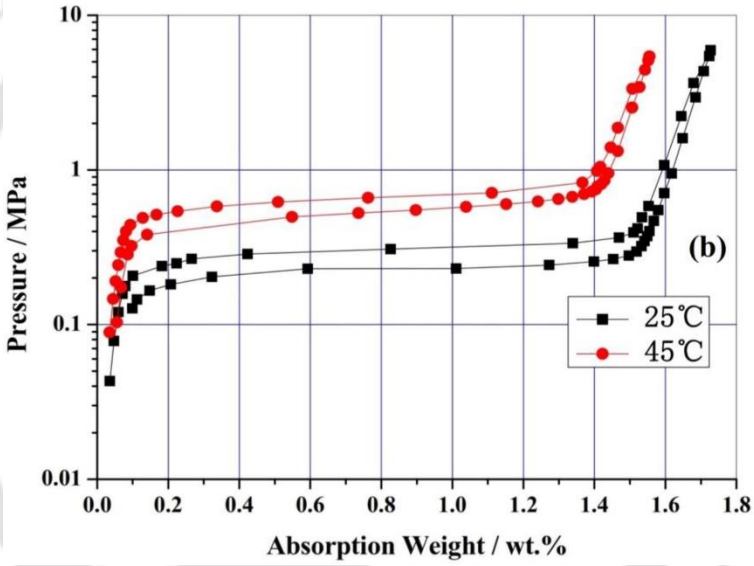

(b)

Fig. 5.2. Pressure-composition-isotherms (a) $LaNi_5$ and (b) $La_{0.7}Ce_{0.1}Ca_{0.3}Ni_5$

5.3 Experimental protocol

5.3.1 Setup and procedure

Fig. 5.3 shows the schematic and photographic views of the experimental setup. The experimental setup consists of a hydrogen gas line, a heat transfer fluid (HTF) line, an MH reactor, and a data acquisition system. The hydrogen gas line contains a hydrogen gas cylinder, ball valves, a Coriolis mass flow meter, and a vacuum pump. The hydrogen line is made with a ¼-inch stainless steel tube. Stainless steel ball valves (part number: SS-43GS4; make: Swagelok) are used in the hydrogen line to divert the hydrogen flow during the experiments. A water tank of 80 L fitted with a secondary heat exchanger is connected to the hot water bath

and cold-water bath in the HTF line, as shown in Fig. 5.3. The secondary heat exchanger is used to exchange the heat to the HTF coming from the MH reactor. The secondary heat exchanger operates in coordination with the cold-water bath during absorption, whereas it operates in coordination with the hot water bath during desorption. An ½ inch copper coil (length = 7.5 m) is used as a secondary heat exchanger. However, the design of the secondary heat exchanger is not in the scope of the present work. The inlet temperature is maintained within ±1°C with the help of a secondary heat exchanger. A DC submersible pump is fitted inside the 80 L water tank for supplying the HTF to the MH reactor during the experiments. The MH reactor is evaluated for its absorption and desorption characteristics.

Before the absorption and desorption experiments, the MH bed must be activated by repeatedly evacuating and filling the reactor with high-pressure hydrogen. After activation, the absorption and desorption characteristics of the MH reactor were investigated.

5.3.1.1 Absorption

Hydrogen absorption into the MH bed is performed at different supply pressures for a fixed inlet temperature of HTF of 25°C. The hydrogen gas is supplied at a set pressure during absorption, while the exothermic heat is extracted from the MH bed by circulating the HTF from the water tank at the set temperature. The valves V1, V2, and V4 remain open during the absorption. The remaining valves are closed. The absorption is continued until the MH alloy reaches the saturation storage capacity for a given supply pressure.

5.3.1.2 Desorption

Before starting the desorption, the reactor is heated to the required desorption temperature from room temperature. The hydrogen gas is discharged from the MH reactor to 1 bar absolute. The endothermic heat of desorption is supplied by circulating water from the water tank at the set temperature. Hydrogen desorption is carried out at different desorption temperatures. After desorption, the reactor is naturally cooled to the absorption temperature. The valves V1, V3, V5, and V7 are opened during the desorption process.

5.3.2 Measurements of the hydrogen storage system

A Coriolis mass flow meter (Make: Emerson; mass flow accuracy: ±0.25% of the rate) is used to measure hydrogen gas's mass flow rate. Also, the minimum flow rate recorded by Coriolis mass flow meter is 0.001 g/s. Hot and cold-water baths (accuracy: ±1°C) with the help of a

secondary heat exchanger are used to maintain the constant HTF temperature. In the $LaNi_5$ reactor, five stainless steel sheathed K-type thermocouples (accuracy: ±0.5°C) are used to measure the temperature at different locations of the MH bed and the HTF. Three thermocouples (TC1, TC2, and TC3) are placed inside the reactor to measure the MH bed's temperature, as shown in Fig. 5.3(b). The remaining two are positioned in the water circuit to measure the inlet and outlet temperature of the HTF, which is circulated through the MH reactor. Two piezoresistive type pressure transducers (make: Equinox; accuracy: ± 0.5% on full-scale) are fitted to the reactor. One is fitted at the supply end of the reactor (P1) to measure the supply pressure of the hydrogen, and another (P2) is placed at a distance of 915 mm to measure the pressure inside the MH reactor.

Whereas in $La_{0.7}Ce_{0.1}Ca_{0.3}Ni_5$ reactor, a piezoresistive pressure transducer (Range: 0-100 bar; Accuracy of ±0.5% on full-scale) is fitted in the hydrogen line of the reactor to measure the pressure during absorption/ desorption processes. Four K-type thermocouples (accuracy: ±1°C) are used to measure the temperature inside the MH bed, as shown in Fig. 5.3(b). Two T-type thermocouples (accuracy: ±0.5°C) are used to measure the circulating water's inlet and outlet temperatures. The water flow rate from the submersible pump is measured using the catch bucket method/ bucket test method. The bucket test method is repeated three times for better accuracy. A multiple-output DC power supply unit is used to control the power input to the DC submersible pump as per the required flow rate of HTF. During the experiments, the reactor is insulated with nitrile rubber of 24 mm thickness. The MH bed temperature, inlet and outlet temperatures of the HTF, supply pressure, and hydrogen flow rate are recorded with a data acquisition system (Make: Keysight Technologies) during the experiments.

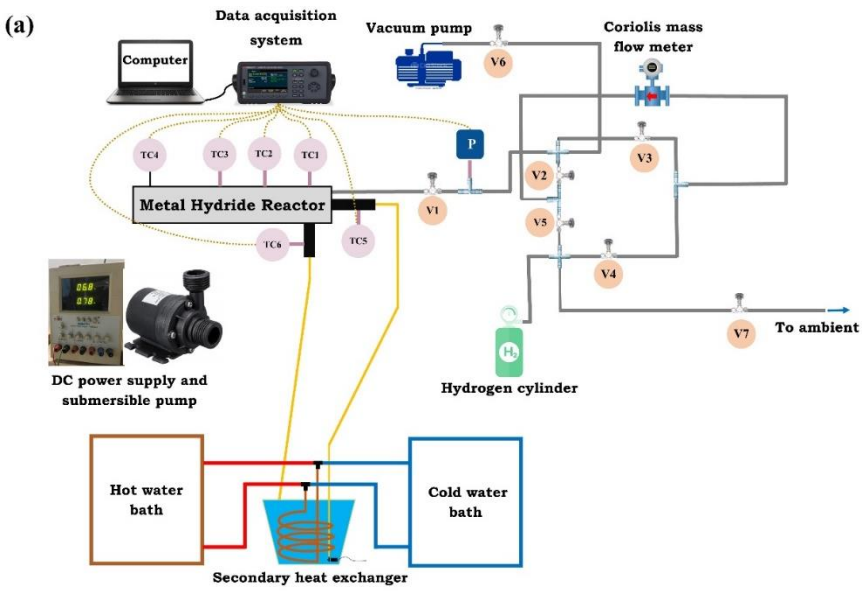

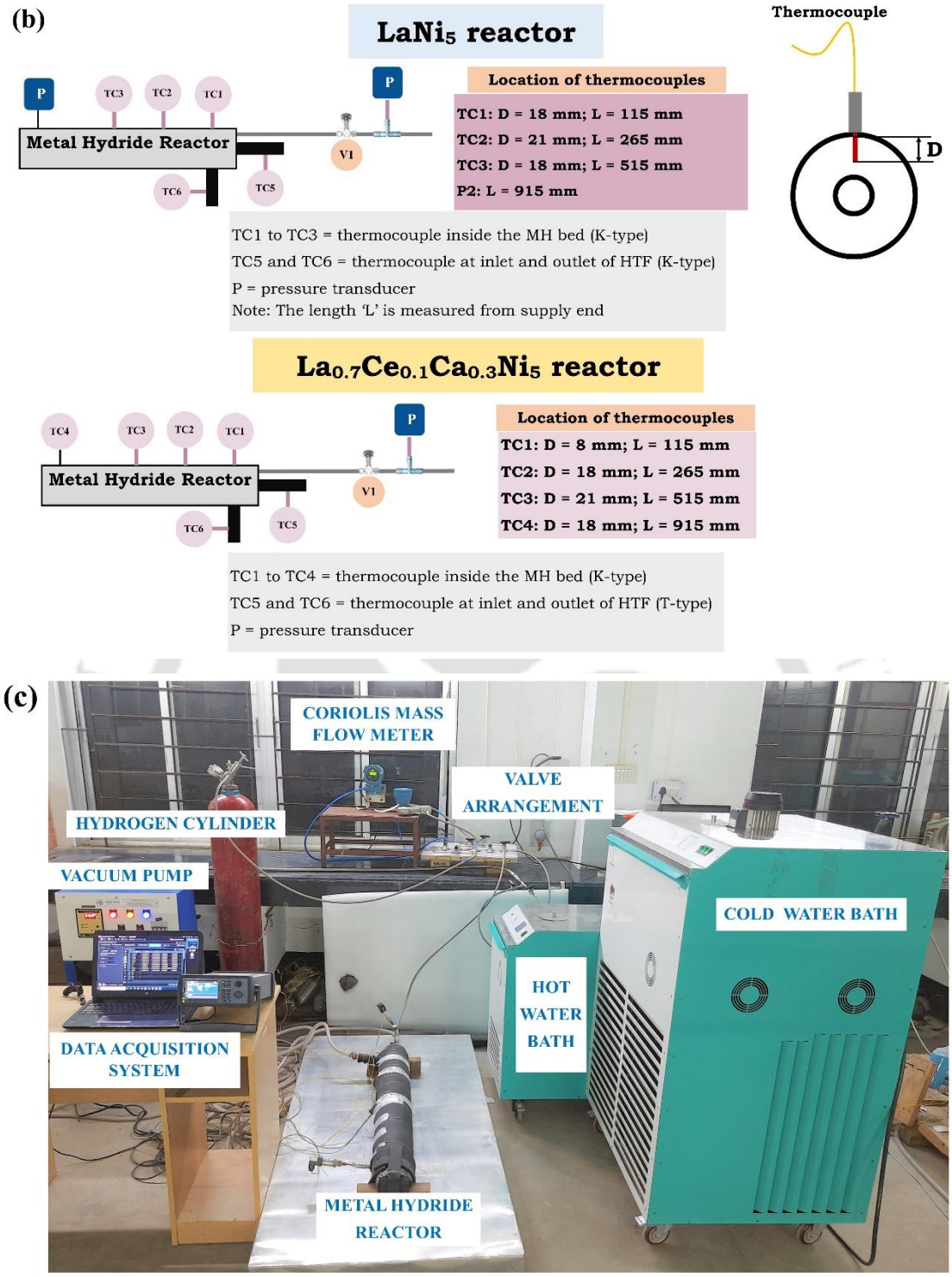

Fig. 5.3. (a) Schematic, (b) thermocouple location and (c) photograph of the experimental Setup ($LaNi_5$ reactor is fitted in the set up)

5.4 Results and discussion: $LaNi_5$

This section presents the experimental results of the annular MH reactor filled with $LaNi_5$ during absorption and desorption processes. During absorption, the supply pressure was varied

from 10 bar to 30 bar, and the inlet temperature was varied from 15°C to 30°C. During desorption, the heating fluid temperature was varied from 40°C to 70°C. The flow rate of HTF was maintained at 2.5 lpm during the absorption and desorption processes. For all the absorption and desorption experiments, the inlet temperature of the HTF and the initial temperature of the MH bed were kept the same. The results are presented in terms of bed temperature, amount of hydrogen absorbed/ desorbed, temperature gain/ drop by the HTF, and the driving potential. The results shown from section 5.4.2 onwards were obtained after 20 cycles of absorption and desorption.

5.4.1 Activation of $LaNi_5$

Activation of the MH alloy involves removing surface oxides and internal cracking of metal particles to increase reaction sites (Badding et al., 1996; Sandrock, 1999b). Firstly, the reactor is checked for leaks by supplying argon gas at a pressure of 60 bar. The reactor is then heated to 70°C and evacuated down to a 10^{-5} bar pressure to remove traces of moisture and other foreign gases. After each absorption process, the hydrogen is desorbed from the reactor at 60°C and evacuated to 10^{-5} bar pressure. The results of the hydrogen absorbed during the activation cycles are shown in Fig. 5.4. During the second activation cycle, the alloy reached a storage capacity of 1.32 wt.% in 990 s. There is no significant change in the reaction kinetics of the $LaNi_5$ after the second cycle, indicating the activation completion.

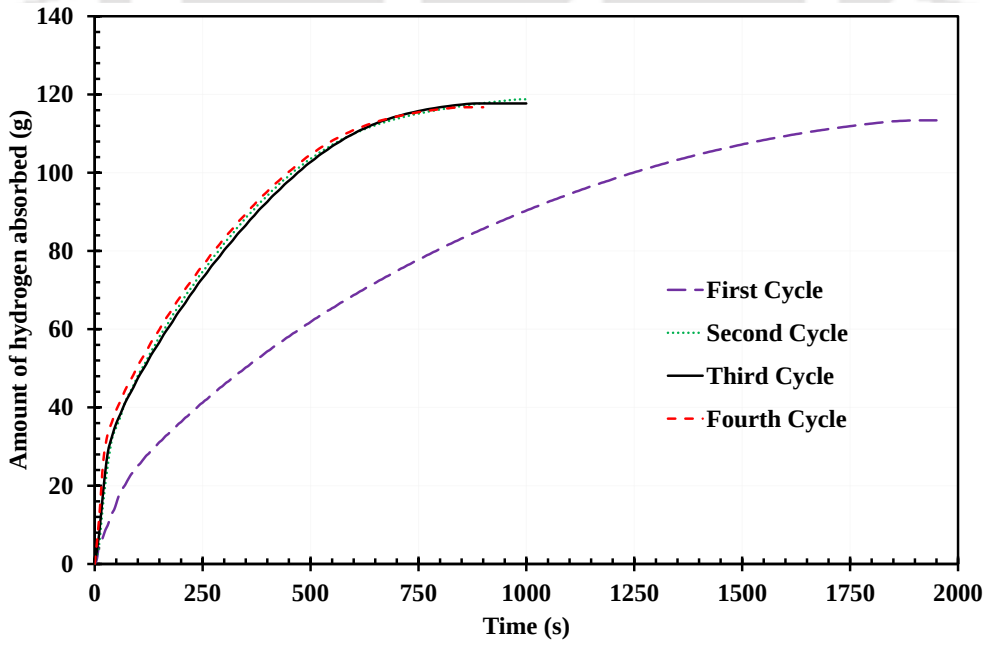

Fig. 5.4. Amount of hydrogen absorbed during activation cycles

5.4.2 Absorption

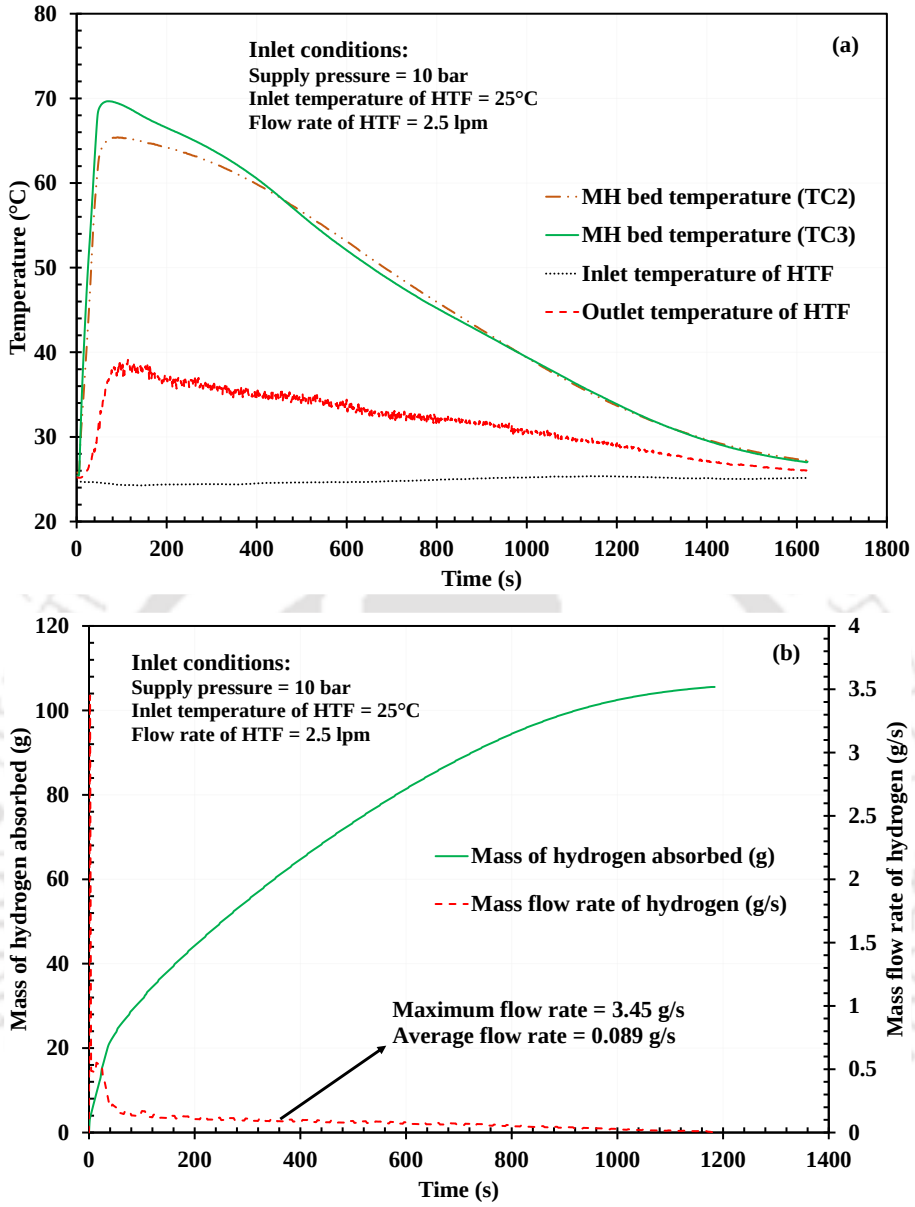

Fig. 5.5. Absorption process: (a) Temperature variations and (b) amount of hydrogen absorbed and mass flow rate of the absorbed hydrogen

The variations in MH bed temperature, HTF temperature and mass of hydrogen absorbed are shown in Fig. 5.5. The results were obtained for the supply pressure of 10 bar while the inlet temperature and mass flow rate of HTF were maintained at 25°C and 2.5 lpm, respectively. During the initial stages of the absorption, the driving force (difference between the hydrogen supply pressure and the metal hydride equilibrium pressure) is higher, leading to faster absorption. During this period, the heat extracted by the HTF from the MH bed is much smaller than the heat generated due to an exothermic reaction, which leads to a sharp rise in the bed temperature (Fig. 5.5a). The MH bed temperature (TC3) was increased to a peak temperature

of 70°C due to a large amount of exothermic heat during the initial stages of the reaction. In later stages, the driving force decreases due to an increase in the bed temperature, due to which the absorption rate drops. During this period, the heat removed by the HTF is dominant, due to which the bed temperature started decreasing (Fig. 5.5a).

The inlet and outlet temperature variations of HTF are also shown in Fig. 5.5a. The outlet temperature of the HTF depends on the amount of heat generated inside the MH bed. Similar to MH bed temperature, the HTF temperature peaked during the initial stages and decreased towards the inlet temperature of the HTF during later stages. In the present study, the reactor is designed such that the HTF takes a double pass before leaving the reactor, leading to a higher temperature gain of the HTF. Such an arrangement enables the extraction of the complete cooling potential of the HTF without affecting the reaction rate of the MH bed. A maximum temperature difference of 14.8°C was obtained between inlet and outlet temperatures of HTF for the given operating conditions (Fig. 5.5a). At the same time, an average temperature difference of 8.4°C was observed during the absorption process. From Fig. 5.5b, it is observed that the alloy absorbed 105.6 g of hydrogen in 1184 s, with an average mass flow rate of 0.089 g/s. The mass flow rate of hydrogen peaked at 3.45 g/s during the early stages of the reaction due to higher driving potential. In later stages, the mass flow rate of hydrogen decreased due to the reduced driving potential.

5.4.3 Desorption

The desorption is an endothermic process during which the MH bed releases hydrogen by absorbing the heat from the HTF. The variations in MH bed temperature, the HTF temperature, and the amount of hydrogen desorbed with flow rate are shown in Fig. 5.6. Before the start of the desorption, the temperature of the MH bed was raised to 60°C, and an amount of 111 g of hydrogen was charged into the system. The inlet temperature and flow rate of HTF were maintained at 60°C and 2.5 lpm, respectively. Endothermic heat uptake is much higher during the initial stages than the heat received by the MH bed from the HTF. Therefore, a sudden drop in the temperature of the MH bed is observed. The rapidity of the endothermic reaction is due to higher driving potential. During this period, the MH bed temperature was dropped to 31.2°C. The bed temperature was increased during later stages due to the improved heat transfer between the HTF and MH bed (Fig. 5.6a).

From the inlet and outlet temperature variations of the HTF (Fig. 5.6a), a peak temperature difference of 11.5°C was achieved between the inlet and outlet temperatures of HTF. At the

same time, the average temperature difference of 6.4°C was obtained during the desorption process. It was observed that the alloy desorbed 110 g of hydrogen in 1590 s, with an average hydrogen gas flow rate of 0.0692 g/s (Fig. 5.6b).

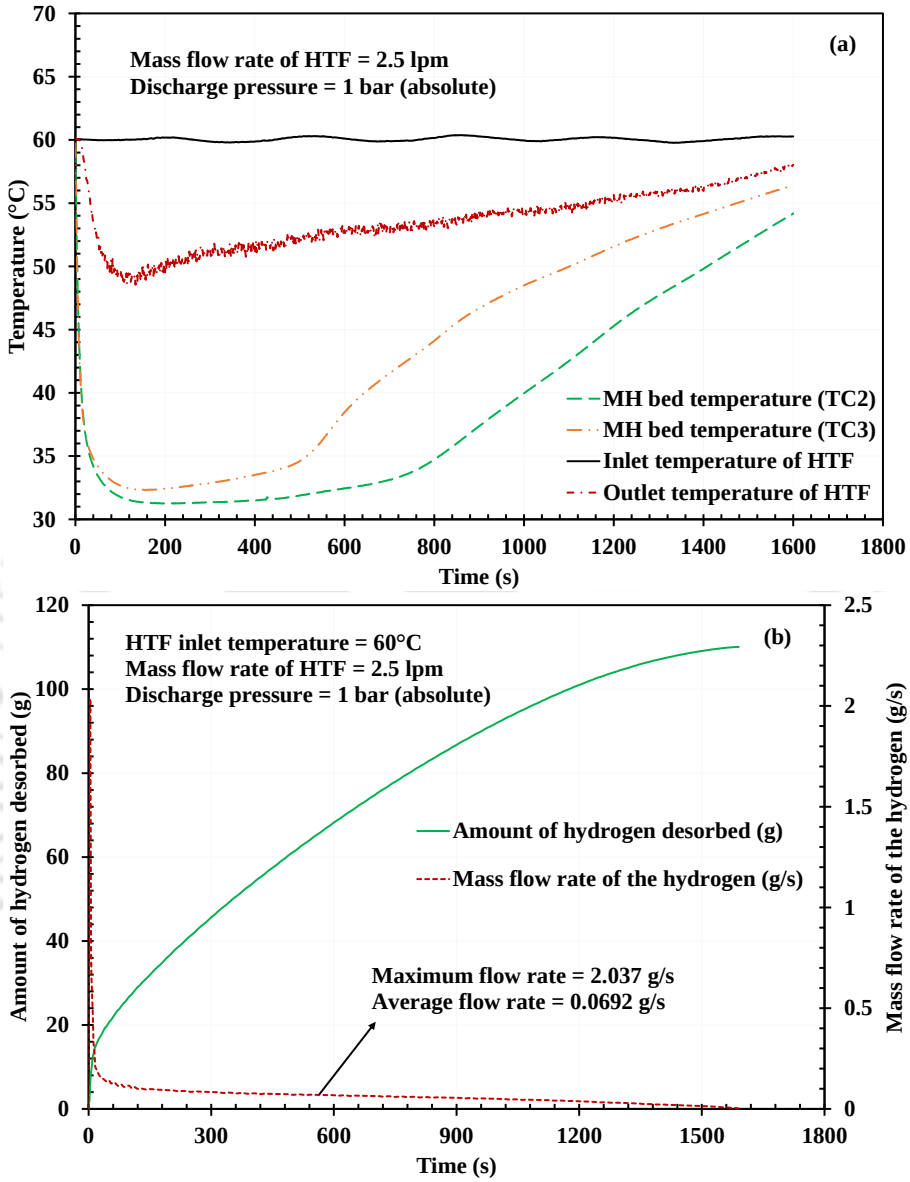

Fig. 5.6. Desorption process: (a) Temperature variations and (b) amount of hydrogen desorbed and mass flow rate of the desorbed hydrogen

The axial and radial locations of the thermocouples TC2 and TC3 are shown in Fig. 5.3(a). The thermocouple TC2 is located near the HTF's inlet (at a distance of 265 mm) and closer to the inner cooling tube in the radial direction than the thermocouple TC3. Due to this, TC2 experiences better cooling and heating than TC3. During absorption (Fig. 5.5a), the peak temperature recorded by TC2 is less than the TC3. But, both TC2 and TC3 showed similar temperatures during later stages of the absorption. The possible reason for this behavior is that the supply pressure exhibited a more significant effect on the absorption process than the inlet

temperature of the HTF (see section 5.4.4). In contrast, the temperature recorded by TC2 reached the inlet temperature of the HTF at a faster rate than the TC3 during desorption (Fig. 5.6a) because the inlet temperature of the HTF showed a significant effect on the desorption process (see section 5.4.5). Further, the temperatures recorded by thermocouple TC1 are not presented here because of the absurd temperature profile recorded by TC1. The possible reason for such a profile is improper contact between the thermocouple with the powder bed.

5.4.4 Sensitivity analysis: absorption

During absorption, the supply pressure and the inlet temperature of the HTF are the major performance affecting parameters. Therefore, the absorption performance is evaluated at three different supply pressures, namely, 10, 20, and 30 bar, and four inlet temperatures of HTF, 15, 20, 25, and 30°C. The mass flow rate of the HTF was maintained at 2.5 lpm for all the experiments.

As the supply pressure increases, the driving potential gain improves the reaction rate (Fig. 5.7a). The time to absorb 90% of the storage capacity (i.e., 104.5 g) is 1100, 640 and 475 s, respectively, for 10, 20, and 30 bar supply pressure. The percentage decrease in absorption time when the supply pressure was raised from 10 to 20 bar is 41.8%, whereas the same was 25.8% when the supply pressure was increased from 20 to 30 bar. The gain-in temperature of the HTF (ΔT) as it flows in the heat exchanger is shown in Fig. 5.7b. A higher temperature gain was achieved for the higher supply pressure due to the faster absorption rate. The maximum ΔT of 14.8, 18.7, and 22°C, respectively, were obtained for 10, 20, and 30 bar supply pressure.

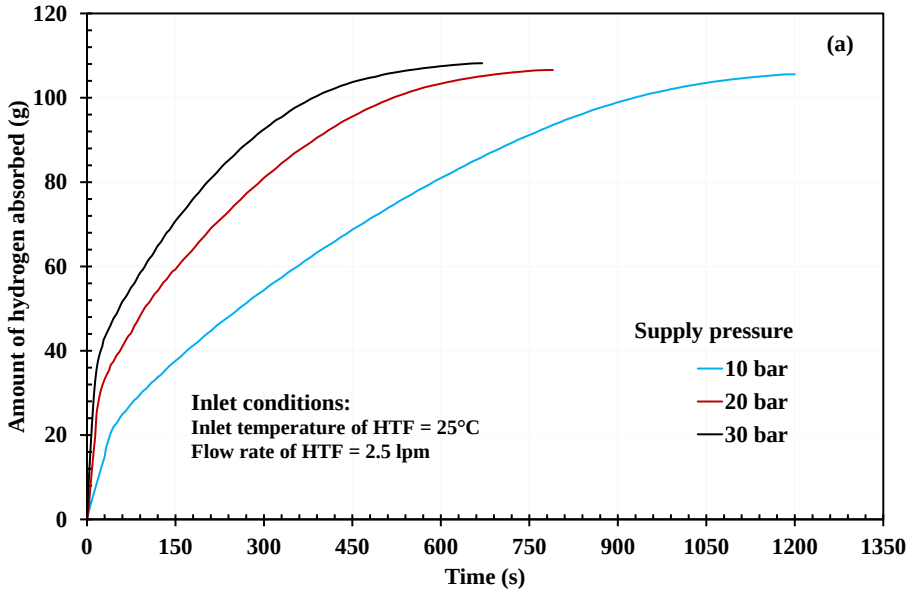

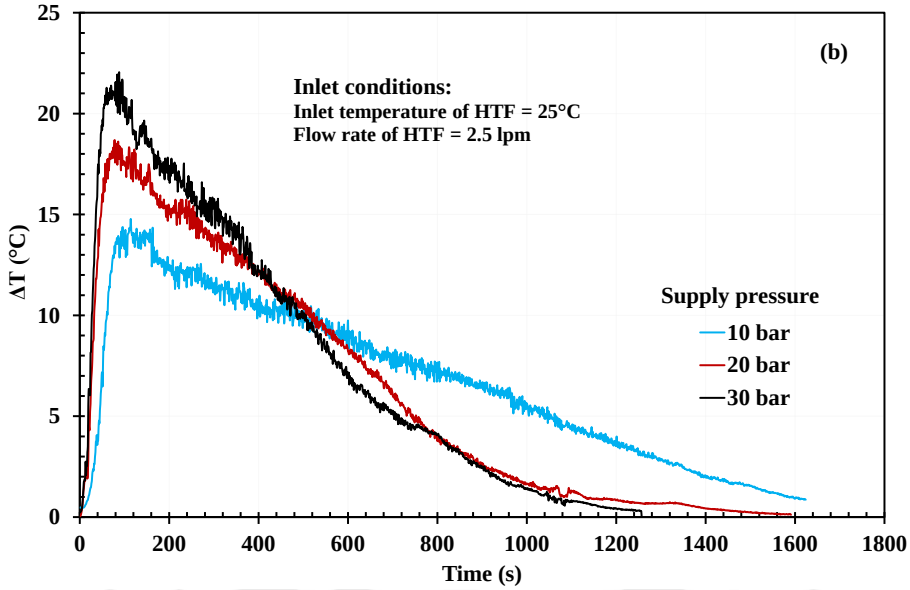

Fig. 5.7. Effect of supply pressure on (a) amount of hydrogen absorbed and (b) temperature gain of the HTF (ΔT) during absorption

From the van't Hoff equation, it is observed that a lower bed temperature gives a lower equilibrium pressure which means a higher driving potential. Consequently, the lower the inlet temperature of the HTF, the higher will be the driving potential. The effect of the inlet temperature of the HTF on the amount of hydrogen absorbed and the temperature gain of the HTF is shown in Fig. 5.8. During the experiments, the supply pressure is maintained at 10 bar. The MH bed absorbed 104.36, 103.9, 105.57 and 101.83 g of hydrogen in 1000, 1060, 1200 and 1225 s, respectively, for the inlet temperatures of HTF of 15, 20, 25 and 30°C (Fig. 5.8a). It is observed that there is no significant change in the final absorbed amount of hydrogen and absorption time with the increase in the inlet temperature of the HTF for the supply pressure of 10 bar. Similar behavior was observed in the temperature gain of the HTF (ΔT), as shown in Fig. 5.8b. Hence, it is observed that a lower HTF temperature improves the performance, but the impact is relatively less compared to the supply pressure. Also, the cost involved in reducing the temperature of HTF is not justifiable for the performance enhancement obtained. Hence, absorption at the ambient temperature is recommended. However, HTF inlet temperature may significantly affect the absorption time for lower supply pressures (< 10 bar). This is due to the significant effect of temperature on the driving potential at lower supply pressures.

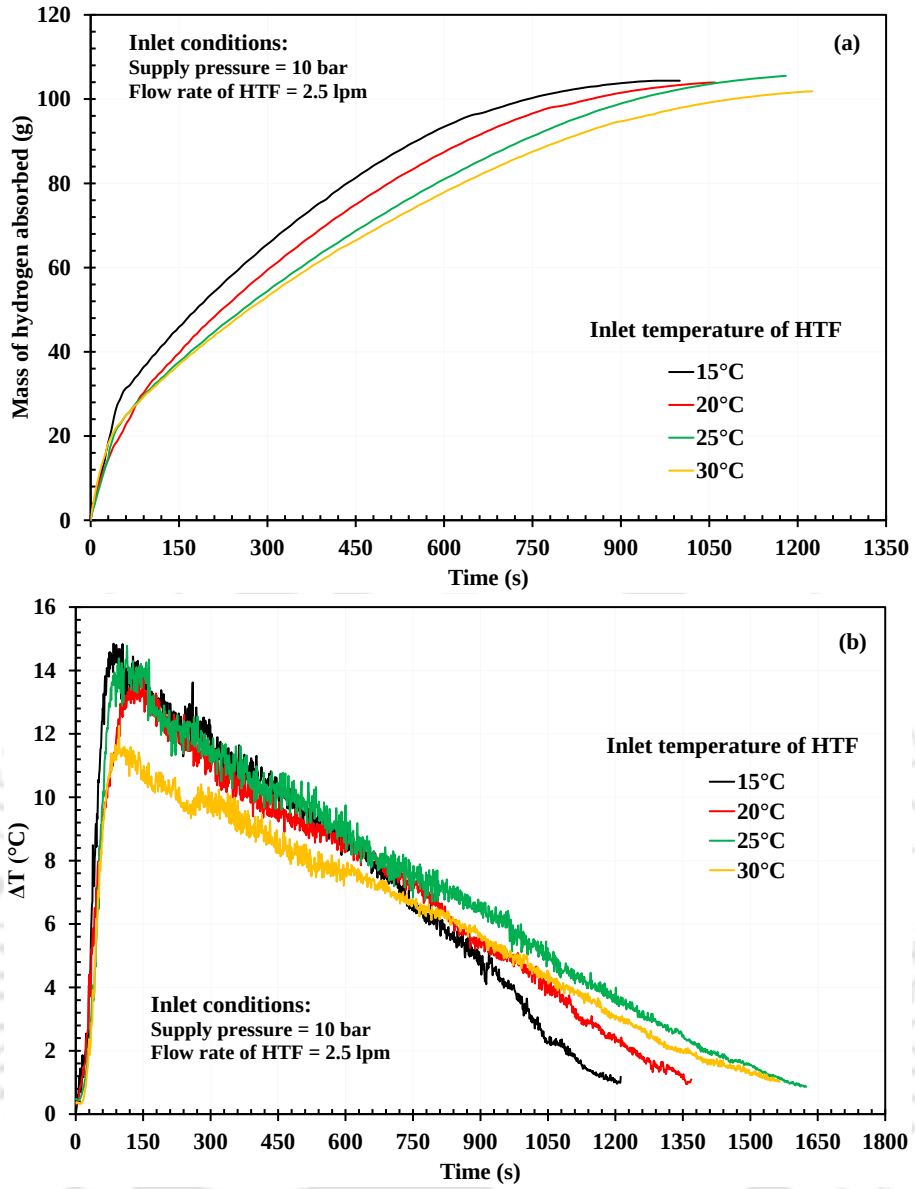

Fig. 5.8. Effect of inlet temperature of HTF on (a) amount of hydrogen absorbed and (b) temperature gain of the HTF (ΔT) during absorption

5.4.5 Sensitivity analysis: desorption

During desorption, the inlet temperature of the HTF is the primary performance parameter. Therefore, the desorption experiment was performed at four different inlet temperatures of HTF, namely, 40, 50, 60, and 70°C, while the flow rate of HTF was maintained at 2.5 lpm. Before each desorption experiment, approximately 111 g of hydrogen was charged into the MH bed. The effect of the inlet temperature of the HTF on driving potential, the mass of hydrogen desorbed, and the temperature drop of the HTF (ΔT), is shown in Fig. 5.9. Usually, the driving potential is the difference between the gas pressure and the local equilibrium pressure of the MH bed. However, measuring local equilibrium pressure on large reactors is extremely difficult. Hence, the difference between the pressure recorded by P2 and the ambient

pressure is considered as the driving potential. Since the pressure transducer P2 is located at a distance of 915 mm from the discharge end of the reactor, it is appropriate to consider this pressure for calculating the driving potential. The driving potential is highly influenced by the inlet temperature of the HTF (as shown in Fig. 5.9a). Initially, the pressure recorded by the transducer P2 was 37.4, 42.5, 48.7, and 54.5 bar, respectively, for inlet temperatures of 40, 50, 60, and 70°C. Even though hydrogen is charged into the reactor at the same supply pressure before the desorption, the initial pressures are different for different inlet temperatures due to the dependency of the equilibrium pressure of the MH bed on the temperature. The higher the inlet temperature of the HTF, the higher is the driving potential, as shown in Fig. 5.9a. Therefore, faster desorption rates were obtained at the higher inlet temperature of the HTF.

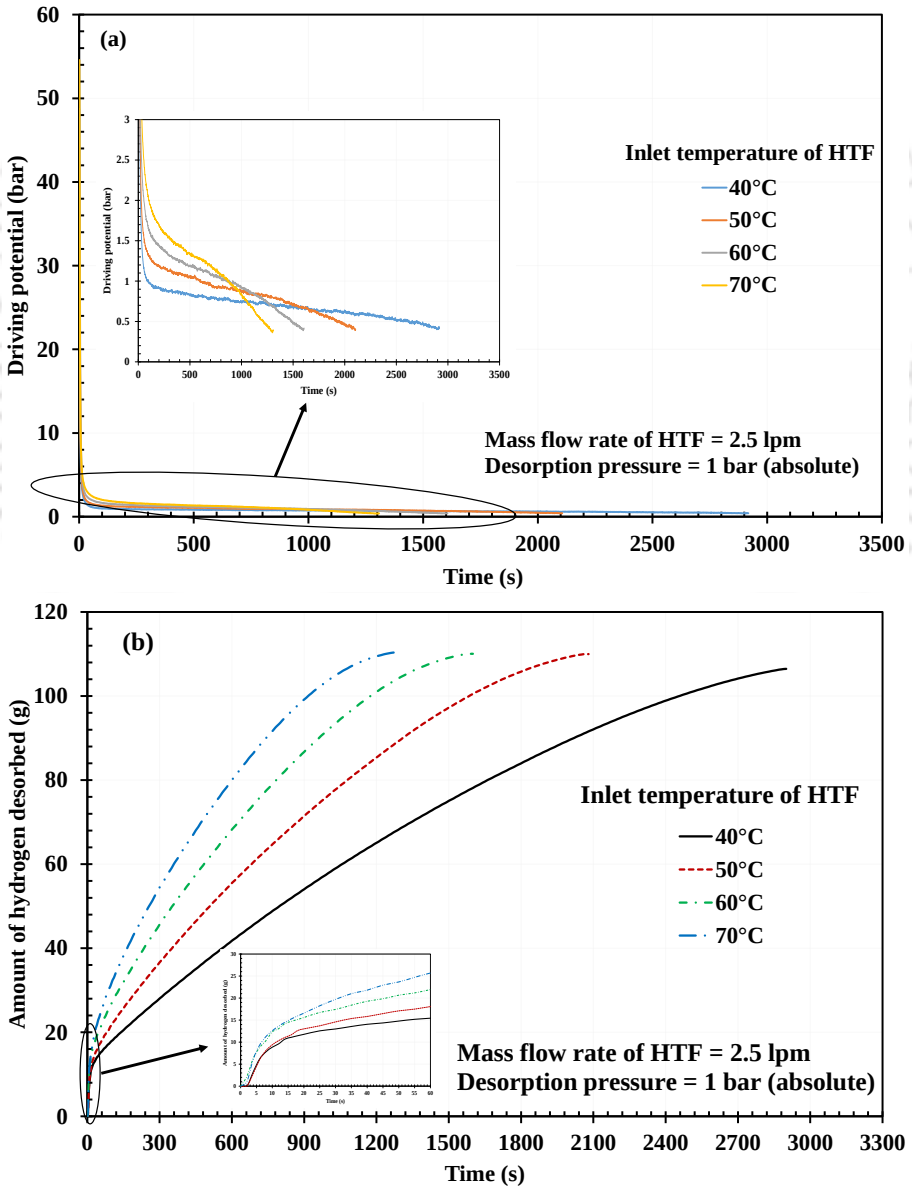

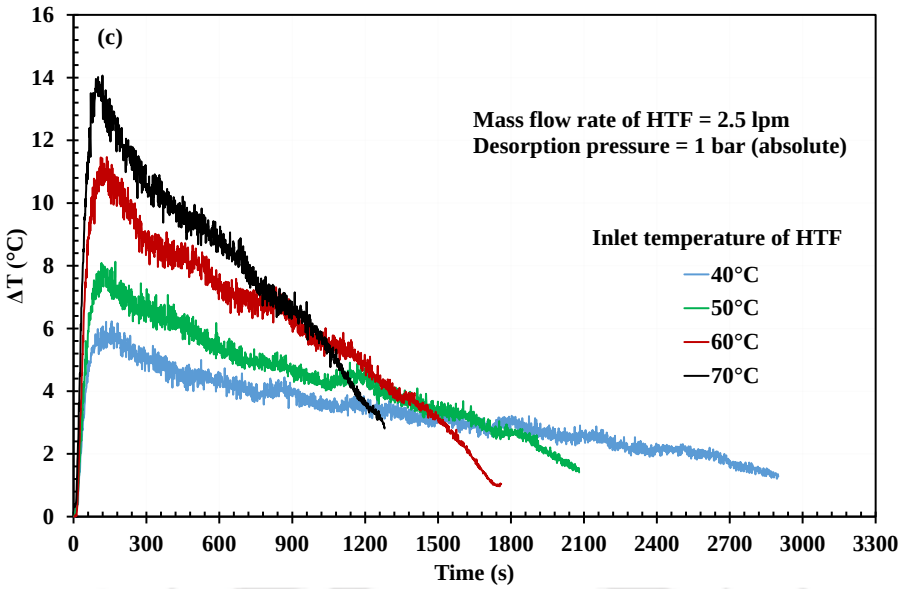

Fig. 5.9. Effect of inlet temperature of HTF on (a) driving potential, (b) mass of hydrogen desorbed and (c) temperature drop of the HTF

The amount of hydrogen desorbed for different inlet temperatures of the HTF is shown in Fig. 5.9b. During the initial stages of the reaction, the desorbed mass of hydrogen is very high due to the higher equilibrium pressure inside the reactor. The alloy desorbed 15.4, 18, 21.9, and 25.7 g during the first 60 s, respectively, for inlet temperatures of 40, 50, 60, and 70°C. The driving potential played a crucial role in improving the desorption rate in later stages, as shown in Fig. 5.9(a and b). The time to desorb 90% of the storage capacity (i.e., 104.5 g) was 2900, 1830, 1372, and 1075 s, respectively, for the inlet temperatures of 40, 50, 60, and 70°C. The percentage decrease in desorption time when the inlet temperature of HTF was raised from 40°C to 70°C is 62.9%. However, the degree of reduction in desorption time decreases with an increase in the inlet temperature of the HTF. It is also observed that the complete desorption of 111 g (i.e., all absorbed mass of hydrogen) was only achieved at 70°C. In contrast, the complete desorption was accomplished by intermediate sensible heating for the other inlet temperatures (Sunku Prasad et al., 2020).

The drop-in temperature of the HTF as it flows in the heat exchanger is shown in Fig. 5.9c. A higher drop was achieved for the higher inlet temperature of HTF due to the faster desorption rate. The maximum reduction in the temperature achieved was 6.2, 8.1, 11.5, and 14°C, respectively, for the inlet temperatures of 40, 50, 60, and 70°C.

The system gravimetric and volumetric storage densities of the developed MH hydrogen storage reactor are calculated. The calculated values of the system gravimetric and volumetric

storage densities of the developed MH reactor are 0.73% and 20.4 kg of H_2 per m^3, respectively. It should be noted that the storage mass of 111 g of hydrogen was adopted to calculate the storage densities, as the alloy absorbed/ desorbed 111 g (equivalent to 1.23 wt.%) of hydrogen after 20 cycles.

5.4.6 Comparison of the annular MH reactor with the literature

The current experimental results are compared with the literature to study the performance of the MH reactor in terms of absorption and desorption times. An embedded cooling tube reactor with an outer cooling jacket (Karmakar et al., 2021) is considered for comparison due to the same scale of alloy mass and alloy material. The operating conditions considered for the comparison study are presented in Table 5.3. The pictorial representation of the reactors and the results of the comparative study during absorption and desorption processes are shown in Fig. 5.10. The annular MH reactor equipped with internal radial fins showed a better performance than the embedded cooling tube reactor with an outer cooling jacket. The absorption comparison results (Fig. 5.10b) revealed that the time required to reach 1 wt.% was reduced by about 56% and 67%, respectively, for 10 and 20 bar supply pressure.

Moreover, the desorption time was reduced by about 44% and 58% for HTF inlet temperatures of 50 and 70°C (Fig. 5.10c). The performance improvement is due to the internal heat transfer enhancement provided by the radial fins. It is also observed that the percentage improvement is more significant at higher supply pressure (20 bar) and higher inlet temperature (70°C), indicating the radial fins are more effective under higher driving potential.

Further, better absorption and desorption rates were achieved in the annular MH reactor, operated at the HTF flow rate of 2.5 lpm instead of a very high flow rate of 20 lpm in the embedded cooling tube reactor with an outer cooling jacket. This is because the significant heat transfer constraint (low thermal conductivity of the MH bed) is imposed on the MH bedside than on the waterside. The MH bed thickness between the cooling surfaces is 11 mm and 21 mm, respectively, for the annular MH reactor and an embedded cooling tube reactor with an outer cooling jacket. Despite having a higher flow rate of HTF, the embedded cooling tube reactor with an outer cooling jacket showed poor reaction kinetics due to higher bed thickness. Further, the literature also reported that increasing the mass flow rate of HTF over a specific value will not significantly enhance the absorption and desorption rates. Therefore, the internal heat transfer enhancement of the MH bed is very much significant.

Table 5.3 Comparison of the present experimental results with Karmakar et al., (2021)

Author(s)	Alloy mass (kg)	Reactor details	Operating conditions
Present study	9	Annular MH reactor equipped with radial fins Weight ratio = 1.44 Working pressure = 80 bar *Heat transfer area: Tube area = 0.296 m^2 Finned area = 2×0.261 m^2	*Absorption:* Supply pressure = 10 and 20 bar HTF inlet temperature = 25°C HTF flow rate = 2.5 lpm Absorption time: 1020 s (10 bar) and 585 s (20 bar) *Desorption:* HTF inlet temperature = 50 and 70°C HTF Flow rate = 2.5 lpm Desorption time (for 1.02 wt.%): 1360 s (50°C) and 780 s (70°C)
Karmakar et al. (2021)	10	Embedded cooling tube (4 Nos.) reactor with an outer cooling jacket Weight ratio = ~1.1 Working pressure = 70 bar Heat transfer area = 0.202 m^2	*Absorption:* Supply pressure: 10 and 20 bar HTF inlet temperature = 25°C HTF flow rate = 20 lpm Absorption time (for 1.14 wt.%): 2272 s (10 bar) and 1663 s (20 bar) *Desorption:* HTF inlet temperature = 50 and 70°C HTF flow rate = 20 lpm Desorption time (for 1.02 wt.%): 2687 s (50°C) and 1835 s (70°C)

*heat transfer area is calculated based on the outer diameter

(a)

Annular porous MH reactor (present study)

Embedded cooling tube reactor with an outer cooling jacket (Karmakar et al. 2021)

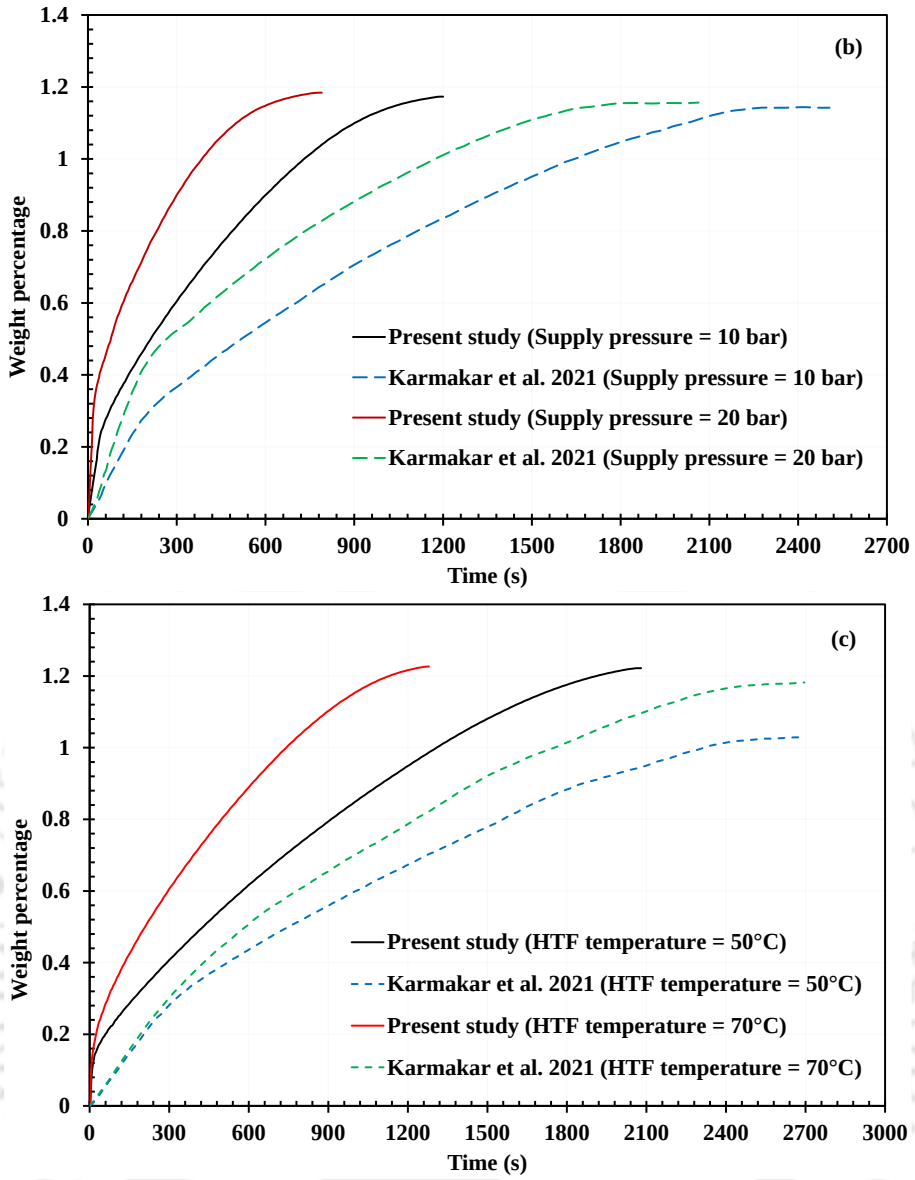

Fig. 5.10. Comparison of the present study results with Karmakar et al. (2021) (a) pictorial representation of the reactors, (b) weight percentage during absorption and (c) weight percentage during desorption

Next to enhanced absorption and desorption performances, the developed annular MH reactor offered a weight ratio of 1.44, which is much greater than the MH reactor designs available in the literature (Ahluwalia, 2007; Bürger et al., 2021; A. Kumar et al., 2019; Na Ranong et al., 2009). The higher weight ratio provides lower overall weight and lowers the sensible heat capacity of the reactor. Further, the annular MH reactor with internal heat transfer enhancement with radial fins requires a lower HTF flow rate, saving pumping power. Lastly, the developed annular MH reactor contains fewer welded joints than any embedded cooling tube reactor, facilitating fabrication ease.

5.5 Results and discussion: $La_{0.7}Ce_{0.1}Ca_{0.3}Ni_5$

The results obtained during the activation, absorption, and desorption processes of $La_{0.7}Ce_{0.1}Ca_{0.3}Ni_5$ are discussed in this section. The supply pressure was varied from 5 to 20 bar during the absorption process, while the HTF temperature was maintained at 25°C. The desorption behavior was studied by varying the HTF inlet temperature from 30 to 50°C while the hydrogen was discharged to a pressure of 1 bar (absolute). Further, the storage efficiency is evaluated for the developed hydrogen storage system. All the results reported for the absorption and desorption processes were obtained after 20 cycles. During activation, the alloy absorbed 1.54 wt%, but the storage capacity was dropped to 1.35 wt.% after 20 cycles.

5.5.1 Activation of $La_{0.7}Ce_{0.1}Ca_{0.3}Ni_5$

The activation of $La_{0.7}Ce_{0.1}Ca_{0.3}Ni_5$ was conducted at a supply pressure of 20 bar. Before the activation, the MH bed was heated to 80°C and evacuated down to a pressure of 10^{-5} bar to remove the traces of moisture and other foreign gases. The hydrogen absorbed during the activation cycles is shown in Fig. 5. 11. The alloy reached a maximum reversible storage capacity of 1.51 wt.% by absorbing 136.29 g in 1000 s during the third activation cycle, indicating completion.

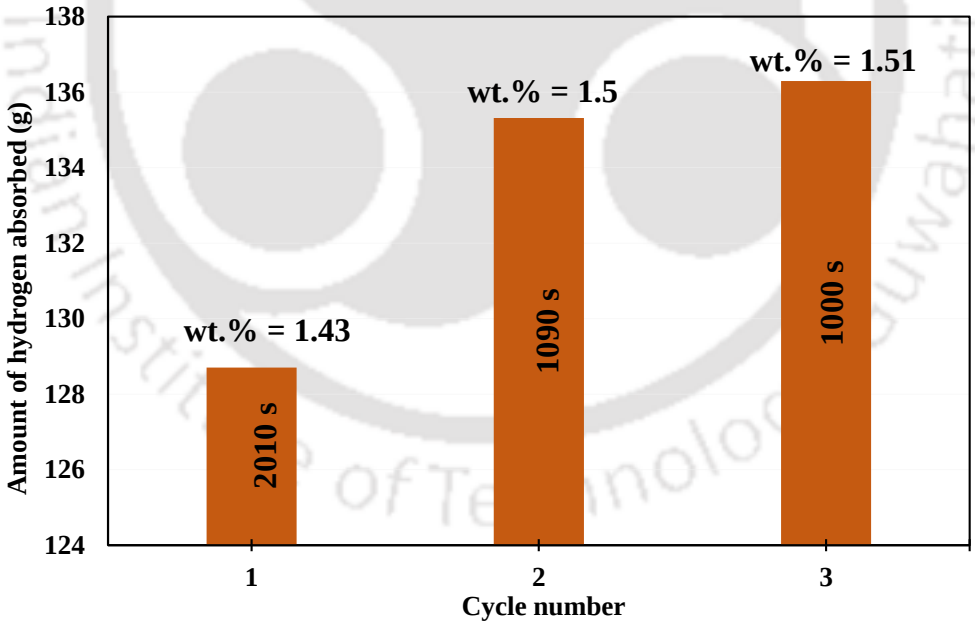

Fig. 5. 11. Amount of hydrogen absorbed during activation cycles

5.5.2 Absorption

The variations in MH bed temperature, HTF temperature, and mass of hydrogen absorbed are shown in Fig. 5.12 for different supply pressures. The supply pressure was varied from 5 bar

to 20 bar. The inlet temperature and mass flow rate of HTF were maintained at 25°C and 3.15 lpm, respectively. The initial temperature of the system was maintained at 25°C for all the absorption experiments.

Absorption is an exothermic reaction, and the MH bed releases the exothermic heat by absorbing the hydrogen supplied at the set pressure. The driving force for the reaction between hydrogen and the metal hydride bed is the difference between the supply and equilibrium pressure (often referred as driving potential). The supply pressure is fixed at a set value and equilibrium pressure increases with MH bed temperature (ideally depicted by the van't Hoff equation, i.e., inside the P-C-I dome). The faster absorption is achieved by maintaining a higher driving potential, which is possible by better thermal management of the MH bed. The temperature variations during the absorption process for different supply pressures are shown in Fig. 5.12(a-d). During the initial stages, the driving potential (supply pressure - equilibrium pressure at 25°C) is maximum and hence high hydrogen transfer rate. During this period, the temperature difference between the MH bed and the HTF is minimum (as the inlet temperature and initial temperature are the same) hence the heat transfer rate. Therefore, the high hydrogen transfer rate and minimum heat transfer rate cause the MH bed temperature to rise to a peak value. The increase in the bed temperature causes a decrease in the driving potential and an increase in the heat transfer rate between the HTF and MH bed. After this time, the heat transfer rate dominates the heat generation rate, due to which the MH bed temperature decreases to the inlet temperature of the HTF.

The location of the thermocouple showed a significant effect on the temperature recorded. The location of the thermocouples (TC1-TC4) is indicated in Fig. 5.3(b). The thermocouple TC1 experiences better cooling than the TC4 for apparent reasons. Hence, the temperature recorded by the TC1 is lower than TC4. From Fig. 5.12(a-d), it is observed that the peak temperatures recorded by TC4 in the MH bed for the supply pressure of 5, 10, 15, and 20 bar are 41.7, 61.8, 73.5, and 85°C, respectively. The inlet and outlet temperatures of the HTF are also shown in Fig. 5.12(a-d). It was observed that the HTF showed a maximum temperature gain (difference between outlet and inlet temperature of the HTF) of 4.2, 10.3, 14.6, and 15°C for the supply pressure of 5, 10, 15, and 20 bar, respectively. The amount of hydrogen absorbed for different supply pressures with time is shown in Fig. 5.12e. The MH bed absorbed 103, 114, 120, and 122 g in 2640, 1465, 1040, and 869 s for 5, 10, 15, and 20 bar supply pressure, respectively.

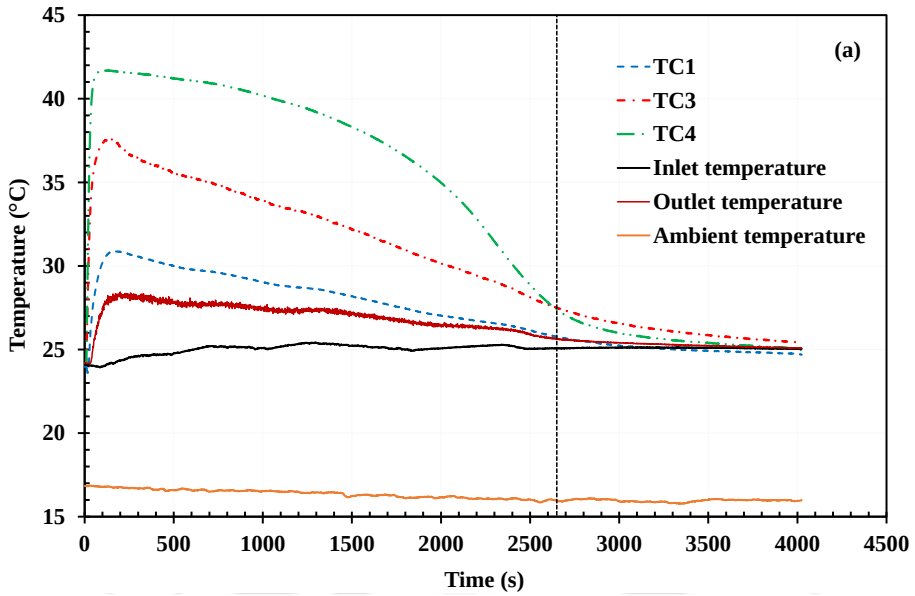

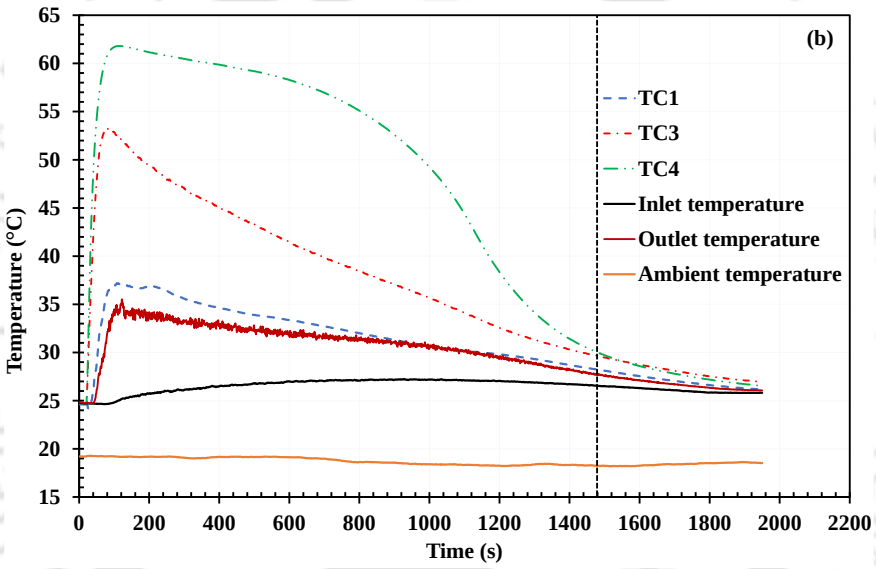

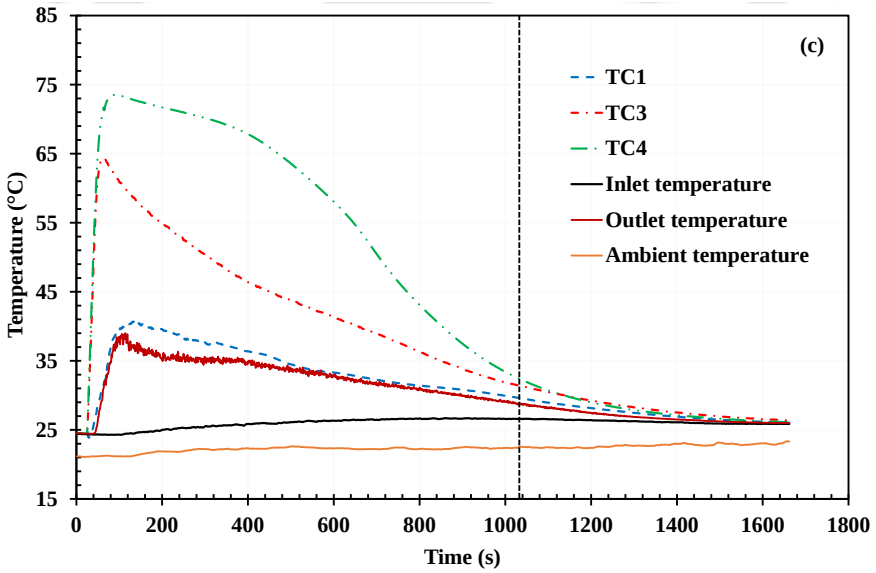

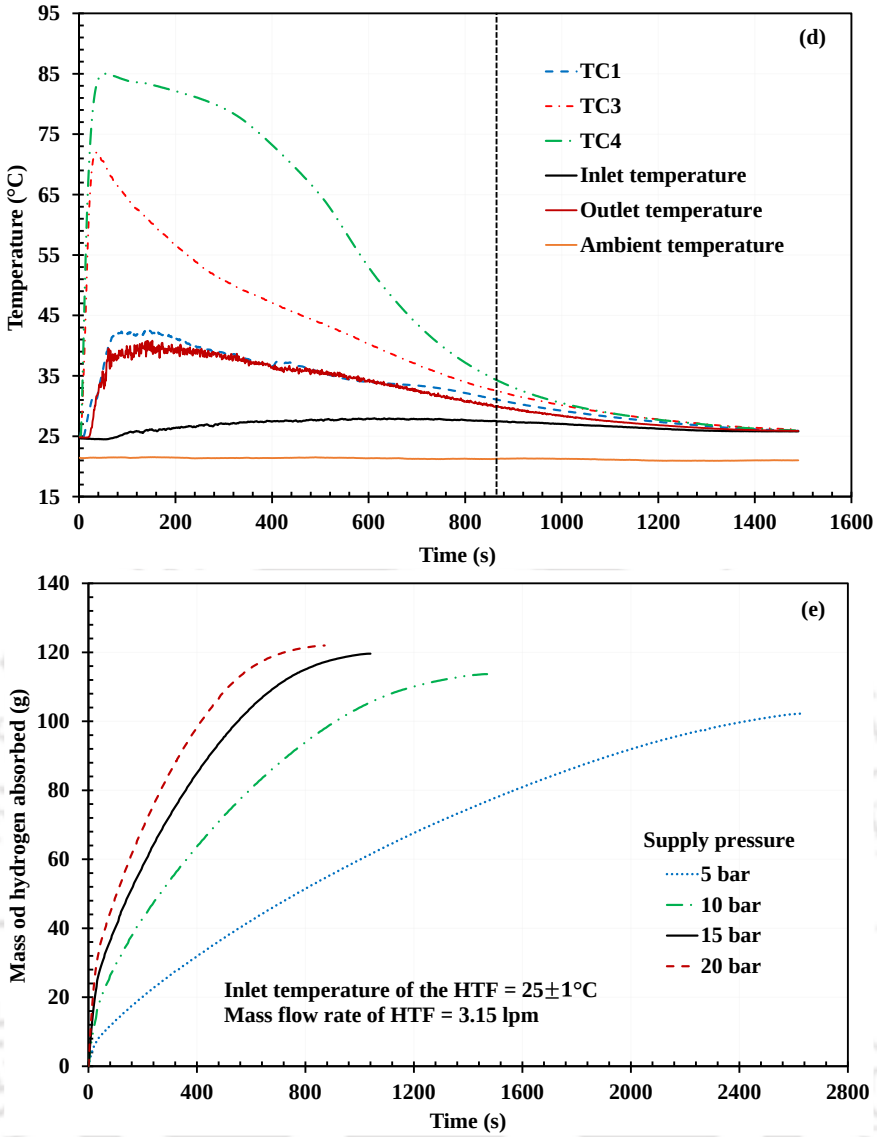

Fig. 5.12. Temperature variations during absorption process: (a) 5 bar (b) 10 bar (c) 15 bar (d) 20 bar and (e) amount of hydrogen absorbed

5.5.3 Desorption

Before all the desorption processes, the reactor was filled with 122 g of hydrogen at 20 bar supply pressure. The desorption process was carried out under different inlet temperatures of the HTF, namely, 30, 40 and 50°C. The flow rate was maintained at 3.25 lpm for all the desorption experiments. The initial temperature of the system was maintained at respective desorption temperatures.

Desorption is an endothermic process during which the MH bed releases hydrogen by absorbing heat. The driving potential is the difference between equilibrium and discharge pressure in desorption. The driving potential is higher for the higher desorption temperatures. The temperature variations during the desorption process for different inlet temperatures of the HTF

are shown in Fig. 5.13(a-c). Like absorption, the hydrogen transfer rate is high, and the heat transfer rate is low in the initial stages of the desorption. But the bed temperature decreases due to the rapid absorption of the endothermic heat from the MH bed itself during the initial stages of the reaction. After this time, the heat transfer rate into the MH bed dominates the endothermic heat absorption rate and the MH bed temperature increases to the inlet temperature of the HTF.

From Fig. 5.13(a-c), it is observed that the bed temperature recorded by TC4 was dropped to 16.2, 23.2, and 28°C for 30, 40, and 50°C inlet temperatures, respectively. The inlet and outlet temperatures of the HTF are also shown in Fig. 5.13(a-c). It was observed that the HTF showed a maximum temperature drop (difference between inlet and outlet temperature of the HTF) of 2.6, 3.8, and 5.5°C for the inlet temperatures of 30, 40, and 50°C, respectively. The amount of hydrogen desorbed for different inlet temperatures of the HTF with time is shown in Fig. 5.13d. The MH bed desorbed 109.24, 118.7, and 120.7 g in 4328, 3112, and 2220 s for 30, 40, and 50°C inlet temperature.

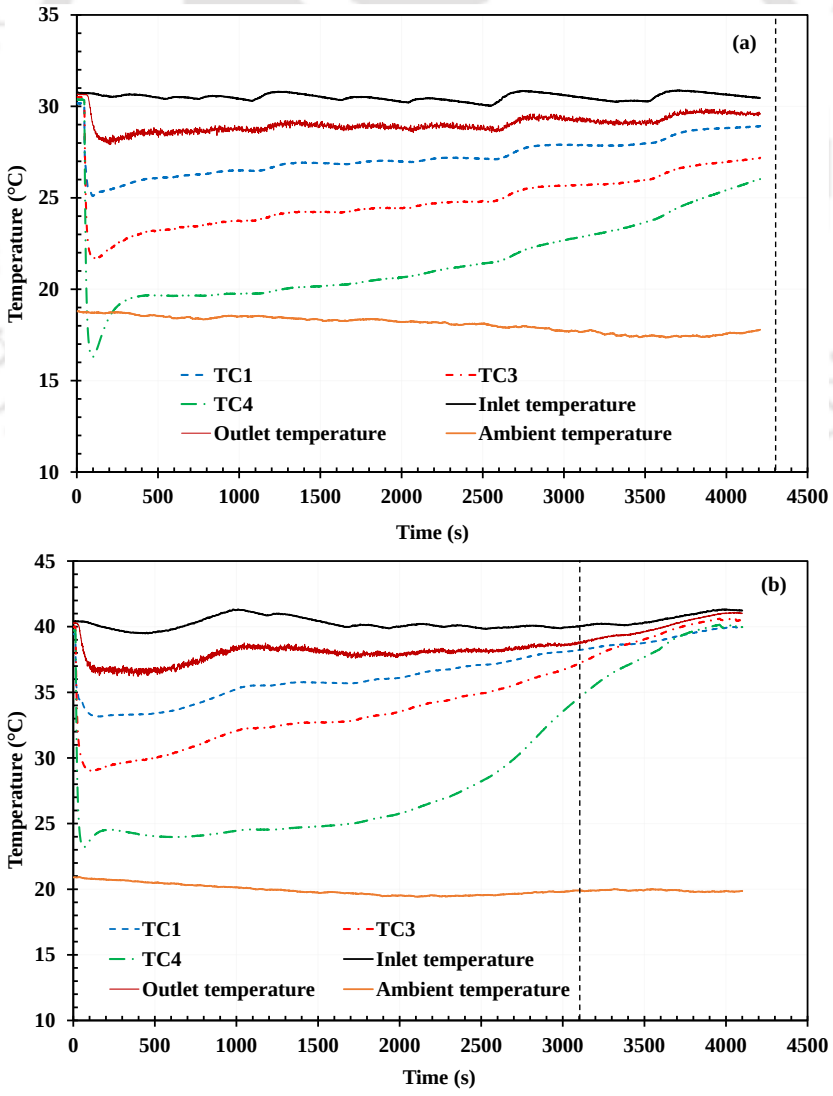

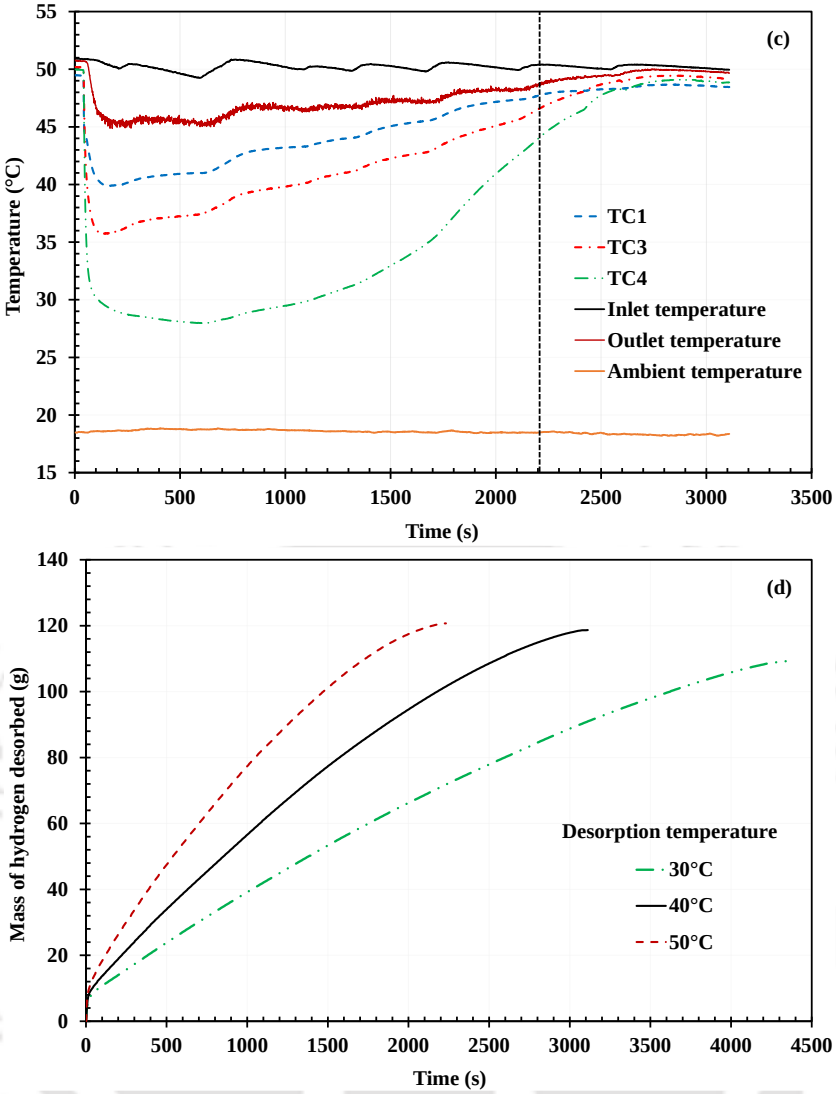

Fig. 5.13. Temperature variations during desorption process: (a) 30°C (b) 40°C (c) 50°C; (d) amount of hydrogen desorbed

5.5.4 System-level storage density

The developed hydrogen storage device's system-level gravimetric and volumetric storage densities are calculated as 0.8% and 22.4 kg of H_2 per m^3, respectively. The storage mass of 122 g was adopted to calculate the storage densities, as the alloy absorbed/ desorbed 122 g of hydrogen after 20 cycles, equivalent to 1.35 wt.%.

5.5.5 Energy efficiency of $La_{0.7}Ce_{0.1}Ca_{0.3}Ni_5$

Energy efficiency for the MH hydrogen storage system is calculated by using Eq. (5.1–5.4), which was defined by Liu et al., (2021). The energy efficiency was determined by considering the required heat input during desorption, cooling during absorption, and pumping power for circulating heat transfer fluid. Liu et al., (2021) used reaction enthalpies calculated from the P-

C-I curves to evaluate the released exothermic heat and the supplied endothermic heat. In the present work, the same quantities are obtained using the heat gained or lost by HTF, as shown in Eq. (5.1–5.4). The heat loss to/ from the reactor is not considered during the energy efficiency calculation. The energy efficiency helps to compare the MH-based hydrogen storage technology with other hydrogen storage technologies in terms of energy consumption. Also, it helps to evaluate the overall efficiency of the hydrogen economy.

$$\begin{aligned}
&Energy\,efficiency = \eta = 1 - \frac{E_t}{E_c} \\
&E_t = \text{total energy consumed to power the MH tank} \\
&E_t = E_1 + E_2 + E_3 \\
&E_c = \text{heat of combustion of the total hydrogen stored in the MH tank} \\
&E_c = \Delta H_c n_{H_2}; \Delta H_c = 285.6 kJ \cdot mol^{-1} \left(higher\,heating\,value\right)
\end{aligned} \tag{5.1}$$

E_1 = energy consumed to remove reaction heat during absorption

$$E_1 = \Delta H_{abs} n_{H_2} + \left(P_{pump} \times t_a\right)_{HTF} = \int_o^{t_a} \dot{m}_w C_{pw} \left(T_{out} - T_{in}\right) dt + \left(P_{pump} \times t_a\right)_{HTF} \tag{5.2}$$

E_2 = energy consumed for sensible heating of the whole reactor before the start of desorption

$$E_2 = \left(mC_p \Delta T\right)_{alloy} + \left(mC_p \Delta T\right)_{reactor} + \left(mC_p \Delta T\right)_{hydrogen} = \int_o^{t} \dot{m}_w C_{pw} \left(T_{out} - T_{in}\right) dt \tag{5.3}$$

E_3 = energy consumed to supply reaction heat during desorption

$$E_3 = \Delta H_{des} n_{H_2} + \left(P_{pump} \times t_d\right)_{HTF} = \int_0^{t_d} \dot{m}_w C_{pw} \left(T_{in} - T_{out}\right) dt + \left(P_{pump} \times t_d\right)_{HTF} \tag{5.4}$$

The density and specific heat variation of water with temperature are as follows:

$$C_p = 12010.1471 - 80.4072879 \times T^1 + 0.309866854 \times T^2 - 5.38186884E-4 \times T^3 + 3.62536437E-7 \times T^4$$

$$\rho = 838.466135 + 1.40050603 \times T^1 - 0.0030112376 \times T^2 + 3.71822313E-7 \times T^3$$

Uncertainty in the experimental result is estimated by root-sum-square method (Moffat, 1988), given by the following equation.

$$\delta_R = \left[\left(\frac{\partial R}{\partial x_1}\delta x_1\right)^2 + \left(\frac{\partial R}{\partial x_2}\delta x_2\right)^2 + \cdots\cdots\cdots\cdots + \left(\frac{\partial R}{\partial x_n}\delta x_n\right)^2\right]^{\frac{1}{2}} \tag{5.5}$$

Where, x_1, x_2…..x_n are the independent variables, $\delta x_1, \delta x_2, \ldots\ldots\ldots \delta x_n$ are the uncertainties in the independent variables, and δ_R is the uncertainty in the result. The uncertainties in temperature, mass flow rate of hydrogen, and mass flow rate of HTF measurements are ±0.5 ºC, ±0.25% of the rate and ±0.5% of the rate, respectively. The uncertainty in energy efficiency is estimated as 8.2%.

The operating conditions considered for the calculation of the storage efficiency are shown in Table 5.4. The supply pressure of 20 bar and desorption temperature of 50°C is considered due to the complete hydrogen transfer under these conditions. The heat transfer rate and pumping power consumed during absorption, sensible heating, and desorption processes are shown in Fig. 5.14.

Table 5.4 Absorption and desorption conditions considered for efficiency calculation

Absorption conditions	Desorption conditions	Energy efficiency
Supply pressure = 20 bar Inlet temperature of HTF = 26°C Initial temperature of reactor = 26°C HTF flow rate = 3.15 lpm Pumping power = 5.3 W (6.8 V and 0.78A) Charging time = 1490 s Mass of hydrogen absorbed = 121.96 g	Inlet temperature of HTF = 50°C Initial temperature of reactor = 25°C HTF flow rate = 3.25 lpm Pumping power = 5.3 W (6.8 V and 0.78A) Discharging time = 3108 s Mass of hydrogen desorbed = 120.7 g	76.76%

A peak heat transfer rate of 3180.6 W was observed during absorption under the supply pressure of 20 bar. The total thermal energy transferred from MH bed to HTF was 1602.7 kJ (area A_1) during absorption. After the absorption process, the reactor was heated to 50°C from 25°C, i.e., sensible heating process. The reactor consumed 565 kJ (area A_2) of thermal energy during the sensible heating process. Desorption was followed after the sensible heating process and a peak power of 1253.5 W was observed during the desorption process. Also, desorption at 50°C was slower than the absorption at 20 bar supply pressure. Hence, desorption took 3108 s, whereas absorption was completed in 1490 s. During desorption, the total thermal energy transferred from HTF to the MH bed was 1798.1 kJ (area A_3). The energy supplied during desorption was higher than the energy released during the absorption process because the desorption enthalpy was greater than the absorption enthalpy. Approximately sixty moles of hydrogen were absorbed and desorbed. From Fig. 5.14, the energy efficiency was calculated as 76.76%. The energy efficiency of 76.76% signifies that 23.24% of the HHV of hydrogen was utilized in operating the developed hydrogen storage system. The results show that 39.83 kJ/mol of energy was needed at 50°C for $La_{0.7}Ce_{0.1}Ca_{0.3}Ni_5$ based hydrogen storage device during sensible heating and desorption processes. The required energy constitutes only 35% of the exhaust heat available in a 60% efficient fuel cell. During absorption, around 26.45 kJ/mol of cooling energy was needed at 25°C.

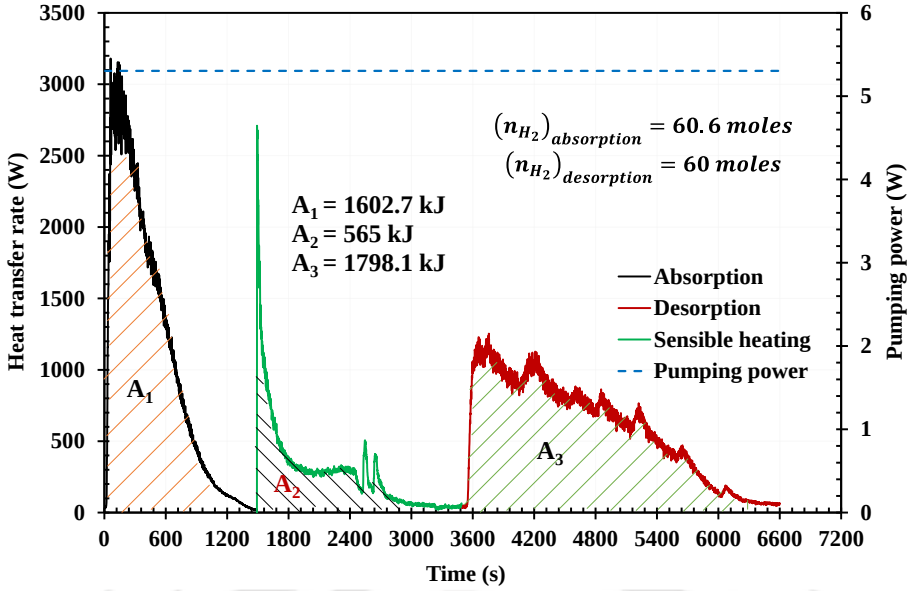

Fig. 5.14. The heat transfer rate and the pumping power during absorption, sensible heating and desorption

5.5.6 Desorption without pre-sensible heating

Desorption was performed without preheating the MH reactor to the set desorption temperature. The reactor was filled with 122 g of hydrogen at 20 bar supply pressure and 25°C inlet temperature before desorption without pre-sensible heating. After that, the desorption was started by circulating the HTF in the MH reactor. During this process, the initial temperature of the MH bed was maintained at 25°C and the HTF was circulated at an average temperature of 50°C.

The temperature variations during the desorption without pre-sensible heating are shown in Fig. 5.15a. Initially, the whole reactor was maintained at 25°C. In this experiment, the inlet temperature of the HTF was not constant at 50°C. However, the time-averaged inlet temperature of the HTF was 50°C with maximum and minimum values at 53.1°C and 43°C, respectively. Unlike the temperature profiles shown in Fig. 5.13, the MH bed temperature was not dropped much for the case of desorption without pre-sensible heating. The significant temperature difference (around 20°C) between the MH bed and the HTF during the initial stages caused high heat transfer rates (Fig. 5.15c). Due to this, the HTF supplied the required endothermic heat for desorbing the hydrogen. Therefore, a sudden drop in the MH bed temperature was not observed here. For the desorption with the pre-sensible heating, the initial temperature difference between the HTF and MH bed was zero hence the heat transfer rate. Therefore, the required endothermic heat for desorbing the hydrogen was taken from the MH bed itself, due to which there was a sudden drop in the MH bed temperature (Fig. 5.14). In the

later stages of the desorption without pre-sensible heating, the temperature of the MH bed continuously raised to the inlet temperature of the HTF, which indicates that the sensible heating of the MH bed and desorption of hydrogen from the MH bed happened simultaneously. Fig. 5.15b shows the comparison of the desorbed mass of the hydrogen between desorption with and without pre-sensible heating. Pre-sensible heating showed a higher rate of desorption during the initial stages. This is due to the higher equilibrium pressure at the set temperature of 50°C during the initial stages. Whereas the desorption without pre-sensible heating process exhibited slower desorption rates during the initial phase as the temperature of the MH bed started from 25°C. During later stages, the desorption rate for the case without pre-sensible heating increased due to a rise in the MH bed temperature. An amount of 120.46 g of hydrogen was desorbed in 2290 s for the case of desorption without pre-sensible heating, whereas the same for desorption with pre-sensible heating was 120.68 g in 2220 s. There was not much difference in the final desorption time between the two cases.

The heat transfer rate and pumping power during the desorption without pre-sensible heating process are shown in Fig. 5.15c. Peak power of 3812.4 W was achieved higher than the absorption process reported in Fig. 5.14. This higher peak power is due to the larger temperature difference between MH bed and HTF. The energy transfer between the HTF and MH bed continued until 2730 s. From Fig. 5.14, it was observed that the time taken for sensible heating and desorption was 5108 s. The total thermal energy transferred from HTF to the MH bed was 2227 kJ during desorption without pre-sensible heating (Fig. 5.15c); the same for desorption with pre-sensible heating was 2363.1 kJ (Fig. 5.14). There was a 5.7% deviation between the two cases in the supplied energy. This deviation is attributed to heat loss incurred during the sensible heating period, measurement uncertainty, minor variations in the temperatures (inlet, outlet, initial, and final temperatures) during the experiment. Hence, desorption without pre-sensible heating is an efficient process as it takes less overall time to transfer the same amount of energy to the MH bed. The overall time of desorption without pre-sensible heating was reduced by 46.5% compared with pre-sensible heating.

The energy efficiency for the desorption without a pre-sensible heating case was calculated as 77.54%. There was no significant improvement in the energy efficiency as the alloy's exothermic and endothermic heat requirement is the same irrespective of the operating conditions. There was a 58.6% reduction in pumping power in the case of desorption without pre-sensible heating. However, this does not affect energy efficiency due to the significantly lesser magnitude of the pumping power than the reaction heat supply rate.

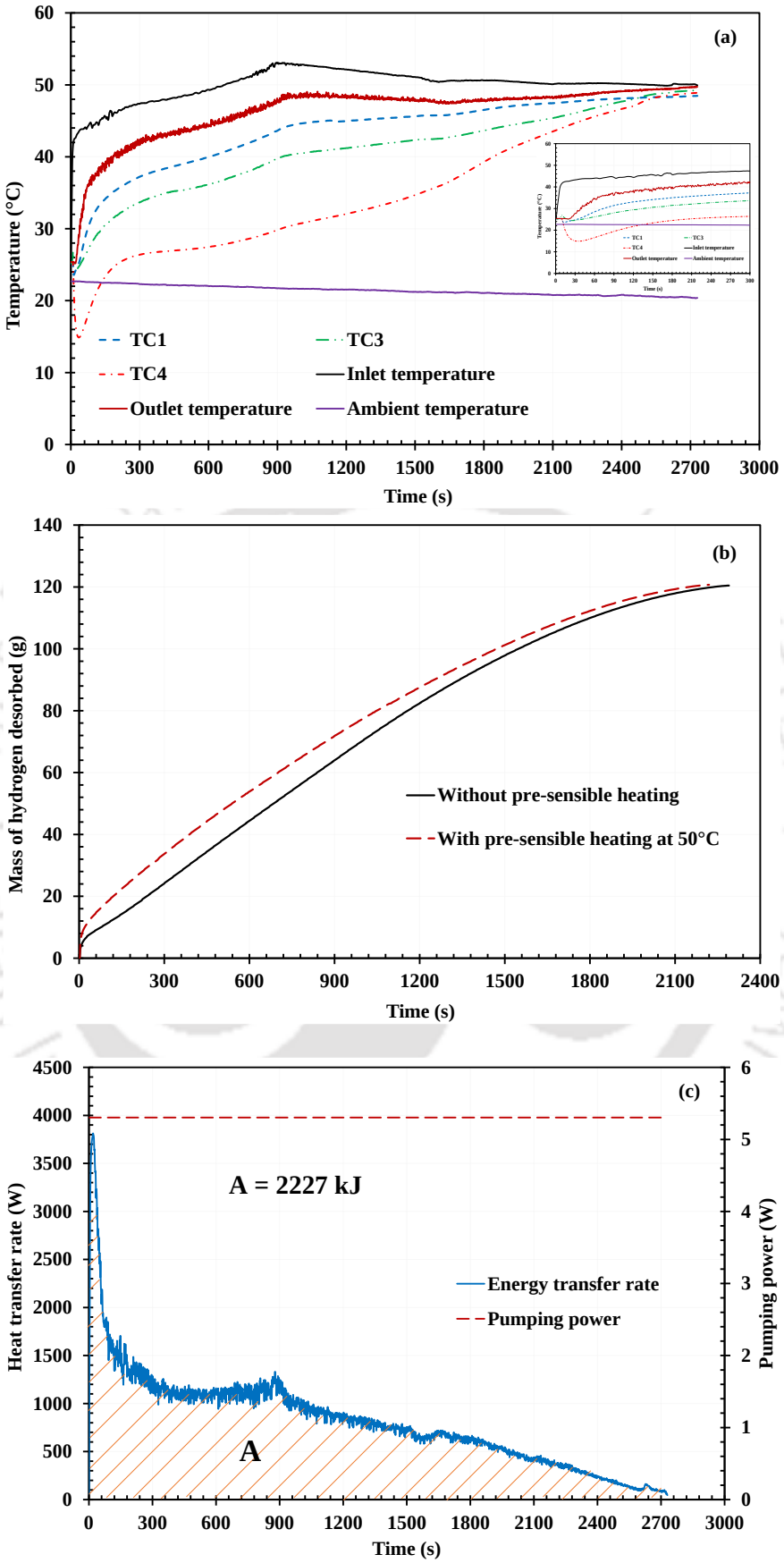

Fig. 5.15. Desorption results without pre-sensible heating (a) temperature variations (b) mass of hydrogen desorbed and (c) heat transfer rate and the pumping power

5.5.7 Comparison between $La_{0.7}Ce_{0.1}Ca_{0.3}Ni_5$ and $LaNi_5$

The absorption and desorption results of $La_{0.7}Ce_{0.1}Ca_{0.3}Ni_5$ were compared with $LaNi_5$ under similar operating conditions. The reason for selecting $LaNi_5$ is due to the availability of extensive studies on this AB_5-type alloy. Pressure-composition-isotherms of $La_{0.7}Ce_{0.1}Ca_{0.3}Ni_5$ and $LaNi_5$ are shown in Fig. 5.2. From P-C-I characteristics (Fig. 5.2), it is observed that the absorption equilibrium pressure at 25°C for $La_{0.7}Ce_{0.1}Ca_{0.3}Ni_5$ and $LaNi_5$ is 3 bar and 2.2 bar, respectively. As far as the equilibrium pressures are concerned, there is no significant difference between these alloys at 25 and 45°C. However, the reversible storage capacity of $La_{0.7}Ce_{0.1}Ca_{0.3}Ni_5$ is higher than $LaNi_5$. The MH bed temperature and amount of hydrogen absorbed/ desorbed are compared and shown in Fig. 5.16. The MH bed temperature recorded by the thermocouple TC3 is plotted in Fig. 5.16 for $La_{0.7}Ce_{0.1}Ca_{0.3}Ni_5$ (location of TC3: D = 21 mm and L = 515 mm) and $LaNi_5$ (location of TC3: D = 18 mm and L = 515 mm). From Fig. 5.16(a and c), it is observed that the temperature profiles of $La_{0.7}Ce_{0.1}Ca_{0.3}Ni_5$ and $LaNi_5$ are significantly different from each other. This is because the thermocouple TC3 of $La_{0.7}Ce_{0.1}Ca_{0.3}Ni_5$ has experienced better heating/ cooling as it is nearer to the inner cooling tube than $LaNi_5$. Another possible reason for the deviation in temperature profiles is the higher reaction enthalpy of $LaNi_5$ (~29.08 kJ/mol during absorption and ~34.09 kJ/mol during desorption) (Pęska et al., 2020) than $La_{0.7}Ce_{0.1}Ca_{0.3}Ni_5$ (~26.5 kJ/mol during absorption and ~30 kJ/mol during desorption).

From Fig. 5.16(b and d), it is observed that the storage capacity of $La_{0.7}Ce_{0.1}Ca_{0.3}Ni_5$ is 1.34 wt.%, whereas the same is 1.18 wt.% for $LaNi_5$. Unlike the temperature profiles, the overall deviation in the rate curves of $La_{0.7}Ce_{0.1}Ca_{0.3}Ni_5$ and $LaNi_5$ is minimal during absorption and desorption processes, except that $La_{0.7}Ce_{0.1}Ca_{0.3}Ni_5$ has a higher storage capacity than $LaNi_5$. This is due to the fact that the rate curves are influenced by the combined effect of P-C-I characteristics, reaction rate constants, reaction enthalpy, and heat management system (i.e., reactor design). It should be noted that the accuracy of the measurements carried out during the experiments also might have some influence in the deviation between the alloys. As per the storage capacity is concerned, $La_{0.7}Ce_{0.1}Ca_{0.3}Ni_5$ is a better choice for hydrogen storage applications than $LaNi_5$.

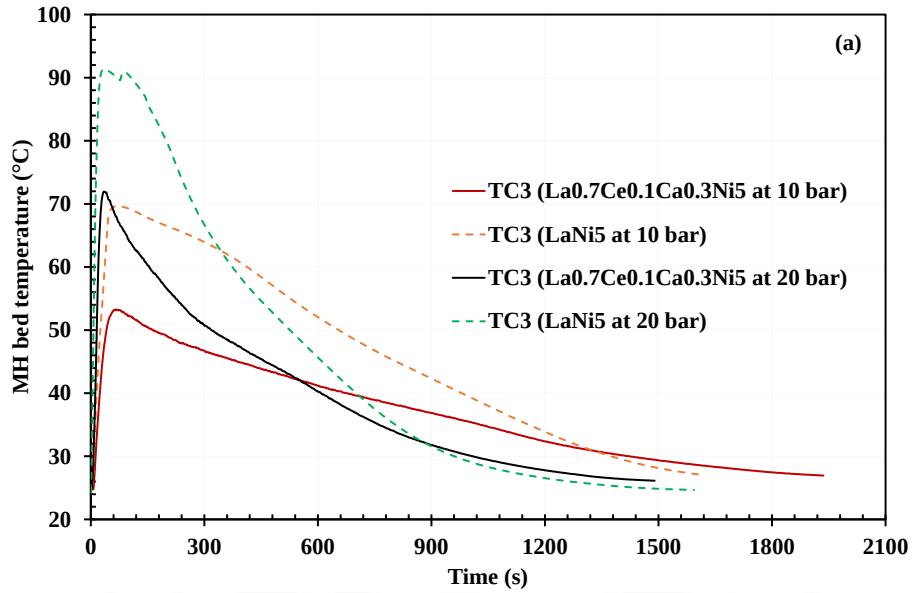

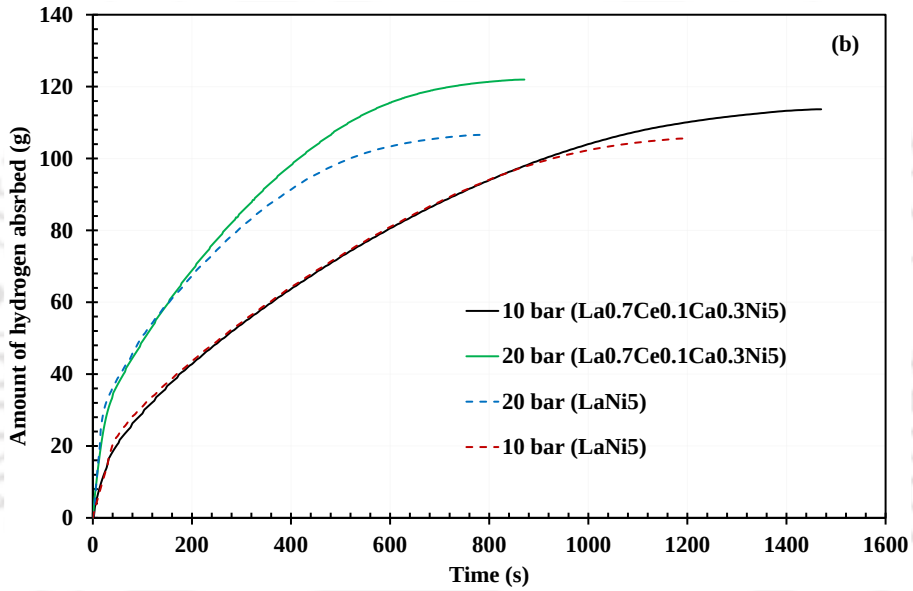

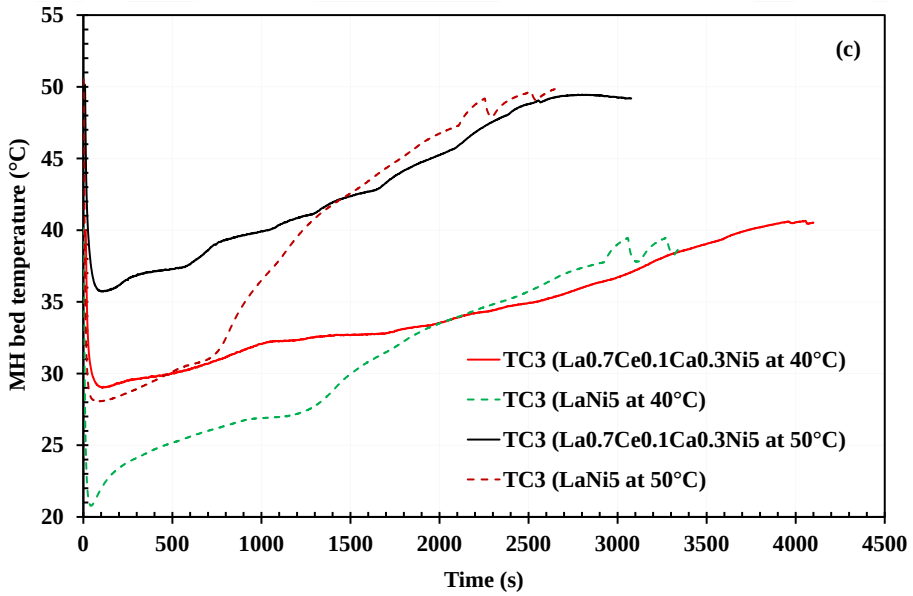

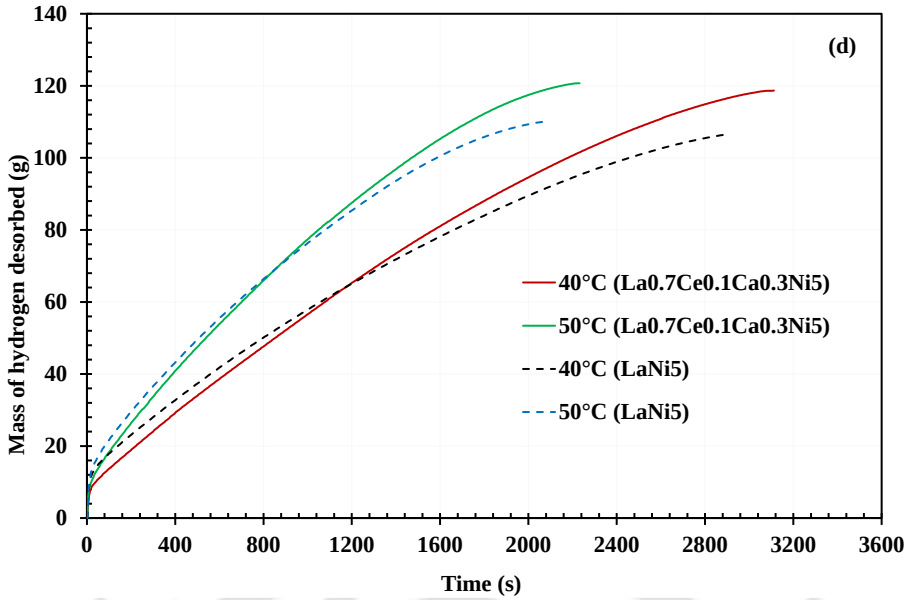

Fig. 5.16. Comparison between $La_{0.7}Ce_{0.1}Ca_{0.3}Ni_5$ and $LaNi_5$ (a) MH bed temperature during absorption, (b) amount of hydrogen absorbed, (c) MH bed temperature during desorption, and (d) amount of hydrogen desorbed

5.6 Summary

An annular metal hydride reactor equipped with internal radial fins was fabricated. The absorption and desorption characteristics of $LaNi_5$ and $La_{0.7}Ce_{0.1}Ca_{0.3}Ni_5$ were studied under different operating conditions. An alloy mass of 9 kg was filled inside the reactor for each alloy. The developed MH reactor offered a hydride to reactor mass ratio of 1.44 with a working pressure of 80 bar. Further, the results of $LaNi_5$ were compared with the published results for an embedded cooling tube reactor with an outer cooling jacket. Also, the energy efficiency of the solid-state hydrogen storage with $La_{0.7}Ce_{0.1}Ca_{0.3}Ni_5$ was evaluated. Finally, the results of were $LaNi_5$ and $La_{0.7}Ce_{0.1}Ca_{0.3}Ni_5$ were compared. The following are the major observations found from the experimental study.

5.6.1 $LaNi_5$ reactor

- System gravimetric and volumetric storage densities of 0.73% and 20.4 kg of H_2 per m^3, respectively, were achieved.
- From sensitivity analysis, it was observed that the supply pressure has a significant effect on the absorption performance than the inlet temperature of the HTF. The desorption time was reduced by 62.9% when the inlet temperature of HTF was raised from 40°C to 70°C, with complete desorption obtained at 70°C.

- With the help of an annular MH reactor with internal radial fins, the absorption/ desorption times were reduced by at least 44% than the ECT reactor with outer cooling jacket reported in the literature (Karmakar et al., 2021). This comparative study found that the internal heat transfer enhancement of the MH bed is beneficial in the improvement of absorption and desorption performance.
- The comparison results also revealed better absorption and desorption rates with a lesser HTF flow rate when the internal heat transfer enhancement is provided, which saves the pumping power.

5.6.2 $La_{0.7}Ce_{0.1}Ca_{0.3}Ni_5$ reactor

- During activation, $La_{0.7}Ce_{0.1}Ca_{0.3}Ni_5$ absorbed 136.29 g of hydrogen in the third cycle, reaching a weight percentage of 1.51 under the supply pressure of 20 bar. After 20 cycles, the storage capacity was dropped to 1.34 wt.% from 1.51 wt.%.
- The developed hydrogen storage system offered a system-level gravimetric storage density of 0.8% and a volumetric storage density of 22.4 kg of H_2 per m^3.
- The developed hydrogen storage system offered an energy storage efficiency of 77.54%.
- The desorption process without pre-sensible heating was found to be more efficient. The overall desorption time and pumping power were reduced by 46.5% and 58.6%, respectively, with desorption without pre-sensible heating.
- $La_{0.7}Ce_{0.1}Ca_{0.3}Ni_5$ exhibited higher storage capacity and steady desorption rates than $LaNi_5$.

The annular MH reactor with internal radial fins is a promising option for medium to large-scale hydrogen storage applications due to its higher weight ratio, ease of fabrication, saving in pumping power, and better performance.

Chapter 6

Experimental studies: HTMH reactor

6.1 Preface

This chapter presents details of the experimental setup, procedure, and results of the high-temperature MH reactor for TCES application. The annular MH reactor with radial fins is used as an energy storage module. Magnesium-nickel alloy is studied under different operating conditions for TCES application. Air is used as an HTF for supplying/ removing the energy to/ from the energy storage module during charging and discharging. The developed MH-based TCES system is operated in the temperature range of 250-400°C. The temperature variations inside the MH bed, and the amount of hydrogen absorbed and desorbed during the charging (desorption) and discharging (absorption) processes are presented. Further, the performance of the coupled MH reactor system with magnesium-nickel alloy as HTMH and $LaNi_5$ and $La_{0.7}Ce_{0.1}Ca_{0.3}Ni_5$ as LTMHs is studied. The alloy pairs magnesium-nickel alloy/$LaNi_5$ and magnesium-nickel alloy/$La_{0.7}Ce_{0.1}Ca_{0.3}Ni_5$ are experimented in coupled reactor mode. The results of the coupled reactor are presented. Finally, the major conclusions of the experimental study are summarized.

6.2 Details of the HTMH reactor

The annular MH reactor with radial fins described in chapter 3 is fabricated for experimenting the TES behavior of the magnesium-nickel alloy. A 3D sectional view, a 2D sectional view, and the energy storage module photograph are shown in Fig. 6.1(a). The reactor is made up of two concentric tubes of SS316 material. The Mg_2Ni powder is filled inside the annular space between the inner and the outer cooling tubes. HTF (Air) is passed through the inner cooling tube and over the outer cooling tube during absorption/ desorption. A hydrogen supply tube and a sintered porous filter are attached to the left end of the reactor to facilitate the supply/ discharge of hydrogen gas to/ from the energy storage module. Further, heat transfer effectiveness is increased by providing perforated radial fins over the inner cooling tube within the MH bed.

The 2D sectional view of the reactor with the dimensions indicated is shown in Fig. 6.1(b). The energy storage module is designed for a maximum working pressure of 60 bar at 400°C. A sintered porous filter made of SS316 (Outer diameter: 12 mm; length: 100 mm; pore size: 2 µm) is used for separating the MH powder particles and hydrogen gas. The dimensions of the seamless tubes used for the fabrication of the reactor are the same as the one presented in Chapter 5. Ninety-one perforated radial fins of 0.6 mm thick are placed inside the MH powder for heat transfer enhancement. The fins are made of aluminum and attached to the inner tube using the press-fit method.

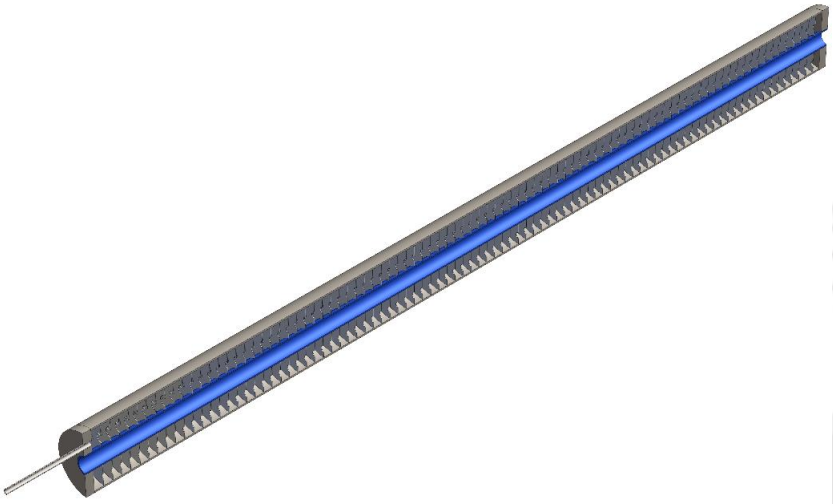

(a)

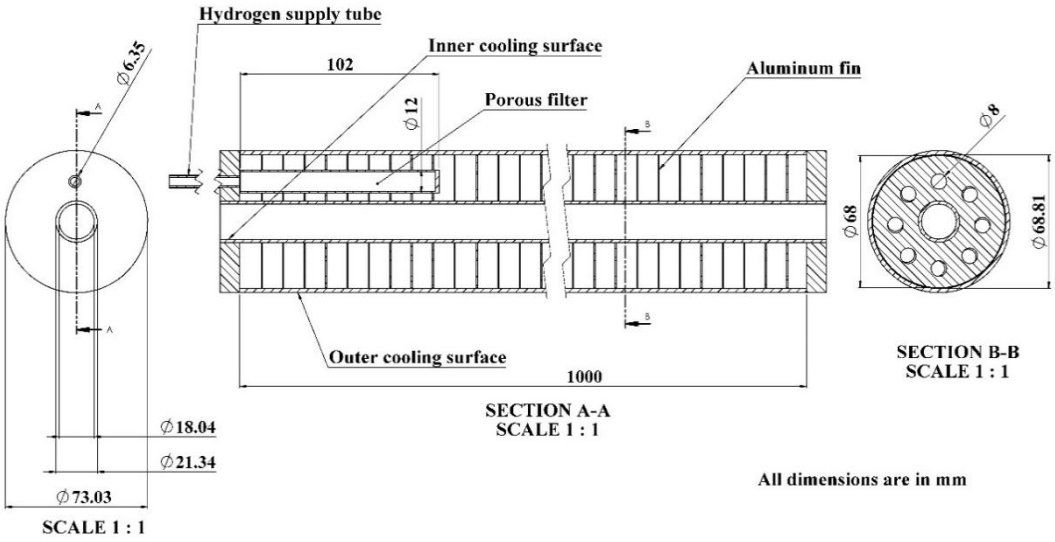

(b)

(c)

Fig. 6.1. (a) 3D sectional view of energy storage module (b) 2D sectional view of energy storage module with dimensions (thermocouple ports are not shown) and (c) photograph of the fabricated energy storage module

The magnesium-nickel alloy was supplied by Energy storage laboratory, Interdisciplinary Centre for Energy Research, IISC Bangalore. P-C-I characterisation of magnesium-nickel alloy was conducted at Thermal Engineering Laboratory, Department of Mechanical Engineering, IIT Tirupati. The P-C-I characteristics of magnesium-nickel alloy are shown in Fig. 6.2. It is observed that the maximum hydrogen storage capacity of the magnesium-nickel alloy is up to 5 wt.%. The alloy exhibited double plateau behavior. Mg_2Ni selected for numerical studies in Chapter 3 is pure and exhibits single plateau P-C-I characteristics. In contrast, the alloy obtained for experiments showed double plateau behavior. The theoretical composition to form pure Mg_2Ni is 45.3 wt % Mg and 54.7 wt % Ni. However, the presence of magnesium in excess of the theoretical composition resulted in a double plateau (Reilly and Wiswall, 1968b). From Fig. 6.2, it is also observed that the maximum hydrogen storage capacity of magnesium-nickel alloy decreased with the decrease of temperature due to incomplete hydrogenation due to kinetic limitations at the lower temperatures.Therefore, the experimental results obtained in this chapter cannot be directly compared with those presented in Chapter 3. Further, the present experiments are carried out with air as an HTF, whereas the results of Chapter 3 were obtained for Therminol-VP1 as the HTF.

The MH powder is filled through the thermocouple ports. During filling, the reactor is shaken at regular intervals to ensure uniform distribution of the powder. The energy storage module is filled with 3.76 kg of magnesium-nickel alloy powder.

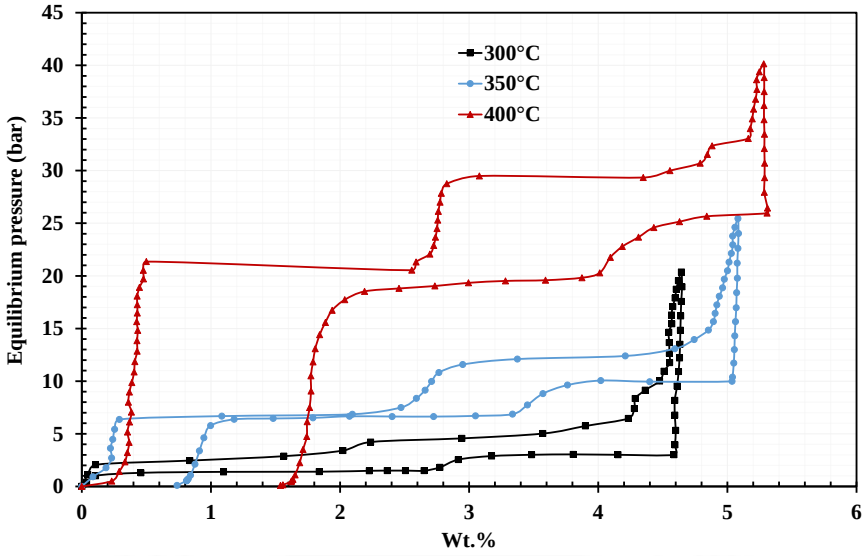

Fig. 6.2. P-C-I characteristics of the magnesium-nickel alloy

6.3 Experiments of HTMH reactor

6.3.1 Description of the experimental setup

The schematic and pictorial view of the experimental setup employed for testing the thermochemical energy storage module is shown in Fig. 6.3. Air is used as heat transfer fluid (HTF). The experimental setup mainly consists of a blower, heating section, air calorimeter, control panel, hydrogen infrastructure, and a data acquisition system. A 0.5-HP centrifugal blower (static pressure: 4-inch water column) is used for conveying the air in the experimental setup. The heater section comprises 25 kW electrical resistance heaters for raising the air temperature to the required charging and discharging temperatures. The electrical load to the heaters is adjusted by a controller based on the set temperature. A butterfly valve is fitted at the delivery side of the blower to regulate the airflow. K-type thermocouples (accuracy: ±2.5°C; calibrated in the operating temperature range) are provided at the inlet and outlet sections of the air calorimeter to measure the temperature. A differential pressure meter (Make: Testo; Model: Testo 512; accuracy: 0.5% FS) is used for measuring the air velocity at the outlet of the calorimeter. The heater section and calorimeter are insulated using a cerawool (density: 64 kg/m^3) of 150 mm thickness to avoid heat loss to the ambient.

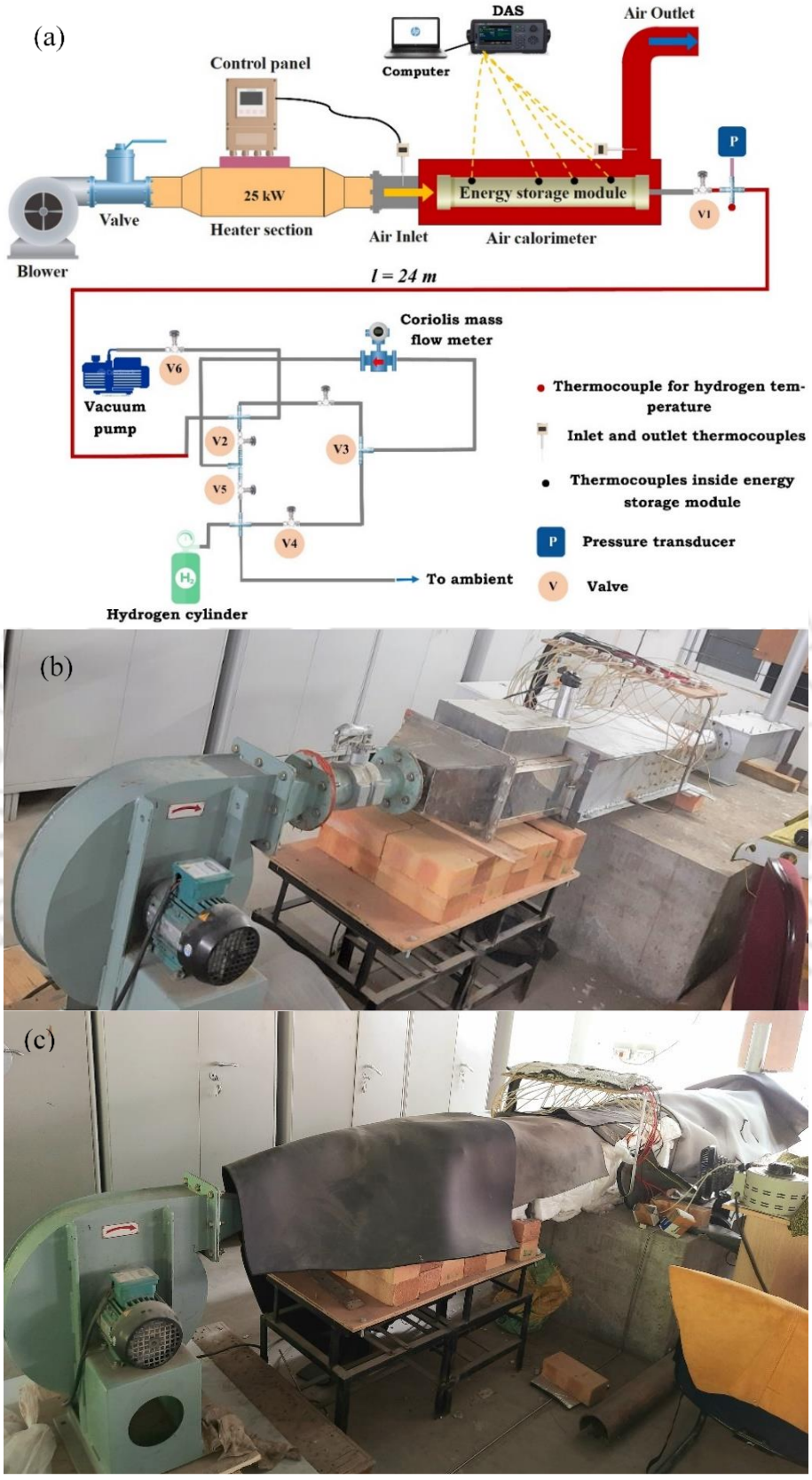

Fig. 6.3. (a) Schematic of the experimental setup and (b) actual experimental setup before insulation (c). experimental setup after insulation

The hydrogen infrastructure consists of a hydrogen gas cylinder, ball valves, Coriolis mass flow meter, and a vacuum pump. A quarter-inch stainless steel tube conveys the hydrogen in the hydrogen circuit. Stainless steel ball valves (part number: SS-43GS4; make: Swagelok) are used to control the hydrogen flow in the gas circuit. A stainless-steel diaphragm sealed valve (part number: SS-DSS4; make: Swagelok) is fitted at the inlet of the storage module due to its high-temperature operation. A piezoresistive type pressure transducer (make: Equinox; accuracy: ± 0.5% on full-scale) is fitted in the hydrogen supply line of the reactor. A Coriolis mass flow meter (Make: Emerson; mass flow accuracy: ±0.25% of the rate) is used for measuring the hydrogen flow rate. A K-type thermocouple is also fitted in the hydrogen circuit near the supply end of the energy storage module to measure the temperature of hydrogen entering/ leaving the reactor.

The 3D sectional view, 2D sectional view and the inside pictorial view of the air calorimeter are shown in Fig. 6.4. The air calorimeter is a cuboid structure with a square cross-section inside which the TES module is placed. Air is allowed to pass over/ through the storage module to exchange heat. Cerawool insulation (density: 64 kg/m^3) is provided inside and outside the calorimeter box to avoid heat loss to the surroundings.

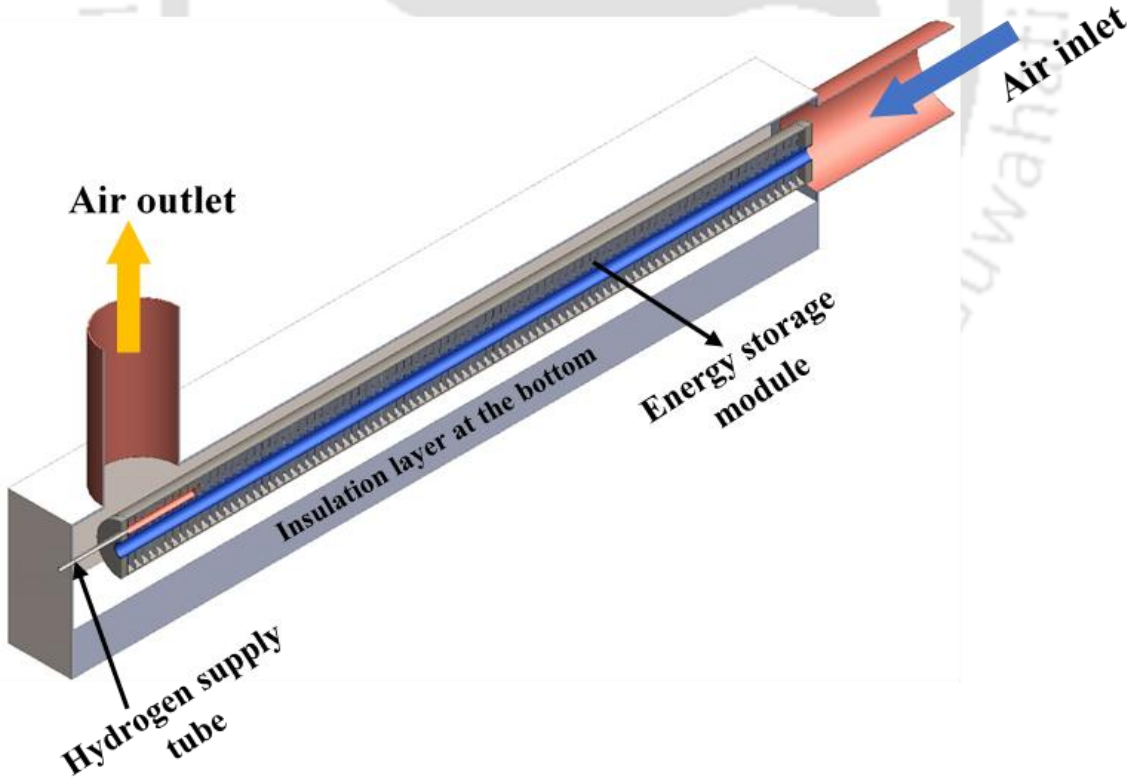

(a)

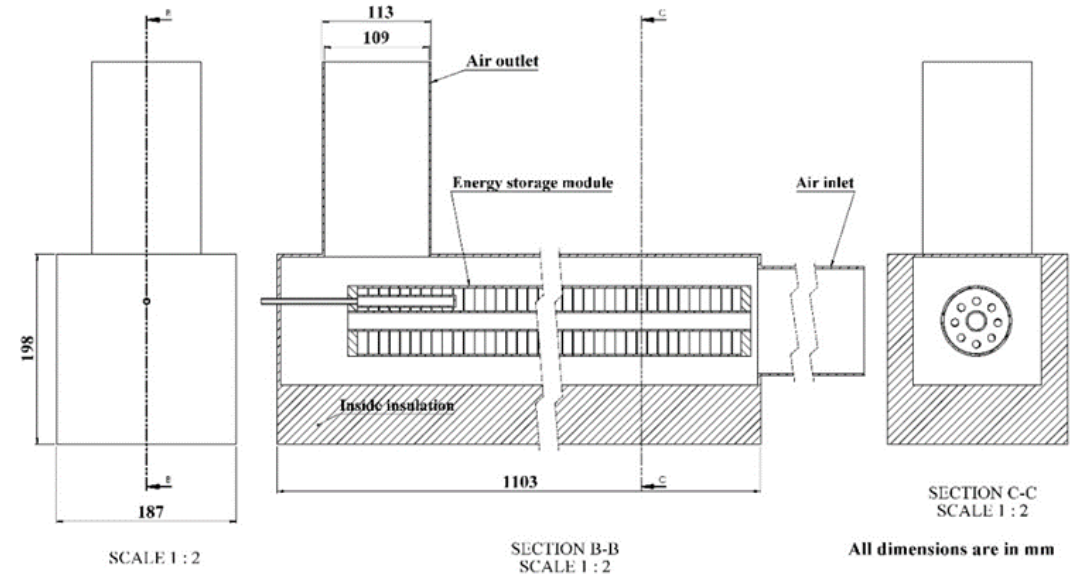

(b)

(c)

Fig. 6.4. Air calorimeter (a) 3D sectional view (right angle bend is not shown in the air outlet) (b) 2D sectional view (c) energy storage module placed inside the calorimeter

6.3.2 Experimental procedure

Absorption is an exothermic reaction during which the MH and the hydrogen are combined to release thermal energy. Before starting the absorption, the reactor, which is in a fully desorbed state, is heated to the set temperature from room temperature, i.e., a sensible heating process. With this, the pressure inside the energy storage module is equal to the equilibrium pressure corresponding to the set temperature. After sensible heating, the hydrogen gas is supplied at a pressure greater than the equilibrium pressure. The exothermic heat of the absorption process is taken by the air provided through the energy storage module at the set inlet temperature. The MH bed temperature, inlet and outlet temperatures of the HTF, and the amount of hydrogen absorbed with respect to time were recorded during the absorption process.

Desorption is an endothermic reaction during which the MH and the hydrogen are separated by supplying thermal energy at a set temperature. Before starting the desorption process, the reactor is heated to the set temperature from room temperature, i.e., sensible heating process. With this, the hydrogen gas pressure inside the energy storage module has risen to the

equilibrium pressure corresponding to the set temperature. After sensible heating, the hydrogen gas is discharged from the energy storage module to 1 bar absolute pressure (i.e., ambient). During hydrogen discharge, the endothermic heat of the reaction is supplied to the energy storage module by HTF provided continuously at the set temperature. During desorption, the MH bed temperature, inlet and outlet temperatures of the HTF, and the amount of hydrogen discharged with respect to time were recorded.

6.4 Coupled MH reactor-based TCES system

The coupled MH reactor-based TCES system consists of an energy storage module (or HTMH) and a hydrogen storage module (or LTMH). The MH-based TCES system involves three major steps: charging, storage, and discharging. During charging, the HTMH receives heat from the high-temperature source for desorbing the hydrogen to the LTMH. The LTMH absorbs the hydrogen released by the HTMH at ambient temperature. The HTMH is disconnected from the LTMH reactor during storage and cooled to ambient temperature for long-term storage. During discharging, the LTMH supplies the hydrogen (by absorbing external heat) to the HTMH, which delivers high-temperature heat by the exothermic reaction. The schematic of the charging, storage, and discharging processes of the MH-based TCES system is shown in Fig. 6.5.

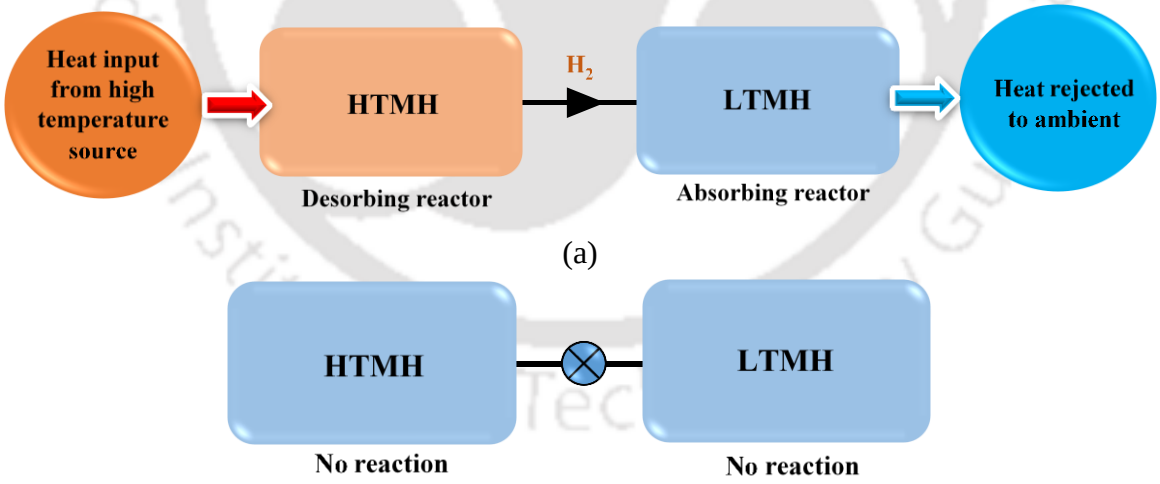

(a)

(b)

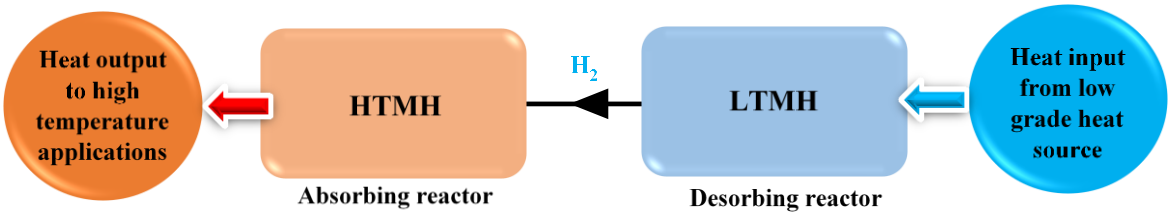

(c)

Fig. 6.5. Schematic of (a) charging, (b) storage, and (c) discharging processes of MH-based TCES system

The difference in plateau pressure of P-C-I corresponding to the operating temperature of each reactor governs the hydrogen flow between the HTMH and LTMH reactors. During the charging process, the pressure of the gas inside the HTMH corresponding to its temperature should be more than that of the gas inside the LTMH and vice versa during the discharging process. The operating temperatures of the HTMH and LTMH are selected to maintain the positive pressure difference between the reactors during the charging and discharging processes. Also, the LTMH is ideally chosen so that its heat of reaction is 2 – 4 times lower than the heat of reaction of HTMH (Nyamsi et al., 2019). During the charging process, the heat rejected from LTMH is discharged to the ambient. During the discharging process, the desorption temperature of the LTMH is selected as per the required discharging temperature of the HTMH. Preferably the desorption heat to the LTMH is supplied at a temperature of 25–60°C, which can be provided from the solar field or the condenser of the power block (Nyamsi et al., 2019). In this work, the alloy pairs magnesium-nickel alloy/$LaNi_5$ and magnesium-nickel alloy/$La_{0.7}Ce_{0.1}Ca_{0.3}Ni_5$ are experimented in coupled reactor mode.

The criterion for sizing the LTMH and HTMH is that the total amount of hydrogen stored in each reactor should be equal. Therefore, the mass of hydrogen stored in LTMH is equal to the mass of hydrogen stored in HTMH. In this study, pure Mg_2Ni was planned as an HTMH and $LaNi_5$ and $La_{0.7}Ce_{0.1}Ca_{0.3}Ni_5$ as LTMHs. During the design stage, the mass of the LTMH alloy was fixed at 9 kg, corresponding to 3.76 kg of pure Mg_2Ni. However, the procured magnesium-nickel alloy showed higher hydrogen storage capacity than the pure Mg_2Ni due to excess magnesium. Further, the storage capacity of the LTMHs decreased over cycling. Hence, the condition of an equal mass of hydrogen between LTMH and HTMH is not maintained in the coupled reactor mode. The single reactor experiments observed that the hydrogen storage capacity of the HTMH reactor is higher than that of the LTMH reactors. From Chapter 5, it is observed that the hydrogen storage capacity of $LaNi_5$ and $La_{0.7}Ce_{0.1}Ca_{0.3}Ni_5$ reactors after 20 cycles is 111 g and 122 g, respectively. Hence, the maximum possible transferrable hydrogen

mass between the reactors is 111 g and 122 g for magnesium-nickel alloy/$LaNi_5$ and magnesium-nickel alloy/$La_{0.7}Ce_{0.1}Ca_{0.3}Ni_5$ alloy pairs, respectively.

6.4.1 Experimental setup for coupled reactors

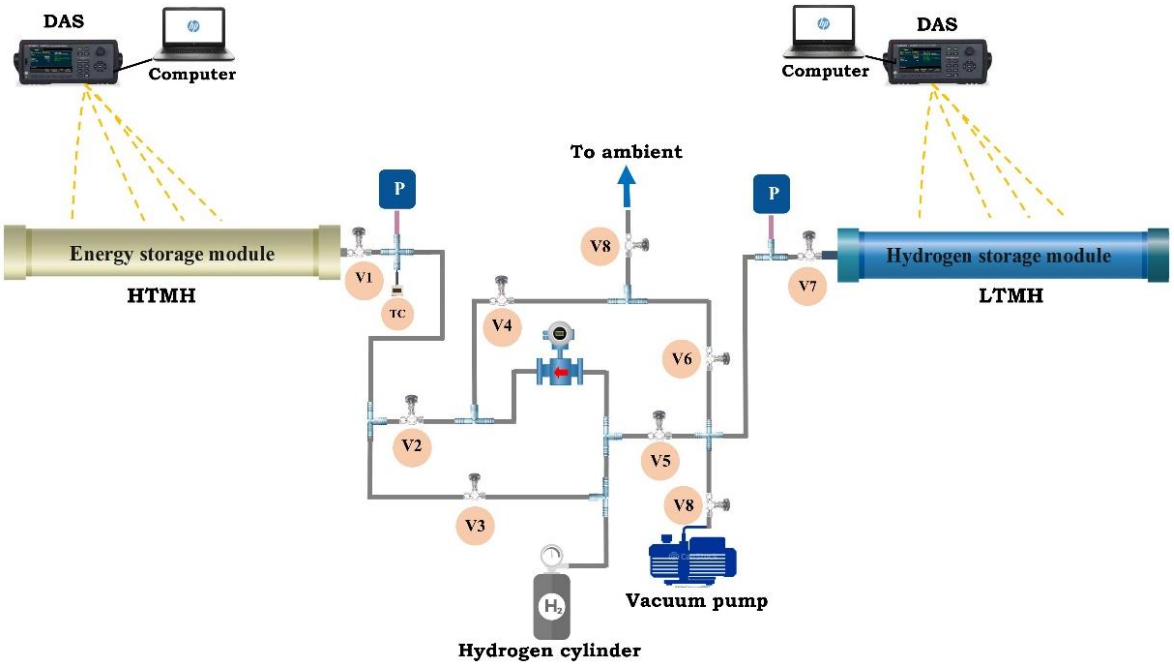

Fig. 6.6. Schematic of the experimental setup used for studying the coupled reactors

The schematic of the experimental setup used for studying the coupled reactors is shown in Fig. 6.6. The HTMH and LTMH reactors connected to the hydrogen circuit in coupled reactor mode are shown in Fig. 6.6. The HTF circuit for supplying/ removing the heat to the LTMH and HTMH is same as the one described in Chapter 5 and Section 6.3 (not shown in Fig. 6.6). During the charging process, the hydrogen transfers from the HTMH to LTMH. Air flowing through the calorimeter at charging temperature supplies the endothermic heat to the HTMH, whereas the exothermic heat of the LTMH is removed by circulating the water at an inlet temperature of 25°C. The valves, V1, V3, V4, V6, and V7 are opened, and the remaining valves are closed during the charging process. During discharging process, the hydrogen transfers from the LTMH to HTMH. The desorbing temperatures of the LTMH are chosen such that there exists a positive pressure differential between the LTMH and HTMH. The exothermic heat of the HTMH is removed by air flowing through the calorimeter. The valves V7, V5, V2, and V1 are opened, and the remaining valves are closed during the discharging process. The temperature of the reactors and pressure readings are recorded during the charging and discharging processes with the help of a data acquisition system.

6.4.2 Experimental procedure for coupled reactors

Unlike in single reactor mode, the hydrogen transfer rate in coupled reactor mode is comparatively low. In coupled reactor mode, the reaction rate constraints come from both alloys. Whereas a single reactor under constant pressure experiences the reaction rate constraint from a single alloy. Therefore, the hydrogen flow rate is comparatively low in coupled reactor mode. The minimum mass flow rate of hydrogen that the Coriolis mass flow meter used in the experiments can record is 0.01 g/s. But in the coupled reactor mode, the mass flow rate of hydrogen is less than 0.01 g/s for most of the time. Therefore, the Coriolis mass flow meter cannot show the amount of hydrogen transferred between the reactors. Hence the following experimental procedure is adopted in coupled reactor mode to determine the amount of hydrogen transferred between the HTMH and LTMH reactors during the charging and discharging processes.

6.4.2.1 Charging process

During the charging process, hydrogen is transferred from the HTMH to LTMH. Hot hydrogen gas leaves the HTMH reactor during its dehydrogenation. The temperature of the hot hydrogen gas leaving the HTMH reactor is measured with a thermocouple (TC) outside the reactor, as shown in Fig. 6.6. As the temperature measurement location is exposed to ambient, the measured temperature of hydrogen gas is after heat loss to ambient. The hydrogen gas temperature higher than the ambient temperature indicates the continuation of the charging process. The end of the charging process is declared when the hydrogen gas temperature becomes equal to/ near ambient temperature. For all the charging experiments, the HTF inlet temperature to LTMH is maintained at 25°C. The following experimental procedure is followed during the charging process.

Step 1: The HTMH is charged with a known mass of the hydrogen at a set supply pressure and inlet temperature of HTF (i.e., air). At the same time, the LTMH is completely desorbed and maintained at a temperature of 25°C.

Step 2: The HTMH is heated to the set charging temperature, and the charging process is initiated by supplying the air at the set charging temperature. During the charging process, hydrogen is transferred from the HTMH to the LTMH. The air flowing through the calorimeter provides the endothermic heat of the HTMH, and water was circulated at 25°C to remove the exothermic heat from the LTMH.

Step 3: The end of the charging process is identified when the hydrogen gas temperature leaving the HTMH reaches room temperature. After the complete transfer of hydrogen, the HTMH is disconnected from the LTMH.

Step 4: The LTMH is desorbed to ambient through the Coriolis mass flow meter. Since the reaction kinetics and hydrogen transfer rates of the LTMH are faster, the mass flow meter recorded the total mass of hydrogen desorbed. From this, the transferred hydrogen between the HTMH and LTMH is determined.

6.4.2.2 Discharging process

During the discharging process, hydrogen is transferred from the LTMH to HTMH. Discharging is performed at an inlet temperature of 300°C to the HTMH. The following experimental procedure is followed during the discharging process.

Step 1: The LTMH is charged with a known mass of the hydrogen at a set supply pressure and inlet temperature of HTF (i.e., water). At the same time, the HTMH is completely desorbed and maintained at the discharging temperature (i.e., 300°C).

Step 2: The LTMH is heated to the set desorbing temperature and the discharging process is initiated. During the discharging process, hot water supplied the endothermic heat to the LTMH and the air supplied at discharging temperatures removed the exothermic heat from the HTMH.

Step 3: After the discharging process, the LTMH is desorbed to ambient through the Coriolis mass flow meter to check for any traces of hydrogen mass present in the LTMH. By subtracting the traced mass from the total charged mass of the hydrogen, the transferred hydrogen between the HTMH and LTMH reactors is determined.

6.5 Results and discussion

This section presents the results of the HTMH in single and coupled reactor modes. Firstly, absorption and desorption characteristics of the magnesium-nickel hydride in single reactor mode are presented. Further, the charging and discharging results of the coupled reactor system with magnesium-nickel alloy/$LaNi_5$ and magnesium-nickel alloy/$La_{0.7}Ce_{0.1}Ca_{0.3}Ni_5$ pairs are presented. During the charging process, the effect of the inlet temperature of the HTMH's HTF was studied while the inlet temperature of LTMH's HTF was maintained at 25°C. During

discharging, the inlet temperature of LTMH's HTF was varied. The results are presented in terms of temperature, pressure, and charging/ discharging times.

6.5.1 HTMH in single reactor mode

This section presents the results of the activation, absorption and desorption characteristics of the magnesium-nickel alloy in single reactor mode. The absorption was carried out under constant supply pressure and the hydrogen was desorbed to ambient pressure.

6.5.1.1 Activation of magnesium-nickel alloy

The magnesium-nickel alloy was activated under different operating conditions (as shown in Fig. 6.7). The activation of the alloy was performed at 250 and 300°C. The reactor is heated to 250°C and evacuated to 10^{-5} bar pressure before sending the hydrogen. In the first activation cycle, hydrogen gas is introduced into the reactor at a 30-bar supply pressure. The inlet temperature of hydrogen to the reactor is 25°C. When the hydrogen was supplied to the reactor for the first time, the temperature of the hydrogen inside the reactor increased from 25°C to 250°C due to which the pressure raised from 30 bar to 53.3 bar. As the alloy is not activated, the hydrogen is not getting absorbed by the alloy. Due to this, the hydrogen accumulated in the free space and heated to 250°C. Hence, the supply pressure in the first activation cycle should be carefully selected considering design pressure. In the first activation cycle, the alloy absorbed 18.8 g of hydrogen. In subsequent cycles, the amount of absorbed hydrogen is increased, and 147.2 g of hydrogen is absorbed by alloy in the seventh activation cycle, which corresponds to 3.91 wt.% H.

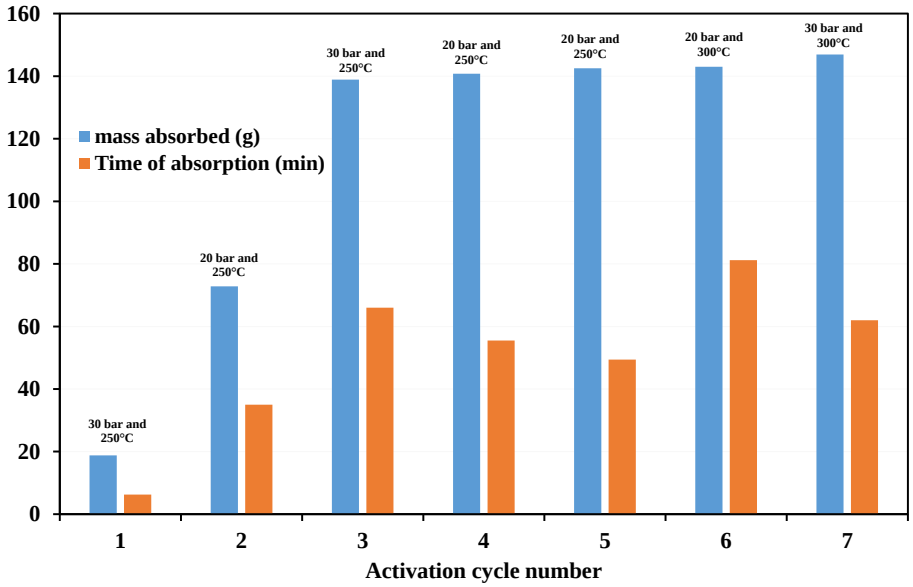

Fig. 6.7. Amount of hydrogen absorbed and absorption time during activation cycles

6.5.1.2 Absorption characteristics of magnesium-nickel alloy

The absorption characteristics of the magnesium-nickel alloy under the supply pressure of 20 bar while the inlet temperature of the air was maintained at 300°C are presented in Fig. 6.8 for two different absorption cycles (cycles 13 and 15). From Fig. 6.8a, it is observed that the alloy exhibited a double plateau. The peak temperature of the MH bed is observed as 407.2°C (TC4). The thermocouple TC1 behaved differently than TC4. The peak temperature attained by TC1 is 327.2°C. The hydrogen gas is introduced into the reactor at room temperature, and the low-temperature hydrogen gas has a cooling effect on TC1 as its location is near the supply end. Under 20 bar supply pressure, the alloy absorbed 142 g of hydrogen in 78.3 min (Fig. 6.8b). The inlet and outlet temperatures of air are shown in Fig. 6.8c. The peak temperature difference of 17.2°C is observed in the air. Even though the absorption of 142 g of hydrogen is completed in 78.3 min, the MH bed and outlet air consumed 109 min to reach the initial temperature. This is because the minimum flow rate recorded by Coriolis mass flow meter is 0.01 g/s and sensible cooling of the MH bed. After 142 g of hydrogen was absorbed, the reaction continued, but the mass flow meter could not record that data. There is no significant deviation in the results between two repeated operating cycles of the absorption under 20 bar supply pressure, i.e., cycles 13 and 15.

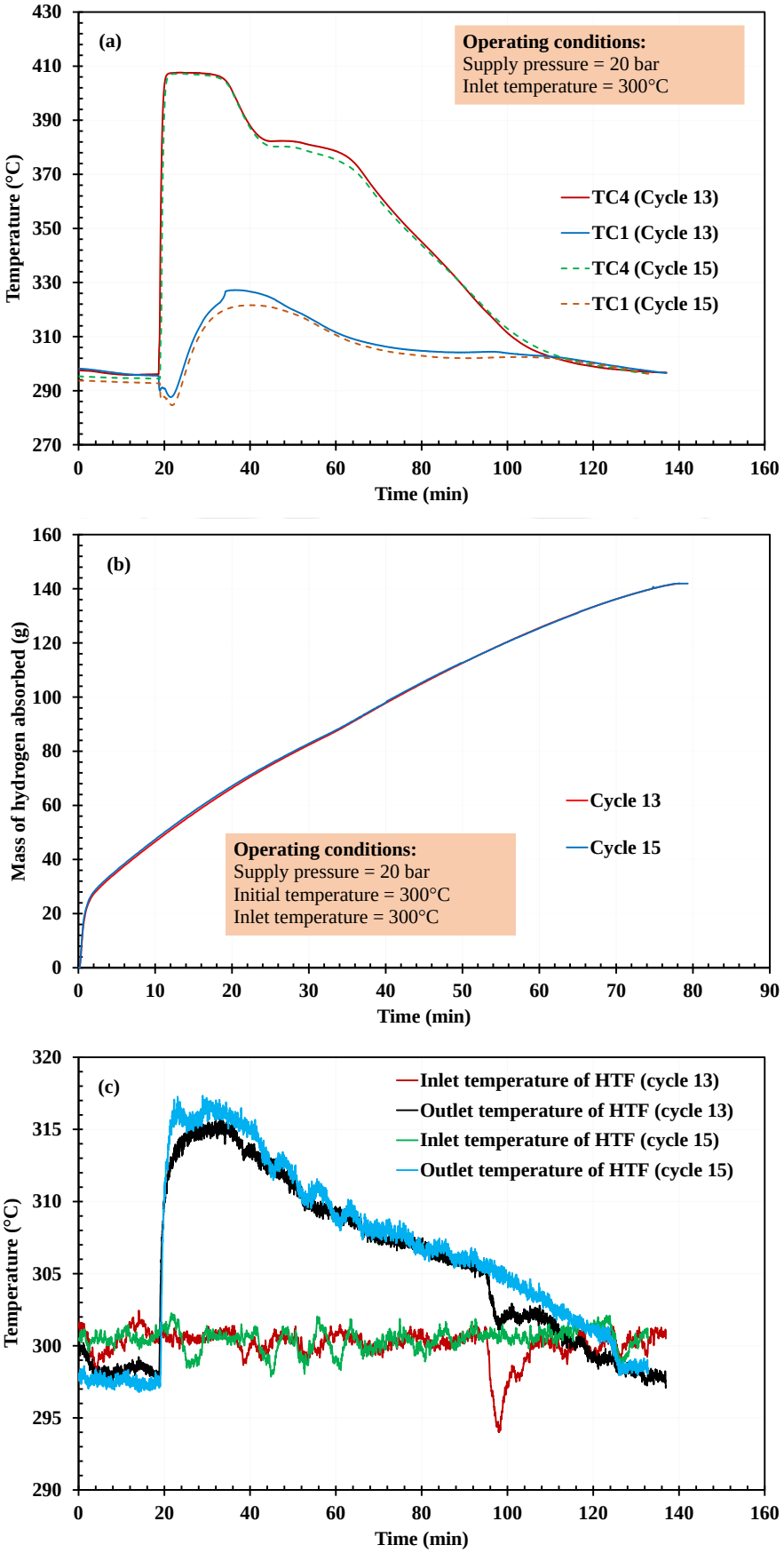

Fig. 6.8. Absorption of the magnesium-nickel alloy under 20 bar (a) temperature variations and (b) amount of hydrogen absorbed and (c) inlet and outlet temperature of HTF

The effect of supply pressure of hydrogen on the temperature recorded by TC4 and the amount of hydrogen absorbed is shown in Fig. 6.9. The alloy absorbed 104, 142, and 143 g of hydrogen in 122, 78.3, and 62.5 min, respectively, under the supply pressure of 10, 20, and 30 bar. The peak temperatures attained by TC4 inside the MH bed are 377, 407.2, and 429.4°C, respectively. Increasing the supply pressure from 20 to 30 bar did not significantly enhance the absorption rate.

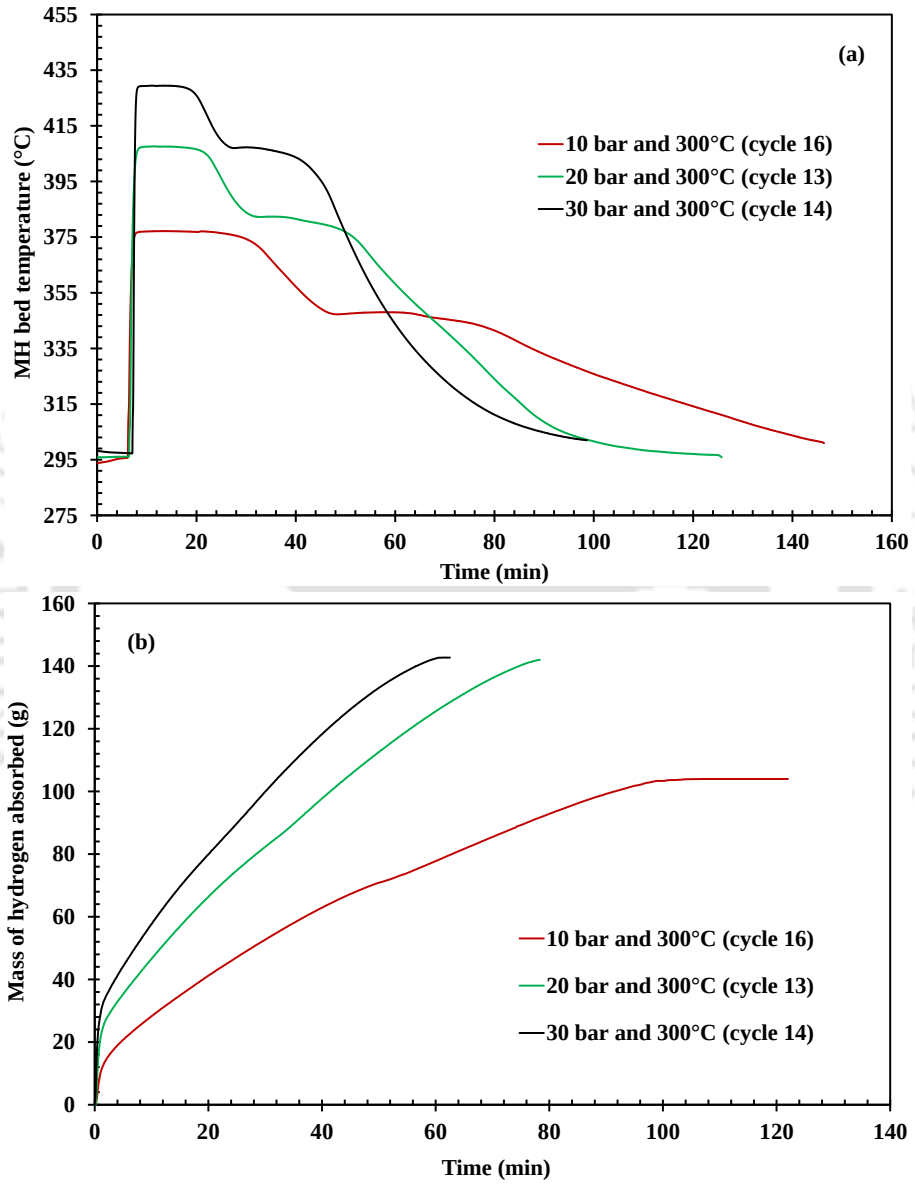

Fig. 6.9. Effect of supply pressure on (a) MH bed temperature and (b) amount of hydrogen absorbed

6.5.1.2 Desorption characteristics of magnesium-nickel alloy

The desorption characteristics of the magnesium-nickel alloy for the average air inlet temperature of 377°C are presented in Fig. 6.10. An amount of 142 g of hydrogen was charged into the alloy before the desorption process at 20 bar supply pressure. The effect of double

plateau is visualized in the MH bed temperature profiles (Fig. 6.10a). There are some fluctuations in the inlet temperature of the HTF, which are also reflected in the outlet temperature. From Fig. 6.10b, it is observed that the alloy desorbed 124 g of hydrogen in 146 min. After 124 g of desorption, the desorption rate became lesser than 0.01 g/s which could not be sensed with the mass flow meter. However, the desorption was continued up to 205.3 min, which is indicated by the hydrogen gas temperature.

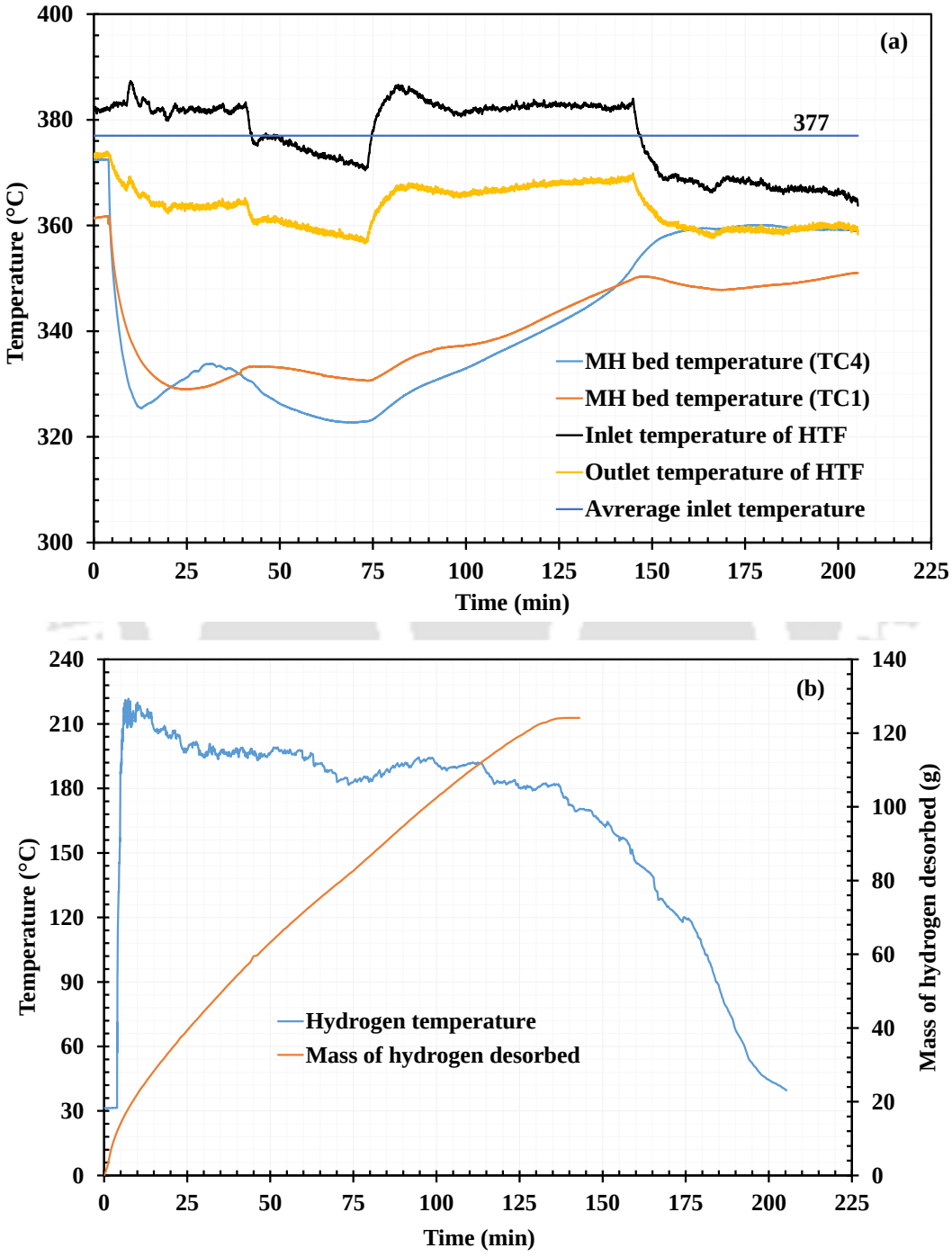

Fig. 6.10. Desorption of the magnesium-nickel alloy at 377°C (a) temperature and (b) hydrogen gas temperature and amount of hydrogen desorbed

The effect of air inlet temperature on the desorption is shown in Fig. 6.11. The amount of hydrogen desorbed through mass flow meter for the inlet temperature of 370, 377, and 390°C is 107.7, 124, and 124 g, respectively. The corresponding desorption time is 136, 140, and 140 min, respectively. There is no significant effect of inlet temperature on the desorption rate.

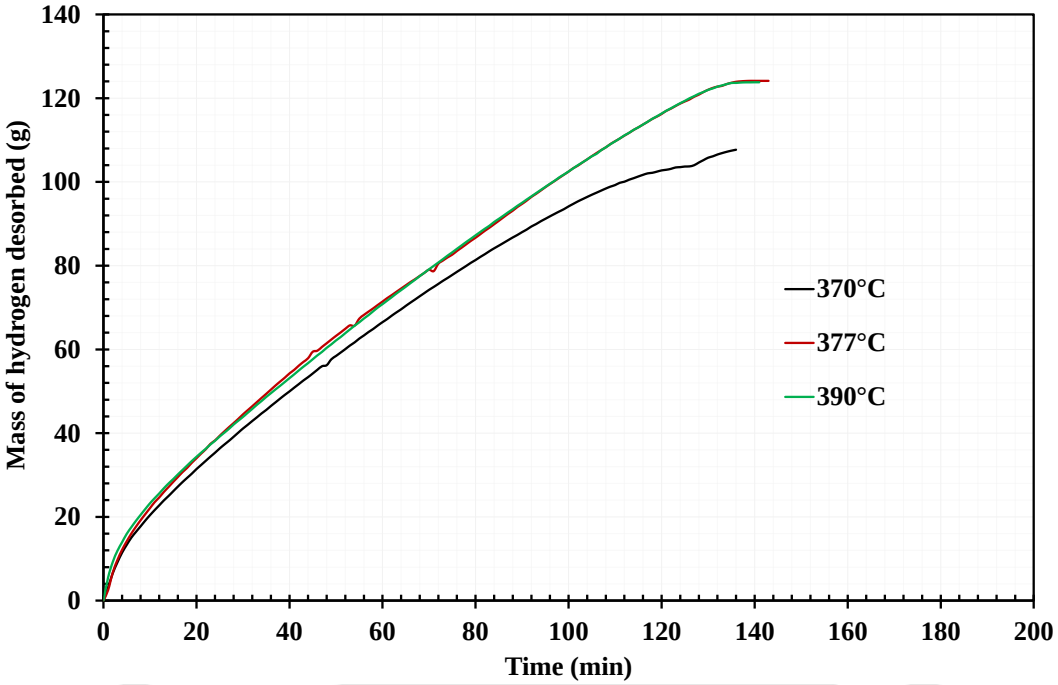

Fig. 6.11. Effect of inlet temperature of HTF on amount of hydrogen desorbed

6.5.2 HTMH in coupled reactor mode

6.5.2.1 Magnesium-nickel alloy/$La_{0.7}Ce_{0.1}Ca_{0.3}Ni_5$ pair

This section presents the results of the experiments conducted on the charging and discharging processes of magnesium-nickel alloy/ $La_{0.7}Ce_{0.1}Ca_{0.3}Ni_5$ pair. During the charging process, the effect of the inlet temperature of the air of the magnesium-nickel alloy reactor is studied on the charging time. Two different inlet air temperatures, 400 and 374°C are considered. During the charging process, the inlet water temperature to the $La_{0.7}Ce_{0.1}Ca_{0.3}Ni_5$ reactor was maintained at 25°C. The discharging was performed with an inlet water temperature of 60°C to the $La_{0.7}Ce_{0.1}Ca_{0.3}Ni_5$ and the magnesium-nickel alloy was supplied with air at 300°C.

Before the charging process at 400°C, the magnesium-nickel alloy was charged with 141.2 g of hydrogen at 30 bar supply pressure, and the $La_{0.7}Ce_{0.1}Ca_{0.3}Ni_5$ alloy was kept in a complete desorbed state. The temperature profiles of magnesium-nickel alloy and $La_{0.7}Ce_{0.1}Ca_{0.3}Ni_5$ are shown in Fig. 6.12(a) and (c) during the charging process. The bed temperature of the

magnesium-nickel alloy exhibited the desorption behaviour and the $La_{0.7}Ce_{0.1}Ca_{0.3}Ni_5$ alloy showed the absorption behaviour.

From the experimental procedure explained in section 6.4.2, it is found that an amount of 119 g of hydrogen is transferred between the reactors. In this work, the time up to which the hydrogen gas temperature leaving the reactor reaches 35°C is considered as charging time. From Fig. 6.12b, the charging time is observed as 240 min from the hydrogen gas temperature. From single reactor mode experiments of magnesium-nickel alloy and $La_{0.7}Ce_{0.1}Ca_{0.3}Ni_5$, it was found that the reaction kinetics of the magnesium-nickel alloy are slower than the $La_{0.7}Ce_{0.1}Ca_{0.3}Ni_5$. During the charging process of the coupled reactor mode, the mass transfer limitation only comes from the magnesium-nickel alloy due to its slow reaction kinetics. Hence, the line pressure in coupled reactor mode is greatly influenced by the equilibrium pressure of $La_{0.7}Ce_{0.1}Ca_{0.3}Ni_5$ (Fig. 6.12 (b) and (d)).

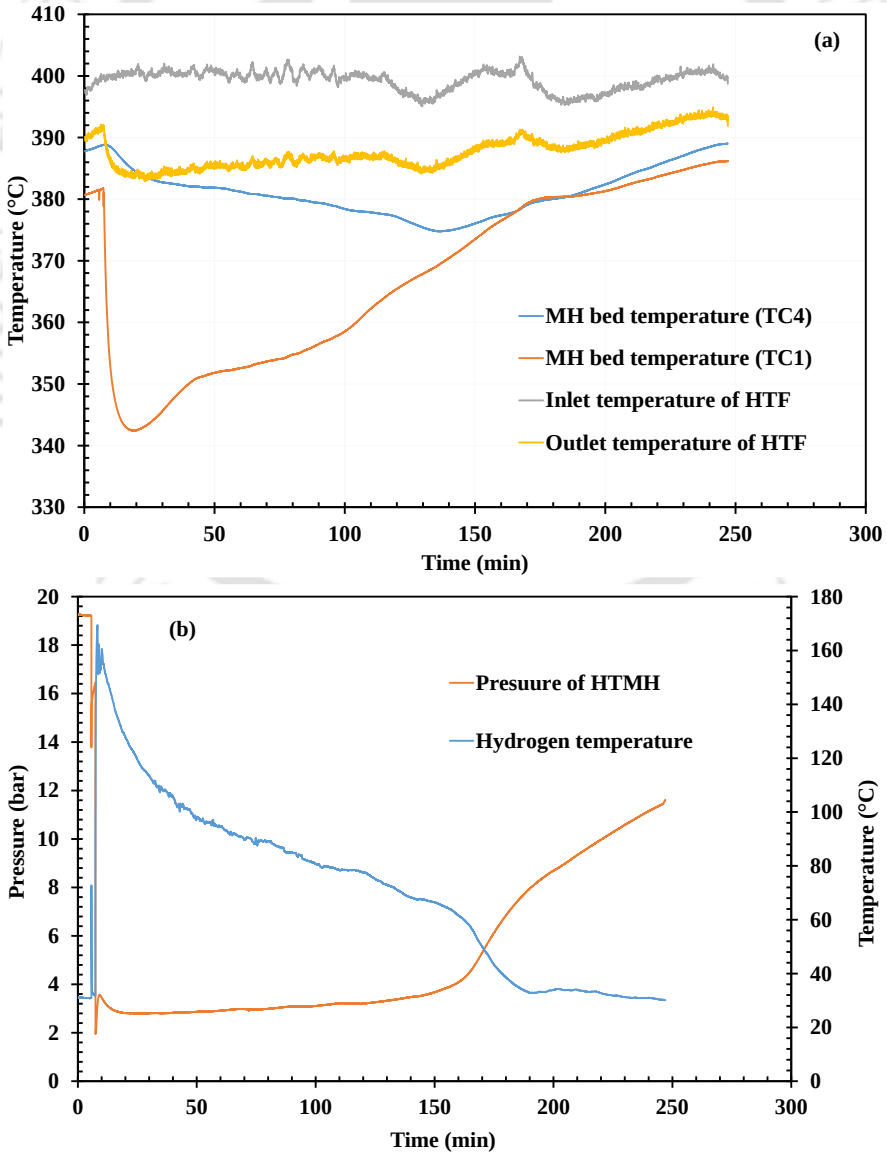

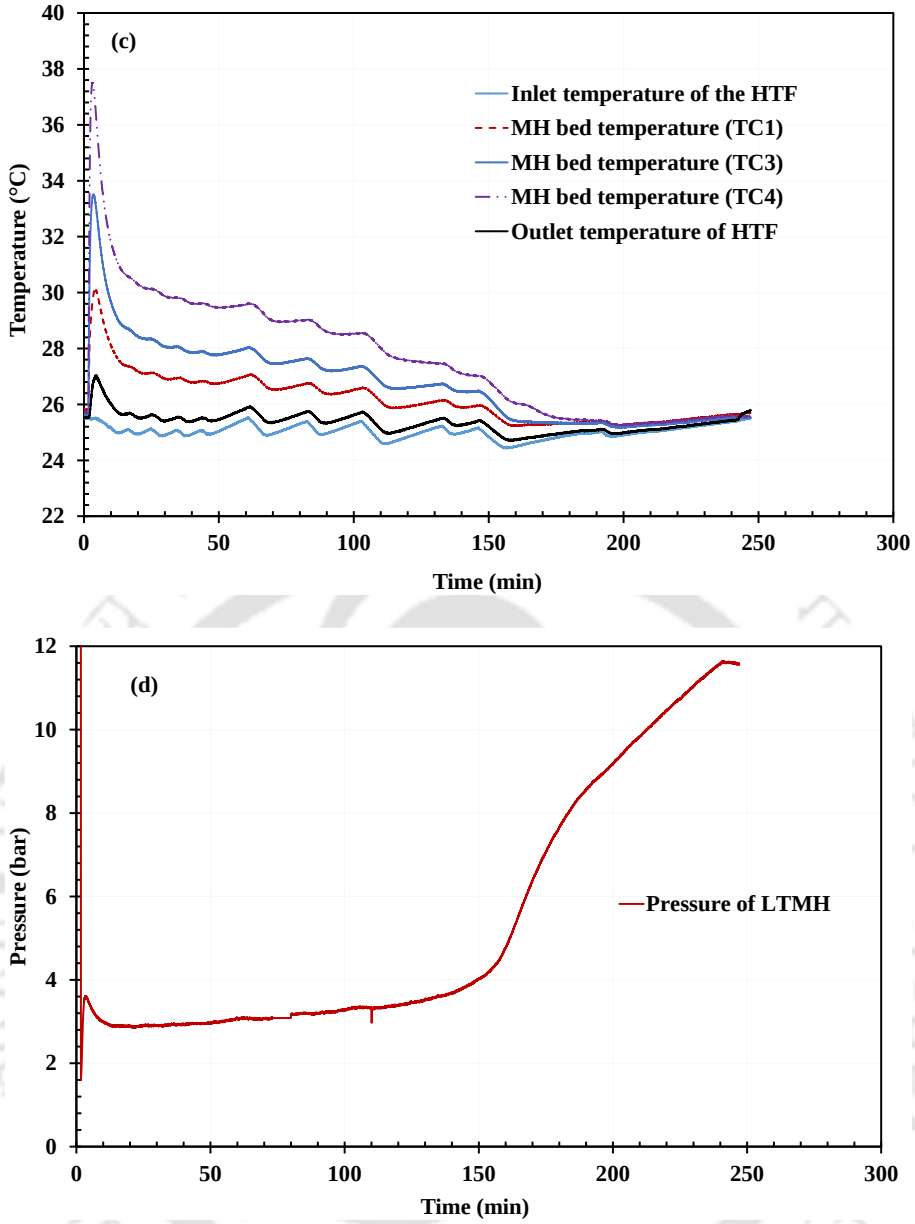

Fig. 6.12. Charging process of magnesium-nickel alloy/ $La_{0.7}Ce_{0.1}Ca_{0.3}Ni_5$ pair: HTMH at 400°C and LTMH at 25°C (a) Temperature variations of HTMH (b) pressure of HTMH and hydrogen temperature variation of HTMH (c) temperature variations of LTMH (d) pressure variation of LTMH

For the charging experiment at 374°C, the magnesium-nickel alloy was charged with 120 g of hydrogen at 20 bar supply pressure, and the $La_{0.7}Ce_{0.1}Ca_{0.3}Ni_5$ alloy was kept in a complete desorbed state. The temperature and pressure profiles of magnesium-nickel alloy and $La_{0.7}Ce_{0.1}Ca_{0.3}Ni_5$ are shown in Fig. 6.13(a-d) for the charging experiment at 374°C. The behavior of temperature and pressure are similar to 400°C. But, some fluctuations were observed in the hydrogen gas temperature due to the presence of fluctuations in the inlet

temperature of the air to the magnesium-nickel alloy. It is observed that 115 g of hydrogen is transferred between the reactors in 377 min (Fig. 6.13b).

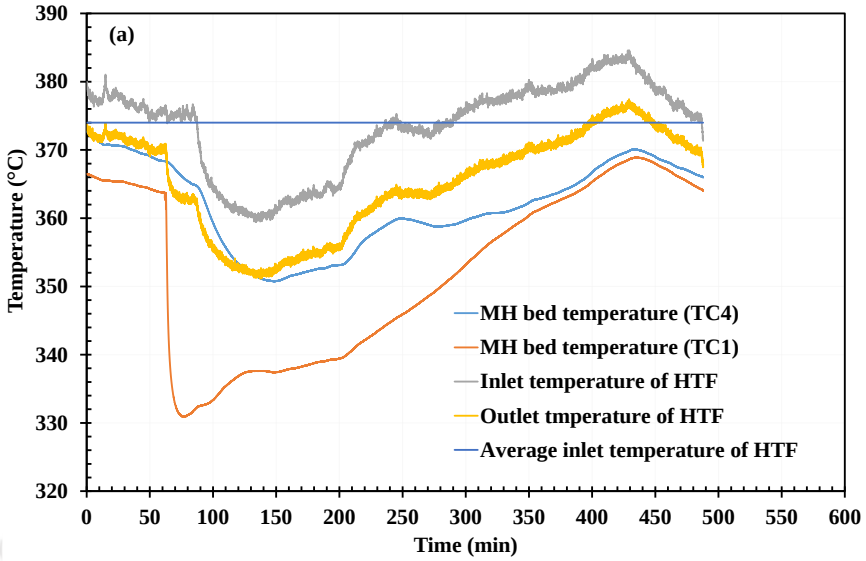

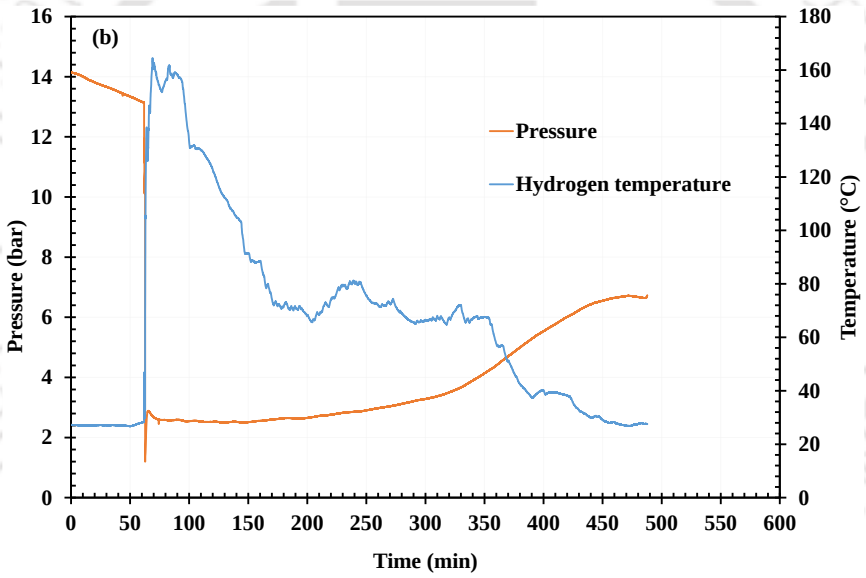

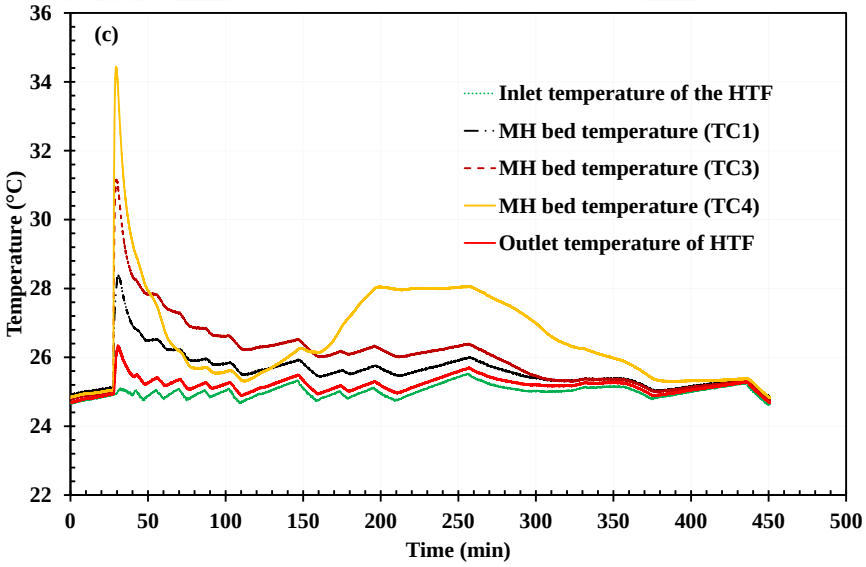

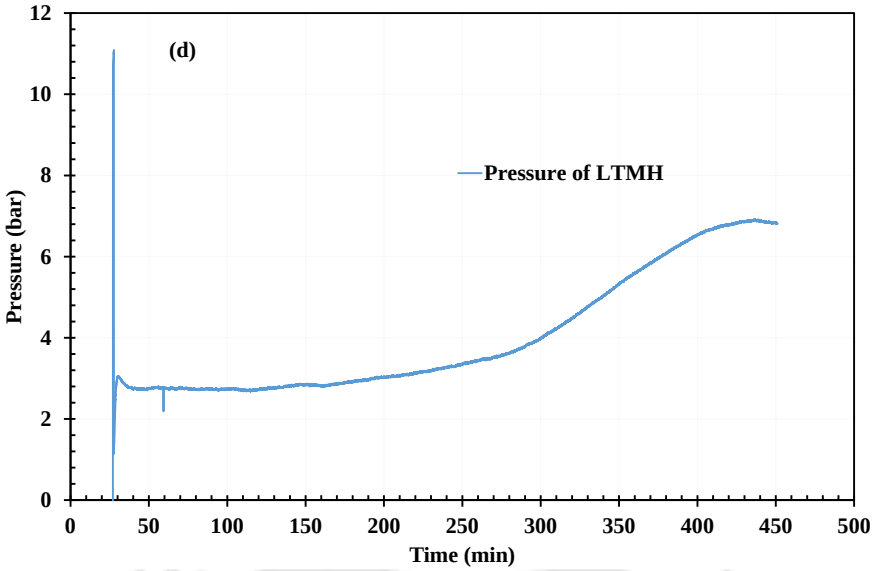

Fig. 6.13. Charging process of magnesium-nickel alloy/ $La_{0.7}Ce_{0.1}Ca_{0.3}Ni_5$ pair: HTMH at 374°C and LTMH at 25°C (a) Temperature variations of HTMH (b) pressure of HTMH and hydrogen temperature variation of HTMH (c) temperature variations of LTMH (d) pressure variation of LTMH

The discharging process was conducted at inlet hot water temperature of 60°C to $La_{0.7}Ce_{0.1}Ca_{0.3}Ni_5$ reactor while the inlet air temperature to the magnesium-nickel alloy reactor was maintained at 300°C. The temperature and pressure variations inside the reactors during the discharging process are shown in Fig. 6.14. The MH bed temperature of magnesium-nickel alloy showed exothermic characteristics, whereas the $La_{0.7}Ce_{0.1}Ca_{0.3}Ni_5$ alloy showed the endothermic characteristics. Before the discharging process at 60°C, the $La_{0.7}Ce_{0.1}Ca_{0.3}Ni_5$ was charged with 121 g of hydrogen at 20 bar supply pressure, and the magnesium-nickel alloy was kept completely desorbed. From the experimental procedure explained in section 6.4.2, it is found that 101 g of hydrogen was transferred between the reactors in 210 min.

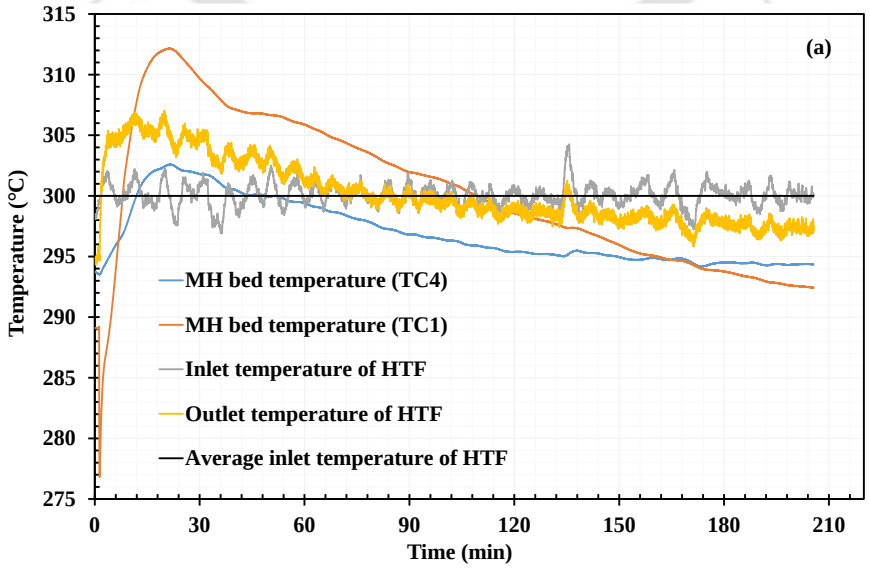

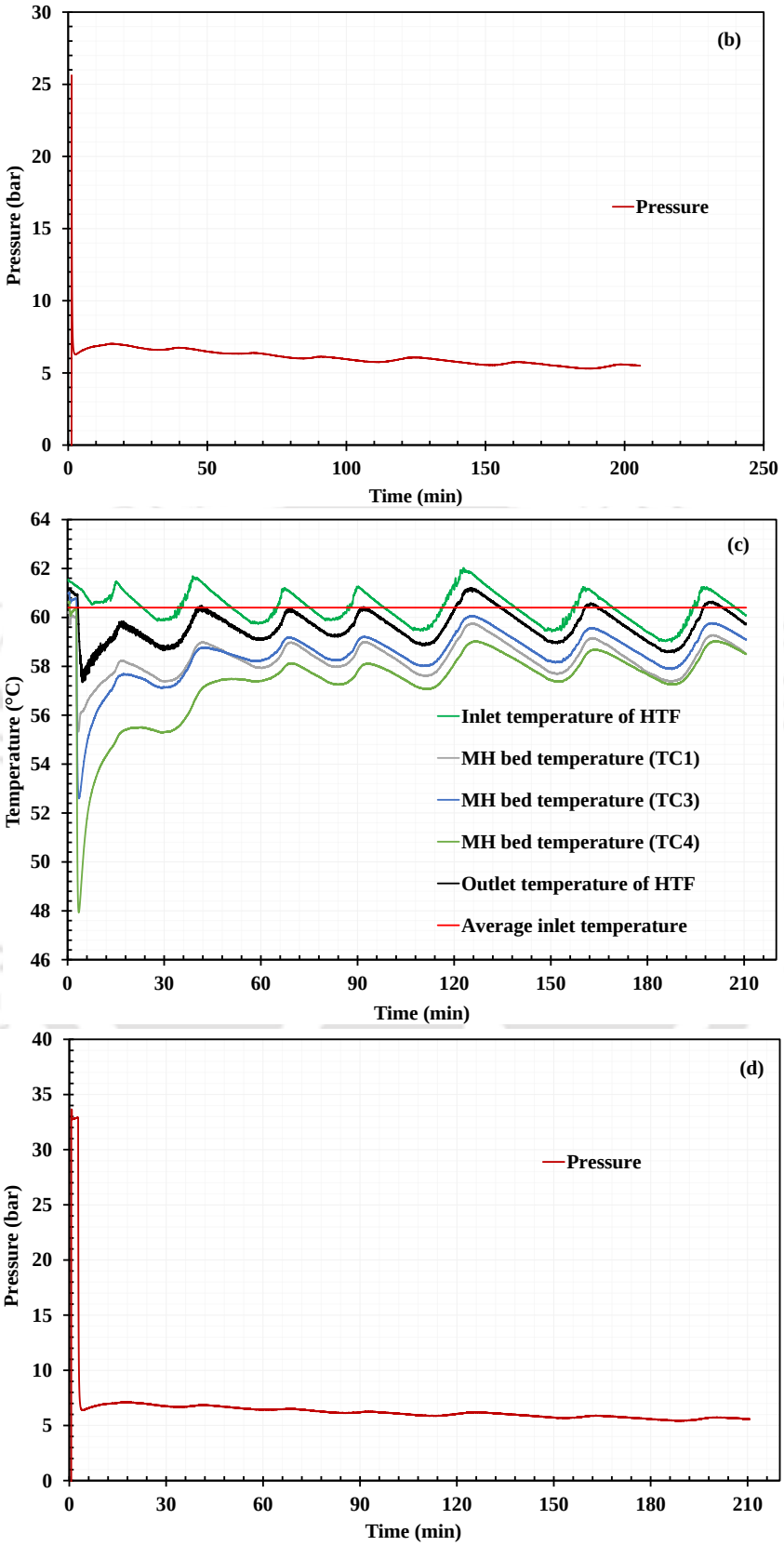

Fig. 6.14. Discharging process of magnesium-nickel alloy/ $La_{0.7}Ce_{0.1}Ca_{0.3}Ni_5$ pair: LTMH at 60°C and HTMH at 300°C (a) Temperature variations of HTMH (b) pressure of HTMH and hydrogen temperature variation of HTMH (c) temperature variations of LTMH (d) pressure variation of LTMH

6.5.2.2 Magnesium-nickel alloy/$LaNi_5$ pair

This section presents the results of the experiments conducted on the charging and discharging processes of magnesium-nickel alloy/ $LaNi_5$ pair. The charging process was conducted at air inlet temperature of 380°C while the inlet water temperature to the $LaNi_5$ reactor was maintained at 25°C. Discharging was conducted for the hot water temperature of 60°C while the inlet air temperature to magnesium-nickel alloy was maintained at 300°C.

Before the charging process at 380°C, the magnesium-nickel alloy was charged with 118 g of hydrogen at 20 bar supply pressure, and the $LaNi_5$ alloy was kept in a complete desorbed state. The temperature profiles of magnesium-nickel alloy and $LaNi_5$ are shown in Fig. 6.15(a) and (c) during the charging process. The explanation for temperature profiles is same as the Section 6.5.2.1. It is found that an amount of 101 g of hydrogen is transferred between the reactors. From Fig. 6.15b, the charging time is observed as 287 min from the hydrogen gas temperature.

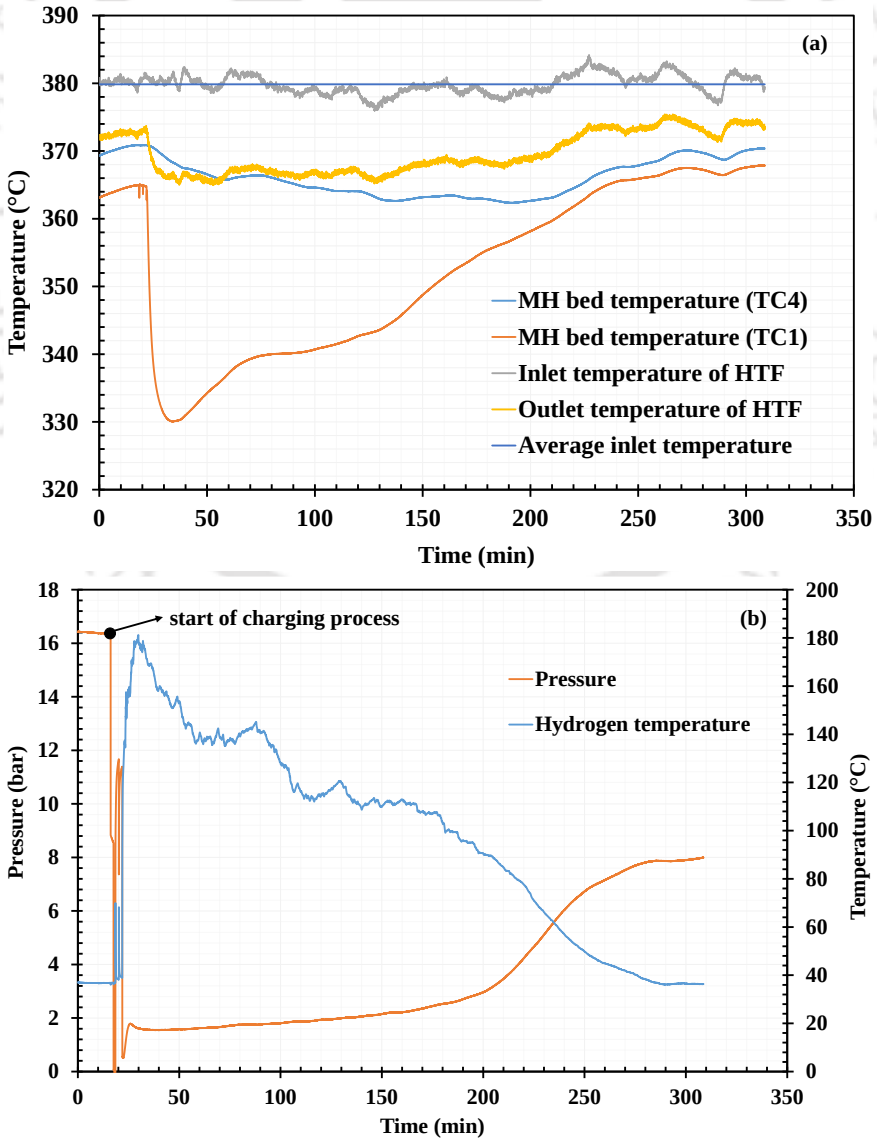

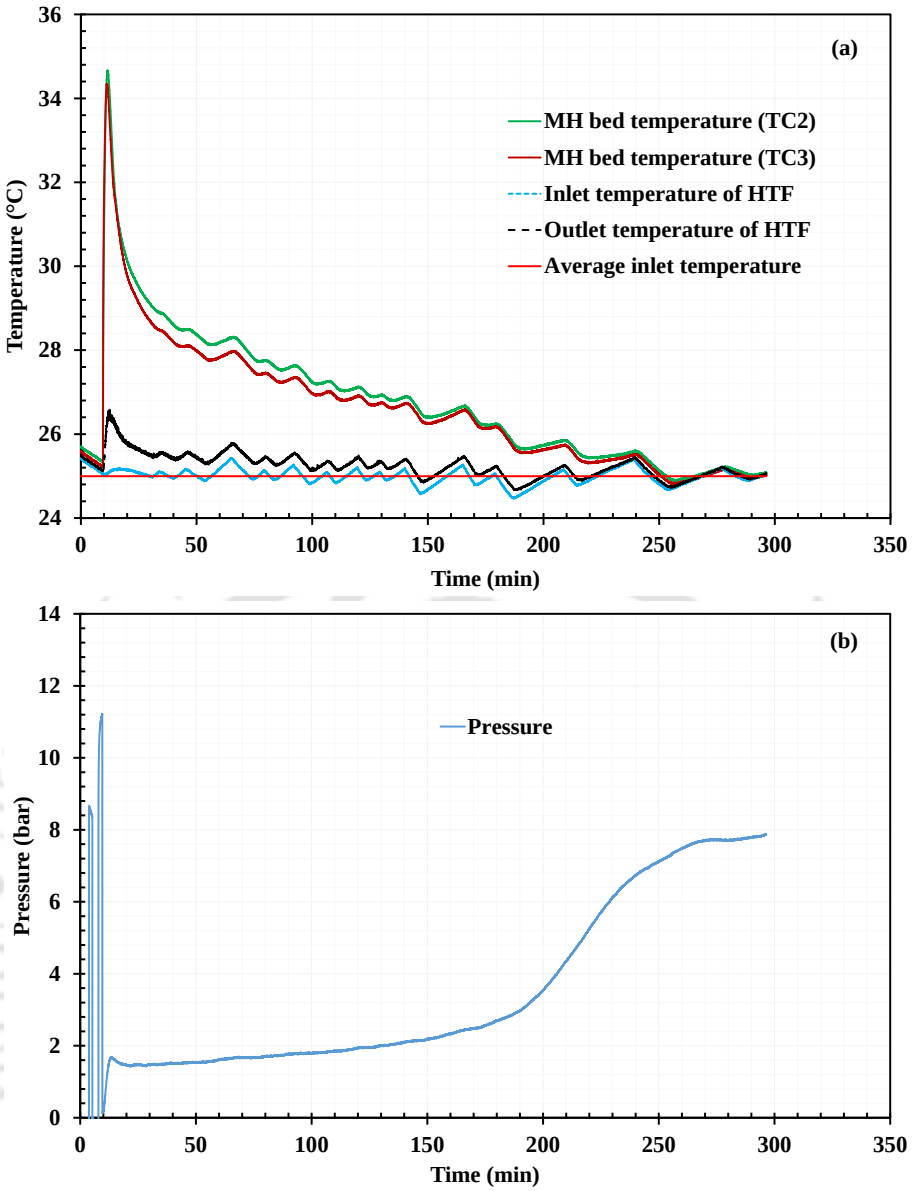

Fig. 6.15. Charging process of magnesium-nickel alloy/ $LaNi_5$ pair: HTMH at 380°C and LTMH at 25°C (a) Temperature variations of HTMH (b) pressure of HTMH and hydrogen temperature variation of HTMH (c) temperature variations of LTMH (d) pressure variation of LTMH

The discharging results for magnesium-nickel alloy/ $LaNi_5$ pair are presented in Fig. 6.16 for inlet hot water temperature of 60°C while the inlet air temperature to the magnesium-nickel alloy reactor was maintained at 300°C. Before the discharging process at 60°C, the $LaNi_5$ was charged with 108 g of hydrogen at 20 bar supply pressure, and the magnesium-nickel alloy was kept completely desorbed. From the experimental procedure explained in section 6.4.2, it is found that 100 g of hydrogen was transferred between the reactors in 246 min (i.e., the discharging time).

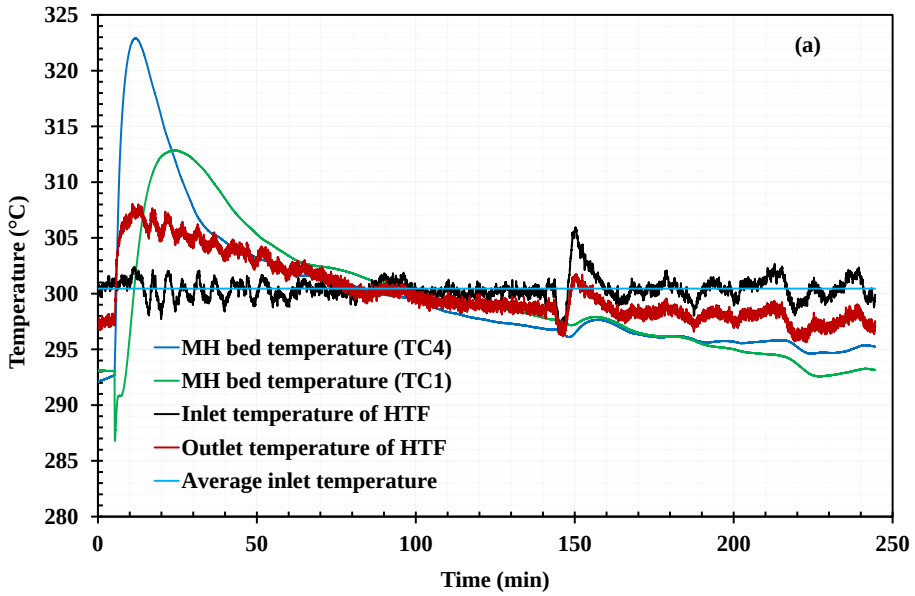

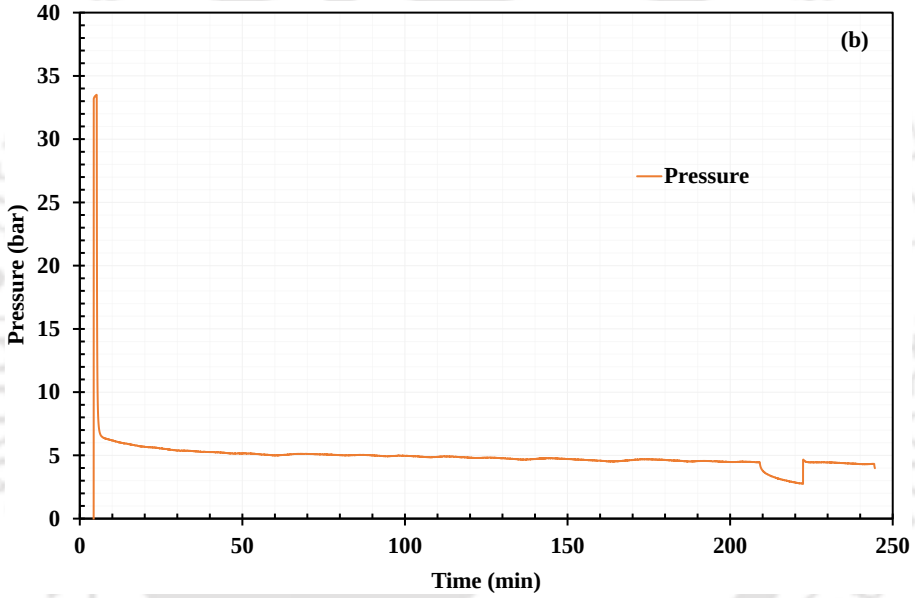

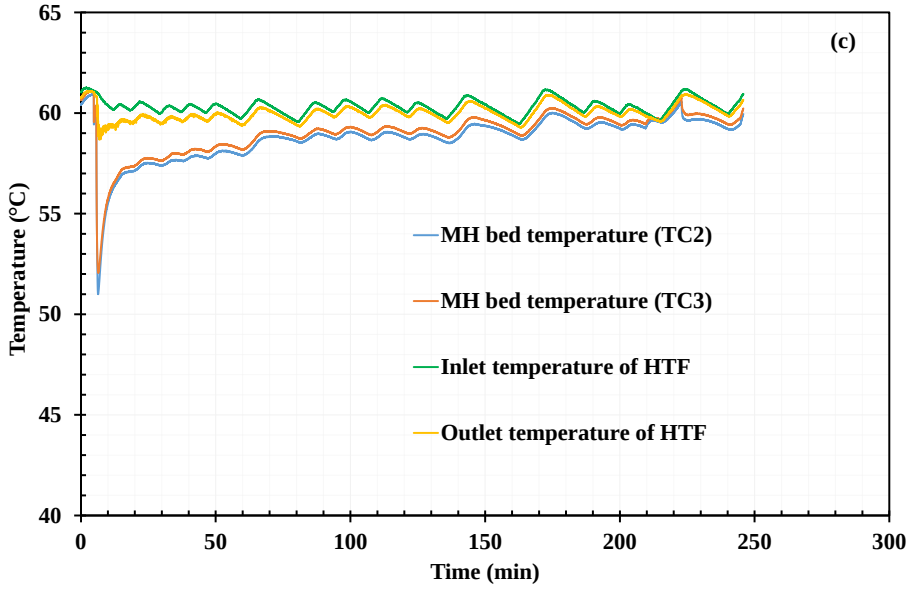

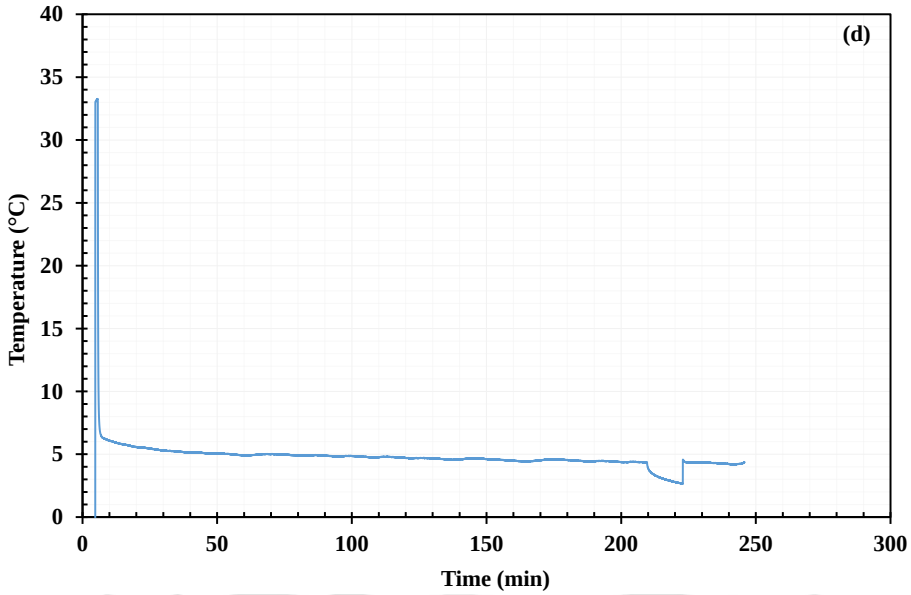

Fig. 6.16. Discharging process of magnesium-nickel alloy/ $LaNi_5$ pair: LTMH at 60°C and HTMH at 300°C (a) Temperature variations of HTMH (b) pressure of HTMH and hydrogen temperature variation of HTMH (c) temperature variations of LTMH (d) pressure variation of LTMH

The charging and discharging results for both alloy pairs are summarized in Table 6.1. It is observed that both the charging and discharging times are within 360 min, except for charging at 374°C for Magnesium-nickel alloy/ $La_{0.7}Ce_{0.1}Ca_{0.3}Ni_5$. Higher hydrogen mass is transferred for the alloy pair: magnesium-nickel alloy/ $La_{0.7}Ce_{0.1}Ca_{0.3}Ni_5$ due to high storage capacity of $La_{0.7}Ce_{0.1}Ca_{0.3}Ni_5$. The discharging times are lower than the charging times because the discharging process was conducted at 60°C. The main reason for this is the poor desorption kinetics of magnesium-nickel alloy. Another possible reason is the driving potential (the difference between the equilibrium pressures of LTMH at 60°C and HTMH at 300°C) during the discharging process is more than the charging process.

Table 6.1 Summary of charging and discharging processes of in coupled reactor mode

Alloy pair	**Charging**			**Discharging**		
	Temperatures (°C)	Mass transferred (g)	Time (min)	Temperatures (°C)	Mass transferred (g)	Time (min)
Magnesium-nickel alloy/ $La_{0.7}Ce_{0.1}Ca_{0.3}Ni_5$	400/ 25	119	240	60/ 300	101	210
	374/ 25	115	377			
Magnesium-nickel alloy/ $LaNi_5$	380/ 25	101	287	60/ 300	100	246

6.6 Compressor-driven coupled reactor system

For the thermal-driven MH-based TES system, the role of the LTMH is limited to H_2 storage. During the discharging of the coupled reactor system, the pressure of H_2 coming out from the LTMH is less than the pressure of absorption during the charging process due to the hysteresis effect in LTMH (Bogdanovic et al., 1995), leading to the reduction in the driving potential. The temperature of energy release in HTMH decreases because of the drop in H_2 pressure from the LTMH. A compressor-driven MH-based TES system is proposed to overcome this drawback.

The proposed compressor-driven MH-based TES consists of HTMH, compressor, and LTMH. The schematic of the compressor-driven MH-based TES system is shown in Fig. 6. 17. The compressor is connected between HTMH and LTMH. The LTMH is connected on the suction side, while the HTMH is connected on the delivery side of the compressor. The charging process of the compressor-driven system is the same as that of the thermal-driven system (Fig. 6. 17(a)). Towards the end of the charging process, the LTMH is saturated with hydrogen, while the HTMH is in desorbed condition. During the discharging process (Fig. 6. 17(b)), the proposed system drives the hydrogen from LTMH to HTMH with the help of a compressor. A cooling effect is generated in the LTMH due to hydrogen desorption to the suction side of the compressor. The compressed hydrogen is supplied to the HTMH from the delivery side of the compressor. The HTMH releases heat by absorbing H_2 from the delivery side of the compressor. The heat released from HTMH is utilized as per the demand. Further, to obtain simultaneous cooling and heat up-gradation, the delivery pressure of the compressor is set to a higher value than the desorbing pressure of HTMH during the charging process.

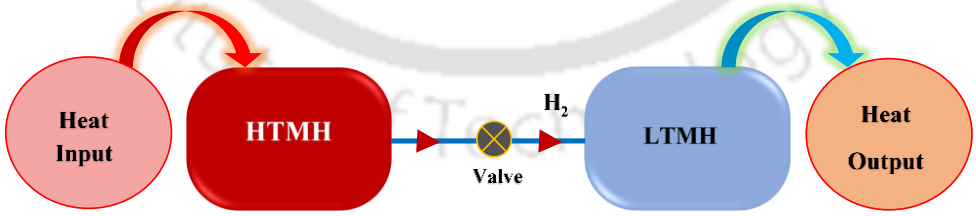

(a). Charging process

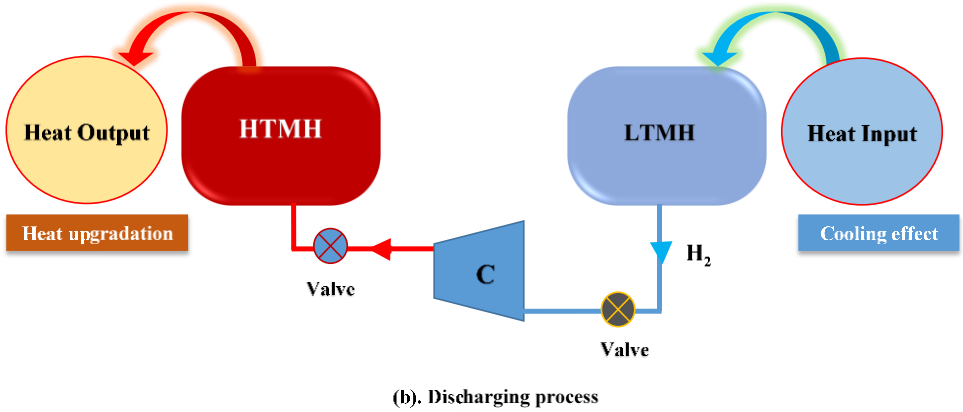

Fig. 6. 17. (a) Charging and (b) discharging processes of compressor-driven MH-based TES system

The discharging process of the compressor-driven MH-based TES system is studied with magnesium-nickel alloy/ $La_{0.7}Ce_{0.1}Ca_{0.3}Ni_5$ pair. The system is operated for the LTMH's ($La_{0.7}Ce_{0.1}Ca_{0.3}Ni_5$) desorption temperature of 20°C and HTMH's (magnesium-nickel alloy) absorption temperature of 300°C. An electrically driven water-cooled reciprocating compressor (designed for R-134a), with customized fireproof winding, is used for hydrogen compression from LTMH to HTMH. The oil separator fitted to the compressor has a maximum delivery pressure limit of 20 bar. Hence, the delivery pressure of the compressor is limited to below 20 bar. Before the discharging process, the LTMH was charged with 119 g of hydrogen at a 15-bar supply pressure, and the HTMH was in a desorbed state. The temperature profiles, pressure profiles, and mass of hydrogen transferred during discharging process of the compressor-driven MH-based TES system are presented in Fig. 6. 18. During the discharging process, the rate of absorption in the magnesium-nickel alloy is lower than the compression rate. Due to this, the delivery pressure increased continuously. Therefore, the compressor was operated in ON/ OFF mode to limit its delivery pressure below the 20 bar. The main reasons for the continuous rise of the delivery pressure of the compressor are slower reaction kinetics of magnesium-nickel alloy than the $La_{0.7}Ce_{0.1}Ca_{0.3}Ni_5$ alloy and the air as an HTF in magnesium-nickel alloy reactor. The desorption rate from $La_{0.7}Ce_{0.1}Ca_{0.3}Ni_5$ is higher than the absorption rate in the magnesium-nickel alloy, due to which the pressure on the delivery side of the compressor rises. Further, air as an HTF in the magnesium-nickel alloy reactor showed lower heat transfer characteristics than water in $La_{0.7}Ce_{0.1}Ca_{0.3}Ni_5$.

Due to ON/ OFF mode of the compressor, the pressure on the suction side of the compressor is varied between the suction pressure of the compressor and equilibrium pressure of $La_{0.7}Ce_{0.1}Ca_{0.3}Ni_5$ as shown in Fig. 6. 18a. The similar behavior was observed for magnesium-

nickel alloy (Fig. 6. 18c) where the pressure was cycled between equilibrium pressure of magnesium-nickel alloy and delivery pressure of the compressor. From Fig. 6. 18b, it is observed that the MH bed temperature of $La_{0.7}Ce_{0.1}Ca_{0.3}Ni_5$ experienced simultaneous desorption and sensible heating due to the ON/ OFF mode of the compressor. The TC4 of $La_{0.7}Ce_{0.1}Ca_{0.3}Ni_5$ reached as low as 9°C during desorption. Further, the peak ΔT of 12°C was obtained in the outlet air temperature of the magnesium-nickel alloy (Fig. 6. 18d). The mass of hydrogen transferred between the reactors is shown in Fig. 6. 18e. A total of 103 g of hydrogen was transferred between the reactors. The discharging time for ON/ OFF mode is 210 min. Whereas the actual time of hydrogen transfer in ON mode is 97 min. Therefore, with the help of the compressor, the LTMH desorbed 103 g of hydrogen in 97 min at 20°C with an additional cooling effect produced. The discharging time of the magnesium-nickel alloy/ $La_{0.7}Ce_{0.1}Ca_{0.3}Ni_5$ pair in thermal-driven mode (60°C/ 300°C) is reduced by 2.16 times with the help of the compressor.

From the discharging results of the compressor-driven MH-based TES system, it is observed that it is possible to produce cooling from LTMH. However, care has to be taken to obtain similar heat transfer characteristics in both reactors, such that near constant pressures are maintained on the suction and delivery side of the compressor.

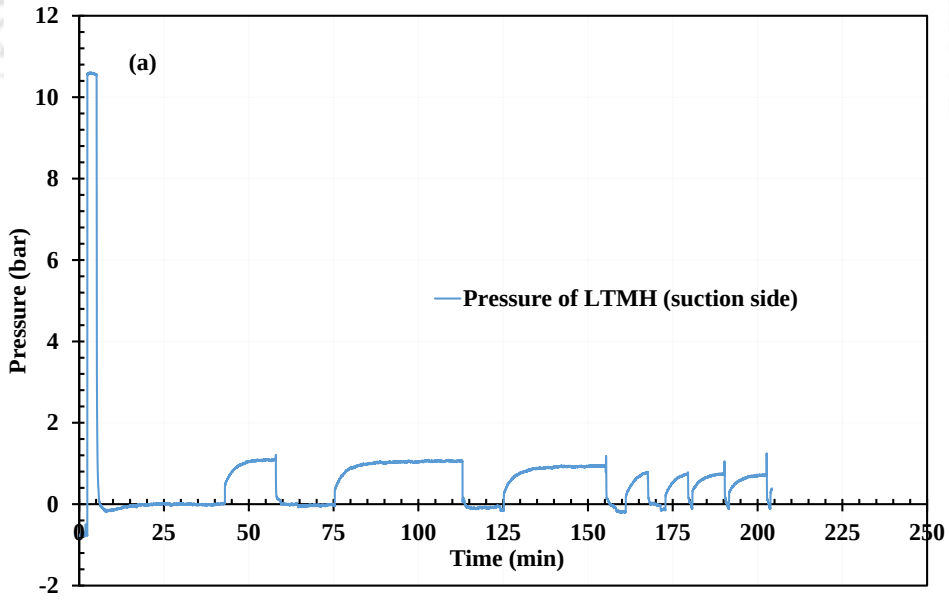

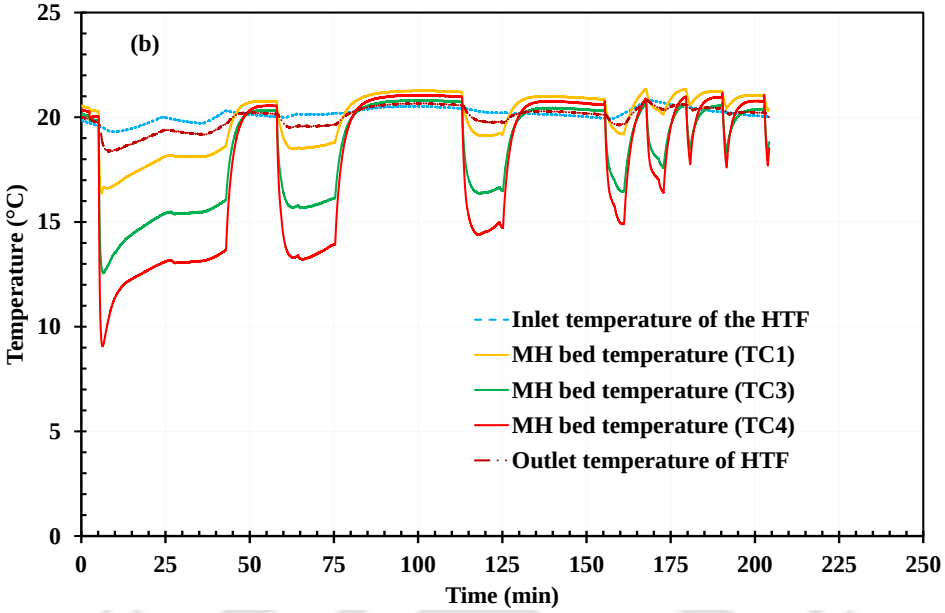

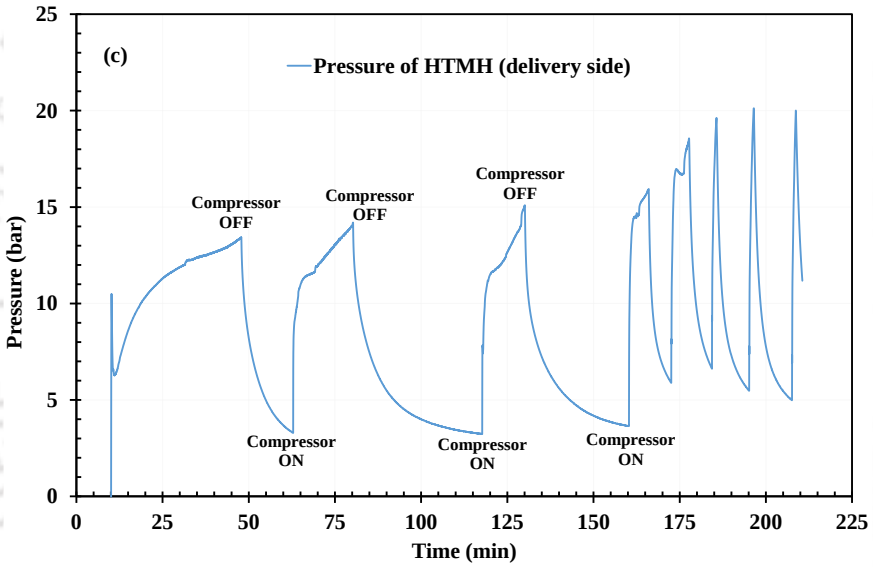

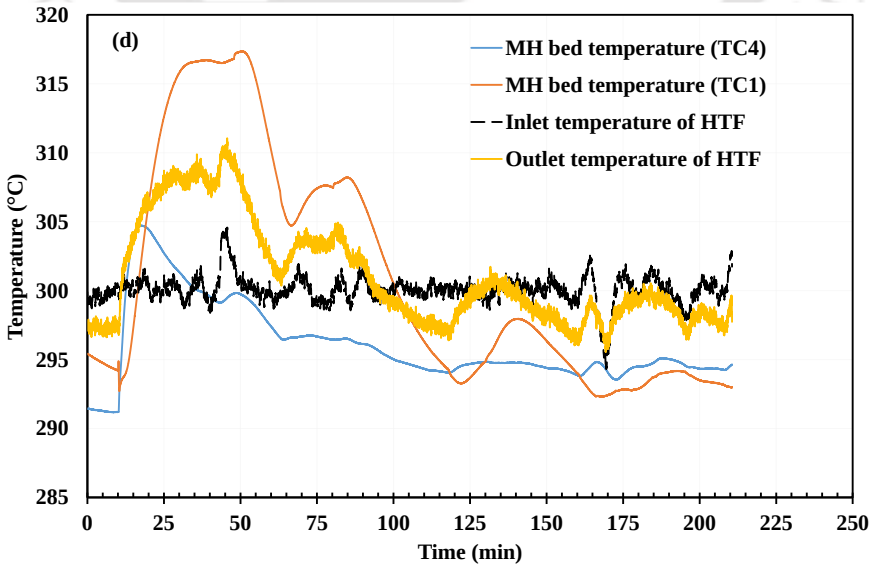

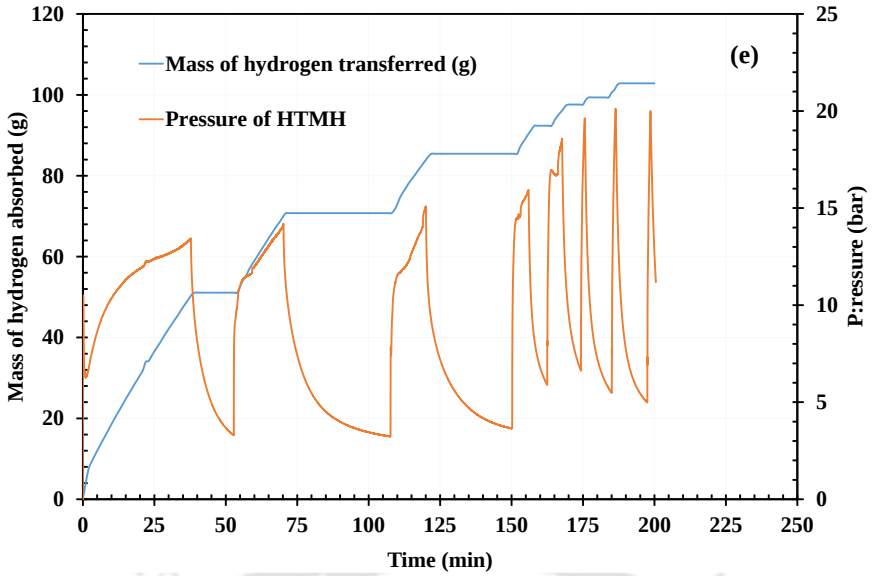

Fig. 6. 18. Discharging processes of compressor-driven MH-based TES system (a) pressure of LTMH (b) temperatures of LTMH (c) pressure of HTMH (d) temperatures of HTMH and (e) mass of hydrogen transferred

6.7 Summary

The annular metal hydride reactor with internal radial fins was experimented for thermal energy storage application. The magnesium-nickel alloy and air are chosen as MH material and HTF for the experiments. The reactor was filled with 3.76 kg of magnesium-nickel alloy. Firstly, the absorption and desorption characteristics of the magnesium-nickel alloy were studied in a single reactor mode. Further, two alloy pairs: magnesium-nickel alloy/ $LaNi_5$ and magnesium-nickel alloy/ $La_{0.7}Ce_{0.1}Ca_{0.3}Ni_5$, were studied in coupled reactor mode under different operating conditions. Finally, a compressor-driven MH-based TES system is proposed to produce an additional cooling effect in the LTMH reactor. The following are the significant observations from the experimental study of the energy storage module.

6.7.1 HTMH in single reactor mode

- Magnesium-nickel alloy is activated in the seventh activation cycle, reaching 3.91 wt.%.

- The alloy absorbed 104, 142, and 143 g of hydrogen in 122, 78.3, and 62.5 min, respectively, under the supply pressure of 10, 20, and 30 bar. Increasing the supply pressure from 20 bar to 30 bar did not significantly enhance the absorption rate.

- Desorption time is approximately two times more than the absorption time. Increasing the desorption temperature has not shown any significant effect on the rate of desorption.

6.7.2 HTMH in coupled reactor mode

- The charging and discharging times are within 360 min, except for charging at 374°C for Magnesium-nickel alloy/ $La_{0.7}Ce_{0.1}Ca_{0.3}Ni_5$.
- In the thermal-driven system, the line pressure was influenced by the equilibrium pressure of LTMH due to its faster reaction kinetics and better heat transfer characteristics.
- The discharging time of the thermal-driven system is reduced by 2.16 times with the help of the compressor-driven system.
- In the compressor-driven system, the cooling effect is produced in the LTMH and hydrogen is transferred faster than in the thermal-driven system.

The annular MH reactor design showed promising heat transfer characteristics in single and coupled reactor modes. The obtained charging and discharging times were within the DOE target limit for the given operating conditions. Therefore, the annular MH reactor design is promising for large-scale TES applications.

The coupled reactor experiments showed promising charging and discharging times in the present work. However, the sizing of the LTMH and HTMH is not done for an equal amount of hydrogen. The main reasons for this are the degradation of the storage capacity of LTMH after 20 cycles and the presence of excess magnesium in the procured Mg_2Ni alloy. Also, the proposed compressor-driven MH-based TES is not operated continuously due to the limitation of the delivery pressure of the compressor. Also, the delivery side pressure of the compressor continuously increased due to poor reaction kinetics and heat transfer characteristics of the magnesium-nickel alloy. Therefore, it is suggested that the proposed coupled reactor systems should be tested with any liquid HTF in the magnesium-nickel alloy reactor for equal hydrogen storage capacity in HTMH and LTMH. The liquid HTF in the magnesium-nickel alloy reactor improves the heat transfer characteristics and enables the complete hydrogen transfer between the reactors at a reasonable rate. Also, the increasing pressure in compressor-driven MH-based TES systems could be eliminated with liquid HTF in the magnesium-nickel alloy reactor.

Chapter 7

Conclusions and Future scope

The significant conclusions obtained from the numerical and experimental studies of the MH-based TES system and hydrogen storage system are presented in this chapter. Further, this chapter summarizes the outcomes of the coupled MH reactor system.

7.1 Numerical studies

A numerical model is developed to investigate the heat and mass transfer characteristics of the MH reactors. Firstly, the model is used to analyze the discharging behavior of the tubular reactors for TES application. Based on the outcomes, an annular MH reactor is proposed to have higher energy storage density and lower discharging times. Magnesium-nickel hydride and Therminol VP1 are considered as MH material and heat transfer fluid for the analysis. Later the model is extended to analyze the absorption and desorption characteristics of the $LaNi_5$ with HTF flow simulation for hydrogen storage application. Three configurations of annular MH reactor are compared to analyze the effect of fluid flow direction and adding radial fins on the absorption and desorption processes of $LaNi_5$. Further, a sensitivity analysis is carried out on the annular MH reactor with radial fins to study the impact of operating parameters on absorption and desorption times. Furthermore, the performance of the finned tube reactor is compared with the literature. The abstract conclusions arrived from the numerical studies are summarized below.

7.1.1 Thermal energy storage module/ HTMH reactor

- The discharging time increased with the diameter of the tubular reactor. The smaller tubular reactors provided a lesser volume to surface area ratio, due to which higher discharging rates were achieved. However, the energy storage density increased with the diameter of the tubular reactor.
- The major drawbacks of a smaller diameter tubular reactor are less energy storage density and the requirement of a greater number of tubes for the given energy storage capacity. For the storage capacity equivalent to a 2.5-inch reactor, approximately 25 3/8-inch tubular reactors are needed.

- With an annular MH reactor design, the discharging time of a 2.5-inch tubular reactor is reduced up to 70%, with only a 16% compromise in gravimetric energy storage density. Also, the average specific discharge power of the 2.5-inch tubular reactor is increased by ~2.5 times with the annular MH reactor.
- For real-time TES storage applications, the discharging time of the reactors present near the MH array outlet section is much higher than the DOE target's limit. The discharging time for HTF temperature of 250°C (boundary condition for MH reactors present near the inlet section of the array) is 4.7 times lower than the 300°C (boundary condition for MH reactors present near the outlet section of the array).
- The annular MH reactor with radial fins reduced the discharging time of the reactors present near the outlet section of the MH array to 333 min, i.e., 1.93 times lower than the case without fins.
- For the given storage capacity, the annular MH reactor achieved thermal performance equivalent to a 1-inch reactor, and the number of reactors was reduced from five to one. Whereas the annular MH reactor with radial fins achieved thermal performance equivalent to a 3/8-inch reactor, the number of reactors was reduced from seven to one.

7.1.2 Hydrogen storage module/ LTMH reactor

- For $LaNi_5$, adding fins enhanced the absorption and desorption rates by a factor of 1.84 and 1.85, respectively.
- Changing the HTF flow direction (configuration 2) enhanced the peak outlet temperature by 5.7°C during absorption and 3.33°C during desorption.
- From sensitivity analysis, it is observed that the supply pressure and desorption temperature are the most influencing parameters during the absorption and desorption processes, respectively.
- The absorption performance of configuration 3 is compared with the literature. It is observed that the heat transfer rate is much better with radial fins inside the annular MH reactor than in tube bundle and multi-tube reactors.

7.2 Experimental studies: LTMH reactor

The designed annular metal hydride reactor with internal radial fins was fabricated. Two different alloys, $LaNi_5$ and $La_{0.7}Ce_{0.1}Ca_{0.3}Ni_5$, were tested for hydrogen storage under different operating conditions. A mass of 9 kg was filled inside the reactor for each alloy. The developed

MH reactor offered a hydride-to-reactor mass ratio of 1.44 with a working pressure of 80 bar. Further, the results of $LaNi_5$ were compared with the published results for an embedded cooling tube reactor with an outer cooling jacket. Also, the energy efficiency of the solid-state hydrogen storage with $La_{0.7}Ce_{0.1}Ca_{0.3}Ni_5$ was evaluated. Finally, the results of $LaNi_5$ and $La_{0.7}Ce_{0.1}Ca_{0.3}Ni_5$ were compared. The key conclusions of the experiments on hydrogen storage reactors are summarized below.

- $LaNi_5$ reactor showed a system gravimetric and volumetric storage densities of 0.73% and 20.4 kg of H_2 per m^3, respectively.
- The comparison results showed that the annular MH reactor with radial fins reduced the absorption/ desorption times by at least 44% than the ECT reactor with an outer cooling jacket studied by Karmakar et al., (2021).
- The comparison results also revealed better absorption and desorption rates with a lesser HTF flow rate when the internal heat transfer enhancement is provided, which saves the pumping power.
- The $La_{0.7}Ce_{0.1}Ca_{0.3}Ni_5$-based hydrogen storage system offered a system-level gravimetric storage density of 0.8% and a volumetric storage density of 22.4 kg of H_2 per m^3.
- The energy storage efficiency of $La_{0.7}Ce_{0.1}Ca_{0.}3Ni_5$ based hydrogen storage system is 77.54%.
- The alloy $La_{0.7}Ce_{0.1}Ca_{0.3}Ni_5$ exhibited faster absorption characteristics and slower desorption characteristics. However, $La_{0.7}Ce_{0.1}Ca_{0.3}Ni_5$ exhibited steady desorbing behavior, which is suitable for fuel cell applications.
- The desorption process without pre-sensible heating was found to be more efficient. The overall desorption time and pumping power were reduced by 46.5% and 58.6%, respectively, with desorption without pre-sensible heating.

7.3 Experimental studies: HTMH reactor

7.3.1 HTMH in single reactor mode

- Magnesium-nickel alloy is activated in the seventh activation cycle, reaching 3.91 wt.%.

- The alloy absorbed 104, 142, and 143 g of hydrogen in 122, 78.3, and 62.5 min, respectively, under the supply pressure of 10, 20, and 30 bar. Increasing the supply pressure from 20 bar to 30 bar did not significantly enhance the absorption rate.

- Desorption time is approximately two times more than the absorption time. Increasing the desorption temperature has not shown any significant effect on the rate of desorption.

7.3.2 HTMH in coupled reactor mode

- For thermal-driven coupled reactor system, the charging and discharging times are obtained within 360 min. However, the charging time at 374°C for the magnesium-nickel alloy/ $La_{0.7}Ce_{0.1}Ca_{0.3}Ni_5$ is 377 min.

- In the thermal-driven coupled reactor system, the line pressure was influenced by the equilibrium pressure of LTMH due to its faster reaction kinetics and better heat transfer characteristics.

- In the compressor-driven system, the cooling effect is produced in the LTMH and hydrogen is transferred faster than in the thermal-driven system. The discharging time of the thermal-driven system is reduced by 2.16 times with the help of the compressor-driven system.

7.4 Scope for future work

The works presented in this thesis offer opportunities to broaden the research on MH-based thermal energy and hydrogen storage systems. Some of the scopes for future work are given below:

- The possible reasons for the decrease in the material storage capacity are a decrease in particle size, contamination with impurities that might be present in the gas, amorphization, disproportionation, and the appearance of stable phases. Therefore, an extensive analysis can be performed to identify the exact reasons for the drop in the storage capacity of the MH alloys.
- In coupled reactor systems, the hydrogen transfer rate is limited by the poor reaction kinetics of the high-temperature metal hydride. Hence, the reaction kinetics and heat transfer characteristics of the high-temperature metal hydride reactor should be enhanced.

- The coupled reactor system developed in the present study should be tested with any liquid HTF in the magnesium-nickel alloy reactor and with equal hydrogen storage capacity in HTMH and LTMH. This enables complete hydrogen transfer between the reactors at a reasonable rate. Also, the increasing pressure in the compressor-driven MH-based TES system could be eliminated with liquid HTF in the magnesium-nickel alloy reactor.
- The compressor driven system is promising for generating cooling and heating effect simultaneously. However, the tests has to be conducted with a compressor especially designed for hydrogen gas.
- The possibility of modeling a compressor-driven coupled reactor system could be explored to study the effect of different operating parameters on its performance.

References

Afzal, M., Gupta, N., Mallik, A., Vishnulal, K.S., Pratibha, S., 2021. Experimental analysis of a metal hydride hydrogen storage system with hexagonal honeycomb-based heat transfer enhancements-part B. Int. J. Hydrogen Energy 46, 13131–13141. https://doi.org/10.1016/j.ijhydene.2020.11.275

Afzal, M., Sharma, P., 2018. Design of a large-scale metal hydride based hydrogen storage reactor: Simulation and heat transfer optimization. Int. J. Hydrogen Energy 43, 13356–13372. https://doi.org/10.1016/j.ijhydene.2018.05.084

Agrafiotis, C., Roeb, M., Sattler, C., 2016. Exploitation of thermochemical cycles based on solid oxide redox systems for thermochemical storage of solar heat. Part 4: Screening of oxides for use in cascaded thermochemical storage concepts. Sol. Energy 139, 695–710. https://doi.org/10.1016/j.solener.2016.04.034

Agrafiotis, C., Roeb, M., Sattler, C., 2014. Cobalt oxide-based structured thermochemical reactors/heat exchangers for solar thermal energy storage in concentrated solar power plants, in: Proceedings of the ASME 2014 8th International Conference on Energy Sustainability. pp. 1–8. https://doi.org/10.1115/ES2014-6336

Ahluwalia, R.K., 2007. Sodium alanate hydrogen storage system for automotive fuel cells. Int. J. Hydrogen Energy 32, 1251–1261. https://doi.org/10.1016/j.ijhydene.2006.07.027

Akikur, R., 2014. Application of Solar Energy and Reversible Solid Oxide Fuel Cell in a Co-Generation System. Int. J. Innov. Manag. Technol. 5, 134–138. https://doi.org/10.7763/IJIMT.2014.V5.501

Álvarez De Miguel, S., Gonzalez-Aguilar, J., Romero, M., 2013. 100-Wh multi-purpose particle reactor for thermochemical heat storage in concentrating solar power plants. Energy Procedia 49, 676–683. https://doi.org/10.1016/j.egypro.2014.03.073

Anbarasu, S., Muthukumar, P., Mishra, S.C., 2014. Thermal modeling of LmNi4.91Sn0.15 based solid state hydrogen storage device with embedded cooling tubes. Int. J. Hydrogen Energy 39, 15549–15562. https://doi.org/10.1016/j.ijhydene.2014.07.088

André, L., Abanades, S., 2017. Evaluation and performances comparison of calcium, strontium and barium carbonates during calcination/carbonation reactions for solar thermochemical energy storage. J. Energy Storage 13, 193–205. https://doi.org/10.1016/j.est.2017.07.014

André, L., Abanades, S., Flamant, G., 2016. Screening of thermochemical systems based on solid-gas reversible reactions for high temperature solar thermal energy storage. Renew.

Sustain. Energy Rev. 64, 703–715. https://doi.org/10.1016/j.rser.2016.06.043

Andreasen, G., Melnichuk, M., Ramos, S., Corso, H.L., Visintin, A., Triaca, W.E., Peretti, H.A., 2013. Hydrogen desorption from a hydride container under different heat exchange conditions. Int. J. Hydrogen Energy 38, 13352–13359. https://doi.org/10.1016/j.ijhydene.2013.07.115

Andreasen, G.A., Ramos, S.G., Peretti, H.A., Triaca, W.E., 2016. Performance of a thermally coupled hydrogen storage and fuel cell system under different operation conditions. J. Electrochem. Energy Convers. Storage 13, 1–7. https://doi.org/10.1115/1.4035100

Ao, B.Y., Chen, S.X., Jiang, G.Q., 2005. A study on wall stresses induced by LaNi5 alloy hydrogen absorption-desorption cycles. J. Alloys Compd. 390, 122–126. https://doi.org/10.1016/j.jallcom.2004.05.092

Ardahaie, S.S., Hosseini, M.J., Eisapour, M., Eisapour, A.H., Ranjbar, A.A., 2021a. A novel porous metal hydride tank for hydrogen energy storage and consumption assisted by PCM jackets and spiral tubes. J. Clean. Prod. 311, 127674. https://doi.org/10.1016/j.jclepro.2021.127674

Ardahaie, S.S., Hosseini, M.J., Eisapour, M., Eisapour, A.H., Ranjbar, A.A., 2021b. A novel porous metal hydride tank for hydrogen energy storage and consumption assisted by PCM jackets and spiral tubes. J. Clean. Prod. 311, 127674. https://doi.org/10.1016/j.jclepro.2021.127674

Aswin, N., Dutta, P., Murthy, S.S., 2016. Screening of metal hydride pairs for closed thermal energy storage systems. Appl. Therm. Eng. 109, 949–957. https://doi.org/10.1016/j.applthermaleng.2016.04.129

Badding, M.E., McCormack, M.T., Murphy, D.W., Vyas, B., 1996. Process for activation of metal hydrides. US00556O752A.

Bagherisereshki, E., Tran, J., Lei, F., AuYeung, N., 2018. Investigation into SrO/SrCO3for high temperature thermochemical energy storage. Sol. Energy 160, 85–93. https://doi.org/10.1016/j.solener.2017.11.073

Bao, Z., Yang, F., Wu, Z., Cao, X., Zhang, Z., 2013. Simulation studies on heat and mass transfer in high-temperature magnesium hydride reactors. Appl. Energy 112, 1181–1189. https://doi.org/10.1016/j.apenergy.2013.04.053

Bedbak, S.S., Gopal, M.R., 2005. Performance analysis of a compressor driven metal hydride cooling system. Int. J. Hydrogen Energy 30, 1127–1137. https://doi.org/10.1016/j.ijhydene.2004.10.014

Bedrunka, M., Bornemann, N., Steinebach, G., Reith, D., 2021. A metal hydride system for a

forklift: Feasibility study on on-board chemical storage of hydrogen using numerical simulation. Int. J. Hydrogen Energy. https://doi.org/10.1016/j.ijhydene.2021.05.179

Ben Mâad, H., Askri, F., Ben Nasrallah, S., 2013. Numerical investigation of heat and mass transfer during the desorption process of an Mg2Ni-H2 reactor. Int. J. Hydrogen Energy 38, 4597–4610. https://doi.org/10.1016/j.ijhydene.2013.01.144

Ben Mâad, H., Askri, F., Virgone, J., Ben Nasrallah, S., 2018. Numerical study of high temperature metal-hydrogen reactor (Mg2Ni-H2) with heat reaction recovery using phase-change material during desorption. Appl. Therm. Eng. 140, 225–234. https://doi.org/10.1016/j.applthermaleng.2018.05.009

Bhogilla, S.S., 2021. Numerical simulation of metal hydride based thermal energy storage system for concentrating solar power plants. Renew. Energy 172, 1013–1020. https://doi.org/10.1016/j.renene.2021.03.109

Bogdanovi, B., Reiser, A., Schlichte, K., Spliethoff, B., Tesche, B., 2002. Thermodynamics and dynamics of the Mg-Fe-H system and its potential for thermochemical thermal energy storage. J. Alloys Compd. 345, 77–89. https://doi.org/10.1016/S0925-8388(02)00308-0

Bogdanovic, B., Ritter, A., Spliethoff, B., 1990. Active MgH2-Mg Systems for Reversible Chemical Energy Storage. Angew. Chemie Int. Ed. English 29, 223–328. https://doi.org/10.1002/anie.197506551

Bogdanovic, B., Ritter, A., Spliethoff, B., Straburger, K., 1995. A process steam generator based on the high temperature magnesium hydride/magnesium heat storage system. Int. J. Hydrog. Energy 20, 811–822. https://doi.org/10.1016/0360-3199(93)90178-D

Bogdanovlc, B., Hartwing, T., Spliethoff, B., 1993. The development , testing and optimization of energy storage materials based on the MgH2 - Mg system. Int. J. Hydrogen Energy 18, 575–589. https://doi.org/doi.org/10.1016/0360-3199(93)90178-D

Boukhari, A., Bessaïh, R., 2015. Numerical heat and mass transfer investigation of hydrogen absorption in an annulus-disc reactor. Int. J. Hydrogen Energy 40, 13708–13717. https://doi.org/10.1016/j.ijhydene.2015.05.123

Bowrey, R.G., Jutsen, J., 1978. Energy storage using the reversible oxidation of barium oxide. Sol. Energy 21, 523–525. https://doi.org/10.1016/0038-092X(78)90078-6

Bürger, I., Dieterich, M., Pohlmann, C., Röntzsch, L., Linder, M., 2017. Standardized hydrogen storage module with high utilization factor based on metal hydride-graphite composites. J. Power Sources 342, 970–979. https://doi.org/10.1016/j.jpowsour.2016.12.108

Bürger, I., Sourmelis Terzopoulos, V.E., Kretschmer, C., Kölbig, M., Brack, C., Linder, M., 2021. Lightweight reactor design by additive manufacturing for preheating applications

using metal hydrides. Int. J. Hydrogen Energy 46, 28686–28699. https://doi.org/10.1016/j.ijhydene.2021.06.091

Busqué, R., Torres, R., Grau, J., Roda, V., Husar, A., 2018. Mathematical modeling, numerical simulation and experimental comparison of the desorption process in a metal hydride hydrogen storage system. Int. J. Hydrogen Energy 43, 16929–16940. https://doi.org/10.1016/j.ijhydene.2017.12.172

Busqué, R., Torres, R., Grau, J., Roda, V., Husar, A., 2017. Effect of metal hydride properties in hydrogen absorption through 2D-axisymmetric modeling and experimental testing in storage canisters. Int. J. Hydrogen Energy 42, 19114–19125. https://doi.org/10.1016/j.ijhydene.2017.06.125

Chabane, D., Harel, F., Djerdir, A., Candusso, D., Elkedim, O., Fenineche, N., 2019. Energetic modeling, simulation and experimental of hydrogen desorption in a hydride tank. Int. J. Hydrogen Energy 44, 1034–1046. https://doi.org/10.1016/j.ijhydene.2018.11.024

Chaise, A., De Rango, P., Marty, P., Fruchart, D., 2010. Experimental and numerical study of a magnesium hydride tank. Int. J. Hydrogen Energy 35, 6311–6322. https://doi.org/10.1016/j.ijhydene.2010.03.057

Chandra, S., Sharma, P., Muthukumar, P., Tatiparti, S.S. V., 2020. Modeling and numerical simulation of a 5 kg LaNi5-based hydrogen storage reactor with internal conical fins. Int. J. Hydrogen Energy 45, 8794–8809. https://doi.org/10.1016/j.ijhydene.2020.01.115

Chung, C.A., Yang, S.W., Yang, C.Y., Hsu, C.W., Chiu, P.Y., 2013. Experimental study on the hydrogen charge and discharge rates of metal hydride tanks using heat pipes to enhance heat transfer. Appl. Energy 103, 581–587. https://doi.org/10.1016/j.apenergy.2012.10.024

Corgnale, Claudio, Hardy, B., Motyka, T., Zidan, R., Teprovich, J., Peters, B., 2014. Screening analysis of metal hydride based thermal energy storage systems for concentrating solar power plants. Renew. Sustain. Energy Rev. 38, 821–833. https://doi.org/10.1016/j.rser.2014.07.049

Corgnale, C., Hardy, B., Motyka, T., Zidan, R., Teprovich, J., Peters, B., 2014. Screening analysis of metal hydride based thermal energy storage systems for concentrating solar power plants. Renew. Sustain. Energy Rev. 38, 821–833. https://doi.org/10.1016/j.rser.2014.07.049

d'Entremont, A., Corgnale, C., Hardy, B., Zidan, R., 2018. Simulation of high temperature thermal energy storage system based on coupled metal hydrides for solar driven steam power plants. Int. J. Hydrogen Energy 43, 817–830.

https://doi.org/10.1016/j.ijhydene.2017.11.100

d'Entremont, A., Corgnale, C., Sulic, M., Hardy, B., Zidan, R., Motyka, T., 2017. Modeling of a thermal energy storage system based on coupled metal hydrides (magnesium iron – sodium alanate) for concentrating solar power plants. Int. J. Hydrogen Energy 42, 22518–22529. https://doi.org/10.1016/j.ijhydene.2017.04.231

Davids, M.W., Tolj, I., Jao, T.-C., Lototskyy, M., Pasupathi, S., Sita, C., 2016. Development of a Portable Polymer Electrolyte Membrane Fuel Cell System Using Metal Hydride as the Hydrogen Storage Medium. ECS Trans. 75, 553–562. https://doi.org/10.1149/07514.0553ecst

Delhomme, B., De Rango, P., Marty, P., Bacia, M., Zawilski, B., Raufast, C., Miraglia, S., Fruchart, D., 2012. Large scale magnesium hydride tank coupled with an external heat source. Int. J. Hydrogen Energy 37, 9103–9111. https://doi.org/10.1016/j.ijhydene.2012.03.018

Delhomme, B., Lanzini, A., Ortigoza-Villalba, G.A., Nachev, S., De Rango, P., Santarelli, M., Marty, P., Leone, P., 2013. Coupling and thermal integration of a solid oxide fuel cell with a magnesium hydride tank. Int. J. Hydrogen Energy 38, 4740–4747. https://doi.org/10.1016/j.ijhydene.2013.01.140

Di Giorgio, P., Desideri, U., 2016. Potential of reversible solid oxide cells as electricity storage system. Energies 9. https://doi.org/10.3390/en9080662

Dubey, S.K., Kumar, K.R., 2022. Charging and discharging analysis of thermal energy using magnesium nickel hydride based thermochemical energy storage system. Sustain. Energy Technol. Assessments 52, 101994. https://doi.org/10.1016/j.seta.2022.101994

Dunn, B.R., Lovegrove, K., Burgess, G., 2012. A Review of Ammonia-Based Thermochemical Energy Storage for Concentrating Solar Power. Proc. IEEE 100, 391–400. https://doi.org/10.1109/JPROC.2011.2166529

Eichman, J.D., Koleva, M., Guerra Fernandez, O.J., McLaughlin, B., 2020. Optimizing an Integrated Renewable-Electrolysis System, NREL.

Eisapour, A.H., Eisapour, M., Talebizadehsardari, P., Walker, G.S., 2021a. An innovative multi-zone configuration to enhance the charging process of magnesium based metal hydride hydrogen storage tank. J. Energy Storage 36, 102443. https://doi.org/10.1016/j.est.2021.102443

Eisapour, A.H., Naghizadeh, A., Eisapour, M., Talebizadehsardari, P., 2021b. Optimal design of a metal hydride hydrogen storage bed using a helical coil heat exchanger along with a central return tube during the absorption process. Int. J. Hydrogen Energy 46, 14478–

14493. https://doi.org/10.1016/j.ijhydene.2021.01.170

El-Eskandarany, M.S., 2020. Solid-state hydrogen storage nanomaterials for fuel cell applications, in: M. Sherif El-Eskandarany (Ed.), Mechanical Alloying. William Andrew Publishing, pp. 229–261. https://doi.org/10.1016/b978-0-12-818180-5.00009-1

Erin, R.P., 2016. Top 6 Things You Didn't Know About Solar Energy [WWW Document]. Dep. Energy. URL https://www.energy.gov/articles/top-6-things-you-didnt-know-about-solar-energy (accessed 6.6.18).

Ervin, G., 1977. Solar heat storage using chemical reactions. J. Solid State Chem. 22, 51–61. https://doi.org/10.1016/0022-4596(77)90188-8

Fahim, M.A., Ford, J.D., 1983. Energy storage using the BaO2/ BaO reaction cycle. Chem. Eng. J. 27, 21–28. https://doi.org/10.1016/0300-9467(83)80042-2

Fang, Z.Z., Zhou, C., Fan, P., Udell, K.S., Bowman, R.C., Vajo, J.J., Purewal, J.J., Kekelia, B., 2015. Metal hydrides based high energy density thermal battery. J. Alloys Compd. 645, S184–S189. https://doi.org/10.1016/j.jallcom.2014.12.260

Felderhoff, M., Bogdanović, B., 2009. High temperature metal hydrides as heat storage materials for solar and related applications. Int. J. Mol. Sci. 10, 335–344. https://doi.org/10.3390/ijms10010325

Feng, P., Liu, Y., Ayub, I., Wu, Z., Yang, F., Zhang, Z., 2019a. Techno-economic analysis of screening metal hydride pairs for a 910 MWhth thermal energy storage system. Appl. Energy 242, 148–156. https://doi.org/10.1016/j.apenergy.2019.03.046

Feng, P., Wu, Z., Zhang, Y., Yang, F., Wang, Y., Zhang, Z., 2018. Multi-level configuration and optimization of a thermal energy storage system using a metal hydride pair. Appl. Energy 217, 25–36. https://doi.org/10.1016/j.apenergy.2018.02.138

Feng, P., Zhu, L., Zhang, Y., Yang, F., Wu, Z., Zhang, Z., 2019b. Optimum output temperature setting and an improved bed structure of metal hydride hydrogen storage reactor for thermal energy storage. Int. J. Hydrogen Energy 44, 19313–19325. https://doi.org/10.1016/j.ijhydene.2018.04.220

Friedlmeier, G., Wierse, M., Groll, M., 1994. Titanium Hydride for High-Temperature Thermal Energy Storage in Solar-Thermal Power Stations. Zeitschrift fur Phys. Chemie 183, 175–183. https://doi.org/10.1524/zpch.1994.183.Part_1_2.175

Giap, V.T., Lee, Y.D., Kim, Y.S., Ahn, K.Y., 2020. A novel electrical energy storage system based on a reversible solid oxide fuel cell coupled with metal hydrides and waste steam. Appl. Energy 262, 114522. https://doi.org/10.1016/j.apenergy.2020.114522

Gkanas, E.I., Grant, D.M., Khzouz, M., Stuart, A.D., Manickam, K., Walker, G.S., 2016.

Efficient hydrogen storage in up-scale metal hydride tanks as possible metal hydride compression agents equipped with aluminium extended surfaces. Int. J. Hydrogen Energy 41, 10795–10810. https://doi.org/10.1016/j.ijhydene.2016.04.035

Gkanas, E.I., Khzouz, M., 2019. Study on the hydrogenation of an Mm - based AB 5 - intermetallic for sustainable building applications. Int. J. energy Res. 8033–8048. https://doi.org/10.1002/er.4794

Gkanas, E.I., Khzouz, M., Panagakos, G., Statheros, T., Mihalakakou, G., Siasos, G.I., Skodras, G., Makridis, S.S., 2018a. Hydrogenation behavior in rectangular metal hydride tanks under effective heat management processes for green building applications. Energy 142, 518–530. https://doi.org/10.1016/j.energy.2017.10.040

Gkanas, E.I., Khzouz, M., Panagakos, G., Statheros, T., Mihalakakou, G., Siasos, G.I., Skodras, G., Makridis, S.S., 2018b. Hydrogenation behavior in rectangular metal hydride tanks under effective heat management processes for green building applications. Energy 142, 518–530. https://doi.org/10.1016/j.energy.2017.10.040

Gkanas, E.I., Makridis, S.S., 2016. Effective thermal management of a cylindrical MgH2tank including thermal coupling with an operating SOFC and the usage of extended surfaces during the dehydrogenation process. Int. J. Hydrogen Energy 41, 5693–5708. https://doi.org/10.1016/j.ijhydene.2016.01.165

Gonzatti, F., Farret, F.A., 2017. Mathematical and experimental basis to model energy storage systems composed of electrolyzer, metal hydrides and fuel cells. Energy Convers. Manag. 132, 241–250. https://doi.org/10.1016/j.enconman.2016.11.035

Gonzatti, F., Nizolli, V., Ferrigolo, F.Z., Farret, F.A., De Mello, M.A.S., 2016. Experimental Hydrogen Plant with Metal Hydrides to Store and Generate Electrical Power. Int. J. Emerg. Electr. Power Syst. 17, 59–67. https://doi.org/10.1515/ijeeps-2015-0081

Halıcıoğlu, R., Selamet, Ö.F., Bayrak, M., 2013. Effects of reactor design on TiFe-hydride's hydrogen storage. Int. J. energy Res. 37, 698–705. https://doi.org/10.1002/er

Han, G., Kwon, Y.K., Kim, J.B., Lee, S., Bae, J., Cho, E.A., Lee, B.J., Cho, S., Park, J., 2020. Development of a high-energy-density portable/mobile hydrogen energy storage system incorporating an electrolyzer, a metal hydride and a fuel cell. Appl. Energy 259, 114175. https://doi.org/10.1016/j.apenergy.2019.114175

Heubner, F., Mauermann, S., Kieback, B., Röntzsch, L., 2017. Stress development of metal hydride composites for high density hydrogen storage applications. J. Alloys Compd. 705, 176–182. https://doi.org/10.1016/j.jallcom.2017.02.113

IEA, (International Energy Agency), 2019. The Future of Hydrogen: Seizing today's

opportunities. https://doi.org/10.1787/1e0514c4-en

Incropera, F.P., Dewitt, D.P., Bergman, T.L., Lavine, A.S., 2011. Fundamentals of Heat and Mass Transfer, 7th ed. John Wiley & Sons, Inc.

IRENA, 2020. Innovation Outlook: Thermal Energy Storage, International Renewable Energy Agency, Abu Dhabi.

Jafarian, M., Arjomandi, M., Nathan, G.J., 2017. Thermodynamic potential of molten copper oxide for high temperature solar energy storage and oxygen production. Appl. Energy 201, 69–83. https://doi.org/10.1016/j.apenergy.2017.05.049

Jana, S., Muthukumar, P., 2021. Design and Performance Prediction of a Compact MmNi4.6Al0.4 based Hydrogen Storage System. J. Energy Storage 39, 102612. https://doi.org/10.1016/j.est.2021.102612

Javadian, P., 2017. Metal Hydrides as Energy Storage for Concentrated Solar Thermal Applications.

Jehan, M., Fruchart, D., 2013. McPhy-Energy's proposal for solid state hydrogen storage materials and systems. J. Alloys Compd. 580, S343–S348. https://doi.org/10.1016/j.jallcom.2013.03.266

Jiao, K., Li, X., Yin, Y., Zhou, Y., Yu, S., Du, Q., 2012. Effects of various operating conditions on the hydrogen absorption processes in a metal hydride tank. Appl. Energy 94, 257–269. https://doi.org/10.1016/j.apenergy.2012.01.033

Johnson, T.A., Jorgensen, S.W., Dedrick, D.E., 2011. Performance of a full-scale hydrogen-storage tank based on complex hydrides. Faraday Discuss. 151, 327–352. https://doi.org/10.1039/c0fd00017e

Kang, B.H., Yabe, A., 1996. Performance Analysis of a metal-hydride heat transformer for waste heat recovery. Appl. Therm. Eng. 16, 677–690. https://doi.org/doi: 10.1016/1359-4311(95)00080-1

Kang, H. goo, Chung, D. you, Oh, Y.H., Chang, M.H., Yun, S.H., 2016. Experimental comparison on heat transfer-enhancing component of metal hydride bed. Fusion Eng. Des. 109–111, 965–969. https://doi.org/10.1016/j.fusengdes.2016.01.042

Karmakar, A., Mallik, A., Gupta, N., Pratibha, S., 2020. Studies on 10kg alloy mass metal hydride based reactor for hydrogen storage. Int. J. Hydrogen Energy. https://doi.org/10.1016/j.ijhydene.2020.11.091

Karmakar, A., Mallik, A., Gupta, N., Sharma, P., 2021. Studies on 10kg alloy mass metal hydride based reactor for hydrogen storage. Int. J. Hydrogen Energy 46, 5495–5506. https://doi.org/10.1016/j.ijhydene.2020.11.091

Kawamura, M., Ono, S., Higano, S., 1982. Experimental studies on the behaviours of hydride heat storage system. Energy Conserv. Manag. 22, 95–102. https://doi.org/10.1016/0196-8904(82)90030-9

Kawamura, M., Ono, S., Mizuno, Y., 1983. Dynamic characteristics of a hydride heat storage system. J. Less Common Met. 89, 365–372. https://doi.org/10.1016/0022-5088(83)90346-6

Kendall, K., Kendall, M., 2015. High-temperature Solid Oxide Fuel Cells for the 21st Century: Fundamentals, Design and Applications.

Keshari, V., Maiya, M.P., 2018. Design and investigation of hydriding alloy based hydrogen storage reactor integrated with a pin fin tube heat exchanger. Int. J. Hydrogen Energy 43, 7081–7095. https://doi.org/10.1016/j.ijhydene.2018.02.100

Kim, J.B., Han, G., Kwon, Y.K., Bae, J., Cho, E.A., Cho, S.B., Lee, B.J., 2020. Thermal design of a hydrogen storage system using La(Ce)Ni5. Int. J. Hydrogen Energy 45, 8742–8749. https://doi.org/10.1016/j.ijhydene.2020.01.060

Kumar, A., Raju, N.N., Muthukumar, P., 2021. Parametric studies on MmNi4.7Fe0.3 based reactor with embedded cooling tubes for hydrogen storage and cooling application. J. Energy Storage 35, 102317. https://doi.org/10.1016/j.est.2021.102317

Kumar, A., Raju, N.N., Muthukumar, P., Selvan, P.V., 2019. Experimental studies on industrial scale metal hydride based hydrogen storage system with embedded cooling tubes. Int. J. Hydrogen Energy 44, 13549–13560. https://doi.org/10.1016/j.ijhydene.2019.03.180

Kumar, K., Alam, M., Rakshit, D., Dutta, V., 2019. Operational characteristics of metal hydride energy storage system in microgrid. Energy Convers. Manag. 187, 176–190. https://doi.org/10.1016/j.enconman.2019.03.019

Kyaw, K., Shibata, T., Watanabe, F., Matsuda, H., Hasatani, M., 1997. Applicability of zeolite for CO2 storage in a CaO-CO2 high temperature energy storage system. Energy Convers. Manag. 38, 1025–1033. https://doi.org/10.1016/S0196-8904(96)00132-X

Lefebvre, D., Tezel, F.H., 2017. A review of energy storage technologies with a focus on adsorption thermal energy storage processes for heating applications. Renew. Sustain. Energy Rev. 67, 116–125. https://doi.org/10.1016/j.rser.2016.08.019

Lin, X., Zhu, Q., Leng, H., Yang, H., Lyu, T., Li, Q., 2019. Numerical analysis of the effects of particle radius and porosity on hydrogen absorption performances in metal hydride tank. Appl. Energy 250, 1065–1072. https://doi.org/10.1016/j.apenergy.2019.04.181

Linder, M., Mertz, R., Laurien, E., 2010. Experimental analysis of fast metal hydride reaction bed dynamics. Int. J. Hydrogen Energy 35, 8755–8761.

https://doi.org/10.1016/j.ijhydene.2010.05.023

Liu, H., Xu, L., Han, Y., Chen, X., Sheng, P., Wang, S., Huang, X., Wang, X., Lu, C., Luo, H., He, S., Lan, Z., Guo, J., 2021. Development of a gaseous and solid-state hybrid system for stationary hydrogen energy storage. Green Energy Environ. 6, 528–537. https://doi.org/10.1016/j.gee.2020.06.006

Liu, Y., Wang, H., Ayub, I., Yang, F., Wu, Z., Zhang, Z., 2021a. A variable cross-section annular fins type metal hydride reactor for improving the phenomenon of inhomogeneous reaction in the thermal energy storage processes. Appl. Energy 295, 117073. https://doi.org/10.1016/j.apenergy.2021.117073

Liu, Y., Wang, H., Ayub, I., Yang, F., Wu, Z., Zhang, Z., 2021b. A variable cross-section annular fins type metal hydride reactor for improving the phenomenon of inhomogeneous reaction in the thermal energy storage processes. Appl. Energy 295, 117073. https://doi.org/10.1016/j.apenergy.2021.117073

Lototskyy, M., Tolj, I., Klochko, Y., Davids, M.W., Swanepoel, D., Linkov, V., 2020. Metal hydride hydrogen storage tank for fuel cell utility vehicles. Int. J. Hydrogen Energy 45, 7958–7967. https://doi.org/10.1016/j.ijhydene.2019.04.124

Lototskyy, M. V., Tolj, I., Pickering, L., Sita, C., Barbir, F., Yartys, V., 2017. The use of metal hydrides in fuel cell applications. Prog. Nat. Sci. Mater. Int. 27, 3–20. https://doi.org/10.1016/j.pnsc.2017.01.008

Lutz, M., 2021. Coupled Metal Hydride Systems for Energy Storage.

Lutz, M., Bhouri, M., Linder, M., Bürger, I., 2019. Adiabatic magnesium hydride system for hydrogen storage based on thermochemical heat storage: Numerical analysis of the dehydrogenation. Appl. Energy 236, 1034–1048. https://doi.org/10.1016/j.apenergy.2018.12.038

Lutz, M., Linder, M., Bürger, I., 2020. High capacity, low pressure hydrogen storage based on magnesium hydride and thermochemical heat storage: Experimental proof of concept. Appl. Energy 271, 115226. https://doi.org/10.1016/j.apenergy.2020.115226

Malleswararao, K., N, A., Srinivasa Murthy, S., Dutta, P., 2020a. Performance prediction of a coupled metal hydride based thermal energy storage system. Int. J. Hydrogen Energy 45, 16239–16253. https://doi.org/10.1016/j.ijhydene.2020.03.251

Malleswararao, K., N, A., Srinivasa Murthy, S., Dutta, P., 2020b. Performance prediction of a coupled metal hydride based thermal energy storage system. Int. J. Hydrogen Energy. https://doi.org/10.1016/j.ijhydene.2020.03.251

Manickam, K., Mistry, P., Walker, G., Grant, D., Buckley, C.E., Humphries, T.D., Paskevicius,

M., Jensen, T., Albert, R., Peinecke, K., Felderhoff, M., 2019. Future perspectives of thermal energy storage with metal hydrides. Int. J. Hydrogen Energy 44, 7738–7745. https://doi.org/10.1016/j.ijhydene.2018.12.011

Mathew, A., Nadim, N., Chandratilleke, T.T., Humphries, T.D., Paskevicius, M., Buckley, C.E., 2021. Performance analysis of a high-temperature magnesium hydride reactor tank with a helical coil heat exchanger for thermal storage. Int. J. Hydrogen Energy 46, 1038–1055. https://doi.org/10.1016/j.ijhydene.2020.09.191

Mazzucco, A., Dornheim, M., Sloth, M., Jensen, T.R., Jensen, J.O., Rokni, M., 2014. Bed geometries, fueling strategies and optimization of heat exchanger designs in metal hydride storage systems for automotive applications: A review. Int. J. Hydrogen Energy 39, 17054–17074. https://doi.org/10.1016/j.ijhydene.2014.08.047

McElroy, J., Gottmann, M., Finn, J., Mitlitsky, F., 2004. Solid oxide regenerative fuel cell. US6821663B2.

Medrano, M., Gil, A., Martorell, I., Potau, X., Cabeza, L.F., 2010. State of the art on high-temperature thermal energy storage for power generation. Part 2-Case studies. Renew. Sustain. Energy Rev. 14, 56–72. https://doi.org/10.1016/j.rser.2009.07.036

Meier, A., Bonaldi, E., Cella, G.M., Lipinski, W., Wuillemin, D., Palumbo, R., 2004. Design and experimental investigation of a horizontal rotary reactor for the solar thermal production of lime. Energy 29, 811–821. https://doi.org/10.1016/S0360-5442(03)00187-7

Mellouli, S., Abhilash, E., Askri, F., Ben Nasrallah, S., 2016a. Integration of thermal energy storage unit in a metal hydride hydrogen storage tank. Appl. Therm. Eng. 102, 1185–1196. https://doi.org/10.1016/j.applthermaleng.2016.03.116

Mellouli, S., Abhilash, E., Askri, F., Ben Nasrallah, S., 2016b. Integration of thermal energy storage unit in a metal hydride hydrogen storage tank. Appl. Therm. Eng. 102, 1185–1196. https://doi.org/10.1016/j.applthermaleng.2016.03.116

Mellouli, S., Askri, F., Dhaou, H., Jemni, A., Ben Nasrallah, S., 2009a. Numerical study of heat exchanger effects on charge/discharge times of metal-hydrogen storage vessel. Int. J. Hydrogen Energy 34, 3005–3017. https://doi.org/10.1016/j.ijhydene.2008.12.099

Mellouli, S., Askri, F., Dhaou, H., Jemni, A., Ben Nasrallah, S., 2009b. Parametric studies on a metal-hydride cooling system. Int. J. Hydrogen Energy 34, 3945–3952. https://doi.org/10.1016/j.ijhydene.2009.03.010

Mellouli, S., Askri, F., Dhaou, H., Jemni, A., Ben Nasrallah, S., 2007. A novel design of a heat exchanger for a metal-hydrogen reactor. Int. J. Hydrogen Energy 32, 3501–3507.

https://doi.org/10.1016/j.ijhydene.2007.02.039

Mellouli, S., Askri, F., Edacherian, A., Alqahtani, T., Algarni, S., Abdelmajid, J., Phelan, P., 2018. Performance analysis of a thermal energy storage system based on paired metal hydrides for concentrating solar power plants. Appl. Therm. Eng. 144, 1017–1029. https://doi.org/10.1016/j.applthermaleng.2018.09.014

Meng, X., Wu, Z., Bao, Z., Yang, F., Zhang, Z., 2013. Performance simulation and experimental confirmation of a mini-channel metal hydrides reactor. Int. J. Hydrogen Energy 38, 15242–15253. https://doi.org/10.1016/j.ijhydene.2013.09.056

Moffat, R.J., 1988. Describing the Uncertainties in Experimental Results 3–17.

Mohammadshahi, S.S., Gray, E.M.A., Webb, C.J., 2016. A review of mathematical modelling of metal-hydride systems for hydrogen storage applications. Int. J. Hydrogen Energy 41, 3470–3484. https://doi.org/10.1016/j.ijhydene.2015.12.079

Mohan, M., Sharma, M., Sharma, V.K., Kumar, E.A., Satheesh, A., Muthukumar, P., 2019. Performance analysis of metal hydride based simultaneous cooling and heat transformation system. Int. J. Hydrogen Energy 44, 10906–10915. https://doi.org/10.1016/j.ijhydene.2019.02.241

Møller, K.T., Sheppard, D., Ravnsbæk, D., Buckley, C.E., Akiba, E., Li, H.-W., Jensen, T., 2017. Complex Metal Hydrides for Hydrogen, Thermal and Electrochemical Energy Storage. Energies 10, 1645. https://doi.org/10.3390/en10101645

Muthukumar, P., Groll, M., 2010. Metal hydride based heating and cooling systems: A review. Int. J. Hydrogen Energy 35, 3817–3831. https://doi.org/10.1016/j.ijhydene.2010.01.115

Muthukumar, P., Kumar, A., Raju, N.N., Malleswararao, K., Rahman, M.M., 2018. A critical review on design aspects and developmental status of metal hydride based thermal machines. Int. J. Hydrogen Energy 43, 17753–17779. https://doi.org/10.1016/j.ijhydene.2018.07.157

Muthukumar, P., Maiya, M.P., Murthy, S.S., 2005. Experiments on a metal hydride-based hydrogen storage device. Int. J. Hydrogen Energy 30, 1569–1581. https://doi.org/10.1016/j.ijhydene.2004.12.007

Na Ranong, C., Höhne, M., Franzen, J., Hapke, J., Fieg, G., Dornheim, M., Eigen, N., Bellosta von Colbe, J.M., Metz, O., 2009. Concept, design and manufacture of a prototype hydrogen storage tank based on sodium alanate. Chem. Eng. Technol. 32, 1154–1163. https://doi.org/10.1002/ceat.200900095

Nasri, M., Burger, I., Michael, S., Friedrich, H.E., 2016. Waste heat recovery for fuel cell electric vehicle with thermochemical energy storage. 2016 11th Int. Conf. Ecol. Veh.

Renew. Energies, EVER 2016. https://doi.org/10.1109/EVER.2016.7476439

Neises, M., Tescari, S., de Oliveira, L., Roeb, M., Sattler, C., Wong, B., 2012. Solar-heated rotary kiln for thermochemical energy storage. Sol. Energy 86, 3040–3048. https://doi.org/10.1016/j.solener.2012.07.012

Nguyen, H.Q., Shabani, B., 2021. Review of metal hydride hydrogen storage thermal management for use in the fuel cell systems. Int. J. Hydrogen Energy 46, 31699–31726. https://doi.org/10.1016/j.ijhydene.2021.07.057

Nishizaki, T., Miyamoto, K., Yoshida, K., 1983. Coefficients of performance of hydride heat pumps. J. Less-Common Met. 89, 559–566. https://doi.org/10.1016/0022-5088(83)90372-7

NREL, 2004. Technology Brief : Analysis of Current-Day Commercial Electrolyzers, U.S. Department of Energy Office.

Nyamsi, S.N., Lototskyy, M., Tolj, I., 2020. Optimal Design of Combined Two-Tank Latent and Metal Hydrides-Based Thermochemical Heat Storage Systems for High-Temperature Waste Heat Recovery. Energies 13, 1–18. https://doi.org/10.3390/en13164216

Nyamsi, S.N., Lototskyy, M., Tolj, I., 2018a. Selection of metal hydrides-based thermal energy storage: Energy storage efficiency and density targets. Int. J. Hydrogen Energy 43, 22568–22583. https://doi.org/10.1016/j.ijhydene.2018.10.100

Nyamsi, S.N., Lototskyy, M., Tolj, I., 2018b. Selection of metal hydrides-based thermal energy storage: Energy storage efficiency and density targets. Int. J. Hydrogen Energy 43, 22568–22583. https://doi.org/10.1016/j.ijhydene.2018.10.100

Nyamsi, S.N., Tolj, I., 2021. The impact of active and passive thermal management on the energy storage efficiency of metal hydride pairs based heat storage. Energies 14. https://doi.org/10.3390/en14113006

Nyamsi, S.N., Tolj, I., Lototskyy, M., 2019. Metal hydride beds-phase change materials: Dual mode thermal energy storage for medium-high temperature industrialwaste heat recovery. Energies 12. https://doi.org/10.3390/en12203949

Oliva, D.G., Fuentes, M., Borzone, E.M., Meyer, G.O., Aguirre, P.A., 2018. Hydrogen storage on LaNi5−xSnx. Experimental and phenomenological Model-based analysis. Energy Convers. Manag. 173, 113–122. https://doi.org/10.1016/j.enconman.2018.07.041

Omrani, R., Nguyen, H.Q., Shabani, B., 2020. Thermal coupling of an open-cathode proton exchange membrane fuel cell with metal hydride canisters: An experimental study. Int. J. Hydrogen Energy 45, 28940–28950. https://doi.org/10.1016/j.ijhydene.2020.07.122

Omrani, R., Nguyen, H.Q., Shabani, B., 2019. Open-cathode PEMFC heat utilisation to

enhance hydrogen supply rate of metal hydride canisters. Energy Procedia 160, 542–549. https://doi.org/10.1016/j.egypro.2019.02.204

Pardo, P., Deydier, A., Anxionnaz-Minvielle, Z., Rouge´, S., Cabassud, M., Cognet, P., 2014a. A review on high temperature thermochemical heat energy storage. Renew. Sustain. Energy Rev. 32, 591–610. https://doi.org/10.1016/j.rser.2013.12.014

Pardo, P., Deydier, A., Anxionnaz-Minvielle, Z., Rougé, S., Cabassud, M., Cognet, P., 2014b. A review on high temperature thermochemical heat energy storage. Renew. Sustain. Energy Rev. 32, 591–610. https://doi.org/10.1016/j.rser.2013.12.014

Park, C., Tang, X., Kim, K.J., Leland, Q., Gottschlich, J., 2007. Metal hydride heat storage technology for directed energy weapon systems. ASME Int. Mech. Eng. Congr. Expo. Proc. 8, 961–969. https://doi.org/10.1115/IMECE2007-42831

Paskevicius, M., Sheppard, D.A., Williamson, K., Buckley, C.E., 2015. Metal hydride thermal heat storage prototype for concentrating solar thermal power. Energy 88, 469–477. https://doi.org/10.1016/j.energy.2015.05.068

Payá, J., Linder, M., Laurien, E., Corberán, J.M., 2009. Dynamic model and experimental results of a thermally driven metal hydride cooling system. Int. J. Hydrogen Energy 34, 3173–3184. https://doi.org/10.1016/j.ijhydene.2009.01.085

Pelay, U., Luo, L., Fan, Y., Stitou, D., Rood, M., 2017. Thermal energy storage systems for concentrated solar power plants. Renew. Sustain. Energy Rev. 79, 82–100. https://doi.org/10.1016/j.rser.2017.03.139

Peng, X., Root, T.W., Maravelias, C.T., 2017. Storing solar energy with chemistry: The role of thermochemical storage in concentrating solar power. Green Chem. 19, 2427–2438. https://doi.org/10.1039/c7gc00023e

Pęska, M., Dworecka-Wójcik, J., Płociński, T., Polański, M., 2020. The influence of cerium on the hydrogen storage properties of La1-xCexNi5 alloys. Energies 13. https://doi.org/10.3390/en13061437

Poupin, L., Humphries, T.D., Paskevicius, M., Buckley, C.E., 2021. An operational high temperature thermal energy storage system using magnesium iron hydride. Int. J. Hydrogen Energy 46, 38755–38767. https://doi.org/10.1016/j.ijhydene.2021.09.146

Poupin, L., Humphries, T.D., Paskevicius, M., Buckley, C.E., 2020. An experimental high temperature thermal battery coupled to a low temperature metal hydride for solar thermal energy storage. Sustain. Energy Fuels 4, 285–292. https://doi.org/10.1039/c9se00538b

Poupin, L., Humphries, T.D., Paskevicius, M., Buckley, C.E., 2019. A thermal energy storage prototype using sodium magnesium hydride. Sustain. Energy Fuels 3, 985–995.

https://doi.org/10.1039/C8SE00596F

Prieto, C., Cooper, P., Fernández, A.I., Cabeza, L.F., 2016. Review of technology: Thermochemical energy storage for concentrated solar power plants. Renew. Sustain. Energy Rev. 60, 909–929. https://doi.org/10.1016/j.rser.2015.12.364

Rabienataj Darzi, A.A., Hassanzadeh Afrouzi, H., Moshfegh, A., Farhadi, M., 2016. Absorption and desorption of hydrogen in long metal hydride tank equipped with phase change material jacket. Int. J. Hydrogen Energy 41, 9595–9610. https://doi.org/10.1016/j.ijhydene.2016.04.051

Raju, M., Kumar, S., 2012. Optimization of heat exchanger designs in metal hydride based hydrogen storage systems. Int. J. Hydrogen Energy 37, 2767–2778. https://doi.org/10.1016/j.ijhydene.2011.06.120

Reilly, J.J., Wiswall, R.H., 1968a. The Reaction of Hydrogen with Alloys of Magnesium and Nickel and the Formation of Mg2NiH4. Inorg. Chem. 7, 2254–2256. https://doi.org/10.1021/ic50069a016

Reilly, J.J., Wiswall, R.H., 1968b. The Reaction of Hydrogen with Alloys of Magnesium and Nickel and the Formation of Mg2NiH4. Inorg. Chem. 7, 2254–2256. https://doi.org/10.1021/ic50069a016

Rivard, E., Trudeau, M., Zaghib, K., 2019. Hydrogen storage for mobility: A review. Materials (Basel). 12. https://doi.org/10.3390/ma12121973

Ronnebro, E.C.., Whyatt, G.A., Powell, M.R., 2014. Reversible metal hydride thermal energy storage systems, devices, and process for high temperature applications. US 20140238634 A1.

Rönnebro, E.C.E., Whyatt, G., Powell, M., Westman, M., Zheng, F., Fang, Z.Z., 2015. Metal hydrides for high-temperature power generation. Energies 8, 8406–8430. https://doi.org/10.3390/en8088406

Sandrock, G., 1999a. Panoramic overview of hydrogen storage alloys from a gas reaction point of view. J. Alloys Compd. 293, 877–888. https://doi.org/10.1016/S0925-8388(99)00384-9

Sandrock, G., 1999b. A panoramic overview of hydrogen storage alloys from a gas reaction point of view. J. Alloys Compd. 293, 877–888. https://doi.org/10.1016/S0925-8388(99)00384-9

Satya Sekhar, B., Lototskyy, M., Kolesnikov, A., Moropeng, M.L., Tarasov, B.P., Pollet, B.G., 2015. Performance analysis of cylindrical metal hydride beds with various heat exchange options. J. Alloys Compd. 645, S89–S95. https://doi.org/10.1016/j.jallcom.2014.12.272

Satya Sekhar, B., Muthukumar, P., Saikia, R., 2012. Tests on a metal hydride based thermal energy storage system. Int. J. Hydrogen Energy 37, 3818–3824. https://doi.org/10.1016/j.ijhydene.2011.05.114

Schaube, F., Wörner, A., Tamme, R., 2011. High Temperature Thermochemical Heat Storage for Concentrated Solar Power Using Gas–Solid Reactions. J. Sol. Energy Eng. 133, 031006. https://doi.org/10.1115/1.4004245

Shafiee, S., McCay, M.H., 2016. Different reactor and heat exchanger configurations for metal hydride hydrogen storage systems - A review. Int. J. Hydrogen Energy 41, 9462–9470. https://doi.org/10.1016/j.ijhydene.2016.03.133

Shen, D., Zhao, C.Y., 2013. Thermal analysis of exothermic process in a magnesium hydride reactor with porous metals. Chem. Eng. Sci. 98, 273–281. https://doi.org/10.1016/j.ces.2013.05.041

Sheppard, D.A., Buckley, C.E., 2019. The potential of metal hydrides paired with compressed hydrogen as thermal energy storage for concentrating solar power plants. Int. J. Hydrogen Energy 44, 9143–9163. https://doi.org/10.1016/j.ijhydene.2019.01.271

Sheppard, D.A., Corgnale, C., Hardy, B., Motyka, T., Zidan, R., Paskevicius, M., Buckley, C.E., 2014. Hydriding characteristics of NaMgH2F with preliminary technical and cost evaluation of magnesium-based metal hydride materials for concentrating solar power thermal storage. RSC Adv. 4, 26552–26562. https://doi.org/10.1039/C4RA01682C

Shiraki, M., Yakabe, H., Uchida, H., 2013. Efficiency Calculations for SOFC/SOEC Reversible System and Evaluations of Performances of Button-Size Anode-Supported Cell. ECS Trans. 57, 3261–3267. https://doi.org/10.1149/05701.3261ecst

Shkatulov, A.I., Kim, S.T., Miura, H., Kato, Y., Aristov, Y.I., 2019. Adapting the MgO-CO 2 working pair for thermochemical energy storage by doping with salts. Energy Convers. Manag. 185, 473–481. https://doi.org/10.1016/j.enconman.2019.01.056

Singh, A., Maiya, M.P., Murthy, S.S., 2015. Effects of heat exchanger design on the performance of a solid state hydrogen storage device. Int. J. Hydrogen Energy 40, 9733–9746. https://doi.org/10.1016/j.ijhydene.2015.06.015

Singh, A., Maiya, M.P., Srinivasa Murthy, S., 2017. Experiments on solid state hydrogen storage device with a finned tube heat exchanger. Int. J. Hydrogen Energy 42, 15226–15235. https://doi.org/10.1016/j.ijhydene.2017.05.002

Smith, K.C., Fisher, T.S., 2012. Models for metal hydride particle shape, packing, and heat transfer. Int. J. Hydrogen Energy 37, 13417–13428. https://doi.org/10.1016/j.ijhydene.2012.06.087

Solé, A., Martorell, I., Cabeza, L.F., 2015. State of the art on gas-solid thermochemical energy storage systems and reactors for building applications. Renew. Sustain. Energy Rev. 47, 386–398. https://doi.org/10.1016/j.rser.2015.03.077

Souahlia, A., Dhaou, H., Askri, F., Mellouli, S., Jemni, A., Ben Nasrallah, S., 2011. Experimental study and characterization of metal hydride containers. Int. J. Hydrogen Energy 36, 4952–4957. https://doi.org/10.1016/j.ijhydene.2011.01.074

Sunku Prasad, J., Sayantan, J., Muthukumar, P., 2020. Experimental investigation on absorption and desorption characteristics of La0.9Ce0.1Ni5 for hydrogen storage application. Int. J. Energy Res. 1–12. https://doi.org/10.1002/er.5983

Tange, M., Maeda, T., Nakano, A., Ito, H., Kawakami, Y., Masuda, M., Takahashi, T., 2011. Experimental study of hydrogen storage with reaction heat recovery using metal hydride in a totalized hydrogen energy utilization system. Int. J. Hydrogen Energy 36, 11767–11776. https://doi.org/10.1016/j.ijhydene.2011.06.023

Therminol, 2022. THERMINOL VP-1: heat transfer fluid.

Tiwari, S., Sharma, P., 2022. Numerical and Theoretical Evaluation of Coupled Metal-Hydride-Based Thermal Storage System with Embedded Helical Tubes. Energy & Fuels. https://doi.org/10.1021/acs.energyfuels.1c03455

Urbanczyk, R., Peinecke, K., Peil, S., Felderhoff, M., 2017. Development of a heat storage demonstration unit on the basis of Mg2FeH6 as heat storage material and molten salt as heat transfer media. Int. J. Hydrogen Energy 42, 13818–13826. https://doi.org/10.1016/j.ijhydene.2017.02.160

Verga, M., Armanasco, F., Guardamagna, C., Valli, C., Bianchin, A., Agresti, F., Lo Russo, S., Maddalena, A., Principi, G., 2009. Scaling up effects of Mg hydride in a temperature and pressure-controlled hydrogen storage device. Int. J. Hydrogen Energy 34, 4602–4610. https://doi.org/10.1016/j.ijhydene.2008.08.043

Visaria, M., Mudawar, I., 2012. Coiled-tube heat exchanger for High-Pressure Metal Hydride hydrogen storage systems - Part 1. Experimental study. Int. J. Heat Mass Transf. 55, 1782–1795. https://doi.org/10.1016/j.ijheatmasstransfer.2011.11.035

Visaria, M., Mudawar, I., Pourpoint, T., 2011. Enhanced heat exchanger design for hydrogen storage using high-pressure metal hydride - Part 2. Experimental results. Int. J. Heat Mass Transf. 54, 424–432. https://doi.org/10.1016/j.ijheatmasstransfer.2010.09.028

Wang, D., Wang, Y., Huang, Z., Yang, F., Wu, Z., Zheng, L., Wu, L., Zhang, Z., 2019. Design optimization and sensitivity analysis of the radiation mini-channel metal hydride reactor. Energy 173, 443–456. https://doi.org/10.1016/j.energy.2019.02.033

Wang, Y., Chen, Z., 2018. Numerical simulation of thermochemical energy storage in kW-scale based on Mg/MgH2. Energy Procedia 144, 132–142. https://doi.org/10.1016/j.egypro.2018.06.018

Ward, P.A., Teprovich, J.A., Liu, Y., He, J., Zidan, R., 2018. High temperature thermal energy storage in the CaAl 2 system. J. Alloys Compd. 735, 2611–2615. https://doi.org/10.1016/j.jallcom.2017.10.191

Weckerle, C., Bürger, I., Linder, M., 2017. Novel reactor design for metal hydride cooling systems. Int. J. Hydrogen Energy 42, 8063–8074. https://doi.org/10.1016/j.ijhydene.2017.01.066

Weiss-Ungethüm, J., Bürger, I., Schmidt, N., Linder, M., Kallo, J., 2014. Experimental investigation of a liquid cooled high temperature proton exchange membrane (HT-PEM) fuel cell coupled to a sodium alanate tank. Int. J. Hydrogen Energy 39, 5931–5941. https://doi.org/10.1016/j.ijhydene.2014.01.127

Wierse, M., Groll, M., 1996. System performance of a solar-thermal power station with thermochemical energy storage, in: Proceeding of 11th World Hydrogen Energy Conference Stuttgart Germany. pp. 23–29.

Wierse, M., Werner, R., Groll, M., 1991. Magnesium hydride for thermal energy storage in a small-scale solar-thermal power station. J. less-common Met. 174, 1111–1121. https://doi.org/10.1016/S0022-5088(06)80018-4

Wu, Z., Yang, F., Zhang, Z., Bao, Z., 2014. Magnesium based metal hydride reactor incorporating helical coil heat exchanger: Simulation study and optimal design. Appl. Energy 130, 712–722. https://doi.org/10.1016/j.apenergy.2013.12.071

Yan, H., Lu, Z., Jing, Z., Wu, Z., 2020. Study on characteristics of hydrogen fuel cell power generation system using metal hydride as solid-state hydrogen source. Chinese J. Process Eng. 20. https://doi.org/10.12034/j.issn.1009-606X.219173 Study

Yan, J., Zhao, C.Y., 2015. Thermodynamic and kinetic study of the dehydration process of CaO/Ca(OH)2thermochemical heat storage system with Li doping. Chem. Eng. Sci. 138, 86–92. https://doi.org/10.1016/j.ces.2015.07.053

Yan, T., Wang, R.Z., Li, T.X., Wang, L.W., Fred, I.T., 2015. A review of promising candidate reactions for chemical heat storage. Renew. Sustain. Energy Rev. 43, 13–31. https://doi.org/10.1016/j.rser.2014.11.015

Yang, F.S., Wang, G.X., Zhang, Z.X., Meng, X.Y., Rudolph, V., 2010. Design of the metal hydride reactors – A review on the key technical issues. Int. J. Hydrogen Energy 35, 3832–3840. https://doi.org/10.1016/j.ijhydene.2010.01.053

Yang, F.S., Zhang, Z.X., Wang, G.X., Bao, Z.W., Diniz Da Costa, J.C., Rudolph, V., 2011. Numerical study of a metal hydride heat transformer for low-grade heat recovery: Simulation of a MH heat transformer. Appl. Therm. Eng. 31, 2749–2756. https://doi.org/10.1016/j.applthermaleng.2011.04.047

Ye, Y., Lu, J., Ding, J., Wang, W., Yan, J., 2020. Numerical simulation on the storage performance of a phase change materials based metal hydride hydrogen storage tank. Appl. Energy 278, 115682. https://doi.org/10.1016/j.apenergy.2020.115682

Yiotis, A.G., Kainourgiakis, M.E., Kosmidis, L.I., Charalambopoulou, G.C., Stubos, A.K., 2014. Thermal coupling potential of Solid Oxide Fuel Cells with metal hydride tanks: Thermodynamic and design considerations towards integrated systems. J. Power Sources 269, 440–450. https://doi.org/10.1016/j.jpowsour.2014.07.023

Zalba, B., Marin, J.M., Cabeza, L.F., Mehling, H., 2003. Review on thermal energy storage with phase change: materials, heat transfer analysis and applications, Applied Thermal Engineering. https://doi.org/10.1016/S1359-4311(02)00192-8

Zhang, H., Baeyens, J., Cáceres, G., Degrève, J., Lv, Y., 2016. Thermal energy storage: Recent developments and practical aspects. Prog. Energy Combust. Sci. 53, 1–40. https://doi.org/10.1016/j.pecs.2015.10.003

Zhang, S., Yang, F., 2018. A novel multilayer fin structure for heat transfer enhancement in hydride - based hydrogen storage reactor. Int. J. energy Res. 3837–3850. https://doi.org/10.1002/er.4115

Zhuo, Y., Jung, S., Shen, Y., 2021. Numerical Study of Hydrogen Desorption in an Innovative Metal Hydride Hydrogen Storage Tank. Energy and Fuels 35, 10908–10917. https://doi.org/10.1021/acs.energyfuels.1c00666

Appendix-A

Tubular reactor with uniform internal heat generation

Consider a solid cylinder of radius R and length L. The solid cylinder is subjected to uniform internal heat generation of $\dot{q}$. The outer surface of the cylinder is subjected to a convective heat transfer coefficient and fluid temperature of h and T_∞, respectively. The schematic of such an arrangement is shown in Fig. A. 1.

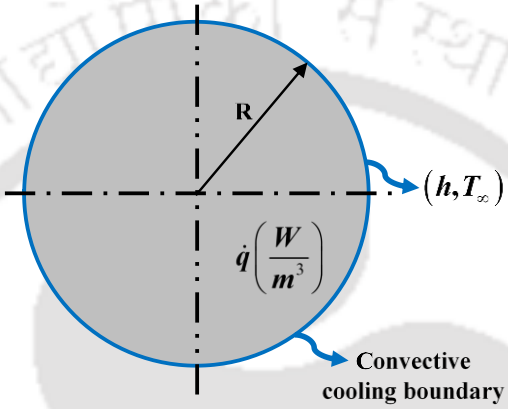

Fig. A. 1. Tubular reactor with uniform internal heat generation subjected to convective cooling on its boundary

The steady state heat conduction equation with internal heat generation in cylindrical coordinates is given by

$$\frac{1}{r}\frac{d}{dr}\left(r\frac{dT}{dr}\right)+\frac{\dot{q}}{k}=0 \qquad (A.1)$$

On integrating

$$T(r)=-\frac{\dot{q}}{4k}r^2+C_1\ln r+C_2 \qquad (A.2)$$

Boundary conditions:

1. $At\ r=0;\ \frac{dT}{dr}=0$

2. $At\ r=R;\ T=T_s\ and\ -k\left.\frac{dT}{dr}\right|_{r=R}=h\left(T_s-T_\infty\right)$

On applying boundary conditions, the temperature distribution inside the tubular reactor is given by

$$T(r)=T_s+\frac{\dot{q}}{4k}\left(R^2-r^2\right) \qquad (A.3)$$

$At\ r=0; T=T_{\max}$

Maximum temperature at the center of the tubular reactor is given by

$$T_{\max} = T_s + \frac{\dot{q}}{4k} R^2 \qquad (A.4)$$

Energy balance: Energy generated = Energy transferred by convective heat transfer

$$\left(\pi R^2 L\right)\dot{q}_g = h\left(2\pi RL\right)\left(T_s - T_\infty\right)$$

The reactor surface temperature is given by

$$T_s = \left(\frac{\dot{q}_g R}{2h}\right) + T_\infty \qquad (A.5)$$

Annular reactor with uniform internal heat generation

Consider a hollow cylinder of length $\boldsymbol{L}$ with inner and outer radii of $\boldsymbol{R_1}$ and $\boldsymbol{R_2}$, respectively. The hollow cylinder is subjected to uniform internal heat generation, $\dot{\boldsymbol{q}}$. The inner surface of the cylinder is subjected to a convective heat transfer coefficient and fluid temperature of $\boldsymbol{h_1}$ and $\boldsymbol{T_\infty}$, respectively. The outer surface of the cylinder is subjected to a convective heat transfer coefficient and fluid temperature of $\boldsymbol{h_2}$ and $\boldsymbol{T_\infty}$, respectively. The schematic of such an arrangement is shown in Fig. A. 2.

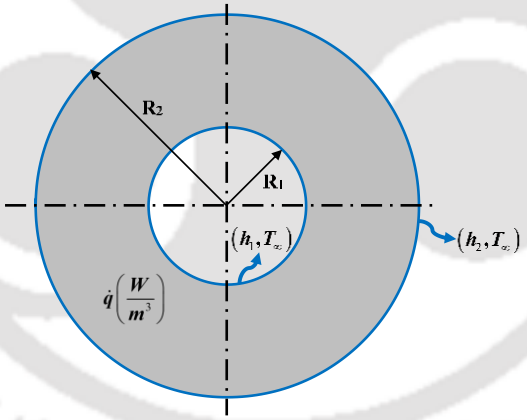

Fig. A. 2. Hollow cylinder with uniform internal heat generation subjected to convective cooling on inner and outer boundaries

Temperature distribution in cylindrical coordinates

$$T(r) = -\frac{\dot{q}}{4k} r^2 + C_1 \ln r + C_2$$

Boundary conditions

$$1.\, At\ r = R_1;\ T = T_{s1};\ and\ -k\left.\frac{dT}{dr}\right|_{r=R_1} = h\left(T_\infty - T_{s1}\right) \qquad (A.6)$$

$$2.\, At\ r = R_2;\ T = T_{s2}\ and\ -k\left.\frac{dT}{dr}\right|_{r=R_2} = h\left(T_{s2} - T_\infty\right) \qquad (A.7)$$

Invoking boundary conditions (2) and (3)

$$T_{s1} = -\frac{\dot{q}}{4k} R_1^2 + C_1 \ln R_1 + C_2 \qquad (A.8)$$

$$T_{s2} = -\frac{\dot{q}}{4k} R_2^2 + C_1 \ln R_2 + C_2 \qquad (A.9)$$

Solving Eqs. (A.8) and (A.9) give

$$C_1 = \frac{\left(T_{s1} - T_{s2}\right) + \frac{\dot{q}}{4k}\left(R_1^2 - R_2^2\right)}{\ln\left(\frac{R1}{R_2}\right)}$$

$$C_2 = T_{s1} + \frac{\dot{q}R_1^2}{4k} - \frac{\left(T_{s1} - T_{s2}\right) + \frac{\dot{q}}{4k}\left(R_1^2 - R_2^2\right)}{\ln\left(\frac{R1}{R_2}\right)} \ln R_1$$

Temperature distribution is obtained as

$$T(r) = -\frac{\dot{q}}{4k} r^2 + \frac{\left(T_{s1} - T_{s2}\right) + \frac{\dot{q}}{4k}\left(R_1^2 - R_2^2\right)}{\ln\left(\frac{R1}{R_2}\right)} \ln r + T_{s1} + \frac{\dot{q}R_1^2}{4k} - \frac{\left(T_{s1} - T_{s2}\right) + \frac{\dot{q}}{4k}\left(R_1^2 - R_2^2\right)}{\ln\left(\frac{R1}{R_2}\right)} \ln R_1 \qquad (A.10)$$

The surface temperatures T_{s1} and T_{s2} are obtained from the energy balance at the respective surfaces.

$$-k \left.\frac{dT}{dr}\right|_{r=R_1} = h_1\left(T_\infty - T_{s1}\right) \qquad (A.11)$$

$$-k \left.\frac{dT}{dr}\right|_{r=R_2} = h_2\left(T_{s2} - T_\infty\right) \qquad (A.12)$$

The surface temperatures are obtained as follows.

$$T_{s1} = \frac{B_2C_1 - B_1C_2}{A_1B_2 - A_2B_1};\quad T_{s2} = \frac{C_1}{B_1} - \frac{A_1}{B_1}\left(\frac{B_2C_1 - B_1C_2}{A_1B_2 - A_2B_1}\right) \qquad (A.13)$$

where,

$$A_1 = \left(\frac{-k}{R_1 \ln\left(\frac{R_1}{R_2}\right)} + h_1 \right);\ B_1 = \frac{k}{R_1 \ln\left(\frac{R_1}{R_2}\right)};\ C_1 = \frac{\dot{q}\left(R_1^2 - R_2^2\right)}{4R_1 \ln\left(\frac{R_1}{R_2}\right)} + h_1 T_\infty - \left(\frac{\dot{q}R_1}{2}\right)$$

$$A_2 = -\frac{k}{R_2 \ln\left(\frac{R_1}{R_2}\right)};\ B_2 = \left(\frac{k}{R_2 \ln\left(\frac{R_1}{R_2}\right)} - h_2 \right);\ C_2 = \frac{\dot{q}\left(R_1^2 - R_2^2\right)}{4R_2 \ln\left(\frac{R_1}{R_2}\right)} - h_2 T_\infty - \left(\frac{\dot{q}R_2}{2}\right)$$

To obtain the location of maximum temperature, i.e., R_{max}

$$-k \left.\frac{dT}{dr}\right|_{r=R_{max}} = 0$$

$$-\frac{\dot{q}}{4k} 2R_{max} + \frac{\left(T_{s1} - T_{s2}\right) + \frac{\dot{q}}{4k}\left(R_1^2 - R_2^2\right)}{\ln\left(\frac{R_1}{R_2}\right)} \frac{1}{R_{max}} = 0$$

$$R_{max} = \pm \sqrt{\frac{2k\left\{\left(T_{s1} - T_{s2}\right) + \frac{\dot{q}}{4k}\left(R_1^2 - R_2^2\right)\right\}}{\dot{q} \ln\left(\frac{R_1}{R_2}\right)}} \qquad (A.14)$$

The maximum temperature inside the annular reactor is obtained by substituting A.14 in A.10.

Boundary conditions

The maximum temperature is obtained under the following boundary conditions:

Concective heat transfer coefficient

$$h = h_1 = h_2 = 250\left(\frac{W}{m^2 K}\right)$$

Fluid temperature, $T_\infty = 250°C$

Volumetric heat generation rate

$$\dot{q}_g = 100000\left(\frac{W}{m^3}\right)$$

Maximum temperatures for the same volume

The maximum temperature of the annular and tubular reactors is compared under constant volume conditions. Twenty cases for constant volume conditions are formulated based on the

standard tube dimensions described in Chapter 3. The dimensions of the annular and tubular reactors for constant volume condition are presented in Table A. 1.

Table A. 1 Dimensions of annular and tubular reactors

Case No.	Annular reactor dimensions		Volume to surface area ratio (mm)	Equivalent diameter of tubular reactor (mm)	Volume to surface area ratio (mm)
	D_1 (mm)	D_2 (mm)			
1	17.15	44.96	7.76	41.56	10.39
2	17.15	57.03	10.65	54.39	13.60
3	17.15	68.81	13.50	66.64	16.66
4	17.15	84.68	17.37	82.93	20.73
5	17.15	97.38	20.50	95.86	23.96
6	21.34	44.96	7.08	39.57	9.89
7	21.34	57.03	9.91	52.89	13.22
8	21.34	68.81	12.73	65.42	16.35
9	21.34	84.68	16.57	81.95	20.49
10	21.34	97.38	19.66	95.01	23.75
11	26.67	44.96	6.26	36.20	9.05
12	26.67	57.03	9.04	50.41	12.60
13	26.67	68.81	11.80	63.43	15.86
14	26.67	84.68	15.59	80.37	20.09
15	26.67	97.38	18.65	93.66	23.41
16	33.40	44.96	5.32	30.10	7.52
17	33.40	57.03	8.01	46.23	11.56
18	33.40	68.81	10.71	60.16	15.04
19	33.40	84.68	14.43	77.81	19.45
20	33.40	97.38	17.45	91.47	22.87

The maximum temperatures obtained for both annular and tubular reactors are plotted in Fig A. 3. Under steady-state conditions, the maximum temperature of the annular reactor is lesser than the tubular reactor in all cases. This is due to the higher heat transfer area and lesser conduction resistance offered by the annular reactor. Hence, annular reactors offer better heat transfer rates than tubular ones for the given volume.

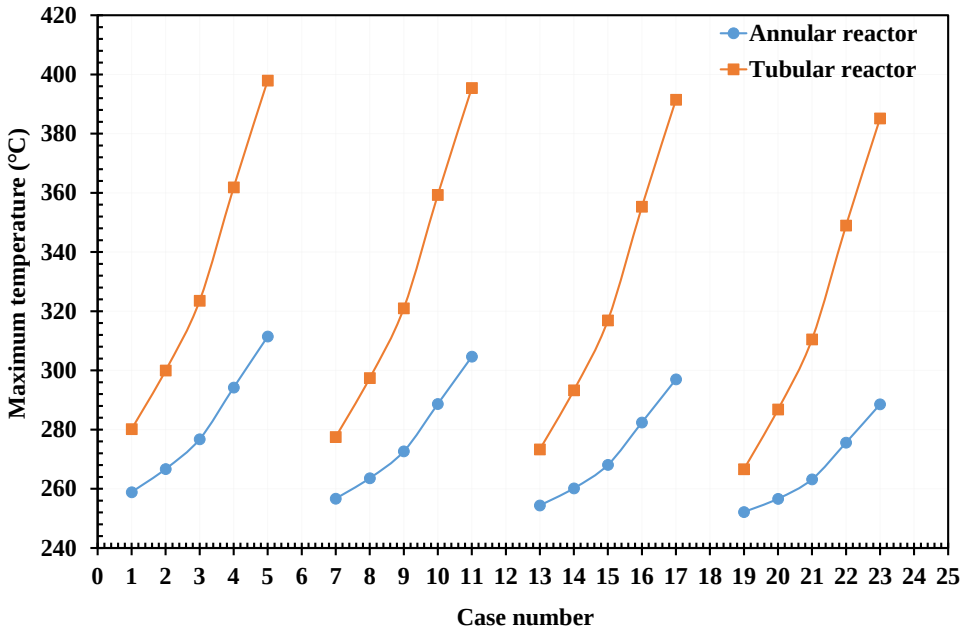

Fig. A. 3. Maximum temperature of tubular and annular reactors under steady state conditions

Appendix - B

Technical specifications of equipment

The measurement during the experimental investigation were conducted using various instruments and equipment. The technical specifications and manufacturing details of the equipment are listed below:

B.1 Mass flow meter

Make	:	Emerson
Model	:	1700R12ABFEZZZ
Type	:	Coriolis mass flow meter
Fluid	:	Hydrogen and any other gas
Flow band	:	0-50 g/s
Accuracy	:	± 0.35%
Precision	:	4 digits after decimal
Sensitivity	:	0.01 g/s
Operating pressure range	:	up to 413 bar at 37 °C
Operating temperature range	:	-10 °C - 80 °C
Output signal	:	4-20 mA

B.2 Data acquisition system (DAQ)

Make	:	Keysight
Model	:	DAQ970A
Scan intervals	:	0-99 hour; 1 ms record time step
Accuracy	:	± 0.004%
Precision	:	6 digits after decimal
Record signals	:	DC (100 mA – 1A; 100 mV – 300 V) AC (100 mA – 2A; 100 mV – 100 V)
Scan temperature	:	-100 – 1820 °C

B.3 Pressure transducer

Make	:	Equinox
Model	:	EQ-PT-1000
Output signal	:	4 – 20 mA
Accuracy	:	± 5% FS
Range	:	0 – 100 bar (LTMH) and 0 – 40 bar (HTMH)

B.4 Thermocouple

Make	:	Industrial Heators
Model	:	Specifically configured for application
Type	:	K-type and T-type
Sensitivity	:	± 0.5 °C (0-100°C) and ± 2.5 °C (250-400°C)

B.5 High temperature recirculating bath

Make	:	Siskin Instruments Co. Pvt. Ltd.
Model	:	HCB200S
Type	:	Recirculating
Fluid	:	Water/Silicon oil
Flow band	:	up to 50 lpm
Bath stability	:	± 0.1 °C
Precision	:	2 digits after decimal
Operating temperature range	:	30 – 180 °C
Bath volume	:	50 l
Heating capacity	:	9 kW
Power input	:	3 Phase AC; 240 V; 32 A (max)
Volts-frequency	:	400 V; 50 Hz

B.6 Low temperature recirculating bath

Make	:	Siskin Instruments Co. Pvt. Ltd.
Model	:	Profichil RCC 7000 ST400
Type	:	Recirculating
Fluid	:	Water/Silicon oil
Flow band	:	up to 50 lpm
Bath stability	:	± 0.1 °C
Precision	:	2 digits after decimal
Operating temperature range	:	-40 – 40 °C
Bath volume	:	50 l
Heating capacity	:	7 kW at 0 °C
Power input	:	3 Phase AC; 240 V; 32 A (max)
Volts-frequency	:	400 V; 50 Hz

B.7 Vacuum Pump

Make	:	Ran-Vac Technologies Pvt. Ltd.
Model	:	Vacpro -2063
Type	:	Rotary vane pump
System cooling	:	Air cooled
Operating fluid	:	Vacpro ultra 3 (6 l)
Pumping speed	:	63 m^3/h (at 50 Hz)

Vacuum pressure range	:	$1 – 10^{-3}$ mbar
Operating temperature range	:	30 – 180 °C
Bath volume	:	50 l
Heating capacity	:	9 kW
Power input	:	2.24 kW
Rotation speed	:	1440 rpm
Frequency	:	50 Hz

B.8 Weighing balance

Make	:	Saffron
Model	:	SES 20TH
Capacity	:	up to 20 kg
Accuracy	:	± 0.1 g

B.9 Valves

Make	:	Swagelok
Model	:	SS-43GS4 and SS-DSS4
Pressure range	:	206 bar and 192 bar at 121 °C
Type	:	Ball valve, Needle valve and Bellow sealed

B.10 Filter

Make	:	Swagelok
Model	:	SS-4F-2
Type	:	Inline
Pressure range	:	60 bar differential pressure
End fittings	:	¼ inch NTP
Pore size	:	2 µm

B.11 Other tube fittings

Make	:	Swagelok
Model (2-way connector)	:	SS-400-6
Model (3-way connector)	:	SS-400-3
Model (4-way connecter)	:	SS-400-2
Model (Braided hose)	:	SS-XT4TA4TA4-78; SS-XT4TA4TA4-24
Model (Tube)	:	THT-3R60-6.35-0.89

List of publications

The outcomes from the present thesis work have been published / communicated to many renowned international journals and presented in several reputed International conferences. The list of all the publications are provided below.

List of research articles

1. J. Sunku Prasad, P. Muthukumar, Design of metal hydride reactor for medium temperature thermochemical energy storage applications, **Thermal science and engineering progress** 37 (2023) 101570. https://doi.org/10.1016/j.tsep.2022.101570.
2. J. Sunku Prasad, P. Muthukumar, Performance and energy efficiency of a solid-state hydrogen storage system: An experimental study on $La_{0.7}Ce_{0.1}Ca_{0.3}Ni_5$, **Applied Thermal Engineering** (2022) 216:119030. https://doi.org/10.1016/j.applthermaleng.2022.119030.
3. J. Sunku Prasad, P. Muthukumar, Experimental investigation on annular metal hydride reactor for medium to large scale hydrogen storage applications. **Journal of Energy Storage** (2021) 44:103473. https://doi.org/10.1016/j.est.2021.103473.
4. J. Sunku Prasad, P. Muthukumar, Design and performance analysis of an annular porous metal hydride reactor for large-scale hydrogen storage applications. **Renewable Energy** (2021) 181: 1155–66. https://doi.org/10.1016/j.renene.2021.09.109.
5. J. Sunku Prasad, P. Muthukumar, Medium temperature thermochemical energy storage system using magnesium-nickel alloy: an experimental study of single and coupled reactors (manuscript under preparation).

List of review articles

1. J. Sunku Prasad, P. Muthukumar, F. Desai, D.N. Basu, M.M. Rahman, A critical review of high-temperature reversible thermochemical energy storage systems. Applied Energy (2019) 254, 113733. doi.org/10.1016/j.apenergy.2019.113733.
2. F. Desai, J. Sunku Prasad, P. Muthukumar, M. Mustafizur, Thermochemical energy storage system for cooling and process heating applications: A review, Energy Conversion and Management 229 (2021) 113617. https://doi.org/10.1016/j.enconman.2020.113617.

Other related publications

1. J. Sunku Prasad, J. Sayantan, P. Muthukumar, Thermal and compressor-driven metal hydride based coupled system for thermal storage, cooling, and thermal upgradation, Thermal science and engineering progress 21 (2021) 100800. https://doi.org/10.1016/j.tsep.2020.100800.
2. F. Desai, A. Atayo, J. Sunku Prasad, P. Muthukumar, M. Rahman, E. Asmatulu, Experimental Studies on Endothermic Reversible Reaction of Salts for Cooling, Heat Transfer Engineering (2020) 1–13. https://doi.org/10.1080/01457632.2020.1777002.

3. J. Sunku Prasad, J. Sayantan, P. Muthukumar, Experimental investigation on absorption and desorption characteristics of $La_{0.9}Ce_{0.1}Ni_5$ for hydrogen storage application, International Journal of Energy Research (2020) 1–12. https://doi.org/10.1002/er.5983.
4. J. Sunku Prasad, R. Anandalakshmi, P. Muthukumar, Numerical investigation on conventional and PCM heat sinks under constant and variable heat flux conditions, Clean Technologies and Environmental Policy (2020) 1–16. https://doi.org/10.1007/s10098-020-01829-8.
5. J. Sunku Prasad, P. Muthukumar, R. Anandalakshmi, H. Niyas, Comparative study of phase change phenomenon in high temperature cascade latent heat energy storage system using conduction and conduction-convection models. Solar Energy (2018) 176:627–37. doi:10.1016/j.solener.2018.10.048.
6. H. Niyas, J. Sunku Prasad, P. Muthukumar, Performance investigation of a lab-scale latent heat storage prototype – Numerical results. Energy Conversion and Management (2017) 135, 188–199. doi.org/10.1016/j.enconman.2016.12.075.

Book chapters

1. Alok Kumar, Nithin N. Raju, J. Sunku Prasad, P. Muthukumar, Engineering Applications of Metal Hydride – Hydrogen System, PATH OF PROGRESS A Voyage of Mechanical Engineering in Sixth IIT, (2021) 161-190.

International Conferences

1. J. Sunku Prasad, P. Muthukumar (2022). Analysis of tubular reactors for sorption based thermal energy storage, heating, and cooling systems, presented at 7th National and 1st International Conference on Refrigeration and Air Conditioning; NCRAC 2022.
2. J. Sunku Prasad, Subham Parashar, P. Muthukumar (2021). Experimental investigation on absorption and desorption characteristics of $La_{0.7}Ce_{0.1}Ca_{0.3}Ni_5$ filled in an annular porous metal hydride reactor, presented at International Conference on Polygeneration (ICP-2021), October 4-6, Universitat Rovira i Virgili, Spain.
3. J. Sunku Prasad, Sayantan Jana, I. Viswa, P. Muthukumar (2019), Experimental investigation on absorption and desorption characteristics of $La_{0.9}Ce_{0.1}Ni_5$ alloy for hydrogen storage application, presented at International Conference on Innovations in Thermo-Fluid Engineering and Sciences (ICITFES-2020), NIT Rourkela.
4. J. Sunku Prasad, Sayantan Jana, P. Muthukumar (2019). Thermodynamic Studies on Metal Hydride-based Tri-generation System for Cooling, Thermal Storage, and Thermal Upgradation, presented at International Conference on Polygeneration (ICP-2019), May 15-17, Kyushu University, Japan.